Stony Brook University

Validation and Improvements of Simulated Cloud Microphysics and Orographic Precipitation over the Pacific Northwest

A Dissertation Presented

by

Yanluan Lin

To

The Graduate School

in Partial Fulfillment of the

Requirements

for the Degree of

Doctor of Philosophy

in

Marine and Atmospheric Science

Stony Brook University

August 2008

Stony Brook University

The Graduate School

Yanluan Lin

We, the dissertation committee for the above candidate for the
Doctor of Philosophy degree, hereby recommend
acceptance of this dissertation.

Dr. Brian A. Colle
Advisor
School of Marine and Atmospheric Sciences, Stony Brook University

Dr. Minghua Zhang
Chairperson, Professor, and Director of ITPA
School of Marine and Atmospheric Sciences, Stony Brook University

Dr. Nicole Riemer
Assistant Professor
Department of Atmospheric Sciences, University of Illinois, Urbana-Champaign

Dr. Dong-Ping Wang
Professor
School of Marine and Atmospheric Sciences, Stony Brook University

Dr. Brad S. Ferrier
Senior Scientist
NOAA National Centers for Environmental Prediction (NCEP)

This dissertation is accepted by the Graduate School

Lawrence Martin
Dean of the Graduate School

Abstract of the Dissertation

Validation and Improvements of Simulated Cloud Microphysics and Orographic Precipitation over the Pacific Northwest

by

Yanluan Lin

Doctor of Philosophy

in

Marine and Atmospheric Science

Stony Brook University

2008

The objective of this thesis is to verify and improve bulk microphysical parameterizations within mesoscale models and to improve some of our understanding of orographic precipitation processes. A moderate orographic precipitation event during the IMPROVE-2 field project is studied using the comprehensive observations and mesoscale model simulations from the WRF model. The intermittent nature of the convective precipitation is highlighted and the impacts of the Oregon coastal range and narrow Cascade ridges on precipitation are quantified using a set of sensitivity runs. As a result of the convective cell development, the precipitation enhancement over the coastal range (500-1000 m above mean sea level [MSL]) was nearly as large as that over the Cascades (1500-2000 m MSL). Simulations selectively eliminating the elevated coastal range and differential land-sea friction across the Pacific coastline illustrate that both effects were important in triggering convection and in producing the observed coastal precipitation enhancement. A sensitivity run employing a smoothed representation of the Cascades illustrates than narrow ridges located on that barrier's windward slope had a relatively small (< 5%) impact on embedded convection and overall precipitation amounts there. This is attributed to the relatively weak gravity wave motions and low freezing level, which limited precipitation growth by riming.

Four Bulk microphysical schemes (BMPs) within WRF are compared and evaluated in terms of the simulated precipitation and microphysical quantities for the event. BMP schemes that overpredict surface precipitation along the Cascade windward slopes have too rapid graupel (rimed snow) fallout. Most BMP schemes overpredict snow in the maximum snow depositional growth region aloft, which results in excessive precipitation spillover into the immediate lee of the Cascades. Sensitivity runs suggest that the graupel accretion of snow generates too much graupel within select WRF BMPs. Snow mass-diameter relationships have a large impact on the snow and cloud liquid water generation. Those BMPs that generate more graupel than snow have shorter cloud residence times and larger removal of available water vapor.

The second part of the study evaluates two bulk microphysical schemes using two cool seasons of high-resolution simulations over the U.S. Pacific Northwest. In addition to the microphysical errors, it is also shown that water vapor transport and synoptic errors are also important contributors to the model precipitation errors. Even with good water vapor transport, model still tends to overpredict when the freezing level is low. The overestimated spillover of snow in the model contributes to overpredcition over the Willamette Valley and the lee of the Cascades when the freezing level is low.

A new bulk microphysical scheme with varying snow characteristics is developed and evaluated for two IMPROVE-2 cases. The new scheme considers both the ice habits and partially rimed particles using a diagnosed riming intensity. Compared with fixed relationships used in traditional BMPs, ice properties (cross-section area, mass, and fall velocity) vary with temperature and riming intensity in the new scheme. It is found the new scheme reduces the snow overprediction aloft and improves the surface precipitation.

Table of Contents

List of Figures

Chapter 2 **Page**

Chapter 3

Chapter 4

Chapter 5

List of Tables

Chapter 3

Chapter 4

Acknowledgements

I would like to thank my advisor, Dr. Brian A. Colle, for his support, guidance, and many fruitful discussions. He taught me how to do things step by step and how to enjoy the sophistication in the real and model world of weather. I am grateful to have Dr. Minghua Zhang, Dr. Dong-Ping Wang, Dr. Nicole Riemer, and Dr. Brad Ferrier (NOAA-NCEP) in my committee. I would like to thank them for valuable suggestions, careful review of my dissertation and encouragements. Discussions and cooperation with Dr. Sandra Yuter (North Carolina State Univ.) improve the seasonal evaluation chapter.

I am grateful to the faculty in the center for teaching the atmospheric and ocean sciences in a fascinating way, especially the courses offered by Dr. Edmund Chang, Dr. Minghua Zhang, and many others. I have learned so much from them. My stay in Stony Brook has been brightened by many friends and colleagues in the center. Wuyin Lin, Moguo Sun, Matt Jones, and Joe Olson always provide warm-hearted help whenever I have computer problems. Weekly basketball games with big fans here give me so much pleasure and help me wade through the hardship of the study and life. Xiaosong Yang, my old classmate and friend, without his help, I could not be this far in my life.

No words can describe my gratitude to my parents, who have devoted their whole lives to raising and educating us four children. I dedicate this work to them and to my wife Fanghua, whom I feel so luck that I can live with.

Chapter 1

Introduction

1.1 Background

a. Orographic precipitation

Mountains have a profound impact on the large-scale atmospheric circulations as well as the local weather. Orographic precipitation has received extensive study and research during the last several decades. Smith (1979) provided an extensive review of orographic precipitation mechanisms, noting the complex interaction between precipitation and the terrain. Rotunno and Houze (2007) emphasized three elements for orographic precipitation: large-scale flow, orographic lifting and condensation, and conversion of condensate to precipitation. More recent review of orographic precipitation (Roe 2005; Smith 2006) summarized further findings from the recent field experiments and studies.

Recent field experiments and observations have facilitated the understanding of orographic precipitation mechanisms significantly. Several recent field projects, such as the Mesoscale Alpine Program (MAP; Bougeault et al. 2001), the Intermountain Precipitation Experiment (IPEX; Schutlz et al. 2002), the California Land-Falling Jets Experiment (CALJET; Neiman et al. 2002), and Improvement of Microphysical Parameterization through Observational Verification Experiment (IMPROVE; Stoelinga et al. 2003) have collected comprehensive kinematic, microphysical, and precipitation datasets over complex terrain. The analysis of recent field datasets has revealed many complex physical mechanisms that can modify orographic precipitation, such as gravity waves in statically stable environments (Bruintjes et al. 1994; Garvert et al. 2007); development of transient turbulent updrafts observed under statically stable conditions in the presence of strong low-level shear (Houze and Medina 2005; Medina et al. 2005); upstream enhancement in statically stable and blocked-flow conditions (Marwitz 1987a,b, Cox et al. 2005, Colle et al. 2005, Rotunno and Ferretti 2001); and windward enhancement in potentially unstable cases (Browning et al. 1974, Hill et al. 1981, Smith et al. 2003, Medina and Houze 2003), which can organize convection into narrow convective bands (Kirshbaum and Durran 2005).

b. Mesoscale model simulations

Our understanding of orographic precipitation has also improved during the past several years with the application of high-resolution models. However, given the complex dynamical, thermodynamical, and cloud microphysical processes involved in

orographic precipitation, progress in quantitative precipitation forecasting (QPF) over complex terrain with regional mesoscale models has been relatively slow during the last two decades (Fritsch et al. 1998; Ebert et al. 2003; Ralph et al. 2005; Richard et al. 2007). Some of the issues include: uncertainties in the initial and boundary conditions, deficiencies in model physics, predictability, and a wide spectrum of scale interactions.

Reliable precipitation forecasts are important over mountainous regions for flash flooding, hydrological forecasting, and transportation. There have been several flash convective flood events in areas of steep terrain, such as the southern slopes of the European Alps (Lin et al. 2001), southern Appalachians (Pontrelli et al. 1999), and the Colorado Front Range (Peterson et al. 2001). Significant increase of computational power has provided the ability to run mesoscale model at high resolution for research and real-time simulations. When run at high resolution (< 5 km), mesoscale models are capable of simulating the complex kinematic and dynamical flow structures around mountainous terrain (Doyle and Bond 2001; Garvert et al. 2005a; Colle et al 2005b; Colle et al. 2008). However, problems in numerical model simulations of orographic precipitation distribution and amounts still remain (Colle et al. 1999, 2000; Colle and Mass 2000; Smith et al. 2003; Garvert et al. 2005b). For example, there was too much precipitation along the steep windward slopes for MM5 simulations using a simple ice scheme (Dudhia 1989) in cool seasons (Colle et al. 2000).

c. Microphysical and precipitation parameterization

When mesoscale models are run at < 5-km grid spacing, orographic precipitation generation is resolved more at the grid scale. As a result, the cloud and precipitation processes are predicted without a convective parameterization, and microphysical parameterizations play an important role on QPF.

Microphysics schemes are classified broadly into two types: bin and bulk schemes. Bin or explicit schemes predict the particle size distribution (PSD) evolution using discrete size or mass bins. Bulk schemes predict one or more bulk quantities (mixing ratio, total number concentration, etc.) by assuming analytical PSDs (Marshall-Palmer distribution, Gamma, etc.). Bulk microphysical parameterizations (BMPs) are the most popular and least computationally expensive schemes. BMPs were initially developed for cloud modeling (Hall 1980; Tripoli and Cotton 1982; Lin et al. 1983; Rutledge and Hobbs 1984; Gilmore et al. 2004). These schemes have been implemented into 3-D NWP models, such as Pennsylvania State University- NCAR mesoscale model (MM5) (Grell et al. 1994), the Weather Research and Forecasting (WRF) model (Skamarock et al. 2005), Regional Atmospheric Modeling System (RAMS) (Pielke et al. 1992), Mesoscale Compressible Community (MC2) model (Benoit et al. 1997), UK Meteorological Office (UKMO) unified model (Cullen 1993), among others, during the last two decades (Dudhia 1989; Hong et al. 1998, 2004; Lynn et al. 2005; Reisner et al. 1998; Thompson et al. 2004; Thompson et al. 2008; Zhao and Carr 1997; Ferrier et al. 2002; Walko et al. 1995; Meyers et al. 1997; Wilson and Ballard 1999). BMPs are also included in cloud resolving models and single column models (Kruger et al. 1995; Wu et al. 1998; Jiang et al. 2000; Tao et al. 2003). BMPs have also been implemented and tested in climate models (Fowler et al. 1996; Lohmann et al. 1999; Rotstayn 1997; Morrison et al. 2005).

In general, BMPs prognose the mixing ratio of cloud water, ice, rain and one or more solid precipitation species (e.g., snow, graupel, hail) and parameterize complex cloud and precipitation processes. The original BMPs are one-moment schemes, which predict only the mixing ratio of hydrometeor species with prescribed particle size distributions. An added level of complexity to the BMPs is the two-moment approach, in which both the total number concentration and mixing ratio of various hydrometeors are prognosed. Ferrier (1994) developed a two-moment BMP including ice crystal, snow, graupel, and hail. Meyers et al. (1997) developed a comprehensive two-moment scheme that calculates number concentrations of all forms of hydrometeors. Girard and Curry (2001) applied a two-moment BMP to simulate the Arctic low-level clouds. Morrison and Pinto (2005) tested a two-moment BMP to predict Arctic clouds. Higher-moment BMPs have also been developed and tested (Milbrandt and Yau 2005; Milbrandt et al. 2008).

Numerous deficiencies in BMPs have been identified (Manning and Davis 1997; Reisner et al. 1998; Colle et al. 1999, 2000; Colle and Mass 2000; Garvert et al. 2005b; Colle et al. 2005a). Vaillancourt et al. (2003) found that Mesoscale Compressible Community (MC2) model (Benoit et al. 1997) generally overpredicts (underpredicts) both the presence and the quantities of ice water content (supercooled liquid water content). Using the Thompson et al. (2004) scheme within MM5 resulted in snow overprediction aloft in the 13-14 December 2001 IMPROVE-2 event over central Oregon Cascades (Garvert et al. 2005b). This resulted in excessive spillover of snow over the crest into the lee off the Cascades during a period of strong low-level cross barrier flow (Garvert et al. 2005a,b). This snow overprediction aloft has not been improved using a triple-moment BMP for the same IMPROVE event (Milbrandt et al. 2008). Using a microphysical budget, Colle et al. (2005a) found that the largest water vapor loss aloft for this IMPROVE case was associated with condensation and snow deposition, while the windward surface precipitation resulted primarily from accretion of cloud water by rain, graupel fallout and melt, and snow melt. In contrast, for IPEX IOP3 over Wasatch Mountain of Utah (Colle et al. 2005b), the Thompson et al. (2004) scheme within MM5 at 1.33-km grid spacing produced too little snow aloft. Although these case studies indicated some similar results, discrepancies among them also indicated a large sensitivity of BMPs to particular environmental conditions.

1.2 Motivation

Most previous studies of orographic precipitation have focused on storms with heavy precipitation (Colle and Mass 2000; Ferretti et al. 2003). Several potential BMP deficiencies have been noted for these cases, but it is unclear whether these results will carry over to other more moderate events. For this thesis, a moderate orographic precipitation event is analyzed using the comprehensive observational datasets collected during the IMPROVE-2 and WRF simulations. A new BMP scheme intended to improve the microphysics aloft and surface precipitation forecast is proposed and tested using the 4-5 and 13-14 December cases of IMPROVE-2.

Since poor QPF forecasts can result from errors other than precipitation parameterizations (Ebert et al. 2003), it is also important to put the IMPROVE results in context with a larger sample of precipitation events over the Pacific Northwest. Two cool seasons of simulations over the Pacific Northwest were conducted to investigate factors

influencing winter QPFs. Simulations of a variety of storms were analyzed and verified using a WSR-88D radar, radiosonde, and precipitation gauge data. The model QPF performance on ambient conditions, such as freezing level height and stability, is investigated.

Specifically, the goals for the thesis are to:

* Understand the orographic precipitation mechanisms for a particular case study before validating the microphysics. Determine the impact of the narrow ridges of the coastal range on the precipitation structures as compared to the wider Cascade barrier.
* Quantify the differences in the BMPs in the Weather Research and Forecasting (WRF) model on surface precipitation and microphysical structures aloft. Explain the differences between the various schemes.
* Investigate the potential deficiencies in these BMPs by verifying the model against comprehensive observations collected during the IMPROVE-2
* Determine the systematic bias of BMPs and analyze the precipitation forecast errors using two cool-season simulations over the Pacific Northwest using radar data, surface precipitation gauges, and sounding data.
* Develop a new BMP scheme, which addresses some of the deficiencies found in previous studies.

The thesis is composed of four parts. The first section utilizes the comprehensive observational datasets of IMPROVE-2 as well as high-resolution mesoscale model simulations to study a precipitation event over central Oregon and to evaluate the model's simulated kinematic fields and microphysical outputs. Several BMPs within WRF are also compared and evaluated using the datasets and presented in section 2. The third part evaluates two cool-seasons of high-resolution mesoscale simulations in terms of surface precipitation, precipitation structures aloft, and water vapor transport over the Pacific Northwest. This also provides a long-term evaluation of the BMP. The fourth part describes a new BMP and its evaluation for two IMPROVE-2 events.

Chapter 2
Orographic Modification of Convection and Flow Kinematics by the Oregon Coastal Range and Cascades during IMPROVE-2

2.1 Introduction

Several recent field projects, such as the Mesoscale Alpine Program (MAP; Bougeault et al. 2001), the Intermountain Precipitation Experiment (IPEX; Schultz et al. 2002), and IMPROVE (Stoelinga et al. 2003) have collected comprehensive kinematic, microphysical, and precipitation datasets over complex terrain. The primary objectives of these field studies were to advance understanding of moist dynamics and cloud microphysics associated with orographic precipitation and to improve bulk microphysical parameterizations (BMPs) in mesoscale models, which will ultimately help improve quantitative precipitation forecasts.

Since orographic precipitation is sensitive to the static stability and terrain variability, this has also been an active area of research. The importance of gravity waves in modulating orographic precipitation was highlighted by Garvert et al. (2005a; 2007) using aircraft in situ and radar observations as well as high resolution (1.33-km grid spacing) simulations from the Penn-State National Center for Atmospheric Research (NCAR) Mesoscale model (MM5). They showed enhancement of vertical motions and precipitation over the narrow ridges of the windward (west-facing) slopes of the Oregon Cascades during the 13-14 December 2001 IMPROVE-2 heavy rainfall event, which resulted in maxima in cloud water and snow production extending up to 6 km MSL over these ridges. When the low-level flow is blocked, the orographic precipitation is shifted upstream of the windward slope (Colle et al. 2005; Rotunno and Ferretti 2001; Bousquet and Smull 2003), and there are less gravity wave and precipitation perturbations over the windward ridges (Colle 2008).

Recent field studies have also added insight into the details of precipitation evolution during the passage of baroclinic waves over complex terrain. Ground-based radar from MAP revealed that in some cases the orographic precipitation enhancement was relatively steady over the windward slope but occasionally there were embedded convective cells of precipitation that propagated up over the barrier and locally intensified over the steep Alpine ridges (Smith et al. 2003). Using vertically-pointing radar data from IMPROVE-2, Medina et al. (2007) developed a conceptual model of the commonly observed progression of precipitation features as extratropical cyclones

traverse mountainous terrain in the Pacific Northwest. As a cyclone approaches, the precipitation echo first appears aloft and descends towards the surface (Leading Edge Echo or LEE). During the time of maximum large-scale ascent, the precipitation consists of a vertically-continuous layer extending from the windward slope up to 5-6 km MSL that persists for several hours. During this period, there is often a Double Maximum Echo (DME) over the windward slopes. One maximum is associated with the melting-induced bright band. A secondary maximum (1-2.5 km above the bright band) results from or is enhanced by interaction of the baroclinic system with the terrain, according to Medina et al. (2007). Finally, the Shallow Convection Echo (SCE) stage is associated with low echo tops in the more unstably stratified later portion of the storm, which is typically post-frontal.

A variety of synoptic environments were observed during IMPROVE-2. Most of the detailed orographic precipitation and microphysical studies conducted thus far have focused on the strong cross-barrier flow events with well-defined frontal passages under moist stable conditions, such as 13-14 December 2001 and 27-28 November 2001 (Garvert et al. 2005a; Medina et al. 2007). These cases involved a deep orographic cloud over the Cascades, with little transient convective activity propagating over the Cascades. These events need to be compared with storms featuring weaker cross barrier flow and stability, since these parameters impact terrain-induced gravity wave contributions to orographic precipitation (Colle 2004; Smith and Barstad 2004) as well as the stratiform vs. convective nature of the precipitation (Rotunno and Houze 2007). There have been no formal IMPROVE-2 studies highlighting the evolution of intermittent convection from the coastal range to the Cascades, so this study focuses on the 4-5 December event, which had a reduced cross-barrier flow, weaker stability, and lower freezing level than previously documented IMPROVE-2 cases.

Most previous simulation studies for IMPROVE-2, IPEX, and MAP events have utilized the Pennsylvania State-National Center for Atmospheric Research Mesoscale Model (MM5). The Weather Research and Forecasting (WRF, Skamarock et al. 2005), which is becoming more widely used, includes higher order numerics and new BMPs [such as that developed by Thompson et al. (2004)]. There have been few formal studies of orographic precipitation using WRF, so this study provides an opportunity to evaluate this relatively new model using the unique high-resolution IMPROVE-2 dataset.

The objectives of this chapter are to document the passage of a baroclinic wave accompanied by embedded convection over the coastal range and Cascade Mountains of western Oregon in order to (1) describe the flow kinematics, precipitation evolution and orographic modification and compare with other IMPROVE-2 events, (2) verify the WRF-simulated mesoscale flow and precipitation patterns using comprehensive in situ and aircraft datasets, and (3) highlight the intermittent nature of the convective precipitation and isolate the respective impacts of the Oregon coastal range and narrow Cascade ridges on precipitation over this complex region. The case analyzed herein is the 4-5 December 2001 IMPROVE-2 event, corresponding to Intensive Observing Period (IOP) 6. Next chapter will highlight the microphysical observations and verification of the WRF BMPs for this event.

2.2 Data and Methods

a. Observational datasets

The IMPROVE-2 project collected a comprehensive set of observations to evaluate the thermodynamic and kinematic structures as well as cloud microphysics of winter storms (Stoelinga et al. 2003). The primary observational facilities during the 4-5 December event used in this study are indicated in Fig. 2.1b. The NCAR S-Pol radar, which was situated in the lower western foothills of the Cascade Mountains, provided a temporally continuous three-dimensional view of the precipitation structures extending from the adjacent Willamette Valley eastward up to the Cascade crest. The University of Washington (UW) mobile sounding unit and NCAR integrated sounding system (ISS) at Irish Bend (IB) were used to obtain the winds and stratification just upstream of the Cascades. The National Oceanic and Atmospheric Administration/Earth System Research Laboratory (NOAA/ESRL) vertically pointing S-band radar (S-Prof) was deployed on the windward slope of the Oregon Cascades at ~500 m MSL (see MB on Fig. 2.1b). Specifications for S-Prof are provided by White et al. (2003), while Stoelinga et al. (2003) and Medina et al. (2007) describe its operation in IMPROVE-2.

The NOAA P-3 and UW Convair aircraft collected in-situ cloud microphysical data as well as the ambient wind, temperature, and moisture data over the Cascades. Since there were limited observations by the Convair for this IOP, this study utilizes the data from the NOAA P-3, which executed multiple flight legs in order to provide continuous, high-resolution dual-Doppler radar coverage (Fig. 2.1b). As described in Bousquet and Smull (2003a), volumetric radial velocity and reflectivity measurements were edited to remove ground clutter contamination, noise, and other artifacts. The radial velocity data were then interpolated to a composite Cartesian grid (240 km x 170 km) with 1-km grid spacing in the horizontal and 0.25 km resolution in the vertical up to 10 km MSL (or echo top, if lower). Radial velocities from the P-3 tail radar were synthesized to estimate 3-D airflow over the Cascades as in Garvert et al. (2007).

b. Model setup

The WRF v2.2 was utilized to simulate the 4-5 December 2001 IMPROVE-2 event. The 36-, 12-, and 4-km domains are the same as those used in Garvert et al. (2005a; 2007) for the 13-14 December event (Fig. 2.1a), while the inner 1.33 km domain was extended farther westward to include the Oregon coastal range and adjacent Pacific waters. Two simulations were completed using initial and time-dependent boundary conditions from the NCEP GFS 6-h analyses. The first 18-h WRF simulation was initialized at 1200 UTC 04 December 2001, while another 12-h WRF run was started at 0000 UTC 5 December. Two separate control simulations were needed, since the first (earlier) simulation had too much subsidence drying with the mid-level trough after 0600 UTC 5 December and thus too little precipitation. Thirty-two unevenly spaced half-sigma levels were used in the vertical, with maximum resolution in the boundary layer. The control simulation used the updated Reisner2 scheme (Thompson et al. 2004), updated Kain-Fritsch cumulus parameterization (Kain 2004), and Eta (MYJ) PBL (Janjic 1994), which are similar to those physics used in Garvert et al. (2005a). The convective parameterization was turned off for the 4- and 1.33-km domains. All simulations used the positive definite advective (PDA) scheme in WRF v2.2 for the moisture and hydrometeor advection (Skamarock 2006). As compared to an equivalent WRF run without PDA, the

PDA resulted in a large (20-30%) reduction of precipitation in the more convective areas near the coast at 1.33-km grid spacing. The non-PDA advective scheme has been shown to generate artificial water mass after setting negative mixing ratios to zero (Braun 2006).

2.3 Synoptic Scale Evolution

a. Upper-level and surface analysis

The 4-5 December event featured two short-wave troughs rotating around a broad upper-level trough centered over the Pacific Northwest. At 1200 UTC 4 December 2001 (Fig. 2.1a), the first 500 mb short-wave crossed over the IOP area. Meanwhile, another shortwave trough was located around 140 ^{o}W, in association with a 60 m s^{-1} jet at 300 mb (Fig. 2.1a) and an area of mid- and upper-level clouds around 47 ^{o}N, 130 ^{o}W (Fig. 2.2a). The open-cellular convection to the north and east of this offshore cloud shield at this time suggests that this baroclinic development was occurring in a relatively cold and unstable air mass left in the wake of the first short-wave trough. At 850 mb (not shown), there was a well-defined trough over eastern Washington and Oregon, with west-northwesterly flow of ~15 m s^{-1} over the study region.

As the offshore 500-mb trough approached the Pacific Northwest coast at 0000 UTC 5 December in the NCEP analysis and the 12-h WRF forecast (Figs. 2.3a,b), the mid- and upper-level clouds increased their spatial coverage, and cloud tops cooled to ~220 K near the Oregon coast (Fig. 2.2b). This development occurred in a favored region for upward motion in the downstream exit region of a 70 m s^{-1} jet along the west side of the advancing trough (Fig. 2.3b). The WRF realistically predicted the 850-mb trough that extended southward along the southwest British Columbia, Washington and Oregon coasts at this time (Figs. 2.4a,b), where winds shifted from west-southwesterly over land to west-northwesterly a few hundred kilometers offshore. The north-south trough orientation is similar to that found in the 13-14 December and 28-29 November IMPROVE-2 storms examined by Medina et al. (2007); however, the trough observed at 0000 UTC 5 December was not as sharp and was accompanied by only weak warm advection. Compared to these other two IMPROVE-2 events, the 850-mb winds of 12-15 m s^{-1} at 0000 UTC 5 December were less than half as strong, while the 850-mb temperatures over the Cascades (-4 ^{o}C) were about 10 ^{o}C cooler.

Across western and central Oregon at 0000 UTC 5 December, both surface observations and the 4-km WRF run showed 5-10 m s^{-1} southwesterly winds at the coast that were deflected northward by the Cascades and thus flowing down the pressure gradient within the Willamette Valley (Fig. 2.5). The wind directions suggest that some of this air had previously crossed over the coastal terrain and merged with channeled flow arriving from the south.

By 1200 UTC 5 December, the 500-mb trough axis had advanced into western Washington and Oregon (not shown). The associated 850-mb trough was located over eastern Oregon at this time (Figs. 2.4c,d), and weak cold advection and west-northwesterly flow covered the study region. The 12-h WRF forecast realistically captures the trough's position and strength of the cross-barrier flow at this time.

b. Vertical Structure

A time-height section of winds from the 915-MHz wind profiler at Irish Bend (IB in Fig. 2.1) and equivalent potential temperatures (θ_e) derived from the UW and Salem (SLE) soundings illustrates the observed wind and temperature profiles over western Oregon during the event (Fig. 2.6a) may be compared to those depicted by the 1.33-km WRF simulation (Fig. 2.6b). Early in the IOP (1800 UTC 4 December), there were relatively weak (< 10 m s^{-1}) south-southwesterlies below 1-km MSL associated with the terrain blocked and channeled flow within the Willamette Valley, which veered to westerly at 7-10 m s^{-1} above 1.5 km MSL. By 0000 UTC 5 December, the low-level southwesterlies deepened to 3-km MSL and increased to 15-20 m s^{-1} between 1-3 km MSL as the upper-level short-wave trough approached. Meanwhile, the veering from 2 to 4-km MSL between 2100 UTC 4 December and 0300 UTC 5 December is indicative of weak warm advection (Fig. 2.4). After 0300 UTC 5 December, the observed stratification was weaker above 5-km MSL, where $d\theta_e/dz \sim 0$. The model simulated the increased southwest winds and warm advection from 2230 UTC 04 to 0330 UTC 05 December 2001 (during the period of the P-3 flight) as well as the decrease in stability aloft.

A forward-tilted trough extending from the surface to 3-km MSL crossed the IB site at 0600 UTC 5 December at 3-km and at the surface at 0900 UTC 5 December (Fig. 2.6a). A reduction in stability accompanied the trough's passage around 3-4 km MSL, with equivalent potential temperatures decreasing after trough passage. The simulated trough-induced windshift at IB was weaker than observed, especially between 2-3 km MSL. During the trough passage, the simulated θ_e values were higher than those observed and the simulated stratification at low-levels was weaker than what was observed. However, there was no sounding data collected for this period (06-12 UTC 5 Dec), which limits the extent to which the model can be validated. The model produced too little drying in the lowest two kilometers after trough passage, so simulated θ_e's were 3-4 K greater than observed after 0900 UTC 5 December.

The UW sounding was used to quantify the stratification and the vertical wind profile just upwind of the Cascades (Fig. 2.1b). At 2100 UTC 4 December, the observed cross-barrier (westerly-component) flow increased from near -3 m s^{-1} at the surface to +15 m s^{-1} at 1.75 km MSL (black line in Fig. 2.7a). The WRF underpredicted the cross-barrier flow at the 1.5 km level and hence underestimated the strength of the low-level shear (gray line in Fig. 2.7a). The WRF-simulated potential temperature profile was close to what was observed (Fig. 2.7b), but the θ_e values in the WRF simulation were 1-2 K greater than observed (Fig. 2.7b), suggesting that the model was slightly too moist. The square of the moist Brunt-Väisälä frequency (N_m^2), as defined in Durran and Klemp (1982), was less than zero just below 1.5 km MSL in both the model and observations (solid gray and black lines in Fig. 2.7c, respectively). Both the observed and simulated atmospheres were sub-saturated below 700 m (not shown), indicating stable stratification at these levels (dry N of ~0.005 s^{-1}), which favored some near-surface flow blocking (Fr = $U/Nh_m \sim 0.8$, where h_m is 2.0 km and U of 8 m s^{-1}) as previously noted in Fig. 2.5. Meanwhile, between 0.7 km and 2.0 km, the 10-15 m s^{-1} cross barrier flow (Fig. 2.7a) was saturated with weak stratification (Fig. 2.7c), so there was little potential for flow blocking at these levels.

Although there were no soundings available at the Oregon coast, Fig. 2.7c shows the WRF-simulated N_m^2 profile at point A (near the coast, Fig. 2.8b) at 2100 UTC 4

December (long-dashed gray line in Fig. 2.7c). The air over the coast was saturated above 0.7 km MSL and in the lowest 2 km MSL it was potentially unstable ($N_m^2 < 0$ in Fig. 2.7c, with maximum CAPE ~200 J kg^{-1} [not shown]). Stratification near the coast was also somewhat more unstable than that farther inland over the windward slopes of the Cascades (solid gray curve in Fig. 2.7c).

By 0330 UTC 5 December, the moist static stability in the observed UW sounding had increased to 0.02 s^{-1} around 1.0 km MSL (Fig. 2.7f), which coincided with the freezing level. This is suggestive of additional cooling from melting of snow and evaporation below this level. The model failed to reproduce this stable layer, in part because the simulated PBL was too moist (saturated) below 1.0 km as revealed by the θ_e profile (Fig. 2.7e). The WRF realistically predicted the winds (Fig. 2.7d), although it had a somewhat greater cross-barrier component below 1-km, which is indicative of underestimated near-surface blocking in the model. The average moist Froude number below 1.0 km at the UW site was ~0.75 and 1.0 in the observed and WRF-simulated profiles, respectively, based upon respective average N_m values of 0.008 s^{-1} and 0.006 s^{-1} and similar layer-averaged U values near 10 m s^{-1} (Fig. 2.7d, f). Meanwhile, above 1.0 km the mean stability was slightly less (N_m ~0.005 s^{-1}), the flow was stronger (U ~15 m s^{-1}), and parcels only had to surmount the remaining ~1.0 km of the Cascades. Thus the moist Froude number was ~3.0, which suggests little if any flow blocking above mid-mountain level. At this time, the layer of potential instability below 2 km MSL observed earlier at the coast (point A in Fig. 2.8b) still persisted (long-dashed gray line in Fig. 2.7f).

2.4 Mesoscale Precipitation and Kinematics

a. Precipitation evolution

Figure 2.8 shows representative 1.5° elevation scans of S-Pol radar reflectivity and 1.33-km WRF simulated reflectivity[1] at 700 mb, which highlights the change in the precipitation structures during the event. Due to the uncertainties inherent in obtaining simulated reflectivity, only qualitative comparisons are made between observed and simulated reflectivity structures. Early in the IOP at 2000 UTC 4 December (Figs. 2.8a,b), convective cells were observed over the Cascades and coastal range, consistent with the prevailing low-level potential instability at this time. The model had less instability (Fig. 2.7c) and hence reduced convective activity as compared to the observations. By 0000 UTC 5 December (Figs. 2.8c,d), the observed precipitation became more widespread and stratiform over the Cascades. By 0400 UTC 5 December, the time preceding the mid-level trough passage (Fig. 6), the precipitation coverage increased and reached its maximum extent around the radar (Fig. 2.8e,f). The precipitation was mainly stratiform (< 30 dBZ) with some embedded convective cells over the coastal range and around the radar site. By 0800 UTC 5 December, a time coinciding with the passage of the mid-level trough (cf. Fig. 2.6), the precipitation had

[1] Model-simulated reflectivities were calculated using empirical relations based on the model cloud and precipitation mixing ratios as in Koch et al. (2005), with modifications to the variable slope intercept for snow based on Thompson et al. (2004).

become more cellular to the north of the S-Pol site (Fig. 2.8g,h). As shown in Fig. 8, the model simulation realistically captured the overall evolution of the precipitation.

A series of west-to-east cross sections (denoted AB in Fig. 2.8b) illustrate the evolving precipitation pattern over the Cascades and coastal range (Fig. 2.9). At 2000 UTC 4 December (Fig. 2.9a,b), both the radar and 1.33-km WRF simulation depict narrow convective plumes below 4-km MSL within the broader precipitation shield blanketing the coastal range and Cascades. According to the 1.33-km WRF simulation (not shown), some of these convective cells originated well offshore over the eastern Pacific, which is consistent with the open cellular convection in the satellite imagery early in the event (Fig. 2.2a). The cells intensified as the airflow ascended over the coastal range (Figs. 2.9b,d), releasing potential instability at low-levels. Meanwhile, reflectivity values decreased sharply toward the lee of the Cascades as a result of lee-side subsidence accompanying a moderate standing wave anchored to the crest (Fig. 2.9b).

The precipitation coverage along cross-section AB increased by 0000 UTC 5 December (Fig. 2.9c,d). Some of the strongest echoes at this time were over the Willamette Valley near the S-Pol site. Both observed and simulated reflectivity values and echo coverage continued to increase over the windward Cascade slopes until 0400 UTC 5 December (Fig. 2.9e,f). At this time the midlevel reflectivity contours (12-18 dBZ) generally sloped upward so as to parallel the underlying terrain. Meanwhile, narrow convective plumes had developed 25-50 km to the west of the S-Pol between 5 and 7-km MSL in conjunction with decreasing stability in this layer with the approach of the upper-level trough (Fig. 2.6a). The simulated stability was also weak in this layer (Fig. 2.6b), but the model did not generate any corresponding elevated convection. Precipitation spillover east of the Cascade crest had increased in comparison to a few hours earlier. This trend continued until 0800 UTC 5 December (Figs. 2.9g,h), with substantially more precipitation (including embedded convective cells) extending into the lee of the Cascades as the upper-level trough crossed the barrier and moved over eastern Oregon.

In order to further illustrate the transient and convective nature of the precipitation during this event, Figure 2.10 shows six observed S-Pol RHI scans along AB every ~22 minutes from 0013 UTC to 0200 UTC 5 December. At 0013 UTC (Fig. 2.10a), there was an intense precipitation cell (> 24 dBZ) over the Willamette Valley (cell number 1), while there was broader area of enhanced precipitation over the Cascade windward slope. Cell number 1 moved eastward such that by 0139 UTC it was over the Cascade crest (Fig. 2.10e), and by 0200 UTC it dissipated in the lee (Fig. 2.10f). Meanwhile, cell number 2 moved onshore between 0013 and 0056 and became enhanced over the coastal range (Figs. 2.10a-d), and subsequently weakened over the Willamette Valley (Figs. 2.10e,f). Cell number 3 made landfall and became enhanced over the coastal range between 0118 and 0200 UTC 5 December, while relatively steady enhanced precipitation was observed over the Cascade windward slope.

Figure 2.11 shows Hovmoller-type plots (i.e., as a function of time and distance from the radar along section AB from 1900 UTC 4 December to 1200 UTC 5 December 2001) comparing maximum reflectivity values above 2.0-km MSL as derived from S-Pol observations and the 1.33-km WRF simulation. This level was chosen since it is high enough to exclude bright-band contamination near the melting level yet low enough to

capture the essential pattern of orographically enhanced precipitation[2]. During the first ~7 hours of the event, both the S-Pol and WRF showed areas of slightly enhanced reflectivity over the Pacific Ocean that further intensified as they reached the coastal range. Beginning around 1900-2100 UTC 4 December, scattered convection (both observed and simulated) increased in coverage over the windward slopes of the coastal range and Cascades, with little spillover beyond the Cascade crest. Cells developed over the coastal range and propagated eastward over the Cascades[3], weakening as they passed over the east side of the coastal range as a result of subsidence in the lee of this modest barrier (Fig. 2.9). The WRF simulation produced more cells over the coastal range than what was observed (Fig. 2.8c,d), thus it had more cell streaks on the Hovmoller plot. This suggests that the WRF simulation may have been slightly more unstable than observed in the coastal region.

After 0000 UTC 5 December there was a gradual increase in the amount of precipitation spilling over the Cascade crest. With the trough's approach between 0200 UTC 5 December and 0700 UTC 5 December, the precipitation intensified over the Cascades and became more widespread in the S-Pol observations (Fig. 2.11), while new clusters of cells continued to be enhanced over the coastal range and then advanced eastward over the Cascades. The maximum reflectivities in the WRF simulation extended to the second peak near the crest (at ~80 km in Fig. 2.11a), which was less pronounced in the S-Pol, suggesting that the model may have produced too much precipitation and spillover beyond the crest. By 0700 UTC 5 December, the trough had passed over the Willamette Valley at around 4-km MSL (Fig. 2.6), and the precipitation weakened over the coastal range and Cascades. Following passage of the frontal rainband over the S-Pol site at 0900 UTC 5 December, the precipitation became more scattered and convective in both the observations and simulation.

The reflectivity sequence seen during the 4-5 December case as illustrated in Fig. 2.11 has some similarities to the convective structure evinced during MAP IOP2b (Asencio et al. 2003; Smith et al. 2003; Georgis et al. 2003; and Rotunno and Houze 2007) as southerly and statically unstable airflow ascended the Apennines, a coastal barrier south of the Alps. In the lee of the Apennines, subsidence weakened the cells, which then drifted northward and became embedded in the stratiform, orographically-

[2] It is possible that the observed values of maximum reflectivity are underestimated at ranges > 75 km from the radar (where the base of the echo intersects the 2.0 km MSL). However this scenario is unlikely given the large degree of embedded convection that was observed in this case. The cells over the coast and farther upstream have high echo tops that extend well above 3-4 km MSL, i.e., to levels where the reflectivity is well sampled even at far ranges (Figs. 9, 10).

[3] The pulsing cell intensity in the simulated output is an artifact of constructing the plot using 10-minute output to match the frequency of the S-Pol data (available only every 11 minutes), which causes artificial gaps in the reflectivity intensity versus time. Since the simulation generated more cells than observed over the coastal range (Figs. 8c,d), the gaps between the WRF-simulated cells are more pronounced than in the S-Pol observations.

forced cloud over the Alps and increased their intensity over local peaks (Asencio et al. 2003, Medina and Houze 2003, Smith et al. 2003).

b. NOAA P-3 observations

The simulated precipitation structures and airflow over the Cascades were compared with the winds derived from the NOAA P-3's Doppler radar data obtained from legs 1-4 between 2300 and 0030 UTC 5 December (Fig. 2.1b). At 1.5 km MSL, the local maxima of reflectivity were not clearly co-located with the individual ridges at this time (Fig. 2.12a,b). The observed winds at 1.5 km MSL decelerated from 15-20 m s^{-1} to 5-10 m s^{-1} and were deflected to become more southwesterly adjacent to the crest. The 1.33-km WRF-simulated winds were roughly 2-5 m s^{-1} stronger than the observations upstream of the Cascades. At 2.5 km MSL (not shown), fairly uniform west-southwesterly flow ~20 m s^{-1} prevailed across the Cascades in both the P-3 observations and the WRF simulation. At this level the maximum precipitation tended to be more focused over the narrow windward ridges.

Figures 2.13a,b shows the cross- and along-barrier winds averaged over a portion of the Cascades as derived from the P-3 Doppler radar from 2330-0100 UTC and the 1.33-km WRF at 0030 UTC. The higher momentum air (> 18 m s^{-1}) observed by the NOAA P-3 sloped upward over the windward slopes of the Cascades between 2 and 3 km MSL. A well-defined low-level shear layer, which has been shown to be a robust feature of orographic winter storms (Houze and Medina 2005; Medina et al. 2005), was also observed. The WRF simulation developed a windspeed maximum over the slope similar to the observations, but the simulated shear layer was both too shallow and too weak—a shortcoming that was also noted in MM5 simulations conducted by Garvert et al. (2005a, 2007). Alternate PBL schemes tested within the WRF model framework exhibit the same problem, suggesting that further attention is needed to properly represent PBL processes leading to this terrain-induced low-level shear layer.

As the P-3 flew westward across the Cascades at 0200 UTC along leg 6 (Fig. 2.1b), winds accelerated from 18 m s^{-1} over the lower windward slope to 24-27 m s^{-1} over the crest at 3-4 km MSL (Figs. 2.13c,d). The WRF-simulated flow maximum over the crest was weaker than the observations. The WRF-simulated airflow suggests that there was a mountain wave over the barrier.

c. Surface precipitation distribution

Figure 2.14a shows the total simulated precipitation from the WRF 1.33-km domain from 2000 UTC 4 December to 0800 UTC 5 December. The heaviest simulated precipitation (45-55 mm) occurred ~45.2 ^{o}N over the coastal range and ~44.9 ^{o}N over the lower windward slope of the Cascades. Interestingly, the precipitation amounts over the coastal range were nearly the same as over the far taller and wider Cascades. In the IOP region of the Cascades (boxed region in Fig. 2.12a), the simulated precipitation over the windward slope ranged from 35-45 mm over the ridges to 15-20 mm in the major valleys. There was a rapid reduction of precipitation to less than 20 mm in the immediate lee of the Cascade crest.

Figure 2.14b shows the percent of observed precipitation that was simulated by the 1.33-km WRF at the SNOTEL and hourly Cooperative Observer sites from 2000

UTC 4 December to 0800 UTC 5 December. Given a characteristic tendency for undercatchment of snow, model overprediction is typically not diagnosed until this ratio exceeds 150% (Colle et al. 2000; Garvert et al. 2005b). Most values in the present case ranged from 100-130% over the central Cascades, indicating no tendency for widespread model overprediction. There is some suggestion of model overprediction immediately downwind of the Cascades, while farther to the east (over the eastern Oregon plateau) the WRF underpredicted precipitation at many sites by at least 30%. The model also underpredicted precipitation by 35-50% at a few coastal observation sites and Willamette Valley, and this error extended northward within the larger 4-km domain (not shown). Next chapter will relate this precipitation verification to the microphysical aircraft data aloft.

2.5 Discussion

a. High-resolution reflectivity evolution

The S-Prof radar illustrates how the precipitation structures changed at a particular point (MB in Fig. 2.1a) over the windward Cascade slopes. The S-Prof observations (Fig. 2.15) are compared with the conceptual model of Medina et al. (2007), which was developed using the most typical and stronger IMPROVE-2 IOPs (i.e., excluding 4-5 December). They noted the initial decent of precipitation originating well aloft as cyclones approached the radar site, which they referred to as the Leading Edge Echo (LEE) pattern. Warm advection was relatively weak in the leading sector of the 4-5 December baroclinic wave (Fig. 2.4); thus, there was less potential for gradual ascent and a lowering cloud deck. In addition, the baroclinic wave of interest passed over the area only 6-7 h after passage of the previous frontal wave, yielding an atypical initial period of reduced stability. Hence precipitation began in the form of relatively shallow convective cells rather than a thickening (and lowering) stratiform shield. Between 1600 and 1900 UTC 4 December (Fig. 2.15), there were periods of convective precipitation extending up to 3-km MSL as the convective cells traversed S-Prof's location; these cells became more frequent and deeper by 2000 UTC 4 December.

By 0000 UTC 5 December, the orographic cloud had deepened to 5.5 km MSL. A region of large vertical gradients of reflectivity was located at ~3 km MSL, near the layer of most rapid model-predicted depositional growth (around -15 ^{o}C). Embedded convective cells appeared above 4-km MSL after 0400 UTC 5 December as the layer of enhanced reflectivities at ~3-km MSL progressively thinned so as to resemble the upper member of the Double Maximum Echo (DME) described by Medina et al. (2007). The lower member, marking the bright band, was not observed given the low (< 1.0 km MSL) prevailing 0°C level.

After 0800 UTC 5 December, there were more narrow plumes of convective enhancement between 3 and 4-km MSL. A Shallow Convection Echo (SCE, Medina et al. 2007) stage associated with lower echo tops and more convective precipitation marked the last stage of the passing storm (after 1100 UTC 5 December).

The results of Garvert et al. (2007) and Medina et al. (2007) suggest that the reflectivity enhancement above the Cascade crest around the time of maximum large-scale ascent may be associated with a mountain wave circulation aloft. For example, Fig.

2.16b shows a time-mean vertical cross-section of S-Pol reflectivity along line CD (Fig. 2.1b), corresponding to the previously analyzed case of 13-14 Dec 2001, averaged during the period highlighted in Garvert et al. (2007) (2300 UTC 13 December to 0100 UTC 14 December). This cross section can be compared to a similar one along line AB (Fig. 2.1b) averaged from 0200 to 0600 UTC 5 December 2001 (Fig. 2.16a). On 13-14 December 2001 precipitation was deeper (> 8-km MSL), with a pronounced bright band at 1.5 km MSL. Over the upper windward Cascade slopes the reflectivity bulged upwards to 6-km MSL in response to a larger-scale mountain wave anchored to the crest (Garvert et al. 2007). In contrast, precipitation on 5 December was shallower (< 6 km MSL). The 0°C level at this time was very low (< 1 km) and therefore a well-defined bright band could not be observed. For this case, the upward bulge of the reflectivity over the crest was very subtle. This is consistent with the comparatively weak mountain wave over the crest on 5 December, for which simulated upward motions were < 0.5 m s^{-1} above 5.0 km MSL (Fig. 2.9f) as compared to 0.5-1.0 m s^{-1} in the presence of far stronger cross-barrier flow on 13-14 December (cf. Fig. 8 of Garvert et al.).

b. Gravity wave impacts on precipitation

The WRF-simulated cross sections suggest that the vertical motions depicted over the Cascades were associated with gravity waves over the small-scale (10-20 km wide) ridges, especially toward the middle of the event as stability increased (Fig. 2.9f). Figure 2.17 shows P-3 flight-level data and WRF output for the north-south leg 2 at 2.4 km MSL between 2351 UTC December to 0008 UTC 5 December. On average, the WRF underpredicted the flow by 3-5 m s^{-1} (Fig. 2.17a), which was also apparent upstream at UW near the 2.4 km altitude (Fig. 7a). As in other IMPROVE-2 IOPs (Garvert et al. 2007), the WRF was able to realistically simulate the vertical velocity perturbations of +/- 1 m s^{-1} over the ridges as the southwesterly cross barrier flow of 15-20 m s^{-1} produced small-scale gravity waves over the narrow ridges (Fig. 2.17c). At 1.33-km resolution, the simulated vertical velocity maxima were underpredicted by 30-40% given the weaker-than-observed flow. In contrast, the 4-km WRF could not reproduce these small-scale oscillations given its inherently smoother topography. Both observations and simulation results in Fig. 2.17 indicate that vertical velocities over the windward slopes were only about half as large as those on 13-14 December 2001 at this altitude (Garvert et al. 2007). As such, observed super-cooled water variations were not as well correlated with areas of observed upward motion as for the 13-14 December event. On 4-5 December, WRF-simulated cloud water variations over the ridges were more pronounced than shown by in situ observations (Fig. 2.17b), suggesting a persistent deficiency in the model microphysics that will be explored in the next chapter.

An outstanding question is whether these wave perturbations were still large enough to impact the precipitation over the Cascades. Figure 2.18 shows the observed NOAA P-3 reflectivity field within a vertical section along leg 2 and the corresponding 1.33-km simulated snow, graupel, and cloud water mixing ratios. In the observations (Fig. 2.18a), little correspondence is noted between the areas of heaviest precipitation (x = 47 km and 110 km) and the narrow ridges, as conditions were influenced significantly by translating convective cells originating westward (Fig. 2.11). This is in sharp contrast to conditions on 13-14 December depicted for this same general “leg 2” location (cf. Fig.

14 of Garvert et al. 2007), in which well-defined and locally-forced plumes of enhanced reflectivity (> 18 dBZ) persisted above each of these ridges. However, the simulation does depict some correspondence between the enhanced cloud liquid water and the individual ridges. The amount of simulated graupel and supercooled water over the ridges in Fig. 18b is about 50% less than on 13-14 December (cf. with Fig. 15 of Garvert et al. 2007), which likely further limited the ridgeline precipitation in the 4-5 December case.

Garvert et al. (2007) quantified the impact of the narrow windward ridges on the net precipitation over the Cascades at 1.33-km grid spacing by completing a run in which the terrain was smoothed so as to be similar to that employed in the 12-km WRF domain. We performed the same smoothed (SMTH) terrain experiment as described in Garvert et al. (2007), while maintaining identical physics and upstream terrain for the coastal range as in the control run. Figure 2.19a depicts the smoothed Cascade terrain and resulting spatial precipitation pattern of precipitation differences between the SMTH and control (CTL) 1.33-km runs for the 2000 UTC 4 December to 0800 UTC 5 December period. The CTL run produced 5-7 mm (5-12%) more precipitation over some of the windward ridges and 4-6 mm (10-20%) less precipitation in the east-west orientated valleys as compared to the SMTH run (Fig. 19a). Compared to the SMTH run, the CTL run produced 9-12mm (10-25%) more precipitation over the crest given the adjacent steep windward slope and it had 1-2 mm (10-20%) less precipitation in the Cascades lee given the water vapor depletion over the Cascades (Fig. 2.20).

Figure 2.20 shows the distribution of simulated precipitation in the cross-barrier direction averaged in latitude over the dashed region in Fig. 2.19a between 2000 UTC 4 December and 0200 UTC 5 December and 0200 and 0600 UTC 5 December for several sensitivity runs. Unlike Garvert et al. (2007), who noted a 10-15% increase in net precipitation on 13-14 December tied to realistic small-scale corrugations of Cascade windward slope, only a 3-6% net increase was found between the CTL and SMTH runs for the 4 - 5 December event. A Hovmoller plot of the vertically integrated water and ice for the SMTH run reveals only minor differences in precipitation evolution over the Cascades as compared to the CTL run (Figs. 2.21a,b), which suggests that these narrow ridges along the windward slopes were not particularly important in modulating the development or evolution of the convective precipitation in this case. Although the 1.33-km WRF simulation underpredicted the small-scale vertical motions over the windward slope, the impact that the narrow ridges had on the actual precipitation was likely small given the inconsistent phasing between observed reflectivity maxima and individual ridges (Fig. 2.18a).

Overall, the reduced impact of small-scale terrain features in the Cascades in our case compared to that of Garvert et al. (2007) is attributed to two factors. First, as highlighted above, the gravity wave vertical motions were about half as strong as in Garvert et al. (2007), so there was less super-cooled water generation and riming (which have been shown to increase the precipitation efficiency over windward ridges; Medina and Houze 2003; Colle and Zeng 2004). Secondly, a relatively low freezing level on 4-5 December, (~1000 m, as compared to ~2000 m for 13-14 December) suggests less super-cooled water and riming and hence less local precipitation fallout over individual ridges. This is consistent with Colle (2008), who used idealized two-dimensional MM5

simulations to show that the net precipitation enhancement over a series of 8-10 narrow ridges increased as the freezing level was raised from 1000 to 750 mb.

c. Coastal range impacts

Garvert et al. (2007) illustrated that the interaction of onshore flow with the coastal range can reduce the cloud water in the lee of this modest barrier (viz. over the Willamette Valley), but did not quantify the associated surface precipitation impacts. We completed a sensitivity experiment in which the coastal range within the 1.33-km WRF domain was replaced by a flat land surface (NOCR). With less upward motion to release potential instability over the coastal range (not shown), the precipitation over the "coastal strip" (i.e. the inland zone extending ~50 km east from the Oregon coast) was reduced by 40-60% (Figs. 2.19b, 2.20). Meanwhile, with more moisture available downstream of the coastal range, the precipitation over the Willamette Valley and lower windward slopes of the Cascades correspondingly increased by 10-20% in the NOCR simulation. Cellular convection was slightly weaker over the coastal strip in NOCR than in CTL (Fig. 2.21a,c), but slightly greater over the Willamette Valley and the lower windward slopes of the Cascades.

Interestingly, even after removing the elevated coastal range terrain, a zone of enhanced precipitation persisted over this region and convective cells continue to intensify shortly after landfall (Fig. 2.21c and dotted lines in Fig. 2.20). This suggests that differential friction at the coast might also have played a role in producing low-level convergence and upward motion at the coast, and persistent precipitation enhancement in that subregion. The importance of differential friction in enhancing coastal precipitation has been highlighted in other studies (Braun et al. 1999; Colle and Yuter 2007). In the 1.33-km CTL WRF simulation at 0000 UTC 5 December (Fig. 2.5b), the surface convergence was ~$4x10^{-4}$ s^{-1} along the coast (not shown), which resulted in enhanced vertical motion and release of the potential instability. To illustrate the importance of the differential friction, an additional 1.33-km simulation was completed in which the area of the (already flattened) coastal mountains was replaced with a water surface (NOCRW). This change reduced the surface precipitation by 60-70% in this zone as compared to the CTL run (Figs. 2.19c; 2.20). Moreover, convective cell coverage and intensity were reduced both over the coastal strip and adjacent waters of the Pacific (Fig. 2.21d). Meanwhile, more intense precipitation cells were triggered over the Willamette and the lower reaches of the Cascades. This illustrates that the precipitation maximum over the coastal range, whose amplitude was nearly equivalent to that over the Cascades in the CTL run (Fig. 2.20), resulted from a superposition of two effects: (1) lifting induced by the presence of an elevated terrain profile corresponding to the coastal mountains, and (2) differential land-sea friction and associated low-level convergent forcing tied to the Pacific coastline.

Accumulated precipitation over the zone extending from the base of the windward Cascade slopes up to the crest in the NOCRW simulation was also 10-20% greater than that in the NOCR simulation and 20-30% greater than in the CTL (Fig. 2.20). The simulated integrated water vapor at the UW site (just west of the Cascades) was 5 and 15% greater in the NOCR and NOCRW runs, respectively, than for the CTL run (not shown). The NOCRW run had more instability at the UW location (not shown), which

favored increased convective activity over the adjacent slopes of the Cascades. The NOCRW simulation shows a gradual increase of the precipitation from the coast toward the Cascade crest, suggesting that this barrier influences the precipitation well upstream (~170 km westward) of the crest.

2.6 Summary

This chapter describes the co-evolving kinematic and precipitation fields over the Oregon Coastal Range and Cascades during the passage of a notably cold, unstable trough on 4-5 December 2001 during the second Improvement of Microphysical Parameterization through Observational Verification Experiment (IMPROVE-2) field project. This event featured a landfalling baroclinic wave, but unlike previously documented IMPROVE-2 events, this trough developed within a colder air mass and was accompanied by comparatively weak cross-barrier flow and thermodynamic stratification. The low-level flow response was complex, since there was sufficient stability below 700 m upstream of the Cascades to generate channeled southerly near-surface winds, while farther aloft the flow was increasingly directed up and over the Cascades. Unlike most landfalling baroclinic waves impacting the Pacific Northwest, the initial phase of this storm was marked by relatively weak warm advection at low-levels, so the precipitation did not begin in the more typical mode of a lowering stratiform shield described by Medina et al. (2007). Over the coast, the onshore flow at low-levels was relatively unstable, and supported embedded convective cells that were preferentially enhanced as they made landfall and encountered the more modest coastal mountains. These cells propagated eastward and briefly weakened while passing over the Willamette Valley before re-intensifying upon arrival over the windward (west-facing) slopes of the Cascades. As the upper-level trough approached, precipitation increased in coverage and intensity, and greater precipitation spillover into the lee of the Cascades accompanied increasing cross-barrier flow and overall orographic cloud depth. What makes this case unique is that there was a superposition of a steady orographically-forced zones of ascent combined with more transient cellular convective precipitation that initially formed and/or intensified near the elevated coastal terrain before advancing eastward and subsequently interacting with the Cascade barrier some 100-150 km downstream.

The Weather Research and Forecasting (WRF) model (version 2.2) was used to simulate the synoptic and mesoscale structures of this event down to horizontal 1.33-km grid spacing. The model was verified using numerous observational platforms including in situ aircraft measurements, S-Pol radar, wind profilers, radiosondes, and surface observations. The model realistically simulated the three-dimensional thermodynamic, kinematic, and precipitation structures, although it underestimated the cross-barrier flow by a few m s^{-1} as well as the depth and strength of an associated shear layer over the windward slopes. The WRF realistically predicted the ~1 m s^{-1} vertical velocities associated with relatively weak gravity waves over the narrow (10-20 km) ridges located on the windward (western) face of the Cascades; however it overestimated cloud water production over these ridges. The 1.33-km grid run simulated precipitation accumulations to within 20% of those observed at many stations over the Cascades, which is in marked contrast to the characteristic tendency for overprediction noted in

previous IMPROVE-2 studies of storms whose environments were characterized by stronger cross-barrier flow and more stable stratification.

The flow over the small-scale windward ridges combined with the embedded convection increased the precipitation locally over these ridges by nearly 50% as compared to adjacent valleys. Even so, a sensitivity run employing an artificially smoothed version of the Cascades illustrates that this modulation had a relatively small (< 5%) impact on the net precipitation given the lack of riming (due to the relatively weak vertical motions over the narrow ridges) and the relatively low freezing level. A sensitivity run eliminating elevated coastal terrain and associated land-sea contrasts in surface friction showed that the broader circulation tied to the larger mountain wave anchored over the Cascade crest enhanced the precipitation well (~100 km) upstream of this more major barrier.

Model sensitivity experiments have further illuminated the importance of the coastal range in triggering convective cells and associated local precipitation enhancement. In this case the net effect of the coastal range had two components: one was the lifting of the flow over the elevated terrain profile and another was the low-level convergence induced by the land-sea frictional contrasts across the coastline. These two sources of forcing contributed to a significant (20-30%) decrease of the precipitation over the Cascades, which lay downwind of this coastal zone. Sensitivity experiments show that the coastal terrain influences the stratiform vs. convective nature and intensity of the precipitation farther downstream by (1) removing moisture from the landfalling low-level airstream and (2) lifting the airflow over the coastal terrain and hence triggering convection which subsequently reduces the of amount convective instability available downstream.

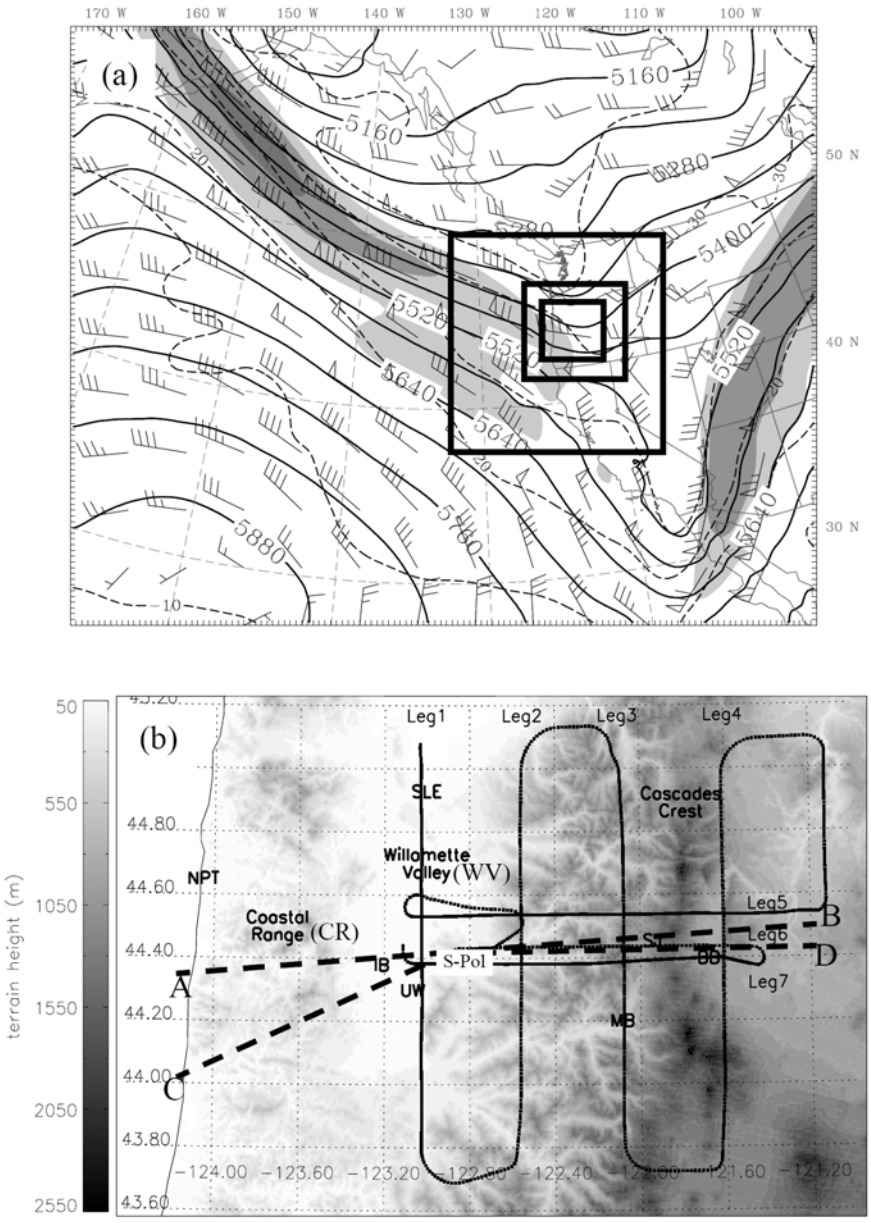

Figure 2.1 (a) WRF Analysis of 500-mb geopotential height (solid contours every 60 m), temperature (dashed contours every 5°C), wind barbs (1 full barb = 10 kt) and 300-mb isotachs (shaded light, medium, and dark gray for 50, 60, and 70 m s^{-1}, respectively) from the 36-km WRF at 1200 UTC 4 December 2001. Inset boxes denote nested 12, 4 and 1.33-km WRF domains. (b) Terrain (shaded in m) and NOAA P-3 flight legs on 4-5 December. Dashed lines AB and CD indicate the orientations of the S-Pol vertical cross-sections shown in Figs. 9, 10, and 16.

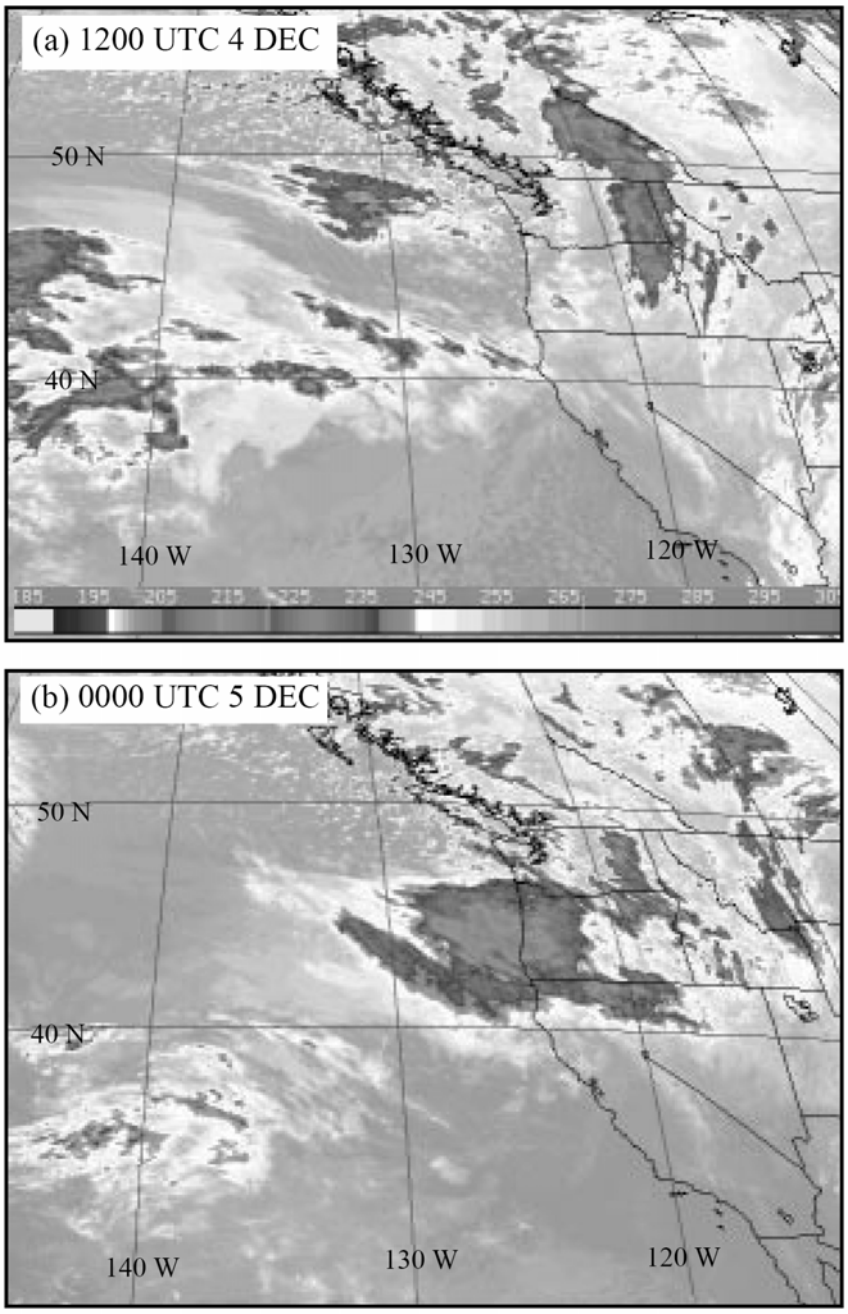

Figure 2.2 GOES infrared satellite image (K, shaded according to inset scale) at (a) 1200 UTC 4 December 2001 and (b) 0000 UTC 5 December 2001.

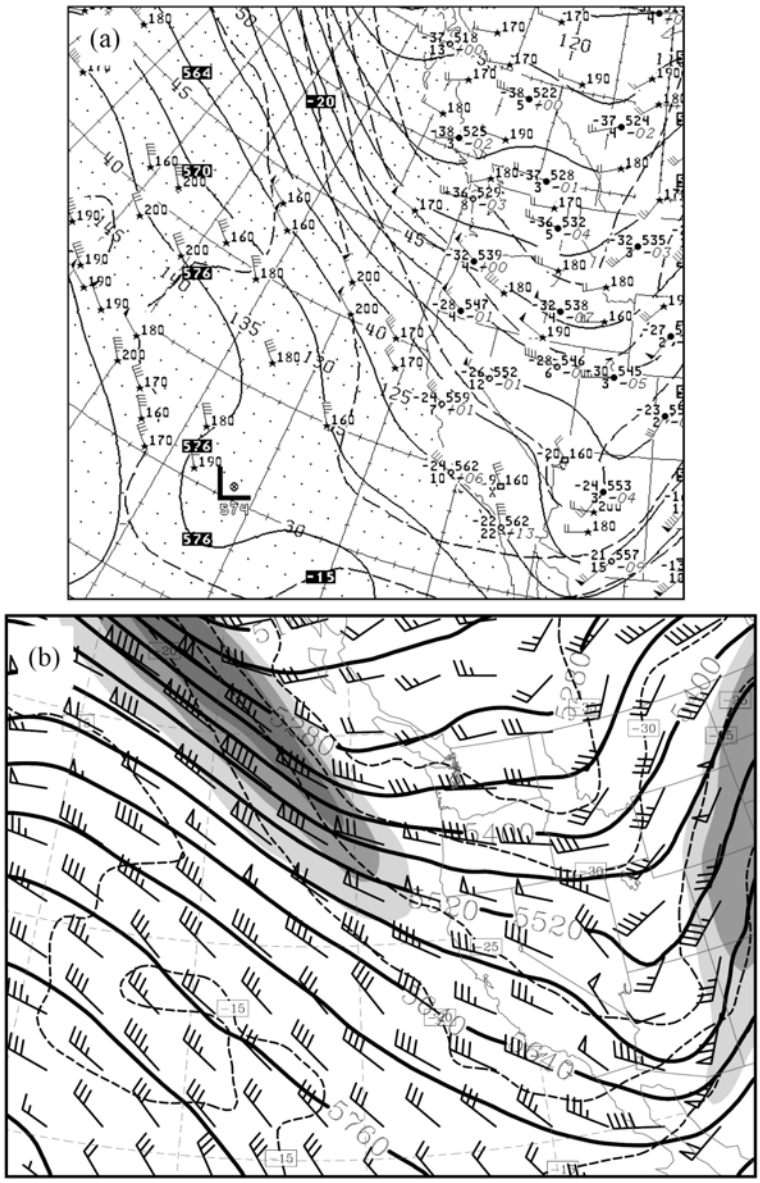

Figure 2.3 (a) NCEP analysis of 500-mb of geopotential height (solid every 60 m), temperature (dashed every 5°C), and winds (1 full barb = 10 kt) at 0000 UTC 5 December 2001. (b) Same as (a) except for the 12-h WRF 36-km simulation and showing the windspeed at 300-mb (light, medium, and dark gray shading denotes speeds exceeding 50, 60, and 70 m s^{-1}).

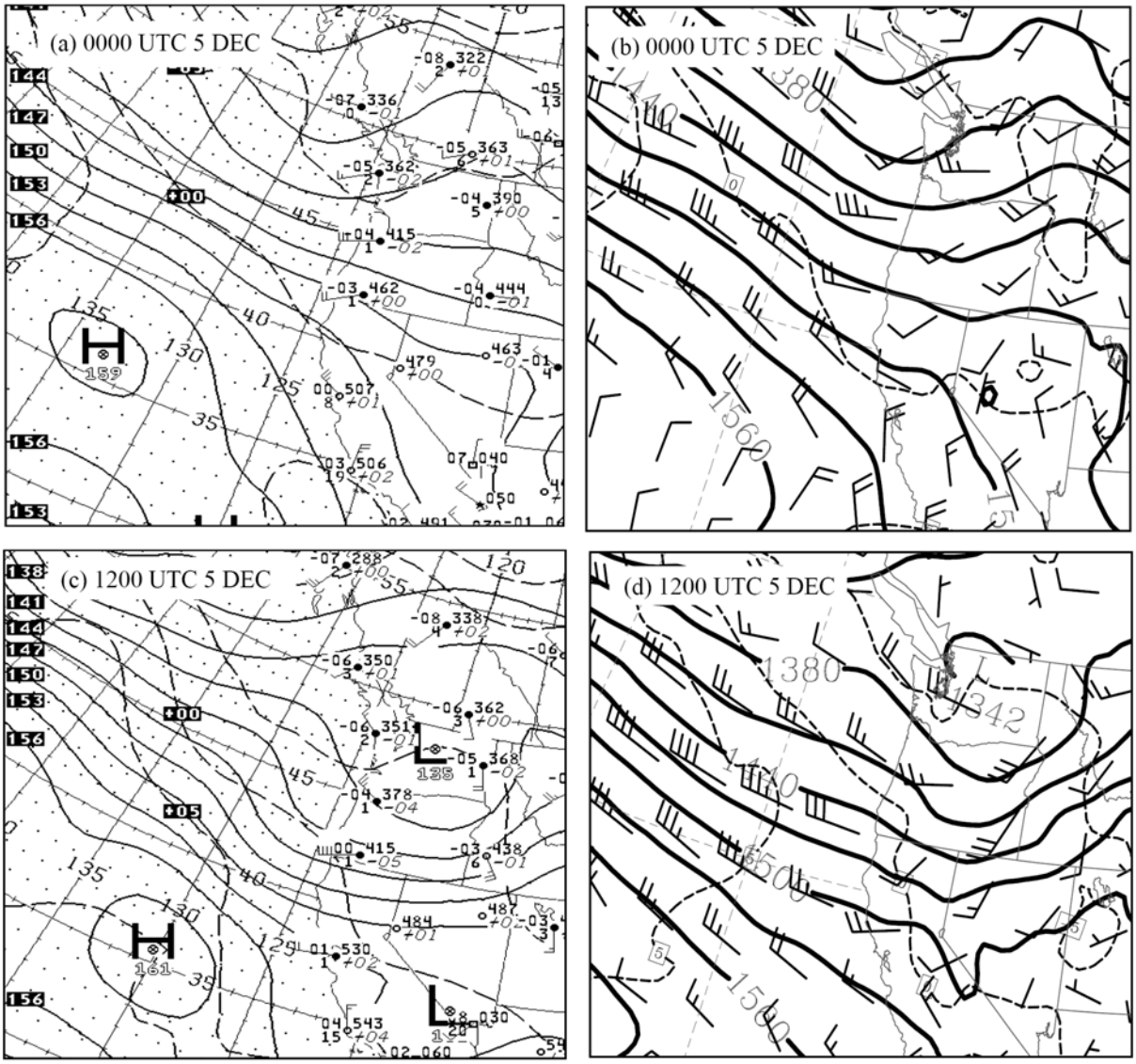

Figure 2.4 (a) NCEP analysis of 850-mb geopotential height (solid every 30 m), temperature (dashed every 5°C), and winds (1 full barb = 10 kt) at 0000 UTC 5 December 2001. (b) Same as (a) except for the 12-h WRF 36-km simulation. (c) Same as (a) except at 1200 UTC 5 December. (d) Same as (c) except for the 12-h WRF 36-km simulation initialized at 0000 UTC 5 December.

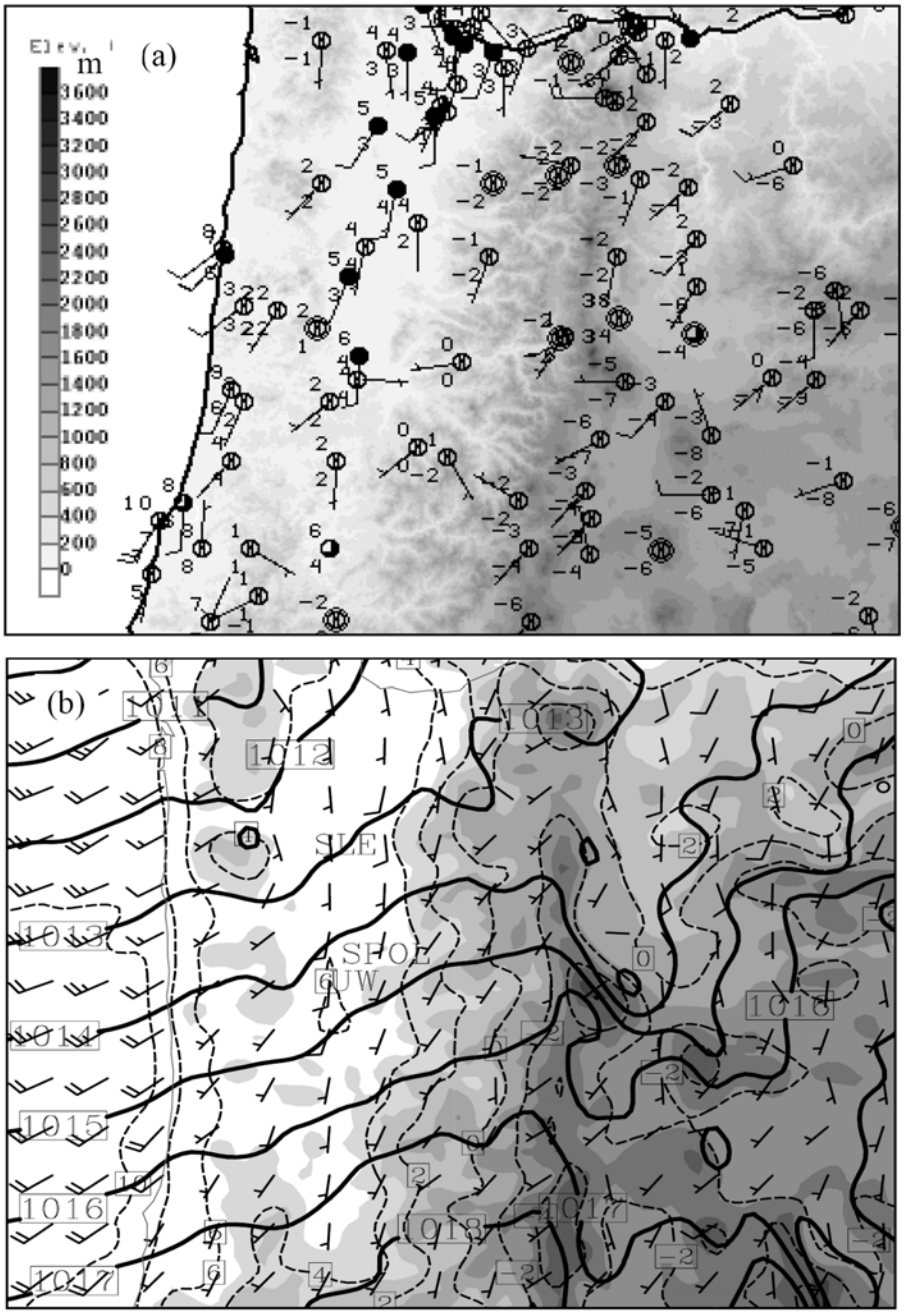

Figure 2.5 (a) Surface observations over western and central Oregon at 0000 UTC 5 December (using standard surface model, full barb = 10 kt) (b) Same as (a) except for the corresponding 4-km WRF simulation showing sea-level pressure (solid every 1 mb), surface temperature (dashed every 2°C), and terrain height (shaded every 500 m).

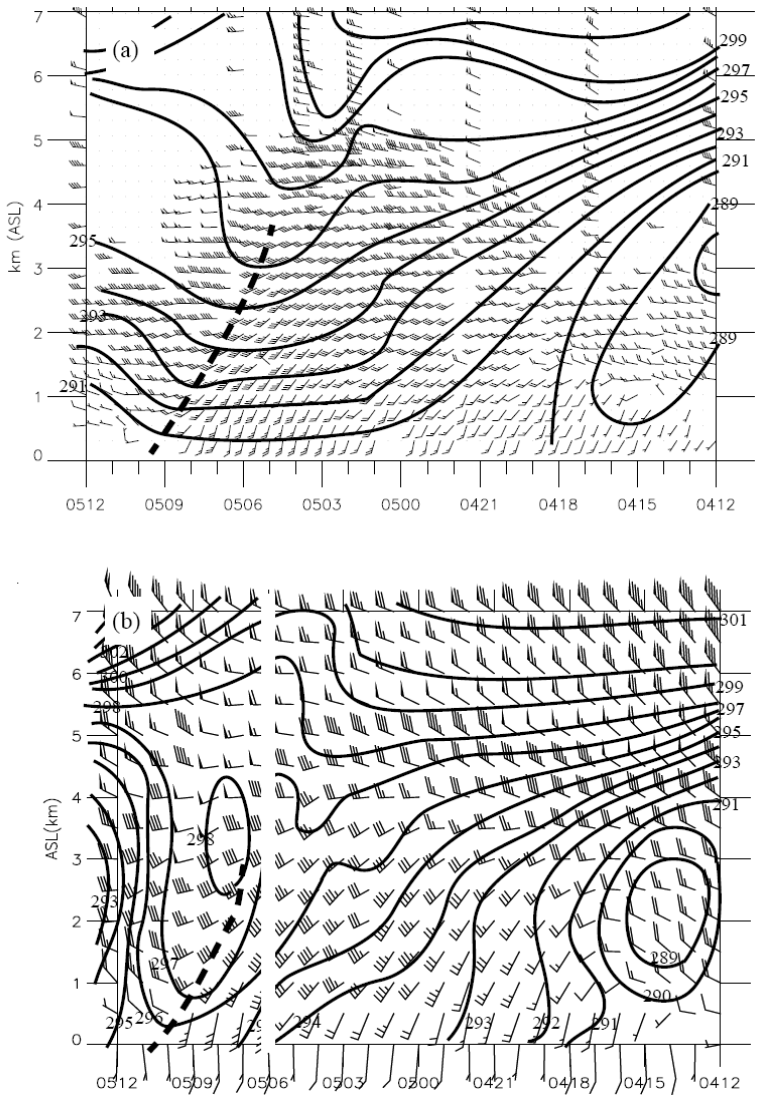

Figure 2.6 (a) Observed time-height series of equivalent potential temperature (solid) every 1 K using the UW and SLE soundings at (day/time) 04/1200, 04/1600, 05/0000, 05/0130, 05/0330, 05/0600, 05/1200 UTC, as well as winds at one-hour intervals from the IB profiler. (b) Same as (a) except for corresponding 1.33-km WRF simulation output of winds at location IB and equivalent potential temperatures at UW.

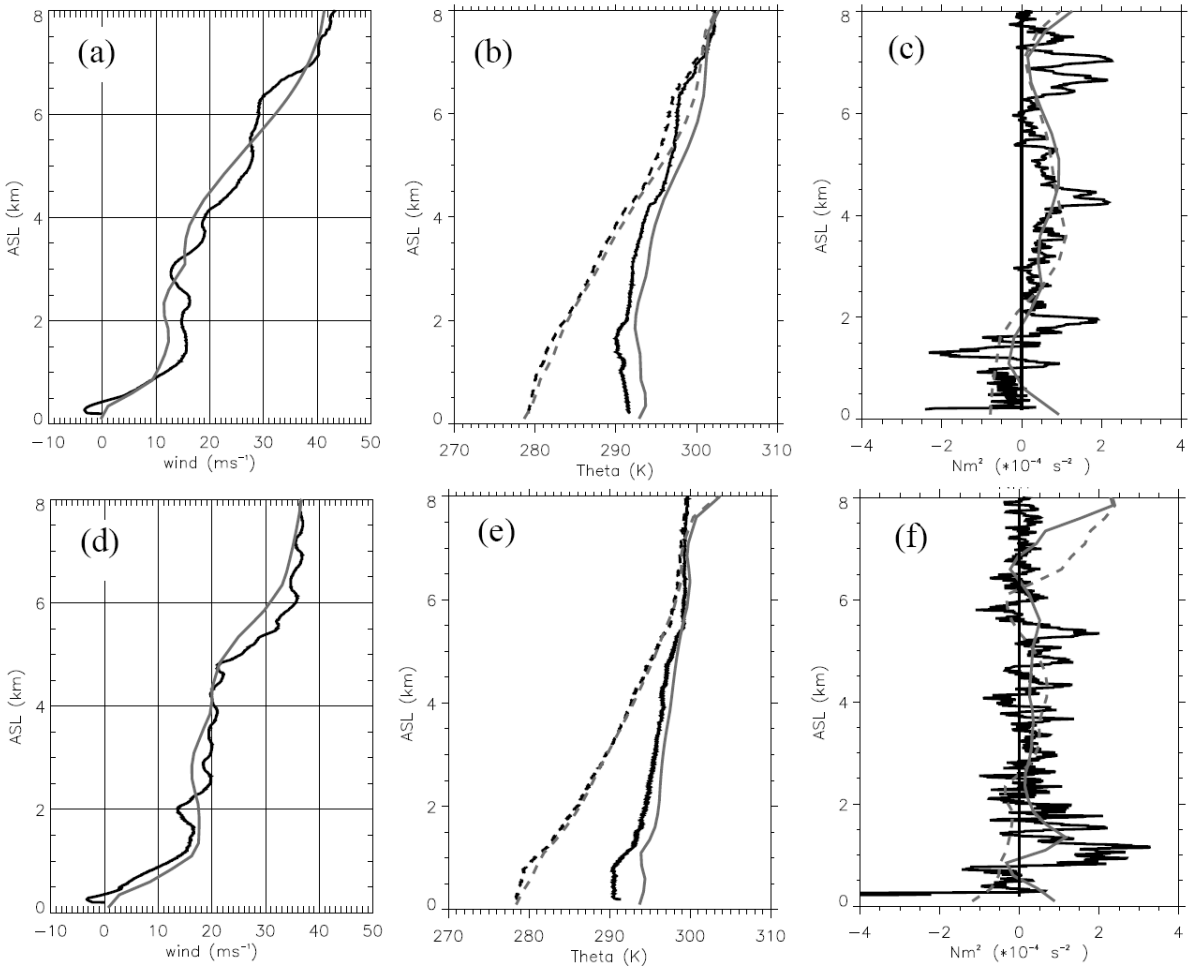

Figure 2.7 Vertical profiles of (a) cross-barrier (west to east) flow (m s^{-1}), (b) potential temperature (short dashed, K) and equivalent potential temperature (solid, K), and (c) the square of moist static stability (N_m^2) at the UW sounding site at 2100 UTC December. Observed (1.33-km WRF-simulated) quantities at the UW site are shown in solid-black (solid-gray). The 1.33-km WRF moist static stability at point A near the coast (Fig. 8b) is shown by the long-dashed gray line in (c). Panels (d)-(f) are the same as (a)-(c) except for 0330 UTC 5 December.

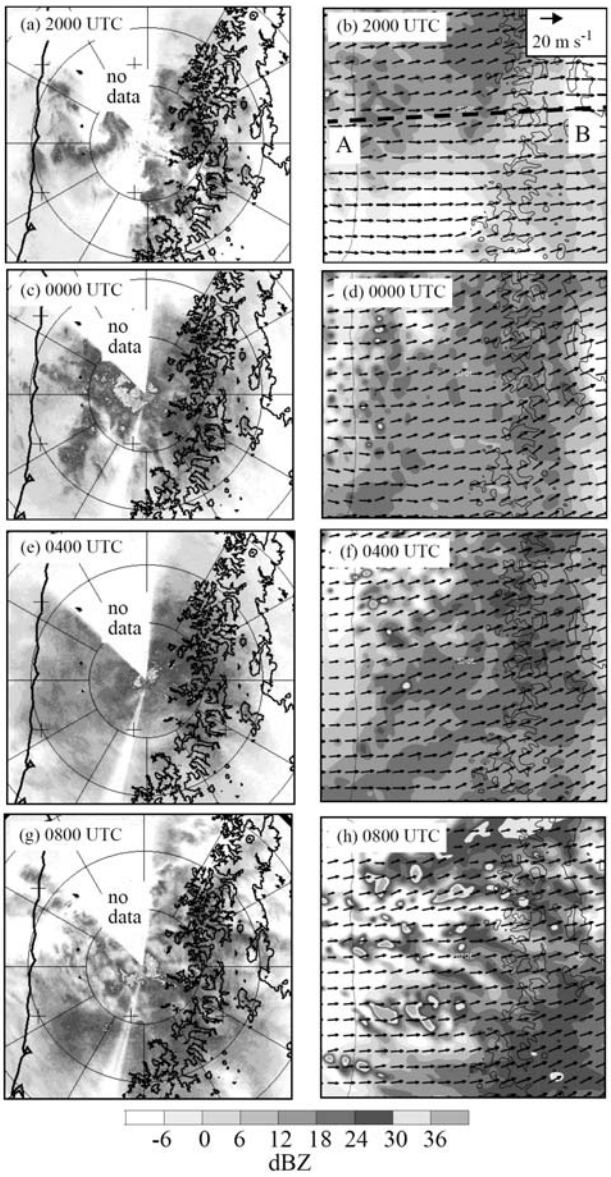

Figure 2.8 Observed S-Pol reflectivities (shaded, 1.5^{o} scan) and terrain (solid, 1.0 and 2.0 km MSL contours) at (a) 2000 UTC 4 December, (c) 0000 UTC 5 December, (e) 0400 UTC 5 December, and (g) 0800 UTC 5 December. WRF-derived reflectivity (700 mb) from the 1.33-km simulation at (b) 2000 UTC 4 December, (d) 0000 UTC, (f) 0400 UTC, and (h) 0800 UTC using gray-shaded scale (every 6 dBZ). The WRF wind vectors at 700 mb are also shown as well as the model terrain (solid, 1.0 and 2.0 m contours). Line AB in (b) is the location for the RHI scans in Figs. 9 and 10.

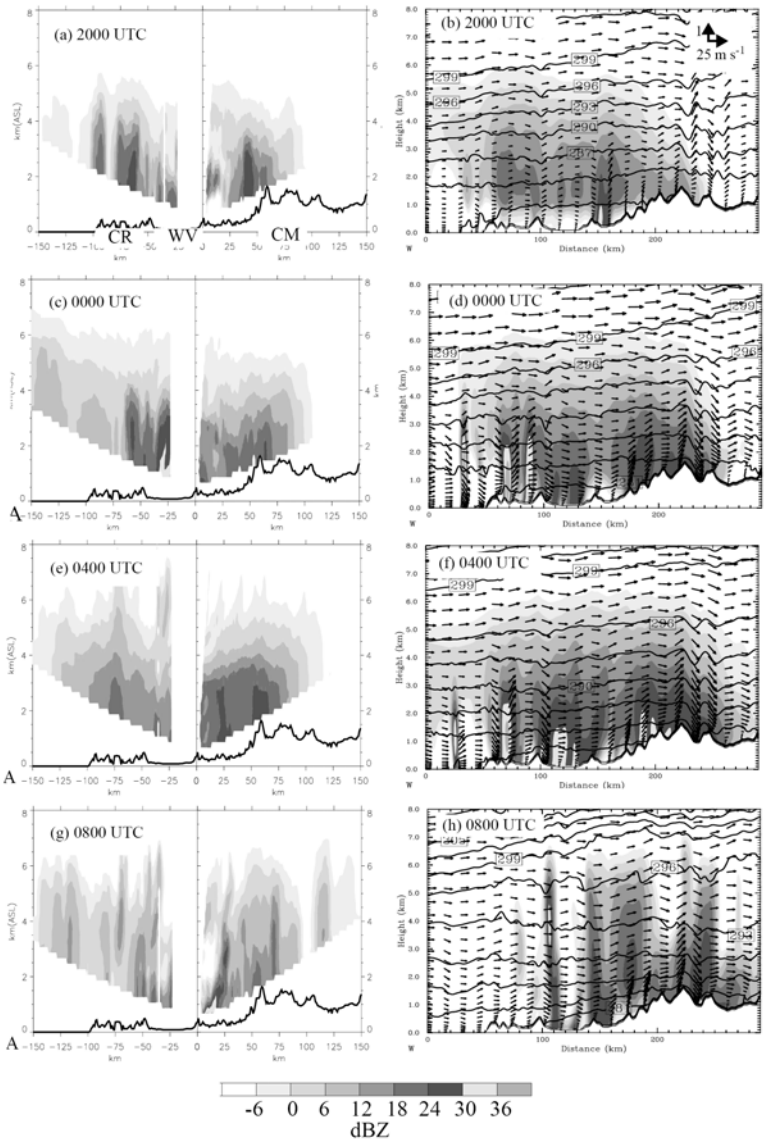

Figure 2.9 Observed S-Pol reflectivities for cross section AB (shown in Fig. 8b) at 2000 UTC 4 December using gray shaded scale (every 6 dBZ) for (a) 2000 UTC 4 December, (c) 0000 UTC 5 December, (e) 0400 UTC 5 December, and (g) 0800 UTC 5 December. The WRF reflectivities, potential temperature (solid every 3 K) and circulation vectors (m s^{-1} using the inset scale in b) from the 1.33-km simulation are shown for (b) 2000 UTC, (d) 0000 UTC, (f) 0400 UTC, and (h) 0800 UTC 5 December.

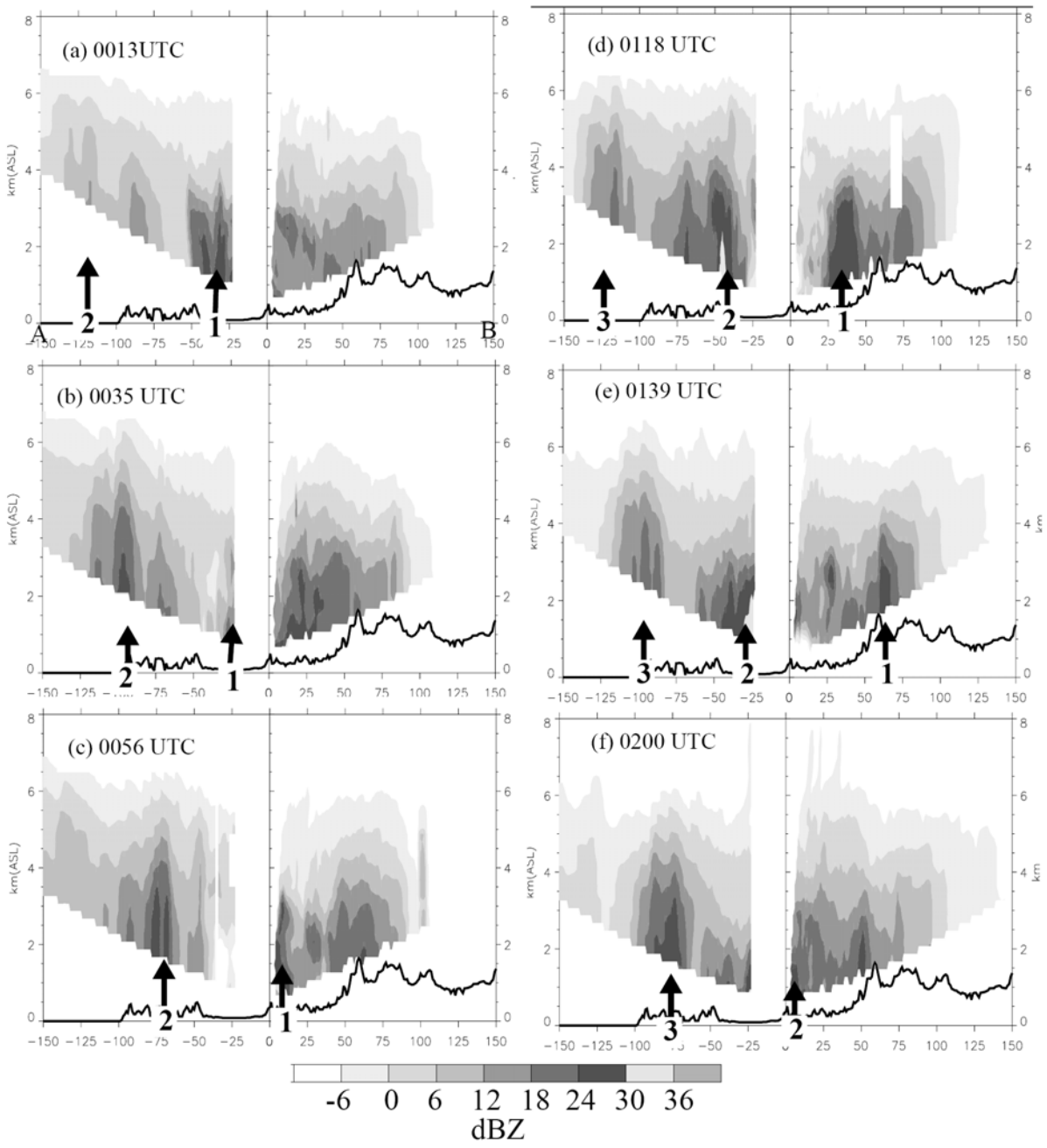

Figure 2.10 Observed S-Pol reflectivities for cross section AB (shown in Fig. 8b) at (a) 0013 UTC, (b) 0035 UTC, (c) 0056 UTC, (d) 0118 UTC, (e) 0139 UTC, and (f) 0200 UTC 5 December using gray-shaded scale (every 6 dBZ). The arrows and numbers indicate the cell locations as they propagate from west to east across the Coastal Range and Cascades.

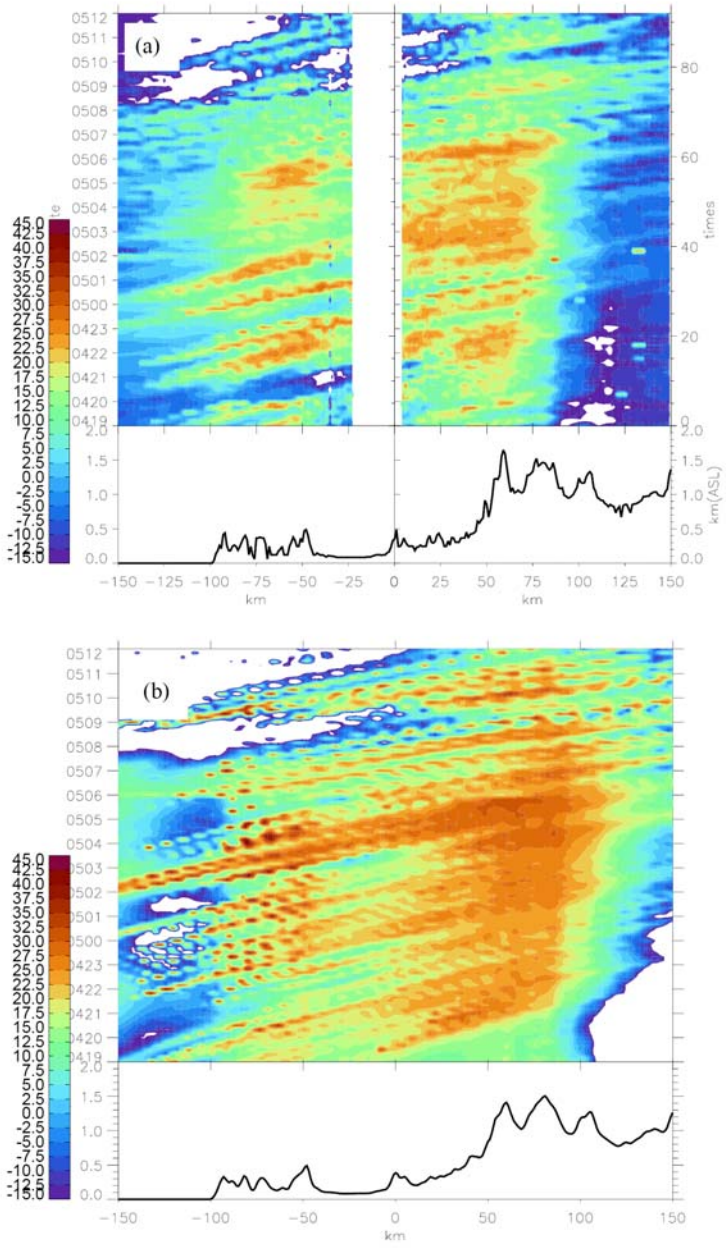

Figure 2.11 (a) Hovmöller-type plot showing the maximum observed S-Pol radar reflectivity (color shaded every 2.5 dBZ) above 1.0 km MSL from 1900 UTC 4 December to 1200 UTC 5 December along AB (see Fig. 8b for location). (b) Same as (a) except for the 1.33-km WRF.

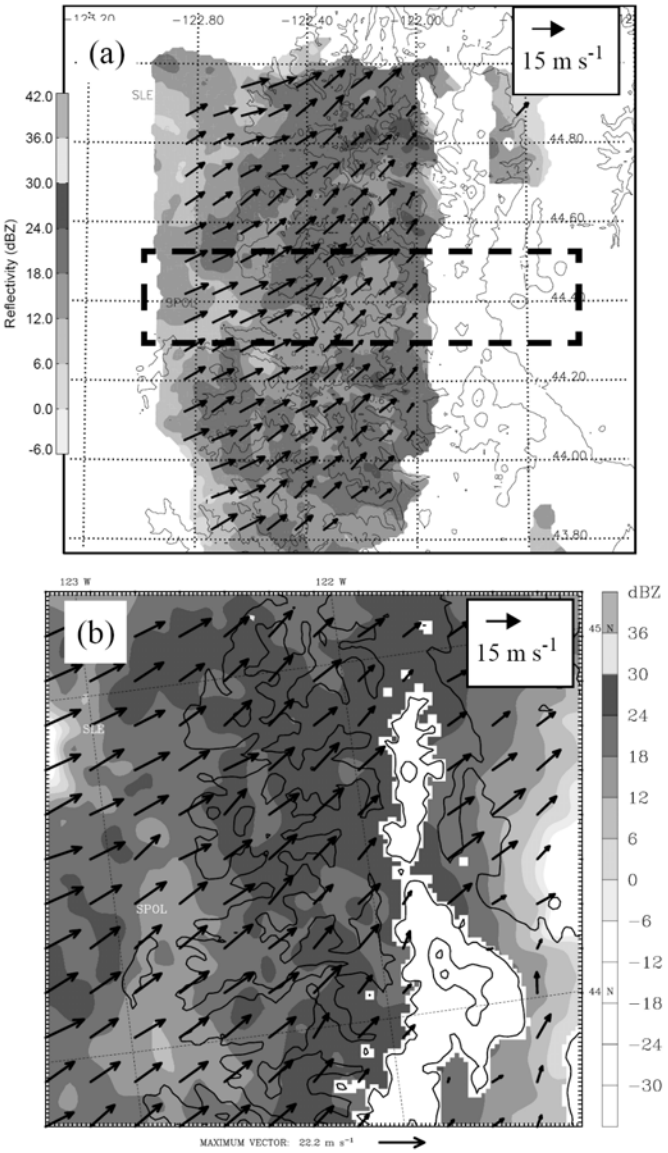

Figure 2.12 (a) Observed NOAA P-3 reflectivity (shaded every 6 dBZ) at 1.5 km MSL for legs 2-4 between 2300 UTC 4 December and 0100 UTC 5 December. There is no data for much of the lee of the Cascades. (b) Same as (a) except for the 1.33-km WRF at 0000 UTC 5 December as well as the wind vectors at 1.5 km MSL. The boxed region in (a) shows the region included in deriving average cross-barrier wind speeds shown in Fig. 14. The terrain is also shown (0.5 km contours).

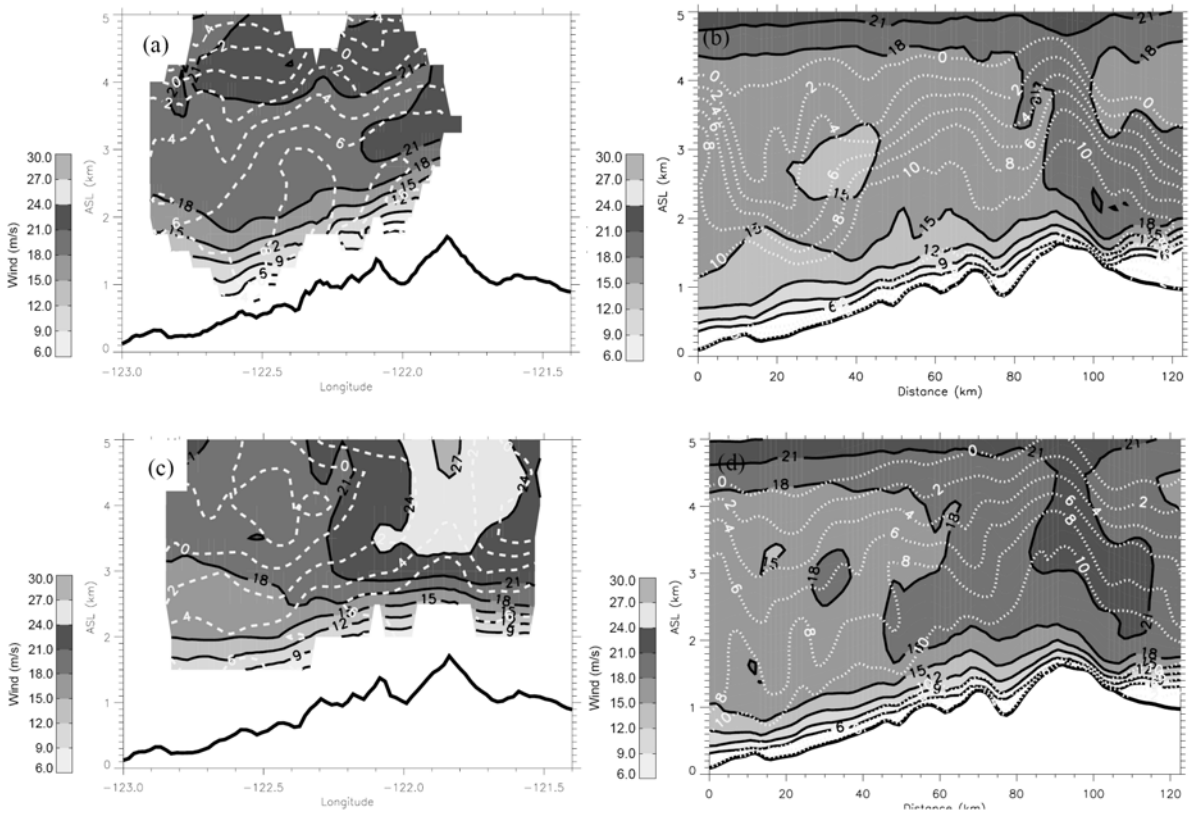

Figure 2.13 (a) Observed wind speeds (shaded every 3 m s^{-1}) and barrier-parallel winds (v-component, dashed every 3 m s^{-1}) from NOAA P-3 Doppler radar averaged over the west-east box across the Cascades for legs 2-4 (boxed region shown in Fig. 12a) between 2351 UTC 4 December and 0055 UTC 5 December. (b) Same as (a) except for the 1.33-km WRF at 0030 UTC 5 December. (c) Same as (a) except for leg 6 at 0144 to 0200 UTC 5 December. (d) Same as (c) except for the 1.33-km WRF at 0200 UTC 5 December.

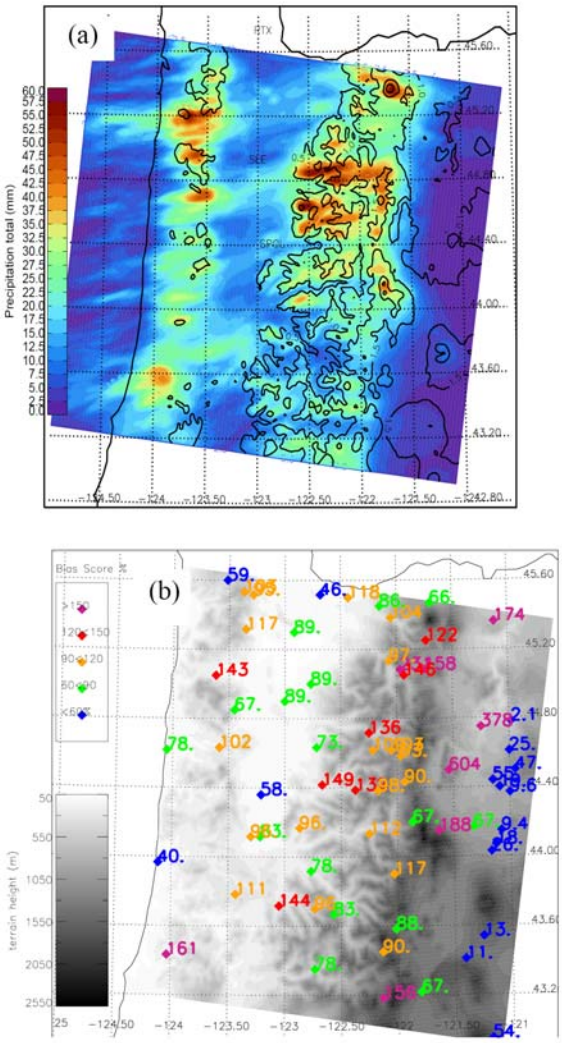

Figure 2.14 (a) Simulated precipitation (shaded every 5 mm) from the 1.33-km WRF between 2000 UTC 4 December to 0800 UTC 5 December and terrain (0.5 km contours). (b) Percent of observed precipitation simulated by the 1.33-km WRF at the precipitation gauge sites between 2000 UTC 4 December to 0800 UTC 5 December. The percent values are color coded using the inset scale in (b), while background shading indicates terrain elevation (m, key at lower-left).

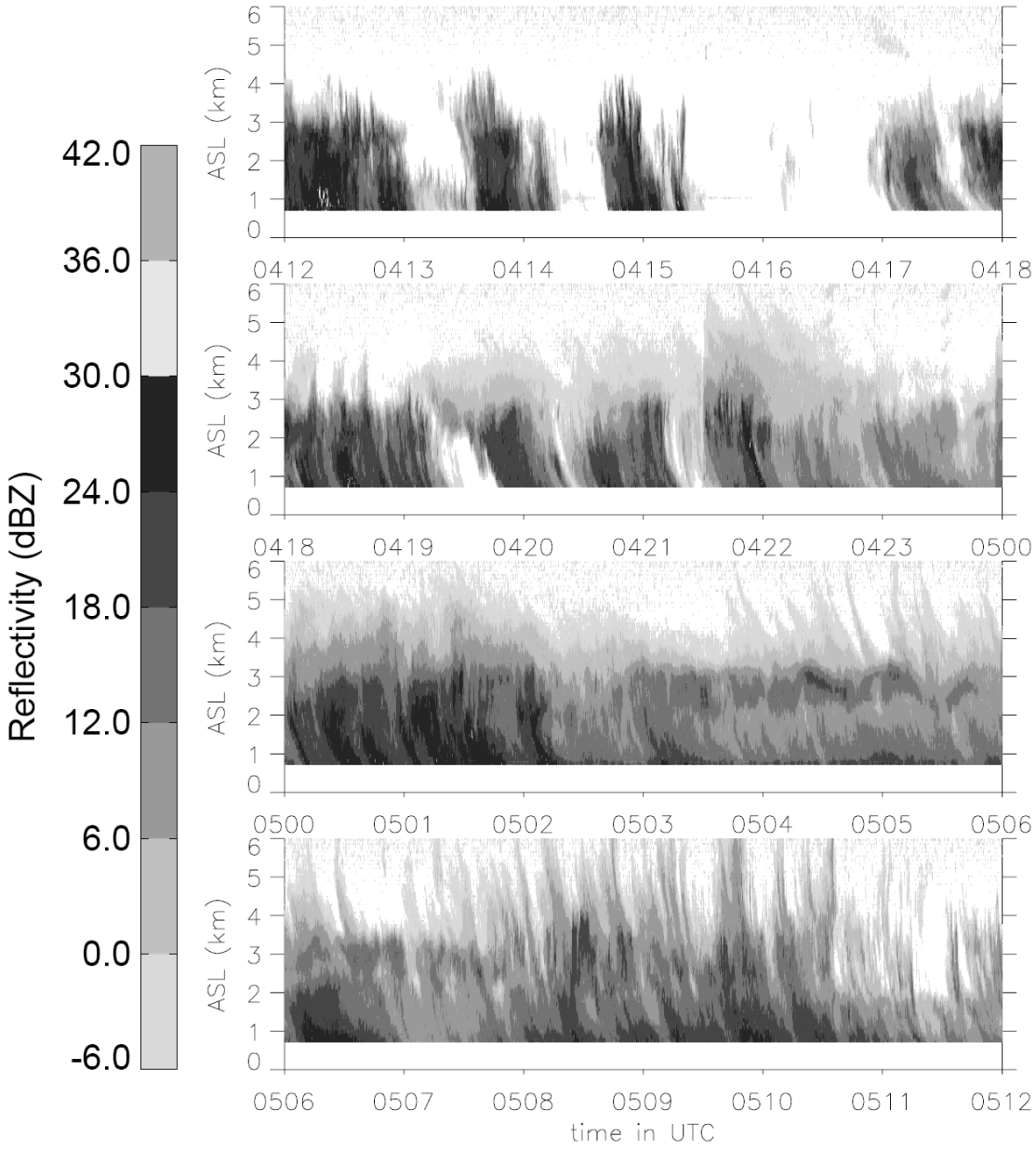

Figure 2.15 Observed vertically-pointing radar reflectivities (shaded every 6 dBZ) from the S-Prof (location MB on Fig. 1b) from 1200 UTC 4 December to 1200 UTC 5 December.

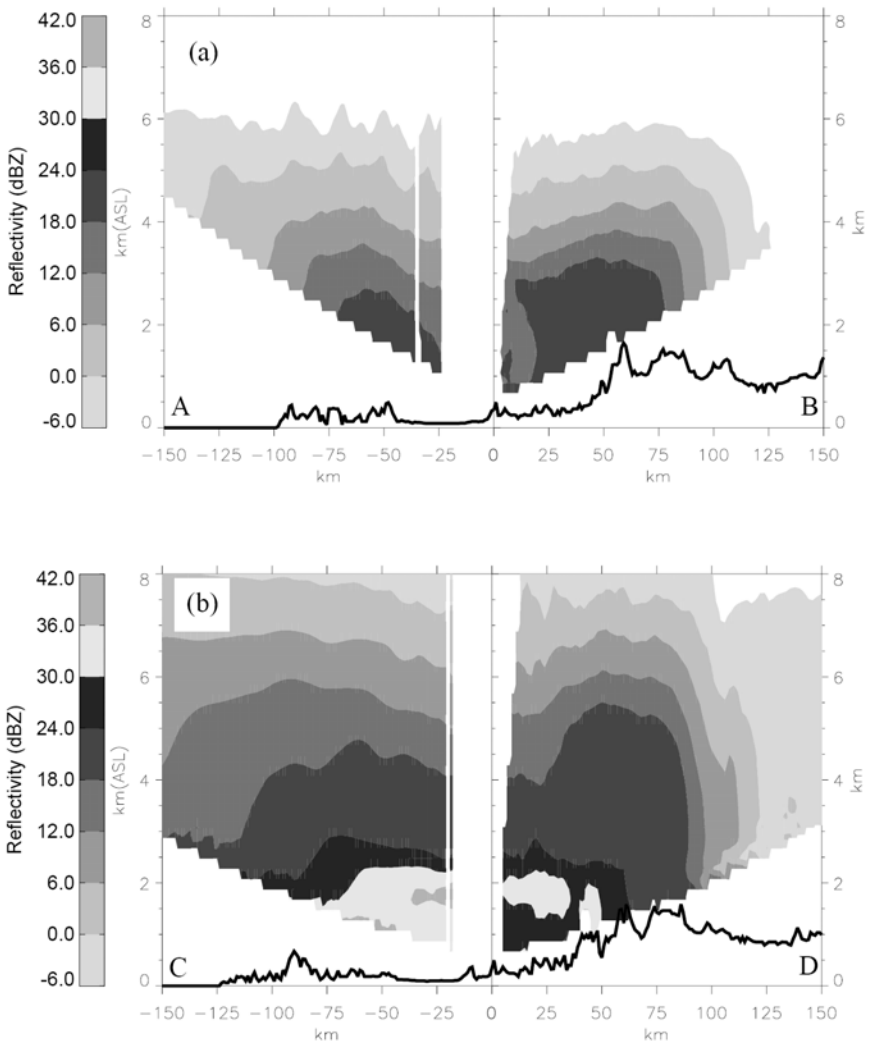

Figure 2.16 (a) Observed time-mean S-Pol radar reflectivity for cross-section AB (shown in Fig. 8b) averaged between 0200 UTC and 0600 UTC 5 December using gray-shaded scale (every 6 dBZ). (b) S-Pol reflectivity for cross-section CD (shown in Fig. 1b) averaged between 2100 UTC 13 December and 0100 UTC 14 December using gray-shaded scale (every 6 dBZ).

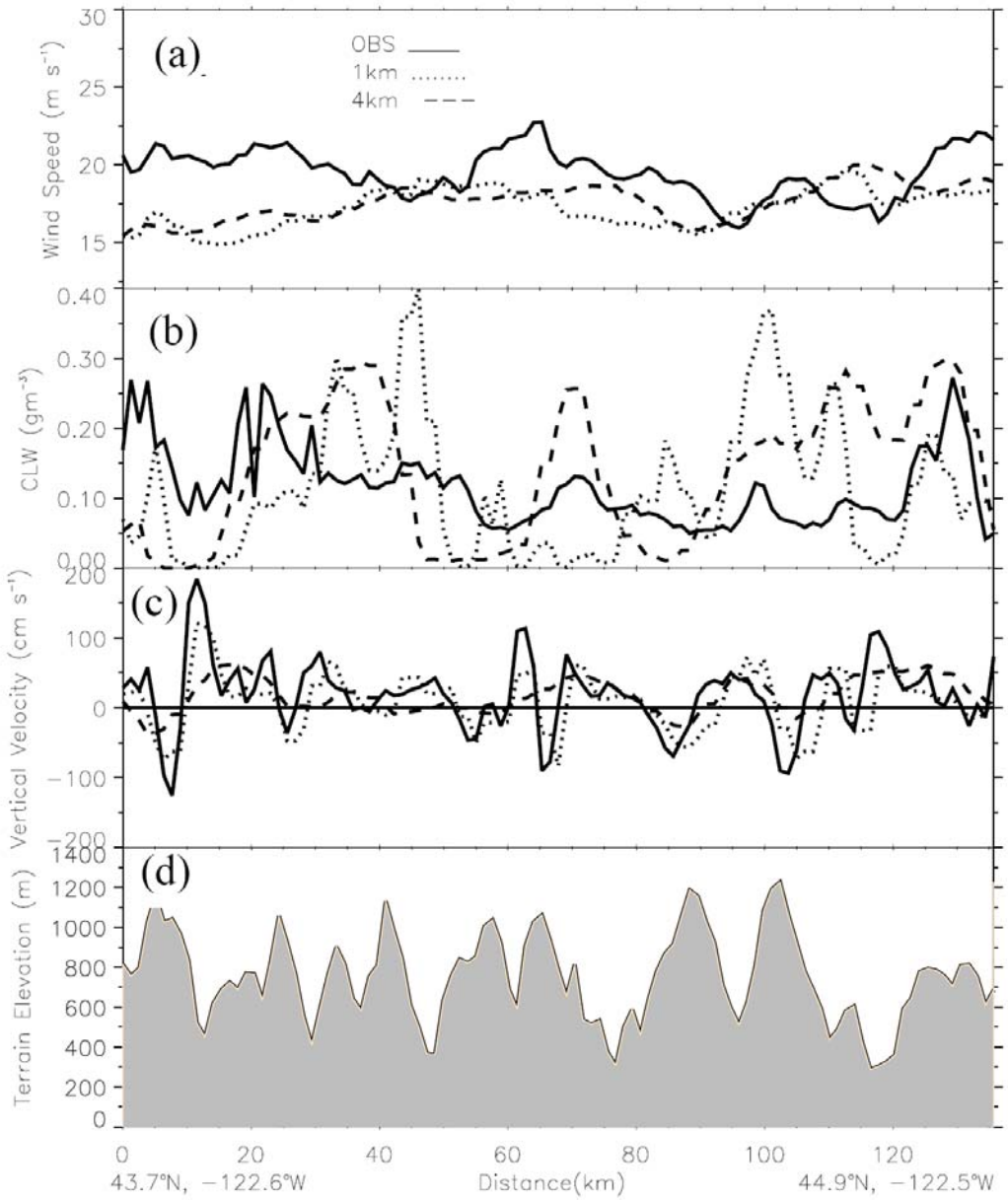

Figure 2.17 Time series from NOAA P-3, 4-km WRF, and 1.33-km WRF along leg 2 from south (left) to north (right) at 2450 m MSL showing (a) wind speed (m s^{-1}), (b) cloud water (g m^{-3}), vertical velocity (cm s^{-1}), and terrain (m) between 2351 UTC 4 December and 0008 UTC 5 December.

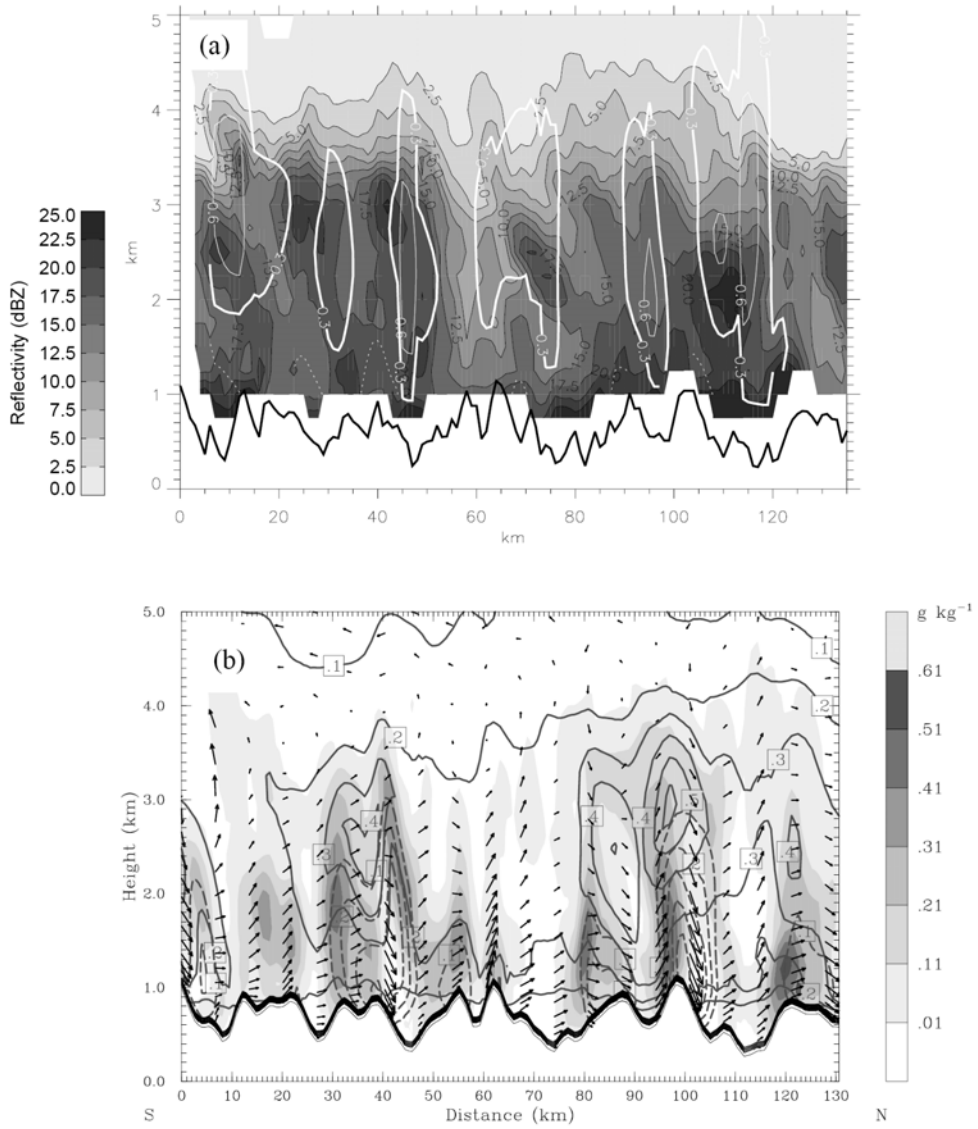

Figure 2.18 (a) Observed NOAA P-3 cross-section of radar reflectivity (every 2.5 dBZ) and dual-Doppler vertical motions (white contour every 0.3 m s^{-1}) along leg 2 from south (left) to north (right) at 2400 m MSL between 2351 UTC 4 December and 0008 UTC 5 December. (b) Same as (a) except for the 1.33-km WRF simulation output showing circulation vectors in the cross section, cloud water (shaded in g kg^{-1}), snow (solid every 0.1 g kg^{-1}), and graupel (dashed every 0.1 g kg^{-1}). The terrain height within the plane of the section is shown at the bottom of each panel.

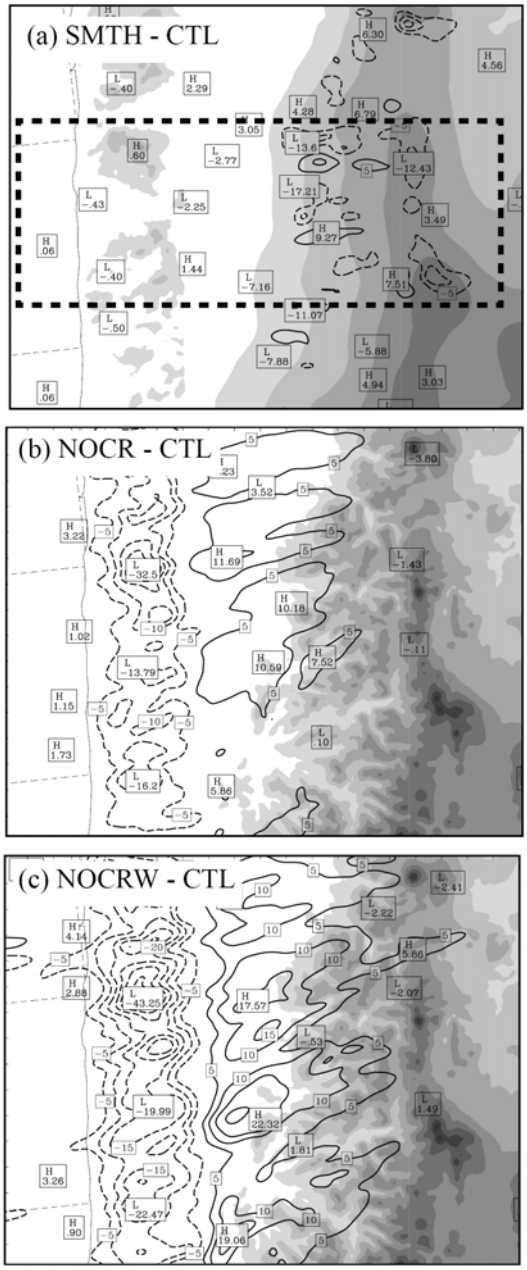

Figure 2.19 Simulated precipitation difference (in mm) for the 1.33-km WRF run of (a) SMTH - CTL, (b) NOCR - CTL, and (c) NOCRW –CTL between 2000 UTC 4 December and 0800 UTC 5 December. The gray shading (every 500 m) in (a) denotes the SMTH terrain, while the shading in (b) represents the NOCR terrain. The dashed box in (a) represents the region in which the precipitation was averaged in latitude for Fig. 20. See text for the CTL, SMTH, NOCR, and NOCRW definitions.

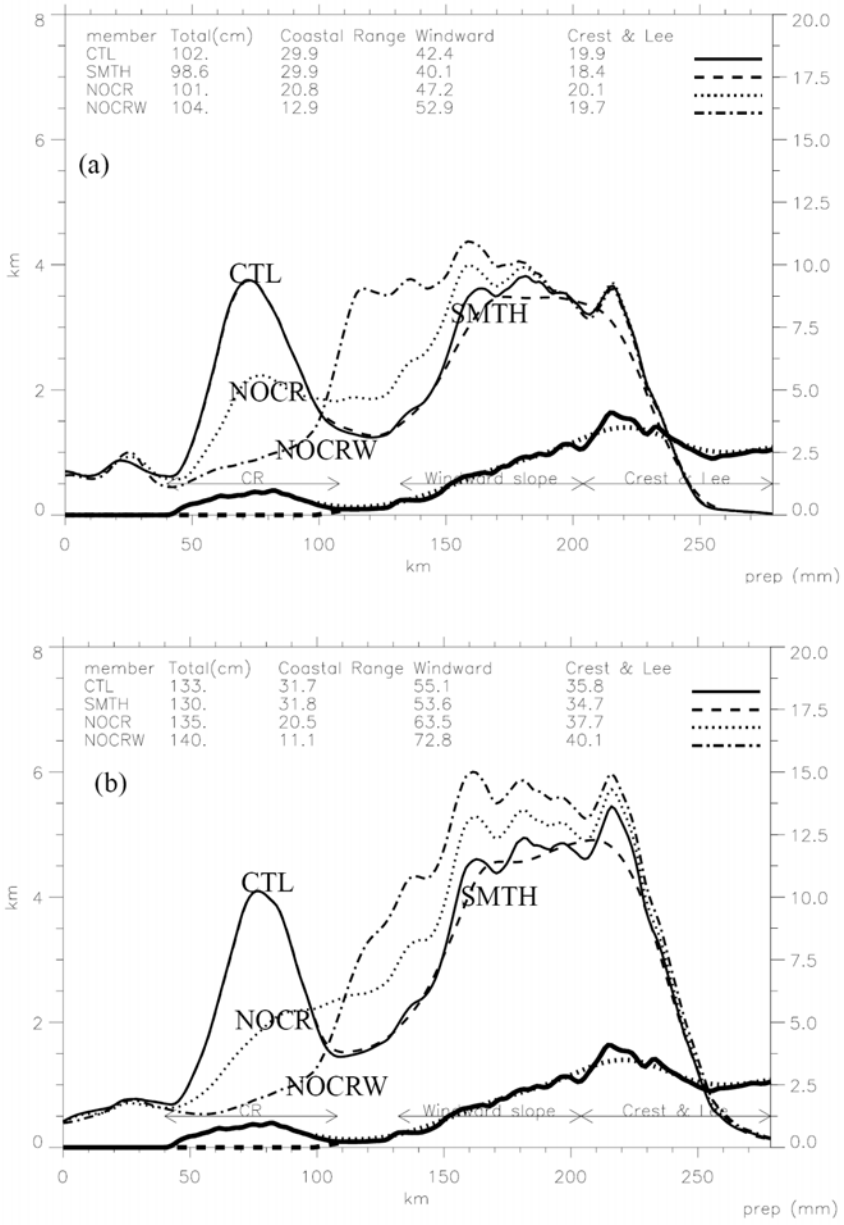

Figure 2.20 Simulated precipitation (in mm) averaged in latitude over the boxed area in Fig. 19a for the CTL, SMTH, NOCR, and NOCRW runs for the (a) 2000 UTC 4 December - 0200 UTC 5 December and (b) 0200 - 0600 UTC 5 December periods. The terrain profile is indicated at the bottom of the panels. The tables at the top of the panels indicate averages over the coastal range, windward slope and crest/lee.

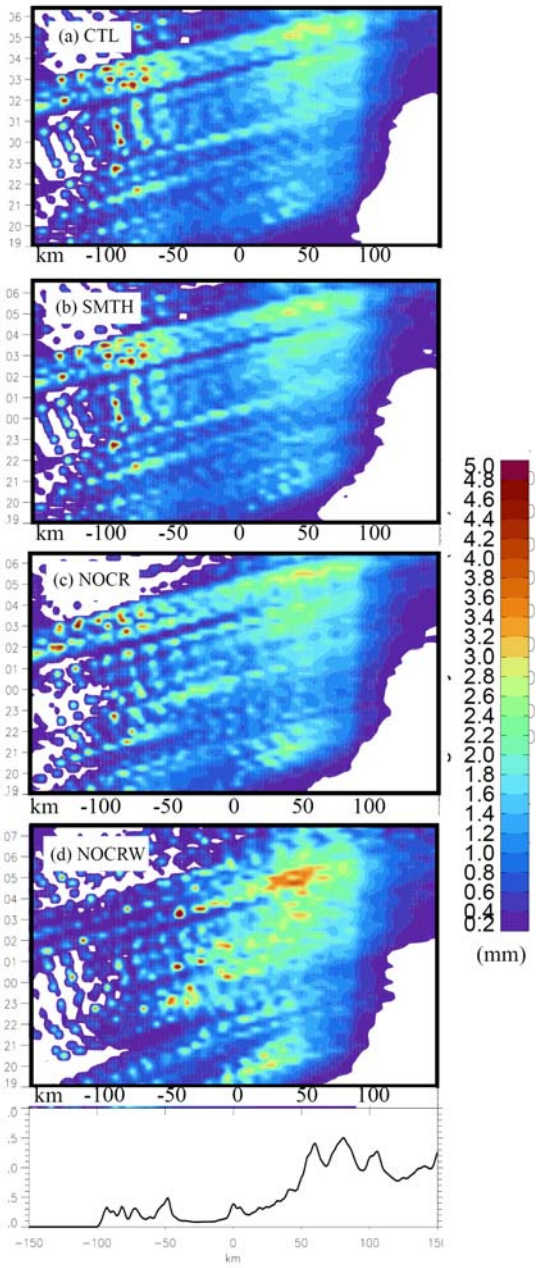

Figure 2.21 Hovmoller plot showing the vertically-integrated water and ice (shaded in mm) for the 1.33-km WRF from 1900 UTC 4 December to 0700 UTC 5 December along AB (see Fig. 8b for location) for (a) CTL, (b) SMTH, (c) NOCR, and (d) NOCRW experiments. The terrain profile for the CTL run is shown in the lower panel.

Chapter 3

Observed and Simulated Cloud Microphysics during 4-5 December of IMPROVE-2: An Evaluation of the Weather Research and Forecasting (WRF) model

3.1 Introduction

Cross barrier flow, freezing level, and static stability have been shown to impact the orographic cloud and precipitation distributions (Rauber 1992; Colle 2004; Medina and Houze 2003). For example, the stable conditions and strong cross barrier flow during the 13-14 December event of IMPROVE-2 resulted in mountain waves over the Cascade crest (Garvert et al. 2005a). The wave over the crest during this event enhanced the snow growth over the upper windward slope (Garvert et al. 2007), with cold-type snow crystals above the –20 ^{o}C level and dendrites and ice particle aggregates near -15 ^{o}C (Woods et al. 2005). Meanwhile, mountain waves over the individual Cascade windward ridges and a relatively high freezing level (~2 km above sea level) enhanced the cloud water generation and riming at low-levels (Garvert et al. 2007).

The various BMPs available in mesoscale models generate large differences in the simulated hydrometeor and surface precipitation distributions over steep terrain (Colle et al. 2005a, b; Grubisic et al.2005; Richard et al. 2007). Richard et al. (2007) found that the Thompson et al. (2004) scheme underpredicted the surface precipitation for MAP IOP2b using the MM5, while there was overprediction for the Goddard BMP scheme (Tao and Simpson 1993). They also found that WSM6 (Hong et al. 2004) scheme predicted ~10 mm more precipitation than the Thompson scheme (Thompson et al. 2004) using the Weather and Forecasting Model (WRF) model.

This chapter focuses on the 4-5 December 2001 IMPROVE-2 event (Chapter 2),

which featured ~50% weaker cross barrier flow, a lower freezing level (~1 km versus 2 km), slightly more unstable at low levels, and one-half less surface precipitation than the 13-14 December 2001 case. As a result, this case provides unique observations and model validation for an event with less snow growth and riming aloft than the 13-14 December event. Furthermore, there have been relatively few verification studies of the WRF BMPs (Hong et al. 2004; Hong and Lim 2006; Thompson et al. 2004; Thompson et al. 2008; Chen and Sun 2002), and no formal comparisons of WRF BMPs using in situ aircraft observations over steep terrain.

The objective of this chapter is to describe the observed microphysical evolution for the same event as well as to evaluate and understand the differences in performance of the WRF BMPs. These results are compared with the well-documented 13-14 December 2001 IMPROVE-2 case. The motivational questions for this chapter are:

- How do the observed microphysical structures compare between the 13-14 and the 4-5 December 2001 IMPROVE-2 events given the different ambient conditions?
- How well do the BMP schemes within WRF simulate the precipitation and microphysical quantities for the 4-5 December IOP? Are the results consistent with the previously investigated 13-14 December IMPROVE-2 event?
- What are the BMP sensitivities for the 4-5 December event and some reasons for the differences between the BMPs?

3.2 Data and methods

a. Microphysical datasets and retrieval

Two research aircrafts, the NOAA P-3 and the UW Convair-580, collected radar and microphysical data over the Cascades during the 4-5 December event (Fig. 3.1a). The P-3 was equipped with a tail Doppler radar, and Particle Measuring System (PMS) 2D-C and 2D-P grayscale imaging probes to obtain ice particle concentrations as well as King (King et al. 1978) and Johnson-Williams probes (Baumgardner 1983) to measure cloud liquid water (CLW). The Convair-580 was equipped with a PMS 2-DC and Forward Scattering Spectrometer Probe (FSSP). Following the approach described in Garvert et al. (2005b) and Woods et al. (2005), the ice mass concentrations were calculated using in situ observations of the number concentrations, classified ice crystal types, and the corresponding mass-diameter relationships for each type [refer to Table 4 of Woods et al. (2005) for the specific relationships used]. This method also gives an estimate of the graupel mass concentration. To further quantify the observed ice mass concentration uncertainty, another independent retrieval using the method used in Colle et al. (2005b) with three different mass-dimension relationships (Brown and Francis 1995, Heymsfield et al. 2002 with the area ratio of 0.7 and 0.5, the three retrieval will be called BF, HEYMS, and AGGR, respectively, later) are conducted. The BF retrieval is in the middle

of the three estimates and will be used later. These estimates are in good agreement with less than 30% divergence. Given the retrieval uncertainty and other instrument measurement uncertainties (Heymsfield et al. 2002), only those model differences > 30% of the observed will be highlighted in this paper.

A radiometer at Santiam Junction (SJ in Fig. 3.1b) was used to obtain the integrated cloud liquid water depth (LWD) and water vapor depth as described in Woods et al. (2005). Together with the calculated integrated water vapor from the sounding at UW and BB (UW and BB in Fig. 3.1b), this provided a good estimation of the observed moisture evolution.

The NCAR S-band Doppler radar (S-Pol), located on the western foothills of the Oregon Cascades (SPOL in Fig. 3.1b) provided the plan position indicator (PPI) and range-height indicator (RHI) scans over the Cascades and coastal range. The dual-Doppler radar on the NOAA P-3 sampled the winds and reflectivities over the windward slopes and immediate lee of Cascades during the IOP (Chapter 2).

Hourly precipitation totals from the National Weather Service (NWS) cooperative sites, National Resources Conservation Service (NRCS) snowpack telemetry (SNOTEL) sites, and the special precipitation gauges deployed over the Oregon Cascades during IMPROVE (Stoelinga et al. 2003) were synthesized to verify the simulated precipitation amounts.

b. Model setup and configuration

The WRF version 2.2 was utilized using the setup described in Chapter 2. The National Centers for Environmental Prediction-Aviation Model (NCEP-AVN) analyses at 1- degree resolution were used for the initial and boundary conditions for a 36-, 12-, 4, and 1.33-km grid-spacing configuration (see Fig. 2.1a). The 36- and 12-km domain applied the Kain and Fritsch (1993) convective parameterization, while no cumulus parameterization was used in the 4- and 1.33-km domains. A positive definite advection (PDA) scheme for moisture and hydrometeors was used in order to prevent artificial moisture gain during the advective time steps (Skamarock 2006), which will be shown to be important in section 5.

Four BMPs were evaluated in this study. A brief comparison of the four BMPs is shown in Table 3.1. The WRF single moment microphysics with graupel (WSM6) is based on modifications from Lin et al. (1983) and Rutledge and Hobbs (1983) (Hong et al. 2004; Hong and Lim 2006). This scheme includes: separate formula for the ice crystal and ice nuclei number concentrations, a self-consistent mass, diameter and number concentration relationships for ice, temperature dependent snow intercept and a maximum ice crystal diameter of 500 microns. The Purdue Lin (LIN) scheme (Chen and Sun 2002) follows the parameterization of Lin et al. (1983) and Rutledge and Hobbs (1984), but with the following modifications. LIN uses a saturation adjustment method from Tao et al. (1989) and a simple Kessler type (Kessler 1969) autoconversion, with a threshold cloud liquid water mixing ratio of 0.7 g kg^{-1}. Snow deposition and riming are

implemented as in Koenig (1971). It also uses a Kessler-type autoconversion for snow to graupel with a threshold snow of 0.6 g kg^{-1}.

The Thompson scheme (THOM1) originated from the Reisner2 scheme in MM5 (Reisner et al. 1998), with modifications by Thompson et al. (2004). Some modifications include: temperature dependent snow intercept as in Houze et al. (1979); a temperature dependent ice number concentration as in Cooper (1986); a Gamma distribution for graupel with a graupel mass dependent intercept; a varying rain intercept to indirectly simulate drizzle drops; a more physical autoconversion formula as in Walko et al. (1995); a snow riming and depositional growth ratio to determine the riming snow transition to graupel.

A new Thompson scheme was developed for WRFV2.2 (THOM2) (Thompson et al. 2008). Some modifications include: sums of two Gamma functions for snow size distribution based on aircraft observations by Field et al (2005), a Gamma size distribution for cloud water with an aerosol dependent dispersion factor; an exponential size distribution for cloud ice, varying rain intercept considering the snow melted rain, varying snow density, and collision and collection processes parameterized using stochastic collision equation. The scheme was designed to behave more like an explicit microphysical scheme by using lookup tables for conversion processes intensively.

3.3 Observed microphysical characteristics

As highlighted in Chapter 2, the 4-5 December 2001 event featured a landfalling baroclinic trough over the Pacific Northwest. This section focuses on the in situ precipitation band microphysical measurements by the S-Pol radar, radiometer, NOAA P-3, and Convair aircraft.

There were numerous convective cells over the coastal range and Cascades during this event. The precipitation structures observed over the Cascades during the airborne microphysical measurements are illustrated using a composite of reflectivities and winds at 3-km above mean sea level (MSL) from the NOAA P-3 along north-south legs 2-4 between 2351 UTC 4 and 0051 UTC 5 December (Fig. 3.1a). There are some precipitation enhancements over the southwest-facing ridges, while other areas of enhanced precipitation originated over the coastal range and propagated east-northeastward with the 15-20 m s^{-1} west-southwest flow at this level (cf. Fig. 2.11). Figure 3.1b suggests that the 1.33-km WRF was able to realistically simulate the enhanced precipitation areas over the windward slopes and crest of the Oregon Cascades as well as the precipitation shadow in the lee of the Cascades.

Figure 3.2 shows the S-Pol RHI reflectivities at 0013, 0035, and 0118 UTC 5 December and the Convair ice water contents (IWC) during this period (CV in Fig. 3.1a). At 0013 UTC (Fig. 3.2a), the IWC is generally less than 0.1 g m^{-3}, with reflectivities less than 4 dBZ at 4.6 km MSL (-26 ^{o}C). The 2D-C imagery suggests small unidentified ice crystals (Stoelinga et al. 2007) at this level (Fig. 3.2a). At 0035 UTC (Fig. 3.2b), the IWC

at 4.5 km MSL peaks at ~0.16 g m^{-3} at -122.6 ^{o}W, where the Convair entered the upper portion of a convective cell of ~10 dBZ. At 0118 UTC (Fig. 3.2c), the IWC reaches ~0.20 g m^{-3} over the eastern portion of the second cross-barrier leg as the Convair entered another convective cell over the Cascade crest at 4.2 km MSL (-22 ^{o}C). Larger stellar and irregular crystals are prevalent within these cells (Fig. 3.2b, c). In contrast, there is less than 0.1 g m^{-3} IWC between the convective cells at 4.2 MSL over the Willamette Valley.

Figure 3.3 shows the P-3 reflectivities and in situ IWC and CLW contents along leg 2 (2351-0009 UTC at 2.45 km MSL or -9.5 ^{o}C) and leg 3 (0016-0032 UTC at 3.35 km MSL or -15 ^{o}C) over the Cascade windward slope (track shown in Fig. 3.1a). There are large variations in the ice and water mass along the legs as a result of the convective cells. Within the enhanced precipitation areas (~20 dBZ) along leg 2 (Fig. 3.3a), there are relatively large IWCs (~0.3 g m^{-3}) and relatively large aggregates of dendrites (2-3 mm). In contrast, between the precipitation cells near 44.25 ^{o}N (Fig. 3.3a), the IWC is ~0.05 g m^{-3} and the dendritic and irregular crystals are < 2 mm. Both the reflectivities and IWCs along leg 3 are approximately 50% less than leg 2 (Fig. 3.3b), which suggests a rapid depositional and aggregate growth between 3.5 and 2.5 km MSL. There is very little riming observed in the 2DP imagery for legs 2 and 3 (not shown). However, at Tombstone, near the Cascade crest (TT in Fig. 3.1b), ground observers reported moderately rimed dendritic assemblages around 0000 UTC 5 December. This suggests that riming was mainly prevalent below 2.5 km MSL during this event. Upstream of the Cascades along leg1 (1.85 km MSL or -5.5 ^{o}C), there are IWC and CLW amounts of 0.09 and 0.06 g m^{-3} (not shown), respectively, associated with lightly rimed bullets and stellar type ice crystals (not shown).

Figure 3.4 shows the leg-averaged ice particle size distributions from NOAA P-3 legs 1-3 and Convair flight legs. The size distribution for snow is less steep along the P-3 leg 2 over the windward Cascades at -10 ^{o}C than the Convair at -26 ^{o}C. The snow intercept from the Convair 2D-C at –26 ^{o}C is one order of magnitude larger than the P-3 at –10 ^{o}C. The snow size distribution for the P-3 has a slightly steeper exponential distribution for particles smaller than 1 mm. Field et al. (2005) labeled this behavior as the shoulder-feature in the size distribution related to aggregation. The snow intercept values for the 4-5 December event are generally 2-3 times less than the heavier precipitation event on 13-14 December for the same temperatures aloft (e.g., Fig. 12 of Woods et al. 2005; Fig. 8 of Garvert et al. 2005b). Thus, the snow intercept increases with greater snow mixing ratio and decreasing temperatures, which is why both variables are used to determine the intercept in some BMPs (Thompson et al. 2008). Model snow size distributions will be compared with observed (Fig. 3.14) and will be discussed in the verification section.

Figure 3.4 suggests that ice particles grew via deposition and aggregation between the Convair and the P-3 altitudes; however, the average IWC along the P-3 leg 3 (0.08 g m^{-3}) is slightly less than the Convair (0.11 g m^{-3}). During the P-3 leg 3 period (0015-0031 UTC), the Convair flew through the tops of convective cells over the Willamette Valley

and lower windward Cascades (Fig. 3.2a, b), where there are more < 0.75 mm ice particles along the Convair legs than at the P-3 leg 3 level (Fig. 3.4). The Convair particles are more compact (and likely more dense) than the P-3 (Figs. 3.2 and 3.3), which may be enhancing the mass at the Convair level. The P-3 leg 3 reflectivities are still 2-4 dBZ larger than the Convair (Figs. 3.2 and 3.3), since there are many crystals along the P-3 leg 3 with a larger cross-sectional area than the Convair.

3.4 WRF microphysical verification

a. Surface precipitation

Figure 3.5 shows the 12-h (2000 UTC 4 December to 0800 UTC 5 December) surface precipitation from four WRF simulations using different BMPs at 1.33-km grid spacing. In general, all four BMPs produce two precipitation maxima, one along the coastal range (20-40 mm) and another over the windward slopes and crest of the Cascades (20-50 mm). THOM1 and THOM2 predict a similar precipitation distribution and maximum of ~50 mm over windward ridges of the Cascades, with THOM2 generating approximately 10% more precipitation than THOM1 over the Cascade windward slopes. In contrast, the WSM6 and LIN schemes generate more localized precipitation maxima over the Cascade windward slopes, with a few 60-70 mm areas. The THOM1 and THOM2 schemes have more precipitation spillover in the lee of Cascades than the LIN and WSM6, with the 5-mm contour extending ~10 km farther to the east in the THOM1 and THOM2.

Figure 3.6 shows an east-west cross section of meridionally-averaged precipitation for the four BMP simulations over the coastal range and Cascades (black box in Fig. 3.5a) from 2000 to 0800 UTC 4-5 December 2001. The maximum precipitation over the coastal range is shifted ~10 km to the west in the LIN and WSM6 than the THOM and THOM2, which suggests a more rapid precipitation fallout in the LIN and WSM6. The LIN scheme produces the largest average precipitation (121 cm) over the coastal range, followed by the WSM6 (119 cm), THOM1 (91 cm), and THOM2 (96 cm). In contrast, the precipitation amounts over the Cascades for the various BMPs are within 10%, and their precipitation profiles have a similar shape. This suggests that the convective cells over the narrow coastal range have a greater microphysical and precipitation sensitivity than the precipitation generation over the broader Cascade barrier.

Figure 3.7 shows the percent of observed precipitation for the 1.33-km WRF between 2000 UTC 4 to 0800 UTC 5 December for the various BMP experiments. All schemes underpredict precipitation by ~30% over the coastal range and Willamette Valley, with LIN and WSM6 having more spatial variability in the verification results. There is overprediction over some areas of the Cascade windward slope in the LIN and WSM6, especially in the IOP region (boxed region in Fig. 3.5a). There is overprediction (> 150%) at a few sites in the immediate lee of the Cascades for all schemes except the

LIN. In contrast, all the schemes underpredict precipitation (by 60-80%) about 40 km to the east of the Cascades crest.

b. Microphysical differences in the WRF BMPs

The east-west cross section of hydrometeors meridionally-averaged over the black box in Fig. 3.5a was constructed for the four BMP simulations (Fig. 3.8). Cloud ice is negligible below 5 km MSL except for WSM6, which uses a relative larger maximum ice size (500 microns) before converting ice to snow (Hong et al. 2004). THOM1 produces the largest CLW (0.2 g kg^{-1}) extending up to 4.5 km MSL over the coastal range and Cascades windward slopes, while the WSM6 and LIN have the least CLW (0.1 g kg^{-1}) below 3 km MSL, especially over the Cascades. THOM1 and THOM2 generate more snow spillover into the lee of Cascades than WSM6 and LIN. THOM1 predicts 2 times more graupel over the coastal range than the Cascades. Graupel is more dominant than snow for the LIN and WSM6, with graupel extending up to 3.5 km MSL. LIN has the smallest hydrometeor mass aloft, which suggests more rapid precipitation fallout. Overall, snow is dominant for the THOM1 and THOM2, while graupel is more prevalent at low levels for WSM6 and LIN.

Figure 3.9 shows the mean vertical profiles of hydrometeor mixing ratios and relative humidity with respect to ice (RHI) for boxes A and B in Fig. 3.5a for each BMP. In general, except for the LIN scheme, there is more snow than graupel within box B over the Cascades than for box A over the coastal range. The THOM2 generates negligible graupel in box B, while the LIN predicts similar amounts of snow and graupel in boxes A and B. There is a relatively large amount of cloud ice (~0.08 g kg^{-1}) in the WSM6 above the freezing level, while the other three schemes predict cloud ice only above 4.5 km MSL (~-20 ^{o}C). Cloud water peaks just above the freezing level for all schemes, and it is largest for THOM1. Snow peaks near 2 km MSL at -7 ^{o}C in the THOM1 and THOM2, but it maximizes around 4 km MSL in the LIN and WSM6. The RHI over the Cascades around -20 ^{o}C peaks at 115% and 112% in the THOM1 and THOM2, respectively. In contrast, WSM6 and LIN have RHIs of 102-104%. The small RHI in WSM6 is likely from the large amount of cloud ice aloft, which depletes the ice supersaturation. The LIN uses the saturation adjustment method of Tao et al. (1989), which adjusts the water vapor to the mass-weighted combination of the saturation values over liquid water and ice. This is in contrast to other BMPs, which adjusts the water vapor to saturation values over liquid water (Dudhia 1989). A separate 1.33-km WRF simulation using the Dudhia (1989) saturation adjustment in the LIN scheme increases the RHI to 130% at ~5 km MSL and it reduces the surface precipitation over the coastal range and Cascade windward slopes and crest by 10-15% (not shown).

c. Cloud water and water vapor verification

Figure 3.10 shows the observed liquid water depth (LWD) from the radiometer at Santium Junction, which is located ~8 km west of the Cascade crest at 1.1 km above

MSL (SJ in Fig. 3.1b). This LWD represents mainly integrated cloud liquid water, since there is little rainwater at this height given the relatively low freezing level (~1 km MSL). Before 0000 UTC 5 December, the LWD measurements oscillate between 0.20 and 0.50 mm in association with intermittent convective cells. Prior to the passage of the mid-level trough between 0000 and 0700 UTC 5 December, the LWD gradually increases from 0.20 mm to 0.55 mm. With the passage of the surface trough at 0900 UTC 5 December, the LWD decreases to 0.18 mm. Afterwards, the LWD is ~0.40 mm with the post-frontal convection. Overall, the LWDs during this event are 80% less than the 13-14 December event (cf. Fig. 7 of Garvert et al. 2005b). The freezing level was near 2 km above MSL and the cross barrier flow was twice as strong in the 13-14 December event, both of which favors more super-cooled water generation at low-levels.

The four BMP simulations produce a gradual increase of observed LWD after 1800 UTC 4 December as observed; however, most schemes underpredict the LWD by 30-70%. In general, THOM1 predicts the largest LWD (~0.25 mm) from 2300 to 0200 UTC 4-5 December, followed by LIN (~0.20 mm). WSM6 and THOM2 predict the smallest LWD (~0.10 mm). The CLW underprediction occurs even though the 1.33-km WRF vertical motions are relatively well predicted along the NOAA P-3 flight legs (Fig. 2.17c).

Figure 3.11a shows the simulated and observed column integrated water vapor (IWV) at the UW and BB sounding sites (Fig. 3.1b). During the early period (from 1500 to 0500 UTC 4-5 December) the IWV increases at both sounding locations, and there is nearly two times more IWV at UW than in the immediate lee at BB. This difference is from the higher altitude at BB (1027 m MSL) and the lee side subsidence near BB (not shown). Before 0300 UTC 5 December, the THOM1 and THOM2 runs have approximately 0.1 cm (~8%) more IWV than observed, while the LIN and WSM6 overprediction is 0.02-0.05 cm. In contrast, at the BB site there is a ~20% IWV underprediction in the LIN, while the THOM1 and THOM2 are only slightly drier than observed (less than 10%) during 0300-0500 UTC 5 December.

To quantify the vertical moisture errors in the WRF, Fig. 3.11b shows the model water vapor mixing ratio bias at UW and BB at 0300 UTC 5 December 2001. At UW, all the simulations overpredict the moisture in the boundary layer (below 1 km MSL), which contributes to the overpredicted IWV in Fig. 3.11a. Above 2 km MSL, the error is generally less than 0.2 g kg^{-1}. All schemes are too dry below 3 km above MSL in the lee at BB. The LIN and THOM1 develop a large dry error from the windward to the lee, which suggests that too much water vapor was removed over the windward slope.

d. Verification using radar and aircraft

Figure 3.12a shows a time series of the observed radial velocities in the vertical over the S-band profiler site (MB in Fig. 3.1b) for a 6-h period (0000 to 0600 UTC 5 December). The radial velocity represents a combination of the vertical air motions and hydrometeor fall speeds; however, the 1.33 km WRF suggests that 90% of the

time-averaged vertical motion is from the fall speed at this S-band valley location at 0.5 km MSL (not shown). As with other IMPROVE-2 events (Medina et al. 2007), there are turbulent updraft cells of ~1 m s^{-1} within a vertical shear layer near 1.5 km MSL (cf. Fig. 2.13). Above 3.5 km MSL, the average velocity for the 6-h period is downward at about 1 m s^{-1} as a result of the falling snow particles. As the snow crystals become more rimed approaching the surface, the net downward motion gradually increases to 1.8 m s^{-1}. There is a secondary reflectivity maximum near 3 km MSL at around –15 ^{o}C (cf. Fig. 2.15), where the mean downward velocity decreases by ~0.2 m s^{-1}. This is consistent with rapid dendritic snow growth at this level (Fig. 3.3), which results in slower fall speeds.

Figure 3.12b,c shows the 6-h mean reflectivity-weighted snow/graupel fall speeds for the various 1.33-km WRF BMPs and their mixing ratios during the same 6-h period at the S-Band site using the 15-minute WRF outputs. The reflectivity-weighted fall speed is calculated by assuming the reflectivity is proportional to D^6 for the THOM1, LIN and WSM6. Refer to Thompson et al. (2008) for the reflectivity-weighted snow fall speed calculation for THOM2. The vertical air motions in WRF were not included in the analysis, since most of the WRF vertical velocities are from the hydrometeor fall speeds. The WSM6 and LIN schemes predict increasing fall speed with decreasing altitude, with maximum fall speed of 3.9 and 5.7 m s^{-1} at 1.5 and 2 km MSL, respectively. In contrast, the fall speed in the THOM1 decreases from 2.4 m s^{-1} to 1.6 m s^{-1} towards the surface, mainly due to the increasing air density and the dominance of snow at low-levels. THOM2 predicts the observed increase in fall speed below 3 km MSL and has a ~0.5 m s^{-1} overprediction below3 km MSL and above the freezing level (~1 km MSL). For the THOM1 and THOM2 above the S-band site, snow dominates over graupel by more than a factor of 5, with peak snow mixing ratios near 2 km MSL. In contrast, nearly all hydrometeors in the LIN and WSM6 runs are graupel below 2 km MSL.

Using the NOAA P-3 and Convair data (P3 and CV leg in Fig. 3.1a), the CLW, IWC, and vertical motions in the 1.33-km WRF runs were verified. The model fields were interpolated in time and space to the flight tracks using 15-minute output from the 1.33-km WRF. To determine whether relatively small timing errors in the WRF had an impact on the results, two other interpolations were done using WRF data an hour before or after the aircraft times. The time-shifted verification results are generally within 10% of the actual times (not shown).

Figure 3.13 shows in situ measured and simulated CLW, IWC, and vertical motions (Convair did not measure vertical motions) for the Convair legs at 4.2-4.6 km above MSL (-22 to -26 ^{o}C) between 0003 UTC and 0115 UTC (leg CV in Fig. 3.1a). The four BMPs predict similar vertical motions along the flight track; however, only the THOM1 generates CLW amounts comparable to the observed (0.01-0.07 g m^{-3}). The Convair measured IWC of ~0.25 g m^{-3} at 4.2 km MSL within the convective cells and ~0.05 g m^{-3} outside the cells. The WSM6, THOM1, and THOM2 schemes have mean IWCs within ~20% of observed at this height (Table 3.2). In contrast, the LIN scheme underpredicts the IWCs by ~30% at this altitude on average. The LIN scheme also

produces about 0.02 g m^{-3} of graupel at this height, while none was observed (not shown).

Overall, all microphysical simulations predict the IWC well at the Convair legs. However, the model snow size distributions have large variance among these microphysical simulations. Mass-dimension (m-D) relationship relates the mass with the size distribution and thus affects all the microphysical parameterizations in the scheme. Figure 3.4a highlights the differences among the different m-D relationships used in the study. The traditional spherical assumption with a constant density of 100 kg m^{-3} (CONST) for snow actually gives much larger mass than those empirical m-D relationships used in the observation retrievals (HEYMS, BF, and AGGR) for large particles, while for small particles, it gives less mass. The implication is that snow particles density is decreasing with the diameter in reality. The constant snow intercept used in LIN is more than one order smaller than measured (Fig. 3.4b). As a result, the mass-mean particle size (the inverse of the slope) is much larger than observed. The temperature dependent snow intercept used in WSM6 and THOM1 is also slightly smaller than observed. THOM2 predicts the size distribution well with the slope close to the observed. As THOM1 and WSM6 underpredict the particles of size around 0.5 mm, more particles larger than 1 mm are predicted to ensure the well- predicted IWCs.

At 3.3 km MSL along leg 3 (Fig. 3.14), the P-3 has < 0.05 g m^{-3} of CLW and ~0.08 g m^{-3} of IWC, with little evidence of riming or graupel in the 2D-C imagery at this level (Fig. 3.3b). All schemes predict negligible CLW at this level, except THOM1, which produces 0.05 g m^{-3} CLW for part of the leg. However, WSM6, THOM1, and THOM2 produce approximately 3 times more IWC than observed at this altitude (Table 3.2). In contrast, the LIN produces comparable amounts of snow and graupel at this level (not shown). The sum of snow and graupel is within 20% of observed for LIN; however, there is overprediction at the surface in the LIN (Fig. 3.7d). At this leg (Fig. 3.4c), THOM2 overpredicts the number of particles smaller than 1 mm with a well-predicted slope for particles larger than 1 mm. THOM1 and WSM6 overpredict the number of particles with sizes larger than 2 mm. LIN underpredicts the intercept with a smaller slope than the observed. This indicates that the overprediction of snow at this leg could result from either the size distributions or m-D relationships.

Figure 3.15 compares the IWCs from the P-3 and 1.33-km WRF along leg 2 (2.45 km MSL or about -9.5 ^{o}C). The four WRF BMPs realistically simulated the vertical motions of +/-0.5-1.5 m s^{-1} along this leg. However, all four schemes underpredict CLW along the leg except the THOM1, which has a mean CLW of 0.13 g m^{-3}. Both THOM1 and THOM2 overpredict the IWC along most of the leg 2 by 55-65% on average (Fig. 3.15a, Table 3.2). LIN produces slightly less IWC (0.14 g m^{-3}) than observed (0.20 g m^{-3}), while WSM6 overpredicts the IWC by ~35% (Table 3.2). The WSM6, THOM1 and THOM2 predict ~2 times larger IWC along the P-3 leg 1 (1.85 km MSL, -5.5 ^{o}C, Table 3.2). At leg2, interestingly, all the schemes underpredict the mean particle size with relatively well-predicted intercept (Fig. 3.4d). The overpredicted IWC by THOM1

implies that the snow density used is larger than observed for large particles (> 1 mm) as indicated in Fig. 3.14a at this leg. So overpredicted snow mass does not necessarily mean larger sizes due to the different m-D relationships used in the scheme and observation retrieval.

Overall, during this IOP there is little snow overprediction at -26 ^{o}C, however, below this level most BMPs (except LIN) produce excessive IWC in the maximum snow depositional growth zone of -10 to -20 ^{o}C (Rogers and Yau 1989). Garvert et al. (2005b) also found that the THOM1 scheme overpredicts snow in this temperature range for the 13-14 December event. The WSM6 and the latest THOM2 scheme produce similar IWC problems, so this error has not been reduced for these newer schemes in WRF.

3.5 Microphysical sensitivity tests and discussion

Both LIN and WSM6 predict more graupel than THOM1 and THOM2 (Figs. 3.8, 3.9). The partition of snow and graupel aloft impacts the fallout and surface precipitation distribution. One question is why the WSM6 and LIN generate more graupel than the Thompson schemes? Several sensitivity runs were completed with the LIN scheme, such as using the same temperature dependent snow intercept and graupel intercept as in THOM1, turning off the snow to graupel autoconversion, and using the same fall speed of snow, rain, and graupel as in THOM1. These sensitivity runs only increased the snow marginally aloft (by < 20%) and did not change the surface precipitation significantly (not shown).

As shown in Lin et al. (1983), the production of graupel by collecting snow (Pgacs) is one order of magnitude larger than the snow depositional growth (Psdep). Pgacs is not used in the Thompson schemes, thus we hypothesized that Pgacs may favor the enhanced graupel growth in the WSM6 and LIN. A simulation with the Pgacs turned off in the run (LIN_NOGACS), significantly (> 90%) reduces the graupel and increases snow aloft over the Cascades (Figs. 3.17c, 3.18c). Consequently, the precipitation bull-eyes are alleviated and the precipitation amounts become more comparable with the Thompson schemes over the Cascades (Fig. 3.16c). Increased snow depositional growth aloft also reduces the CLW generation by condensation. Interestingly, the RHI of ~102% does not change in the LIN_NOGACS run. This is likely from the saturation adjustment, which is called last after all other microphysical processes in the LIN scheme. Another simulation with Pgacs turned off in the WSM6 generated the same effect (not shown).

The spherical assumption with constant density for snow and graupel has been used widely in BMPs to simplify microphysical parameterizations. Obviously, the spherical assumption is inconsistent with the varying snow habits in the observations. In addition, constant snow density is also not realistic for different habits, snow aggregates, and riming amounts. Woods et al. (2007) developed a temperature and relative humidity dependent snow habit prediction method and found that the new method increased the

precipitation for a rainband interacting with the windward slope of the Olympic Mountains. Another sensitivity test (THOM1_MD) was completed for the THOM1, in which the m-D power law for the computation of IWC was used (AGGR), rather than the conventional spherical assumption for snow. This modification is similar to what has been implemented in Thompson et al. (2008, $M=0.069D^2$). More specifically,

$$M = aD^b = 0.0278D^2 \tag{3.1}$$

was used rather than

$$M = \frac{\pi}{6}\rho_s D^3 = 0.0524D^3 \tag{3.2}$$

in which M is in mg and D is in mm. This M(D) relationship indirectly represents the decrease of snow density with diameter (Thompson et al. 2008). With the same snow mixing ratio, this modification decreases the snow slope parameter (e.g., for a snow mass of 0.3 g m^{-3} and a snow intercept of 60000 m^{-3} mm^{-1}, the mass-mean diameter is 0.36 and 0.45 mm, respectively), and thus affects all the snow related processes. Compared with the original THOM1, the precipitation in the THOM1_MD is more localized over the coastal range and Cascades crest, with less precipitation spillover (Fig. 3.16a). This is mainly due to the increased mass-weighted snow fall speed (~10% increase for a snow mass of 0.3 g m^{-3}) in THOM1_MD run. Interestingly, CLW decreases significantly (> 80%) over the Cascades, which is probably due to the enhanced snow depositional growth as discussed in Thompson et al. (2008). As a result, graupel is reduced to negligible values and there is a slight increase of snow over the Cascades (Fig. 3.17a). The aircraft verification shows that the THOM1_MD run has less CLW than observed (Table 3.2). Overall, the CLW and RHI distributions (Fig. 3.18a) in the THOM1_MD are more like THOM2, which uses a similar mass-diameter relationship for snow. The size distributions of THOM1_MD run (Fig. 3.14) shows how the m-D relationship affects the particle size distribution. The particle distribution of THOM1-MD run is much broader than THOM1 run though the IWC is similar (Table 3.2). This indicates a large sensitivity of model performance on the snow mass-diameter relationships.

Snow overprediction aloft has been noted in mesoscale numerical simulations (Garvert et al. 2005b; Colle et al. 2005a; Milbrandt et al. 2008). For the 13-14 December IMPROVE-2 event using the THOM1 scheme, Colle et al. (2005a) found that snow depositional growth contributed ~70% to the snow growth, followed by riming growth (~30%). Snow diffusional growth depends on the environmental supersaturation, particle electrical capacitance, ventilation effect, etc. (Rogers and Yau 1989; Fukuta and Takahashi 1999). Particle capacitance is a function of the size and shape of the ice particle. Capacitance for a sphere (C = 0.5D, where D is the diameter) has been widely used in the snow deposition and sublimation parameterization in BMPs. Recently, Westbrook et al. (2008) showed that capacitance of snow aggregates was only half that of a sphere, which will reduce the snow deposition rate. A third sensitivity run (THOM1_0.5SDEP) that reduced the snow deposition and sublimation rates by one half

was completed to test the snow depositional growth uncertainty on model simulated microphysics and surface precipitation. This run increases the surface precipitation by ~10% over the coastal range and decreases by ~10% over the windward slopes of Cascades (Fig. 3.16b). Snow aloft is reduced by ~60% over the Cascades in the snow depositional growth zone at –20 to -10 ^{o}C, but the graupel and CLW is increased by ~80% and 20% below 3 km MSL, respectively (Fig. 3.18b). As a result, this run verifies better along the flight tracks in terms of IWC; however, the CLW increases by 50% and verifies worse with observations (Table 3.2). This implies that other uncertainties in the snow depositional growth parameterization, such as ventilation effect, need to be refined also. In addition, realistic snow fallout also determines the snow mass aloft.

To check the conservation of water and relate the model cloud and precipitation properties with orographic precipitation theory, a water budget was conducted using the 1.33 km WRF output at 15 minute interval over boxes A and B (cf., Fig. 3.5a) during a 3-h period from 2300 to 0200 UTC 4-5 December. The box-integrated water budget can be expressed as

$$SUM = HFLX + EVAP - PREP - NETQ, \quad (3.3)$$

where EVAP is the evaporation from the surface and *PREP* is the surface accumulated precipitation within the box during the integration period, *HFLX* is the time and vertically integrated horizontal flux convergence of water substances (including water vapor and all the hydrometeors) summed over the four sides of the box (the calculations were integrated from the surface to the model top at ~16 km), and *NETQ* is the residual term, indicating the change of water substance within the box during the integration period. The sum of these four terms (*SUM*) is close to zero if water is conserved.

Orographic precipitation theory (Jiang and Smith 2003; Smith and Barstad 2004; Smith et al. 2005; Colle 2008) introduced some cloud scaling parameters, such as the drying ratio and cloud residence time, which can help quantify the precipitation efficiency within the BMPs. The drying ratio (DR) is defined as the ratio of the precipitation to the incoming water vapor flux (Smith et al. 2003). The characteristic time for the liquid and solid phase water to fall as precipitation is defined by the cloud residence time (Smith et al. 2003):

$$RT = \text{total condensed water} / \text{precipitation rate} \quad (3.4)$$

Table 3.3 summarizes the water budget variables and these DR/RT parameters. *EVAP* is less than one unit (10^9 kg) for all simulations and *NETQ* differs less than 3 units among the simulations. For brevity, these two variables are not included in Table 3.3. For box A, the DRs for the WSM6 (14%) and LIN (16%) are larger than THOM1 (9%) and THOM2 (9%). The DR over the coastal range is approximately 40% less than the Cascades for the WSM6 and LIN, while it is ~60% less than the Cascades for the THOM1 and THOM2. The four BMPs have comparable DRs over box B over the Cascades given their comparable water vapor flux and precipitation (Table 3.3). Corresponding to the larger surface precipitation and smaller hydrometeor mass aloft (c.f. Figs. 3.8, 3.9), LIN has the smallest RT (1200 s and 1000 s for boxes A and B). The RT

for WSM6 is 1900 and 1700 s for box A and B, respectively, while the RT for THOM1 is around 3000 s in box A and 2500 s in box B. THOM2 has a RT of 3100 s in box A and 2200 s in box B. Relatively larger condensed water mass and smaller precipitation rate over the coastal range (especially for THOM1 and THOM2, cf. Fig. 3.6) contribute to the relatively larger RT over the coastal range than Cascades for all schemes. The smaller RTs in the LIN and WSM6 are from their greater graupel production than other schemes.

Braun (2006) examined artificial source terms for cloud and precipitation mass within a hurricane simulation associated with setting negative mixing ratios to zero for the numerical advection of hydrometeors. He found that the accumulative effect of these artificial source terms contributed to a mass equivalent to 15-20% of the surface precipitation. In order to better conserve mass, a positive definitive advection (PDA) scheme has been developed for the WRF (Skamarock 2006) and is found to reduce the large positive precipitation bias (Skamarock and Weisman 2008). To test the impact of the PDA, four additional simulations of the BMPs were completed without the PDA scheme turned on (NOPD simulations in Table 3.3). The non-PDA simulations have 25-45% more surface precipitation than the PDA simulations over box A, compared with ~10% more precipitation than the PDA over box B (Table 3.3). The *SUM* is slightly positive using the PDA (3-8% of the HFLX for the PDA simulations), while SUM is negative (~20% of HFLX) for the non-PDA runs. A negative *SUM* implies the WRF generates more precipitation than available water sources. Overall, water is better conserved for the PDA simulations. The *SUM* is much (3-4 times) larger over Box A than Box B for non-PDA runs, which implies the large horizontal gradient of hydrometeors associated with convective cells over the coastal range tends to generate more negative values without PDA. The non-PDA runs also increase the hydrometeor mass aloft by ~10-20% in general (Fig. 3.17d, Fig. 3.18d). The non-PDA simulation has 30-40% more precipitation than the PDA simulations over the coastal range (Fig. 3.16d).

3.6 Summary

The microphysical structures and model microphysical and precipitation verification was investigated for the 4-5 December event. In situ particle images and retrieved IWC from the Convair and P-3 suggest large vertical and horizontal variation of microphysical characteristics. Small irregular cold type ice particles above 4 km MSL grow in size via deposition and aggregation as they fall towards the warmer temperatures. Large aggregates and dendritic particles were observed in transient convective cells resulting from the increased depositional and aggregation growth, while outside of the convective cells, the ice particles were smaller and the IWC was less.

The 4-5 December event was simulated down to 1.33-km grid spacing using four BMPs within WRF. Model surface precipitation and microphysics were verified with rain gauge data as well as in situ radar and aircraft measurements. All simulations slightly underpredict the precipitation over the coastal range and Willamette Valley, with no

widespread overprediction over the windward slopes of the Cascades. There is an underprediction further east of the Cascades for all the simulations, which implies that the simulated cloud dissipates too rapidly within the lee subsidence. The LIN and WSM6 schemes have more localized and overpredicted areas of precipitation over the windward slope and less spillover into the lee of the Cascades due to the dominance of graupel aloft.

Microphysics verification suggests all BMPs except the LIN scheme tend to overpredict snow in the maximum snow depositional growth region aloft. THOM1 realistically predicts CLW along the flight tracks, while other three schemes underpredict CLW. Graupel dominates over snow for the WSM6 and LIN, while snow dominates over graupel in the THOM1 and THOM2. For the reflectivity-weighted snow/graupel fall speed, the LIN and WSM6 predict a larger fall speed than observed due to the dominance of graupel and associated larger fall speeds. THOM1 generates a decreasing fall speed to 1.6 m s-1 with decreasing altitude. THOM2 is able to reproduce the general pattern of the observed fall speed with ~0.5 m s-1 larger fall speed below 3.5 km MSL.

Sensitivity test with graupel collection of snow turned off in LIN and WSM6 reduces the graupel and increases the snow aloft significantly. Consequently, surface precipitation is more uniform over the Cascades and there is more precipitation spillover into the lee. Another sensitivity test using a new mass-diameter relationship with varying snow density generates a relatively large (10%) sensitivity on the microphysics aloft and surface precipitation. These BMP sensitivity simulations suggest the importance of the snow and graupel partitioning. A third sensitivity simulation with half the snow deposition and sublimation of the THOM1 scheme was completed to test the impact of using an overestimated capacitance for the assumed spherical snow crystals in the model. A simulation with half the capacitance reduces the IWC by ~30% in the snow depositional growth region, which verifies better with observations than THOM1. However, increased CLW and graupel compensate the decreased snow and the total hydrometeor mass aloft only change slightly. The large precipitation of LIN and WSM6 over the coastal range is mainly due to a higher precipitation efficiency associated with faster fallout of graupel. The positive definite advection (PDA) scheme in WRF was compared with the previous approach, which set negative mixing ratios to zero and produced an artificial source of water. Although this artificial water mass is negligible at any given grid point, its accumulative impact is substantial and contributes to 10-20% of the total surface precipitation, especially within the convective cells over the coastal range. A positive definite advection scheme for moisture and hydrometeors improves the water conservation and reduces the surface precipitation over the whole 1.33 km domain by ~10%.

Table 3.1 Summary of different simulations performed. The indices *c,i,r,s,* and *g* denote cloud droplets, cloud ice, rain, snow, and graupel, respectively. Mixing ratio and number concentration is indicated by *q* and *N*, respectively.

Simulation name	Snow → graupel	Specifid size distribution	Fall speed (all with density factor)	References and description
WSM6	**Pgacs**, Psacw, Pgaut	*c,i* monodisperse *r, s, g* exponential $Nos=2e6exp[0.12(T_0-T)]$ (H79) *Nor=8e6*, *Nog=4e6*	*c*--none i--$1.49e4D^{1.31}$ s--$11.72D^{0.41}$ r--$842D^{0.8}$ g--$330D^{0.8}$	Hong et al. 2004
LIN	**Pgacs**, Psacw, Pgaut	*c,i* monodisperse *r, s, g* exponential *Nor=8e6*, *Nos=3e6*, *Nog=4e6*	*c*--none $i=3.29(rho*q_i)^{0.16}$ s--$4.8D^{0.25}$ r--$842D^{0.8}$ g--$94D^{0.5}$	Chen and Sun 2002
THOM1	Psacw, Pscng	*c,i*-- monodisperse *s*--MP *Nos(T)* (H79) *g*--Gamma, $N_{0g}(q_g)$ BS97 *r*--MP with modified N_{0r} to consider drizzle	*c*--none *i--700D* IS(91) s--$11.72D^{0.41}$ r--$842D^{0.8}$ g--$19.3D^{0.37}$	Thompson et al. 2004
THOM2	Psacw, Pscng	*c--Noc=F(Nt_c)* Gamma distribution *s*-- sum of two Gamma based on F05 *r*--varying considering snow melting *i--Noi=F(Nt_i)* *i,g,r* -exponential	*c*-- none *i--2247D* s--$1.5*40D^{0.55}e^{-1.25D}$ r--$4854De^{-195D}$ g--$442D^{0.89}$	Thompson et al. 2008
LIN_NOGACS	Psacw, Pgaut	the same as LIN	the same as LIN	Pgacs turned off
THOM1_MD		the same as THOM1	the same as THOM1	$M=aD^b$
THOM1_0.5SDEP		the same as THOM1	the same as THOM1	Psdep and Pssub are half as in THOM1

Table 3.2 Observed leg mean CLW, IWC, and Graupel (g m^{-3}) vs. model along the P-3 and Convair flight legs. Model IWC includes the snow and ice.

Flight leg	P3 leg1	P3 leg2	P3 leg3	Convair leg
Altitude (m), Temperature (^{o}C)	1850m, -5.5 ^{o}C	2450m, -9.5 ^{o}C	3350m, -15.0 ^{o}C	4600~4200 m, -26~-22 ^{o}C
OBS CLW IWC graupel	**0.06+-0.01** **0.09+-0.02** **0.02+-0.02**	**0.12+-0.01** **0.20+-0.05** **0.02+-0.02**	**0.03+-0.00** **0.08+-0.02** **0.00**	**0.02+-0.00** **0.11+-0.02** **0.00**
THOM1 CLW[IWC]graupel	**0.06 [0.19] 0.01**	**0.13 [0.33] 0.03**	**0.02 [0.25] 0.00**	**0.00 [0.10] 0.00**
THOM1_MD	**0.03 [0.19] 0.01**	**0.01 [0.28] 0.00**	**0.00 [0.25] 0.00**	**0.00 [0.08] 0.00**
THOM1_0.5SDEP	**0.09 [0.21] 0.05**	**0.21 [0.19] 0.06**	**0.05 [0.22] 0.01**	**0.02 [0.10] 0.00**
THOM2	**0.01 [0.19] 0.00**	**0.04 [0.31] 0.00**	**0.00 [0.26] 0.00**	**0.00 [0.12] 0.00**
WSM6	**0.02 [0.16] 0.09**	**0.01 [0.27] 0.10**	**0.00 [0.24] 0.03**	**0.00 [0.13] 0.00**
LIN	**0.05 [0.12] 0.11**	**0.07 [0.14] 0.11**	**0.00 [0.10] 0.05**	**0.00 [0.07] 0.02**
LIN_NOGACS	**0.03 [0.25] 0.00**	**0.04 [0.37] 0.00**	**0.00 [0.21] 0.00**	**0.00 [0.07] 0.00**

Table 3.3 Water budget results for box A and box B (separated by vertical slashes). Water flux and precipitation are in units of 10^9 kg. See text for further details.

Simulation	*PREP*	*HFLX*	*SUM*	*DR (%)*	*RT (100s)*
THOM1	**23.5|54.1**	**26.6|63.7**	**1.9|3.5**	**9|22**	**30|25**
THOM2	**21.9|57.4**	**21.5|63.4**	**0.4|2.0**	**9|24**	**31|22**
WSM6	**33.7|61.2**	**31.9|66.1**	**1.6|0.0**	**14|26**	**19|17**
LIN	**37.3|60.5**	**37.4|66.1**	**2.3|1.5**	**16|25**	**12|10**
THOM1_NOPD	**32.4|59.8**	**23.5|66.9**	**-7.3|0.8**	**13|25**	**28|25**
THOM2_NOPD	**33.8|62.7**	**23.6|65.2**	**-8.0|-1.9**	**14|26**	**24|21**
WSM6_NOPD	**39.3|64.6**	**30.3|68.2**	**-6.0|-1.3**	**16|27**	**19|18**
LIN_NOPD	**46.0|68.0**	**38.4|68.5**	**-6.0|-3.6**	**19|29**	**12/10**

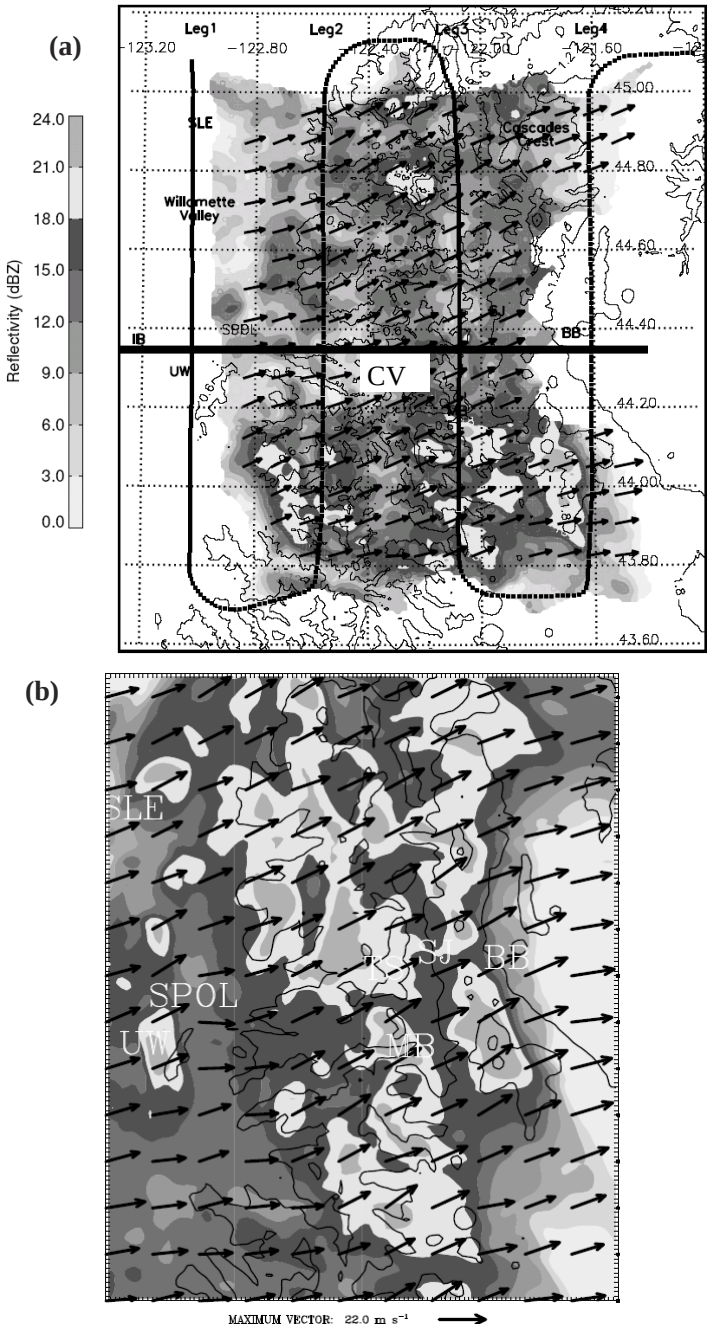

Figure 3.1 (a) Observed NOAA P-3 reflectivity (shaded every 3 dBZ) and Doppler radar derived winds at 3 km MSL for legs 2-4 between 2350 UTC 4 and 0050 UTC 5 December. Black lines are P-3 and Convair (CV) flight legs. (b) Same as (a) except for the 1.33-km WRF at 0000 UTC 5 December. The terrain is also shown every 0.6 km.

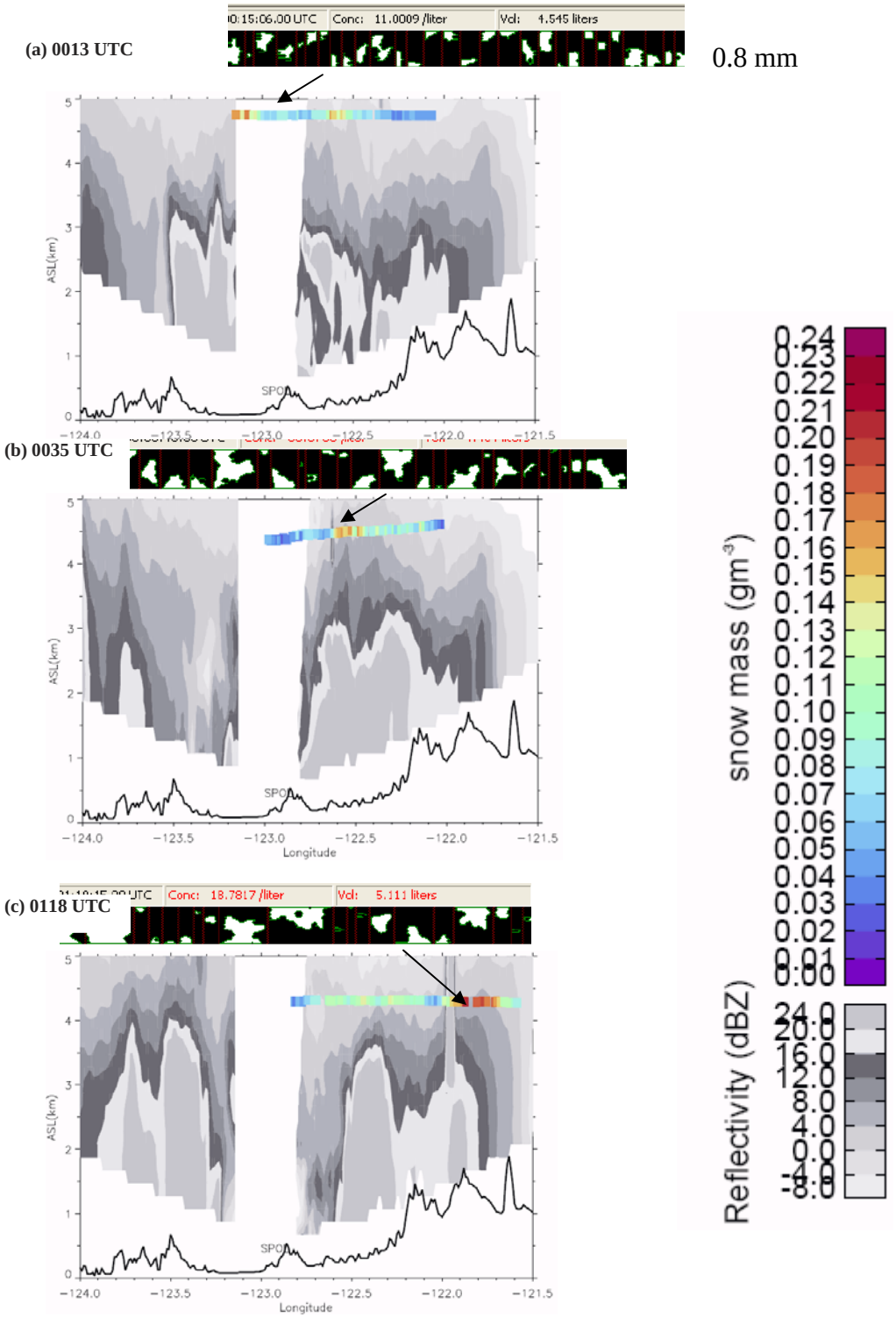

Figure 3.2 S-Pol radar reflectivities for the west-east cross section (gray-shaded every 4 dBZ) at (a) 0013 UTC, (b) 0035 UTC, and (c) 0118 UTC 5 December. In situ ice mass concentrations (g m^{-3}) from Convair are color-shaded along the corresponding flight leg sections (~ 20 minutes within S-Pol RHI scan time). The crystal images collected from the PMS 2D-C probe (with a 0.8 mm vertical dimension) are also indicated.

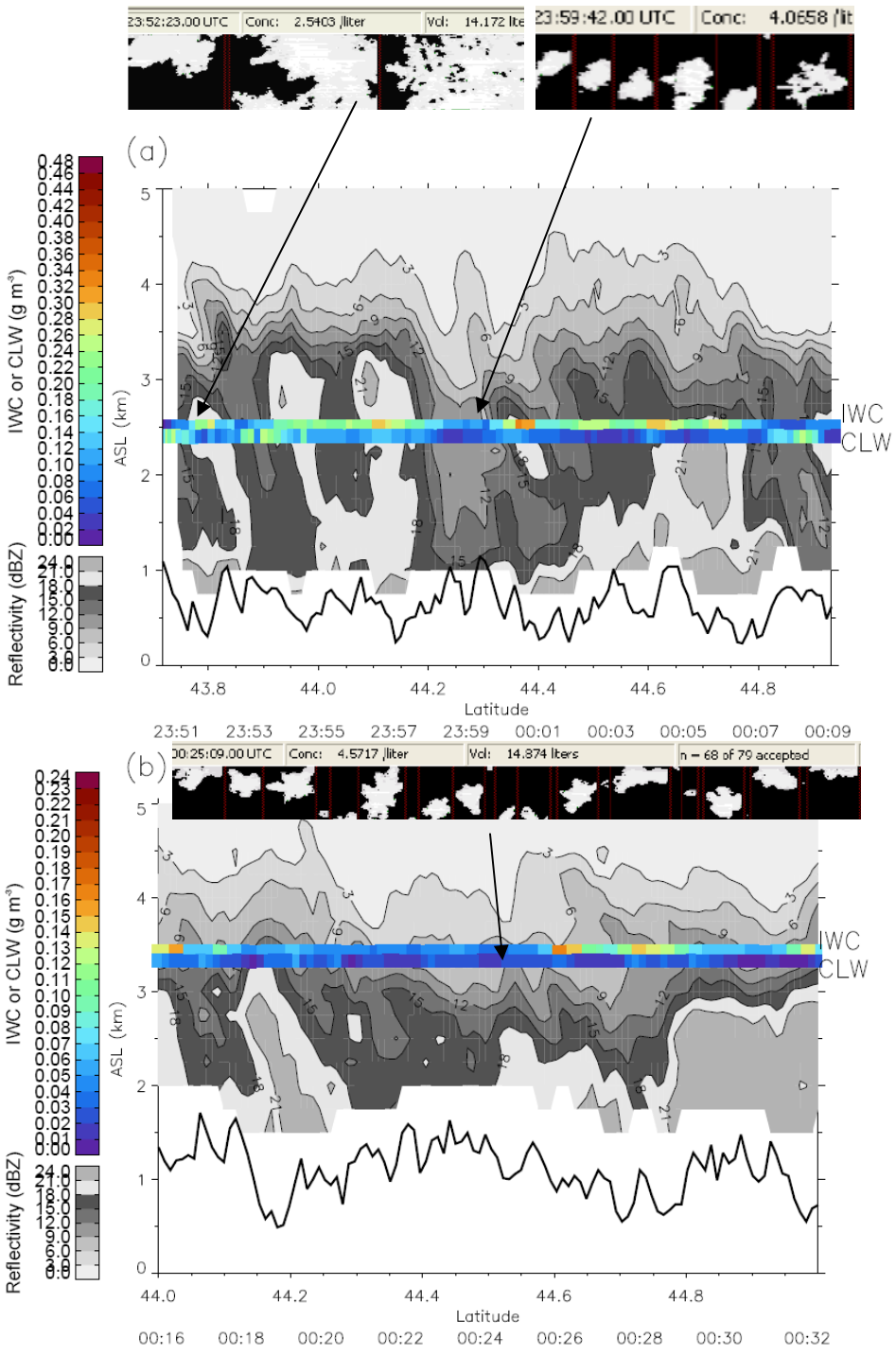

Figure 3.3 (a) P-3 radar reflectivities (gray shaded every 3 dBZ) and in situ ice mass concentrations and cloud liquid water concentrations (color filled every 0.02 g m^{-3}) along leg 2. (b) Same as (a) except along the P-3 leg3. The crystal images collected from the PMS 2D-C probe (with a 1.6 mm vertical dimension) along the P-3 flight legs are also indicated.

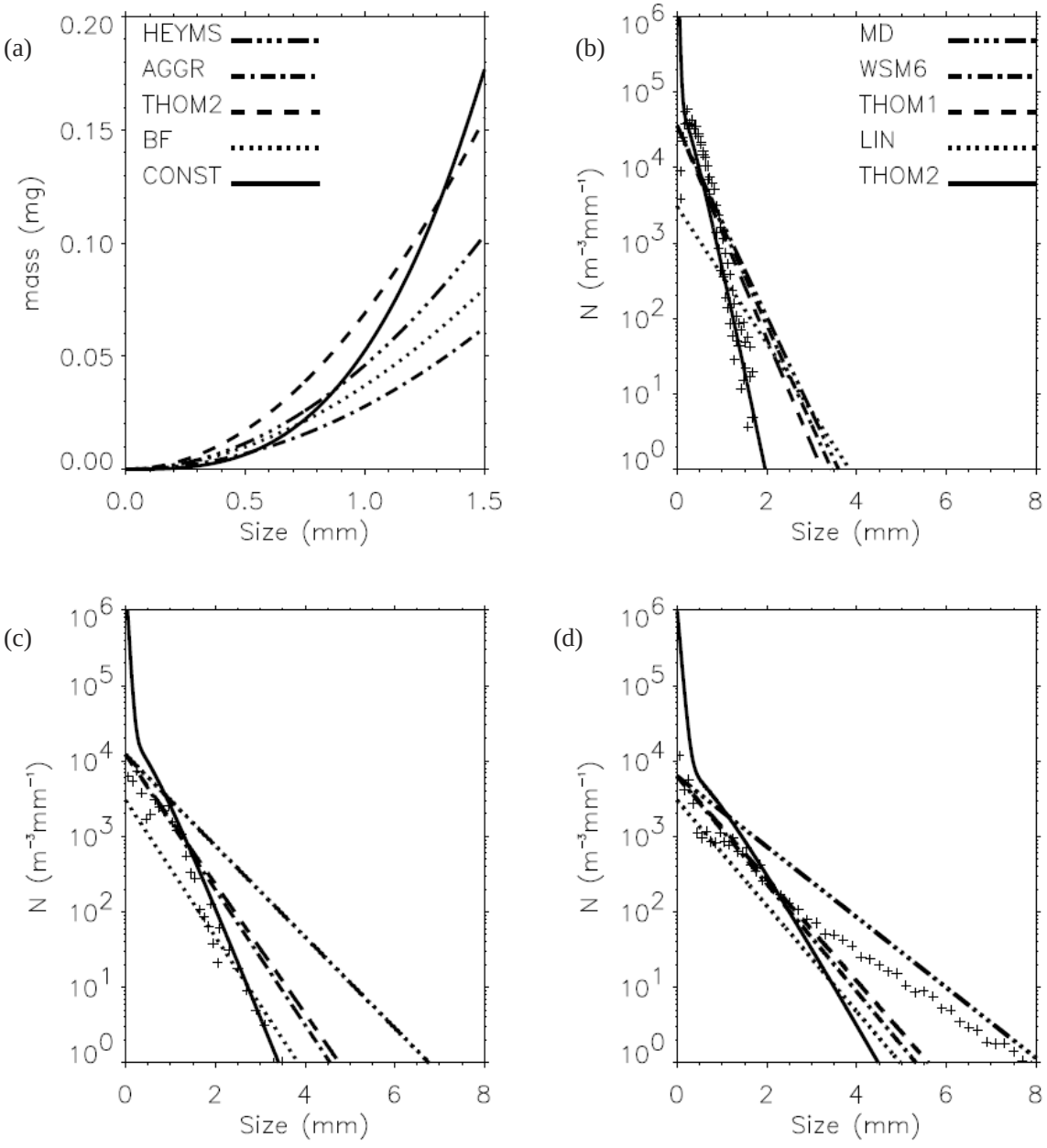

Figure 3.4 (a) Particle size spectra measured by the 2D cloud probes aboard the Convair and P-3. 2D-C data smaller than 1 mm and 2D-P data larger than 1 mm was combined for the P-3. Observed and simulated particle size spectra for the (b) Convair legs, (c) P-3 leg3, and (d) P-3 leg2 for the various microphysical runs (LIN,WSM6, THOM1, and THOM2).

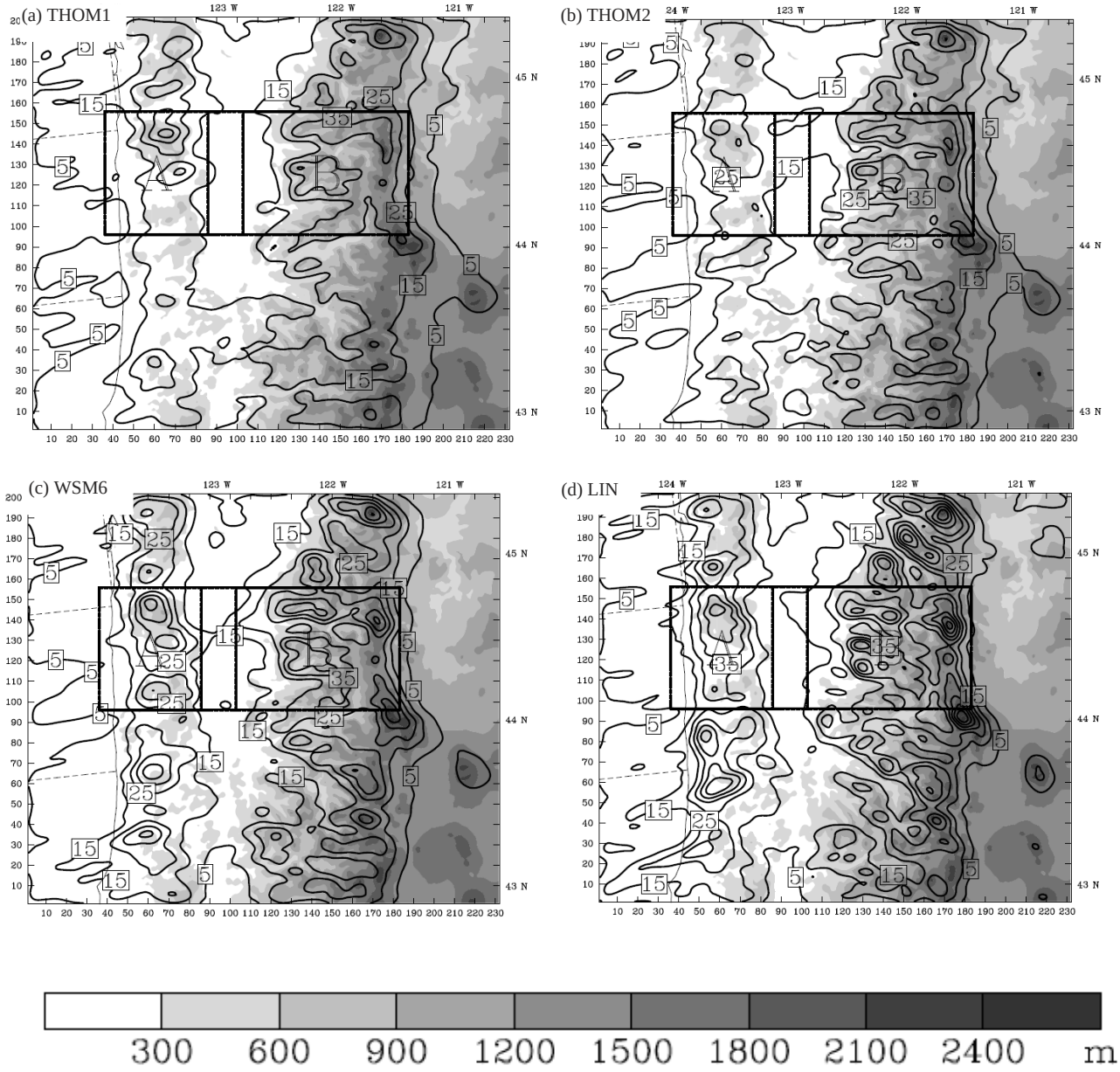

Figure 3.5 Surface precipitation totals (every 10 mm starting from 5 mm) for the 1.33 km domain between 2000 UTC 4 Dec and 0800 UTC 5 Dec for the (a) THOM1, (b) THOM2, (c) WSM6, and (d) LIN schemes. 1.33 km terrain is shaded every 300 m for reference. The box A and B show the region used for the vertical profile and water budget calculations.

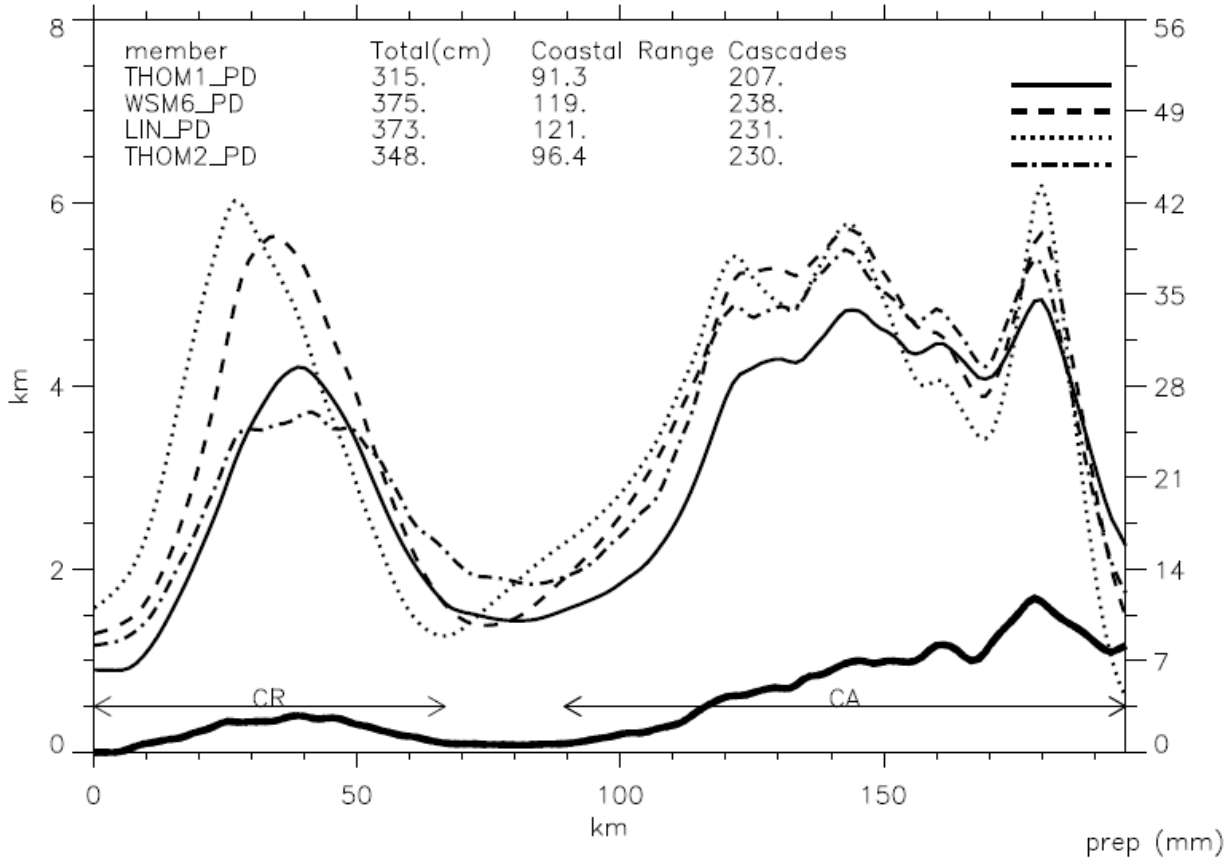

Figure 3.6 Simulated precipitation (in mm) from 2000 UTC 4 Dec to 0800 UTC 5 Dec averaged over the boxed area in Fig. 3.5. The average terrain profile is also indicated. The table at the top indicates the precipitation totals over the box A and B.

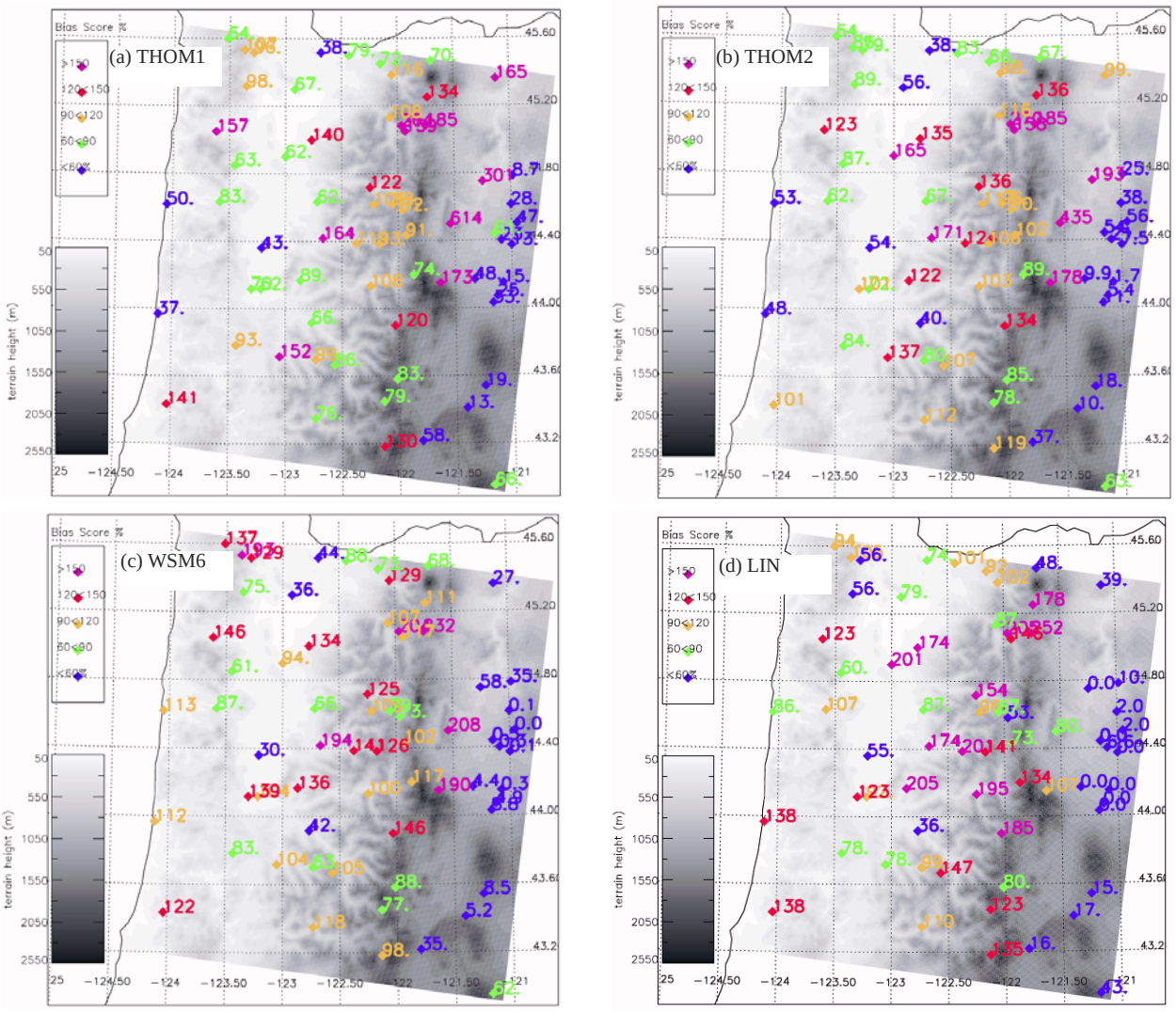

Figure 3.7 Percent of observed precipitation simulated by the 1.33-km WRF at the precipitation gauge sites between 2000 UTC 4 Dec and 0800 UTC 5 December for the (a) THOM1, (b) THOM2, (c) WSM6, and (d) LIN schemes. The percent values are color-coded using the inset scale in upper left. The terrain elevation is shaded (in m) using the inset scale in lower left.

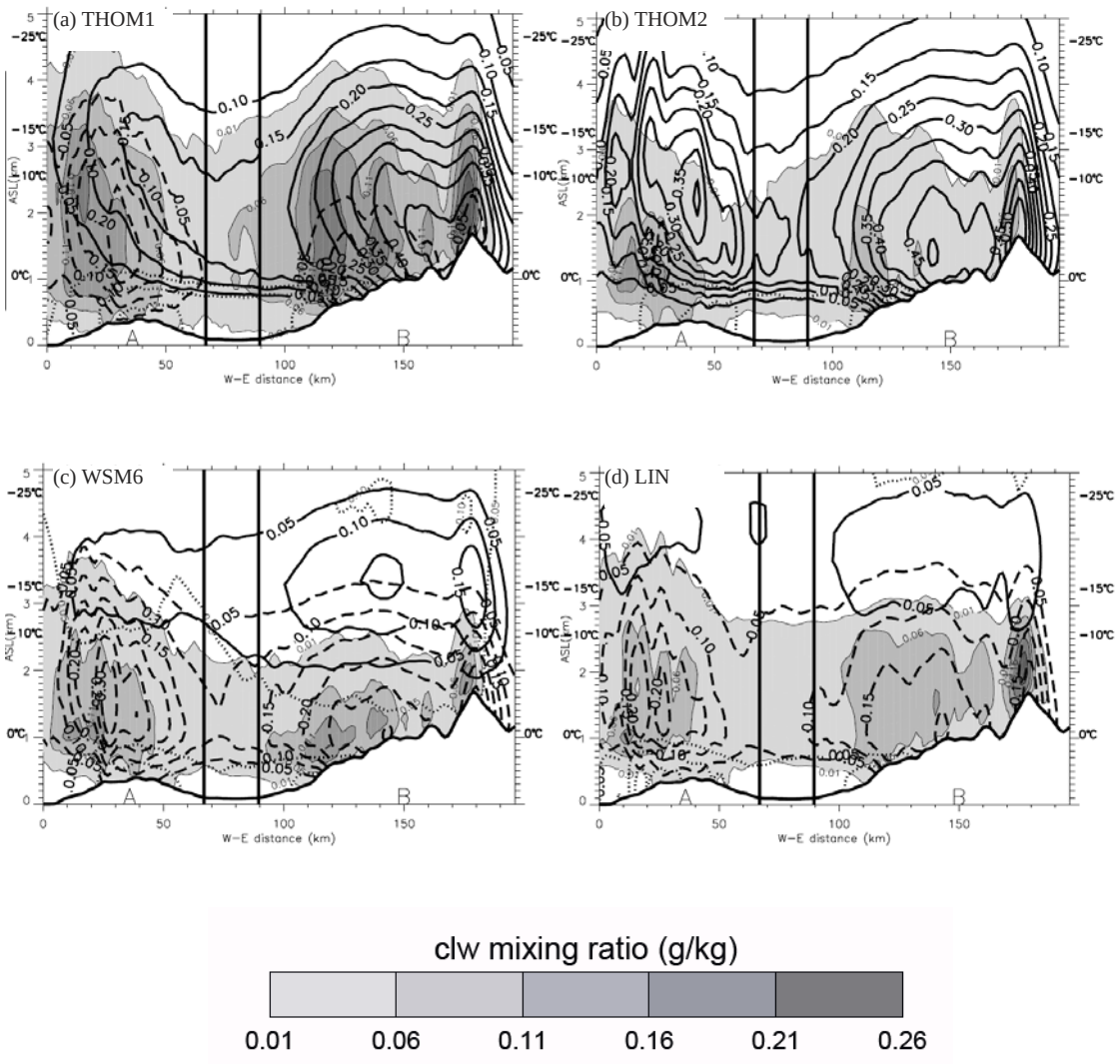

Figure 3.8 Meridionally averaged west-east cross section over the large box in Fig. 3.5 shows mixing ratio of model CLW (shaded every 0.05 g kg^{-1}), snow (black solid, every 0.05 g kg^{-1}), graupel (black dashed, every 0.05 g kg^{-1}), rain (black dotted, every 0.05 g kg^{-1}), ice (black dotted, every 0.05 g kg^{-1}) for the (a) THOM1, (b) THOM2, (c) WSM6, and (d) LIN scheme. Model fields were averaged from 2300 to 0200 UTC 4-5 Dec 2001 (forecast hours 11-14) using model outputs at 15-min intervals. The two vertical lines denote the box A and box B boundaries in Fig. 3.5.

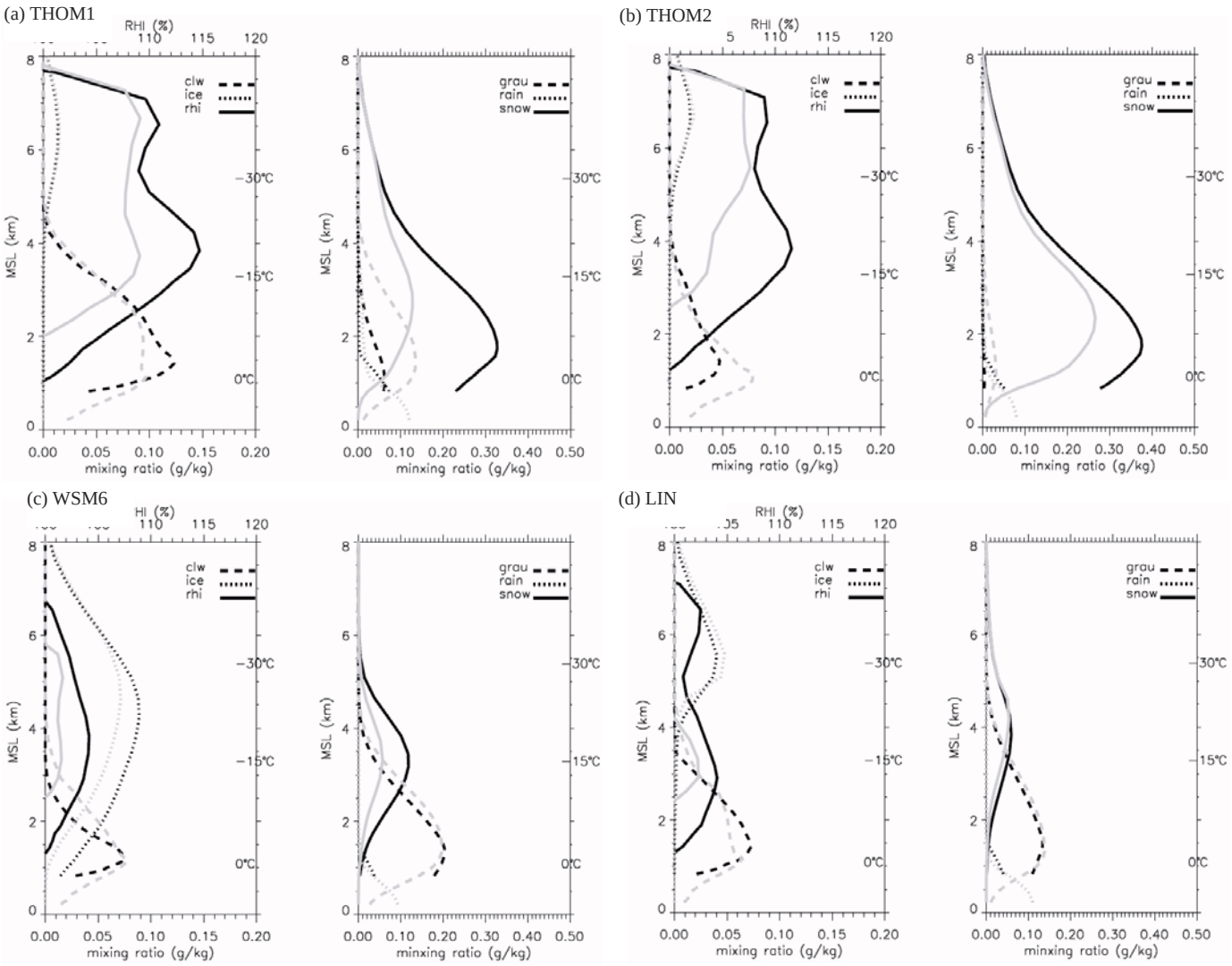

Figure 3.9 3-h mean vertical profiles of hydrometeor mixing ratios (cloud water and ice in the left panel and snow, rain, and graupel in the right panel) averaged over the coastal range (gray, box A on Fig. 3.5a) and the Cascades (black, box B on Fig. 3.5a) from 2300 UTC 4 to 0200 UTC 5 Dec for (a) THOM1, (b) THOM2, (c) WSM6, (d) LIN scheme. Solid lines in left panel also show the model relative humidity with respect to ice (RHI).

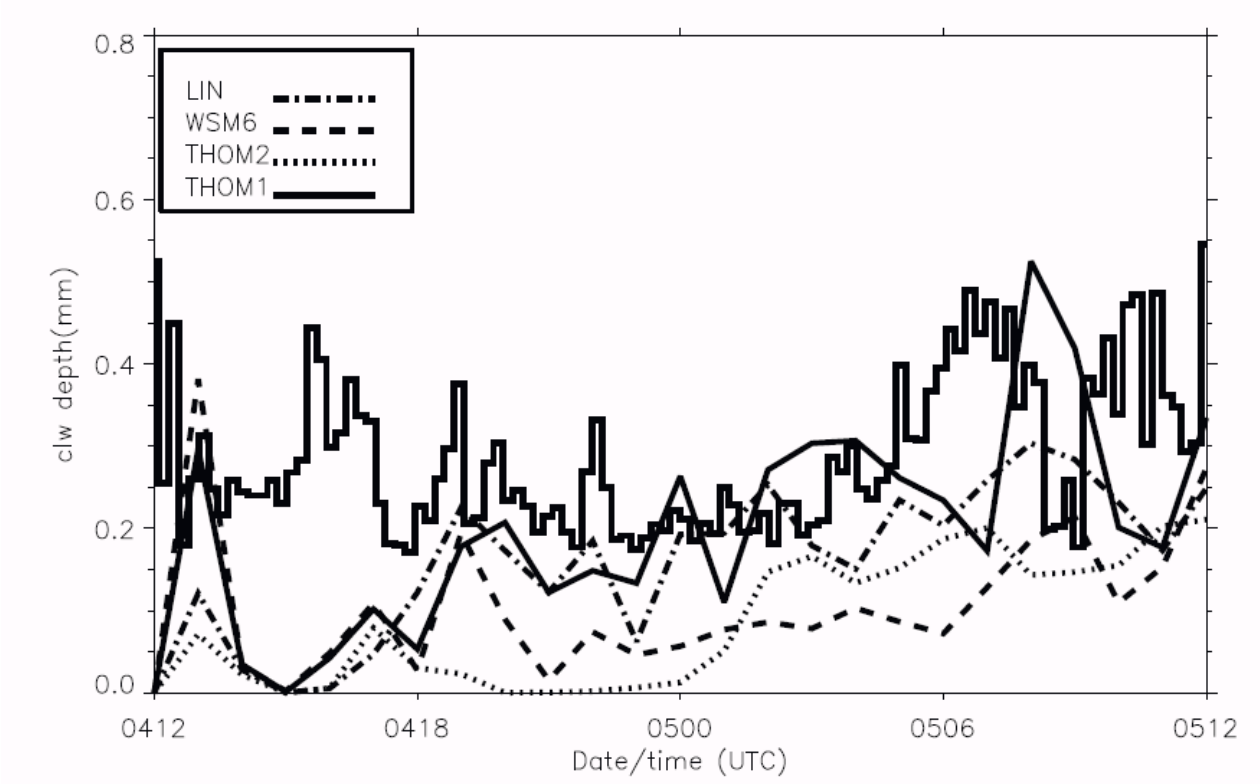

Figure 3.10 Vertically-integrated liquid water depth (LWD) measured by the microwave radiometer at Santium Junction (SJ in Fig. 3.1b) and from the four 1.33-km microphysical simulations from 1200 UTC 4 Dec 2001 through 1200 UTC 5 Dec 2001.

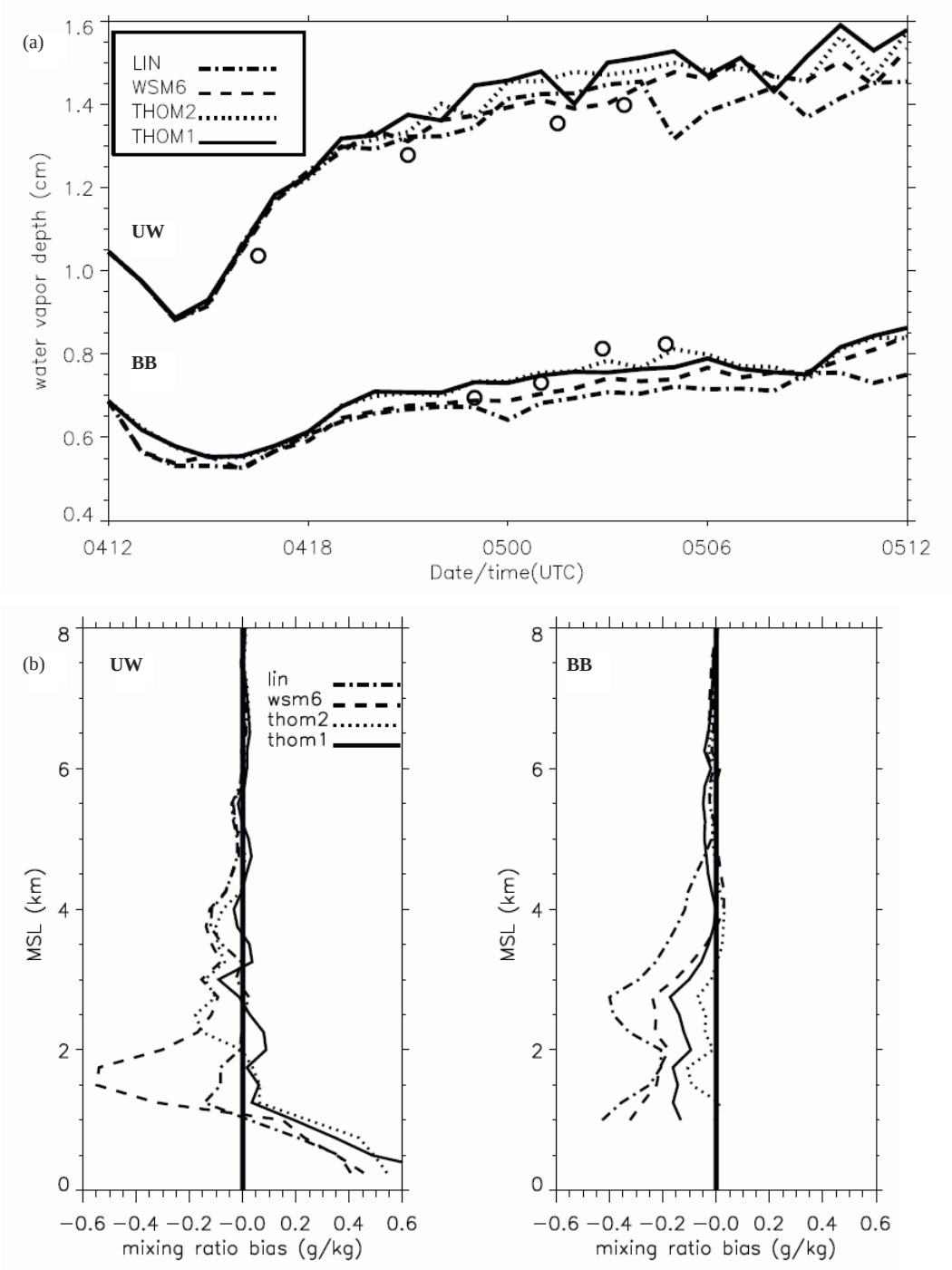

Figure 3.11 (a) Observed (circles) and simulated hourly (solid and dashed lines) column-integrated water vapor depth at UW and Black Butte Ranch (UW and BB in Fig. 3.1b) from 1200 UTC 4 Dec 2001 through 1200 UTC 5 Dec 2001. (b) Model mixing ratio error at UW (left) and BB (right) at 0300 UTC 5 Dec 2001.

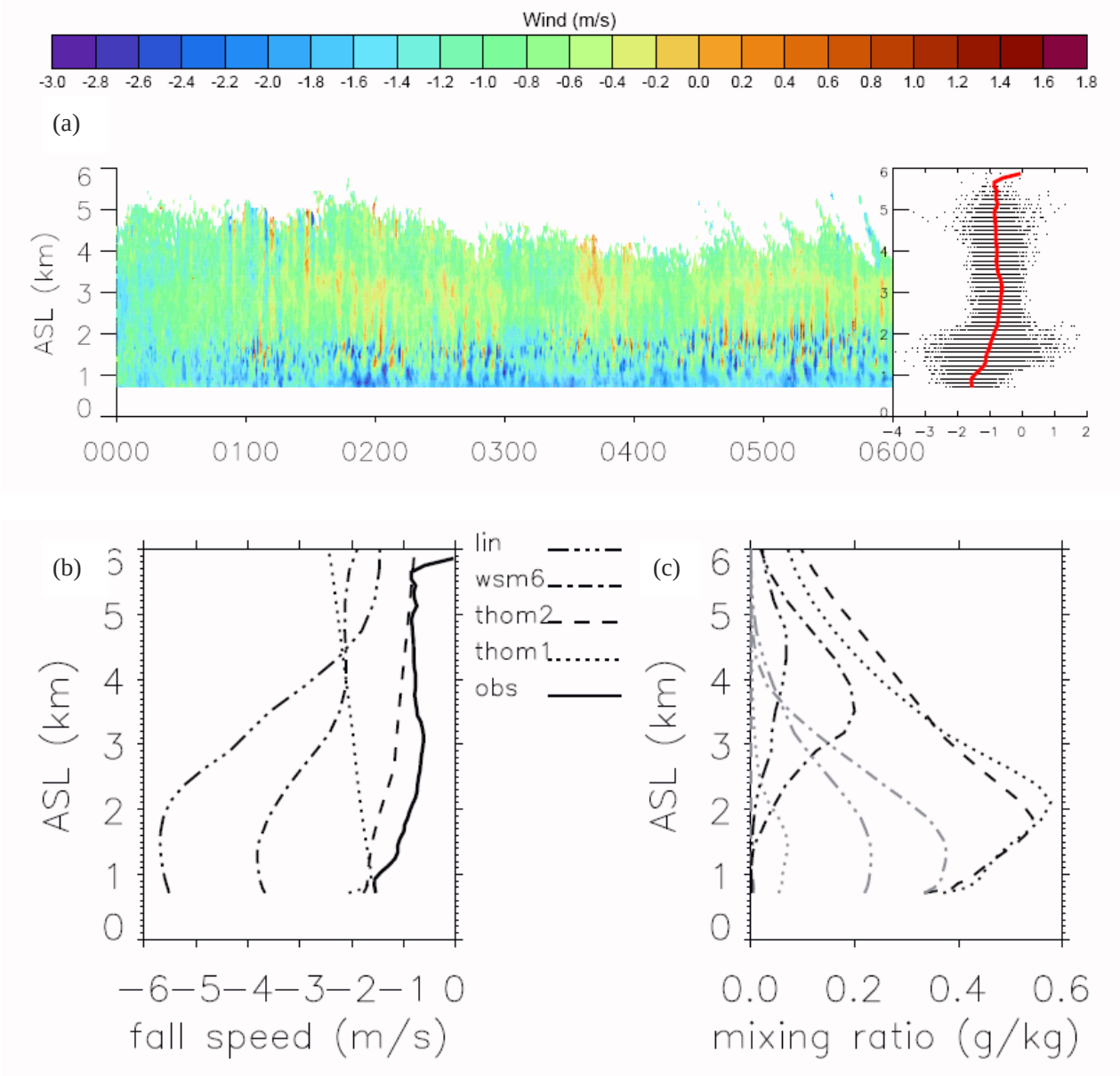

Figure 3.12 (a) Vertical pointing s-band radar (location MB in Fig. 3.1b) measured vertical radial velocity (color shaded every 0.2 m s^{-1}) from 0000 to 0600 UTC 5 December. Right panel shows the scatter plot of radial velocity and the 6-h mean radial velocity during the period (red line). (b) Model 6-h mass-weighted mean snow/graupel fall speed from 0000 UTC to 0600 UTC 5 Dec at the same location for the four microphysical schemes; (c) Model 6-h mean mixing ratio profiles of snow (black) and graupel (gray) at the same location for the four microphysical schemes.

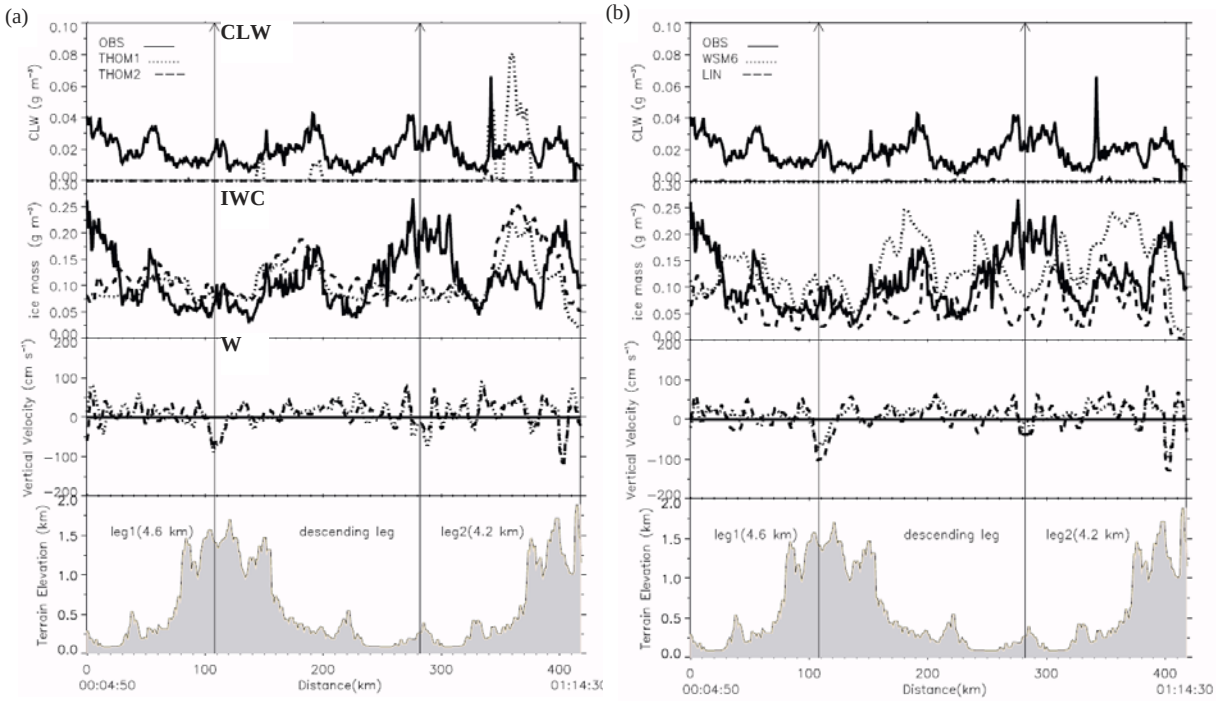

Figure 3.13 (a) Observed (solid lines) and simulated cloud liquid water and ice mass concentrations along the Convair legs for the THOM1 (dotted lines) and THOM2 scheme (dashed lines); (b) the same as (a) except for the WSM6 (dotted lines) and LIN (dashed lines) scheme. The model vertical motion is also shown. The two vertical arrows indicate the three Convair flight legs.

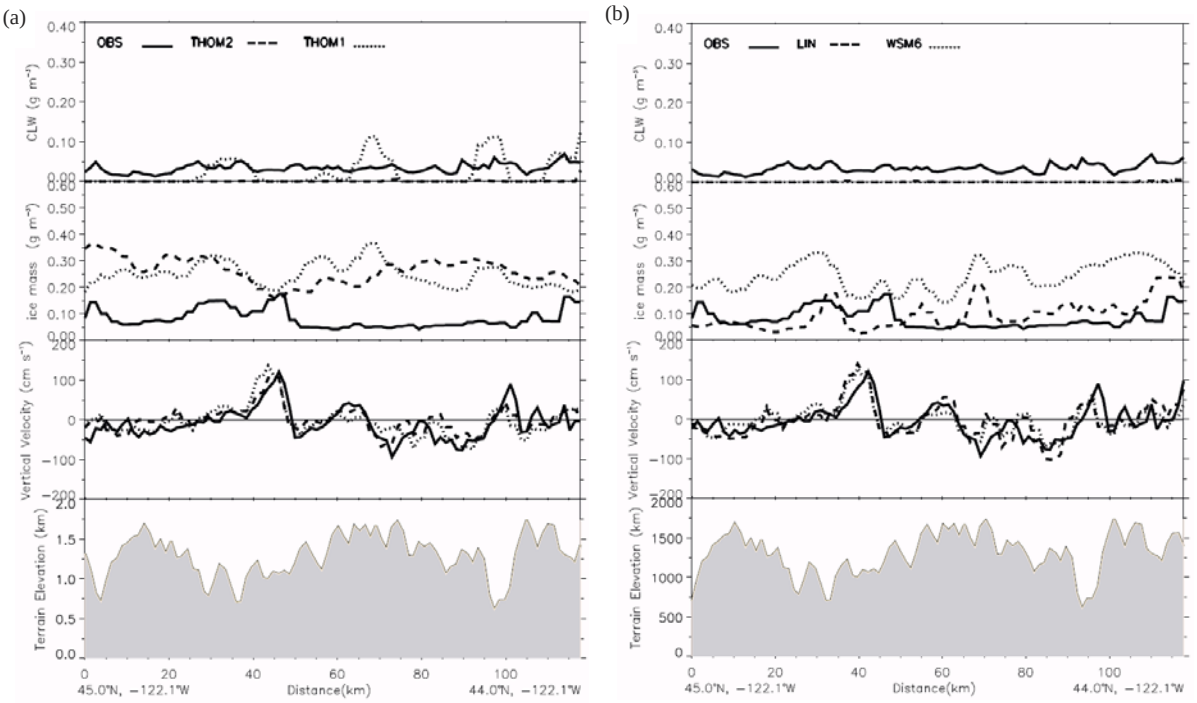

Figure 3.14 (a) Observed (solid lines) and simulated cloud liquid water, ice mass concentrations, and vertical motions along the P-3 leg 3 for the THOM1 (dotted lines) and THOM2 scheme (dashed lines); (b) Same as (a) except for the WSM6 (dotted lines) and LIN (dashed lines) scheme.

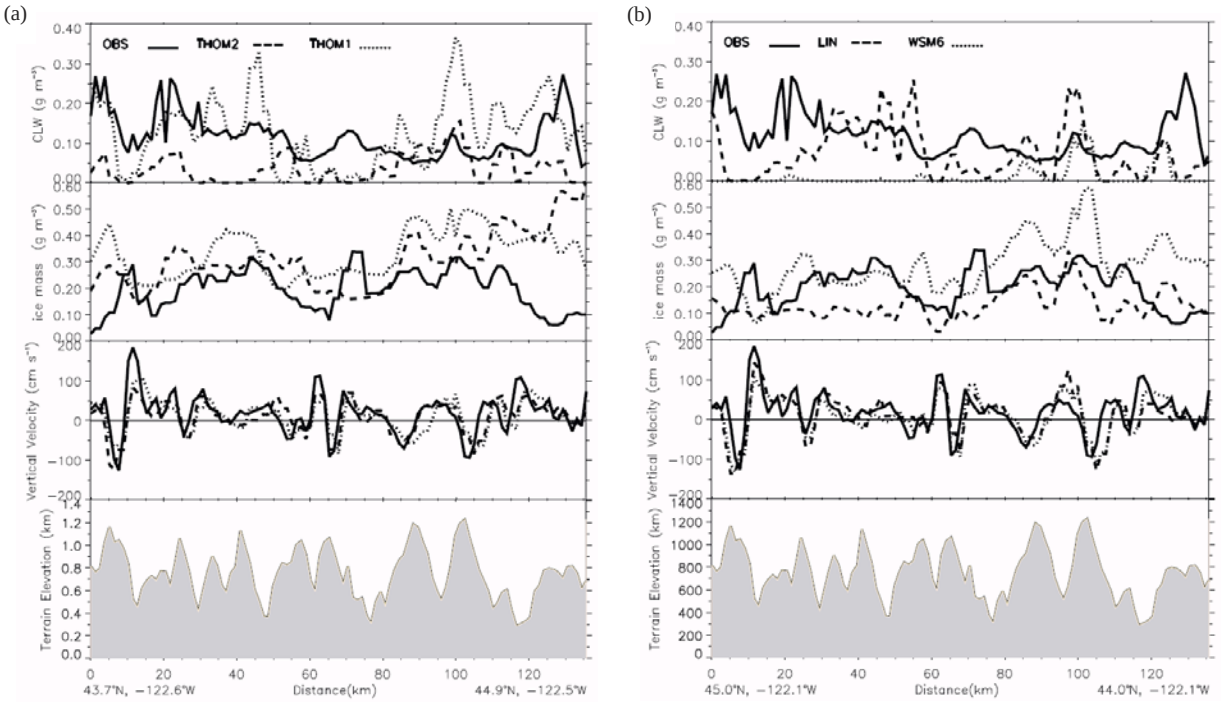

Figure 3.15 (a) Observed (solid lines) and simulated cloud liquid water, ice mass concentrations, and vertical motions along the P-3 leg 2 for the THOM1 (dotted lines) and THOM2 scheme (dashed lines); (b) Same as (a) except for the WSM6 (dotted lines) and LIN (dashed lines) scheme.

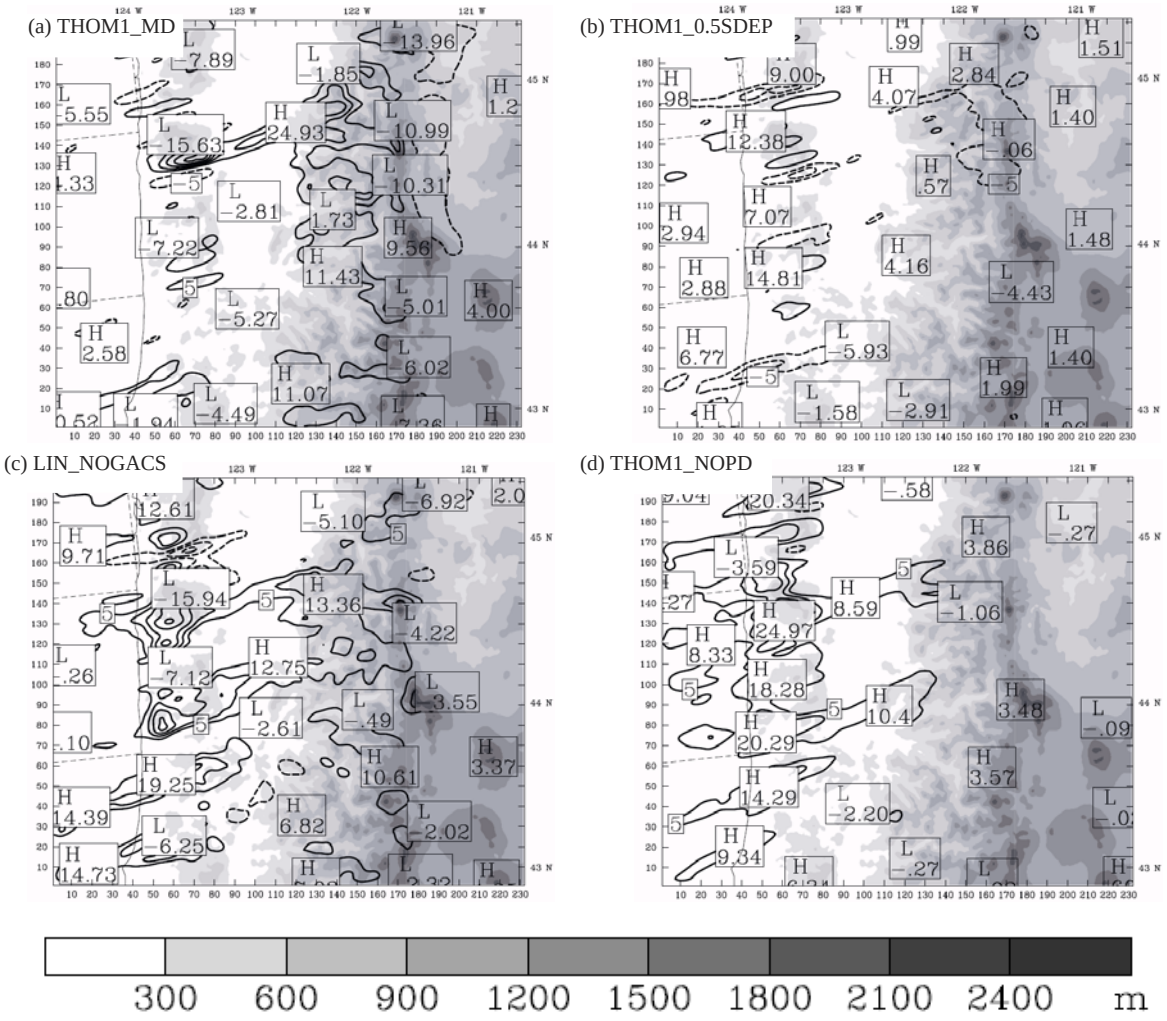

Figure 3.16 Surface precipitation difference (in mm) between the THOM1 (solid lines indicate larger and dashed lines indicate smaller precipitation than THOM1) and (a) THOM1_MD, (b) THOM1_0.5SDEP, (c) LIN_NOGACS, and (d) THOM1_NOPD for the 1.33 km domain between 2000 UTC 4 Dec and 0800 UTC 5 Dec . The 1.33 km terrain is shaded every 300 m for reference.

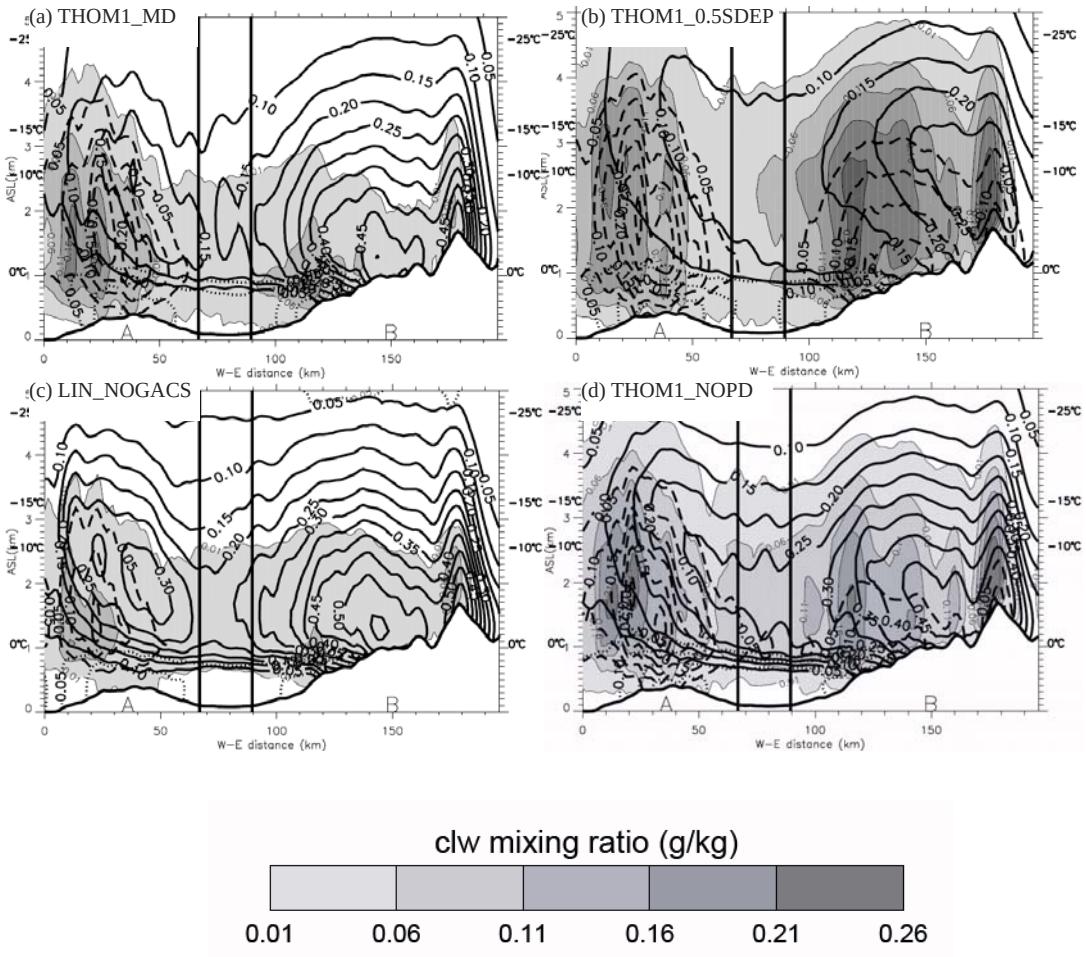

Figure 3.17 Meridionally averaged west-east cross section over the large box in Fig. 3.5 showing simulated mixing ratio of CLW (shaded every 0.05 g kg^{-1}), snow (black solid, 0.05 g kg^{-1}), graupel (black dashed, 0.05 g kg^{-1}), rain (black dotted, 0.05 g kg^{-1}), and ice (black dotted, 0.05 g kg^{-1}) for the (a) THOM1_MD, (b) THOM1_0.5SDEP, (c) LIN_NOGACS, and (d) THOM1_NOPD runs. Model fields were averaged from 2300 to 0200 UTC 4-5 Dec 2001 (forecast hours 11-14) using model outputs at 15-min intervals. The two vertical lines indicate the box A and box B in Fig. 3.5.

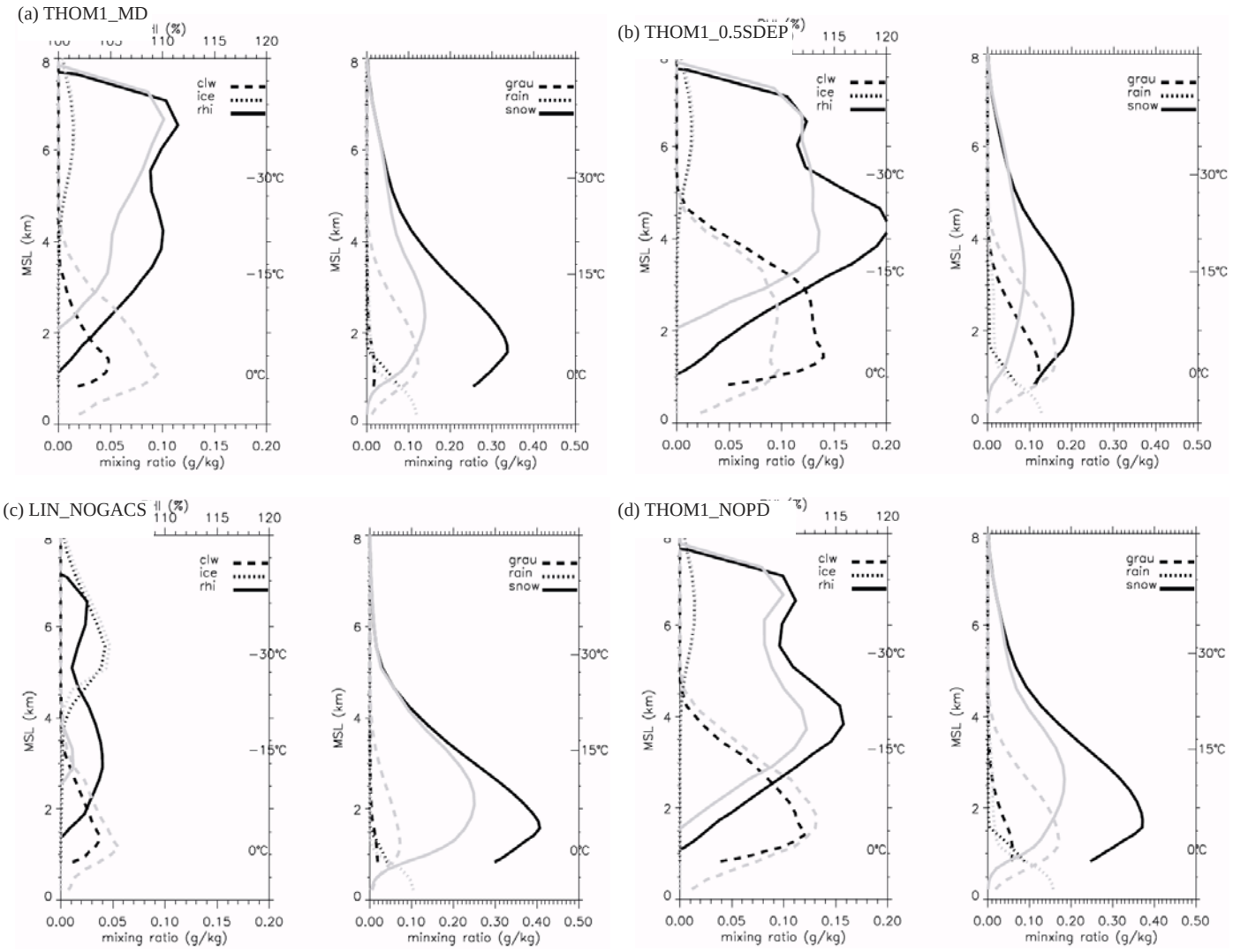

Figure 3.18 3-h mean vertical profiles of hydrometeor mixing ratios (cloud water and ice in the left panel and snow, rain, and graupel in the right panel) averaged over the coastal range (gray, box A on Fig. 3.5a) and the Cascades (black, box B on Fig. 3.5a) from 2300 UTC 4 to 0200 UTC 5 Dec for (a) THOM1_MD, (b) THOM1_0.5SDEP, (c) LIN_NOGACS and (d) THOM1_NOPD runs. Solid lines in left panel also show the model relative humidity with respect to ice (RHI).

Chapter 4

Model Precipitation and Microphysical Evaluation for two cool seasons over the Pacific Northwest

4.1 Introduction

Two IMPROVE case studies (Garvert et al. 2005a,b; Chapter 3) have highlighted snow overprediction aloft and surface precipitation overprediction in the immediate lee of the Cascades in several of the BMPS in the MM5 and WRF models. These results suggest that there are microphysical deficiencies within the models; however, it needs to be determined whether these results are applicable to many cases. For example, Colle et al. (2005) highlighted snow underprediction aloft over the Wasatch Mountains of Utah, which is inconistent with the IMPROVE results. The goal of this chapter is to extend these IMPROVE case studies by conducting and evaluating high-resolution model simulations over two cool-seasons (2005-2007).

Evaluating four cool seasons (2004-2007) of high-resolution precipitation observations and MM5 output at 4-km grid spacing over the western Olympic Mountains, Minder et al. (2008) found that the MM5 performed well in simulating the small-scale precipitation pattern over the ridges and valleys when averaged over a season, but there were major errors for individual storms. They argued that some of these errors may not be related to deficiencies in model resolution or microphysics alone, since errors from synoptic scale, mesoscale, boundary layer processes, land surface processes, and cloud microphysics also contribute to quantitative precipitation forecast (QPF) errors. However, they did not quantify the QPF errors to any of these factors. Using MM5 for a controlled hindcast, Roebber et al. (2008) showed that the synoptic-scale errors can propagate to the mesoscale and impacted the model precipitation skill along the U.S. West Coast.

Most of the winter precipitation in the west coast is usually associated with land-falling baroclinic systems (Neiman et al. 2004; Ralph et al. 2004). Under large-scale forcing, a narrow low level jet (LLJ) transports large amount of moist air impinging on the coastal mountains and inland Cascades. This narrow belt of moisture flux has been referred to as the "atmospheric river" by Ralph et al. (2004). Smith et al. (2003) also found a high correspondence between the net moisture flux and precipitation for a MAP event using different numerical models and a bulk water budget. The strong correlation between upstream water vapor transport and orographic precipitation has been documented using observations collected during the CALJET and PACJET field programs along the California coast (Neiman et al. 2002). There are also small scale

processes associated with orographic precipitation enhancement, such as the convective-scale celluarity (Smith 1979), turbulent overturning in the shear layer (Houze and Medina 2005). Using WSR-88D radar and high resolution mesoscale model simulations, the impact of some of these factors on the orographic precipitation generation and fallout will be investigated.

Model QPF depends on the interplay between many different components of numerical weather prediction models as summarized in Richard et al (2007). They found large sensitivity of model QPF to the model numerics, physics, initial and lateral conditions, and the representation of orography. Some global positioning system (GPS) precipitable water vapor (PWV) data assimilation studies highlighted the large sensitivity of QPF on the model water vapor fields (Falvey and Beavan 2002; Marcus et al. 2007). There have been many studies evaluating mesoscale model QPF during winter storms (Colle and Mass 2000; Grubisic et al. 2005 among others), but not many of these studies have related the model precipitation errors with upstream moisture and wind errors. Colle et al. (1999) separated the precipitation errors on wind directions and found the model tended to overforecast precipitation shadowing in the lee of major orographic barriers when there was significant cross-barrier flow. Overall, the sensitivity of QPF performance on ambient conditions has not been fully evaluated. In addition, there have been no long-term comparisons of radar observations with model simulations for these orographic precipitation events.

The study aims to address the following:

1. How well does a high-resolution mesoscale model predict the precipitation on a daily-average and averaged for the season?

2. How sensitive are the precipitation errors to the upstream wind and moisture errors, the freezing level height, the stability, and flow blocking?

3. Are there microphysical and precipitation errors in the models even when the upstream moisture flux is well predicted?

4. How do the upstream air characteristics affect the observed and simulated orographic precipitation structures?

4.2 Model setup and observational datasets

a) Model setup

The Penn-State/NCAR Mesoscale Model (MM5 Version 3.7) was used with 1.33, 4, and 12 km domains nested within a 36-km domain covering a wide region of the eastern Pacific and Pacific Northwest (Fig. 4.1a). The model was run twice daily initialized at 0000 and 1200 UTC, with initial and lateral boundary conditions derived from the 6-h NCEP Global forecast system (GFS) model analyses. Four dimensional data assimilation (FDDA, analysis nudging; Stauffer and Seaman 1990) was used during the first 12 hours of the 36 and 12-km domains. The MM5 was nested down to the 4 and

1.33-km, with these two domains starting at 0600 and 1800 UTC (hour 6 of the 12-km domain). By nudging the outer domains the strategy was to reduce the large-scale errors as much as possible in order to investigate the performance of the model physics within the inner nests. The last 12 hours of the simulation (6-18 h) for the 4 and 1.33-km domains were used for verification.

The model physics include the ETA PBL (Janjic 1994), Thompson microphysics (Thompson et al. 2004 for the 2005-06 season and the Thompson et al. 2008 for 2006-07 season, respectively). The main differences between these two versions of BMPs are detailed in Chapter 3. The modified Kain Fritsch cumulus scheme (Kain and Fritsch 1993; Kain 2004) was used in the 36 and 12-km domains. Other physics include the Dudhia (1989) short and long wave radiative transfer, the MM5 simple slab land surface model. Initial conditions for snow cover were provided by the Rapid Update Cycle (RUC) analysis (with 20 km horizontal spacing), while SST and soil temperature and moisture were from GFS analyses.

b. Observational datasets

Figures 4.1a, b show the model domains, the precipitation gauge locations, the RTX WSR-88D radar, and the Salem, OR (SLE) sounding site.

1) Rain gauge

Daily rainfall data from the National Weather Service (NWS) Cooperative stations (COOP) and the National Resources Conservation Services (NRCS) snowpack telemetry (SNOTEL) sites were synthesized to evaluate the model surface precipitation performance. The twice-daily precipitation forecasts from the 4 and 1.33-km MM5 domains (12-00 UTC plus the 00-12 UTC amounts) were interpolated to the gauge locations using an inverse distance Cressman (1959) approach (as in Colle et al. 1999) and summed to get the simulated 24-h precipitation. A heavy precipitation event is defined as a day on which either the average of all rain gauges or model rain gauges precipitation within the 1.33-km domain is over 12.7 mm (0.5 inch) over a 24-h period from 0000UTC to 0000 UTC. This threshold was chosen in part to generate enough cases for a statistical analysis. There are 49 and 53 events for the 2005/06 and 2006/07 season, respectively.

A model bias score (B) is defined:

$$B = \frac{F}{O}, \tag{4.1}$$

where F is forecast precipitation and O is the observed precipitation. There are two types of bias scores when considering more than one station or one time. The first one, called precipitation-weighted bias score, is defined as in Colle et al. (1999):

$$B_p = \frac{1}{N}\frac{\sum F_i}{\sum O_i} \tag{4.2}$$

where i is either for the days or stations. B_p is more dominated by larger precipitation days or stations. The second one, called event-weighted bias score, is defined as:

$$B_e = \frac{1}{N}\sum \frac{F_i}{O_i} \tag{4.3}$$

in this way, the bias score is computed first before being averaged. Sometimes a threshold precipitation amount is used to discriminate only those events exceeding some amount of precipitation. For the following description, both bias scores are used (B_p is used for the seasonal bias score and daily bias, while B_e is used to represent each event equally.)

To determine the over- and under-prediction days over a cool season, the mean daily precipitation at all the rain gauges from the 1.33-km MM5 was compared with the corresponding observed mean daily precipitation at the same sites. There are 60 and 66 sites in the 1.33-km domain for the 2005-06 and 2006-07 season, respectively. These stations were also divided into four regions (upstream valley, windward slope, crest, and lee) according to their geographic locations as shown in Fig. 4.3b in order to investigate the spatial variations of QPF performance.

2) Radiosonde

Radiosonde observations of winds, pressure, temperature, and humidity are made twice daily (0000 and 1200 UTC) at Salem, OR and Quillayute, WA (SLE and UIL respectively in Fig. 4.1b). Observations on standard and significant levels were obtained from University of Wyoming (http://weather.uwyo.edu). Both model and observed meteorological variables were linearly interpolated to a vertical grid spacing of 200-m between 100 and 7900 m above MEAN SEA LEVEL. To relate the 12 hourly sounding to the daily precipitation between 00 UTC and 00 UTC, daily profiles of moisture, winds, and temperature were computed following Falvey and Garreaud (2007):

$$V = (V_{-12h} + 2V_0 + V_{12h})/4 \tag{4.4}$$

where V_{-12h} and V_{12h} are moisture, winds, and temperature observations 12 h before and 12 h after the radiosonde observations at 1200 UTC (V_0).

Inspection of the radiosonde data at SLE revealed that the balloon relative humidity (RH) measurements might be systematically too low compared to other sounding sites in the region during periods of saturation. Quantification of moisture errors at SLE was estimated by comparing the corresponding SLE sounding with ~20 mobile soundings launched ~60 km away at UW (see Fig. 2.1b) during the IMPROVE-2 project (Stoelinga et al. 2003). This indicated that the SLE sounding is about 2% drier than the UW sounding when averaged in the vertical (not shown). Thus, we applied a fixed 2% correction to the mixing ratio and precipitable water vapor (PWV) of the SLE and UIL soundings. The 4-km MM5 forecasts at forecast hour 6 (f06) were interpolated to the SLE and UIL sites to get the model sounding at 12-h interval as observed. The same average method for the observations was used to get the daily mean model sounding. Using these data, the simulated and observed column-integrated moisture flux, column-integrated relative humidity (RH) weighted moisture flux, potential instability are computed as follows:

$$qv\_flux = \sum dzV\rho_v \tag{4.5}$$

$$RH\_qv\_flux = \sum dzVRH\rho_v \tag{4.6}$$

$$N_m = \left(\frac{g(\theta_{e1} - \theta_{e0})}{\theta_{e0}\Delta z}\right)^{0.5} \tag{4.7}$$

in which *dz* is the height between the data levels (200m), *V* is wind speed, and ρ_v is water vapor density. In a recent paper, Reinecke and Durran (2008) discussed the computation of Froude number when the flow has nonuniform static stability. They found that the variation in static stability above the mountain crest has little impact on flow blocking. Thus, for potential instability (N_m) calculation, we use the bulk stability from the surface to mountain crest height (100 to 1900 m).

3) WSR-88D radar

The National Weather Service (NWS) Weather Surveillance Radar-1988 Doppler (WSR-88D) radar at Portland (RTX in Fig. 4.1b) provides the 3-D precipitation structure and wind pattern data within ~150 km range of the radar. The Level II data has been processed following James and Houze (2005) at ~ 6 minutes time intervals. A radar grid with 2 km horizontal resolution and 0.5 km vertical resolution was used for the comparison with MM5 model outputs. For the direct comparison, the 4-km and 1.33-km outputs at 15 minute interval are interpolated horizontally and vertically to the corresponding radar grid points.

4.3 Evaluation of model precipitation climatology

The 4-km MM5 seasonal total precipitation as compared with observational precipitation is shown in Fig. 4.2. The precipitation distribution is similar between the 2005-06 and 2006-07 cool seasons, with one maximum along the coastal range and another over the WA/OR Cascades. The precipitation enhancement extends ~30 km offshore of the Coastal Range, which indicates an upstream effect on precipitation by the coastal mountains. There is less precipitation in the Willamette Valley and a clear rain shadow in the lee of the Cascades. There is more precipitation toward north during the 2006/07 season. Overall, MM5 realistically predicts the general precipitation distribution in this region, which is consistent with the results in Minder et al. (2008).

The precipitation difference between the 2006/07 and the 2005/06 seasons (Fig. 4.3) show some positive precipitation differences over the valleys and the lee of volcanic peaks, which indicates more precipitation spillover given the more snow favorable characteristics of the new Thompson scheme (see Chapter 3).

At 1.33-km grid spacing (Fig. 4.4), there are more fine structures in the precipitation field, with small-scale gaps, valleys, and slopes better resolved. The precipitation maxima are situated over the narrow ridges, the volcanic peaks, while precipitation minima are located in the valleys and the lee of high volcanic peaks. There are also two wide spread precipitation minima in the low land of the Columbia River and the lee of the Cascades.

Fig. 4.5 shows the 4-km MM5 seasonal precipitation bias score (B_p) for the two seasons. 4-km MM5 underpredicts the seasonal precipitation over the coastal range by 30-40% in general. Bias score is within 90-120% over the Willamette Valley and windward slopes of the Cascades. MM5 precipitation is up to 2 times of observed over most of the stations in the lee of Cascades, especially for the 2006/07 season. The persistent underprediction over the coastal range is intriguing. An additional 21 more simulations were conducted with a 276 km larger 4-km domain to the west and south (white dashed box in Fig. 4.1a) in order to check whether the domain size impacted the precipitation. It was found that simulations with a larger 4-km domain increased the precipitation over the coastal range by ~ 20% (Fig. 4.6). The larger domain allows more time for the flow and precipitation to spin-up before interacting with the coastal range. As a result of this issue, this thesis will not identify any underprediction over the coastal range until the B_p values are less than 80%.

Previous studies (Garvert et al. 2005b, Colle et al. 2008) have suggested that 1.33-km grid spacing can resolve the vertical motion over the complex terrain better than at 4-km grid spacing; thus, the precipitation verification will focus more on the 1.33-km domain. The 1.33-km MM5 simulates the seasonal precipitation patterns reasonably well for both seasons (Fig. 4.8). There is overprediction just upstream of the WA Cascades over the Columbia River. While over the windward slopes and crest of the Cascades, the model precipitation is generally within 20-30% of the observed. The model overpredicts the precipitation over the lee of Cascades with bias score generally > 130%. Seasonal bias score indicates small differences between the two seasons (Fig. 4.5, Fig. 4.7); therefore, the two seasons were combined for some of the analysis later.

4.4 Dependence on ambient conditions

To investigate the sensitivity of precipitation over the Cascades to the upstream atmospheric conditions, composites were constructed by dividing the model data into subsets defined by some specific ambient conditions at SLE, such as the freezing level, wind speed, wind direction, and stability. Several precipitation thresholds were tested and it was found that a 24-h threshold of 0.5 inch provides enough sample days and minimizes the uncertainty in rain gauge recording light precipitation. For each composite, the mean B_p in the four geographic regions within the 1.33-km domain was computed and shown in Table 1. Generally, MM5 tends to overpredict in the valley and the lee of Cascades, while the precipitation is generally well-predicted over windward slopes and crest of the Cascades. There are variations of B_p with upstream conditions. For example, unstable days have generally ~25% higher B_p than stable days over upstream valley. Post-frontal days (more westerlies) have ~20% larger B_p than pre-frontal days (southwesterlies). The largest B_p changes are with respect to temperature, with low temperatures associated with larger overprediction, especially in the upstream valley and the lee. Thus, we will only focus on the freezing level for the composite analysis below.

Fig. 4.8 shows the variation of domain mean B_p with ambient temperatures and the precipitation magnitude. The composite (65 days) only includes the days with good moisture flux forecast after screening the bad forecasts with obvious synoptic errors (obvious timing error of trough or front passage compared with GFS analyses). The

model B_p tends to decrease with increasing temperatures and precipitation amounts. This indicates the model tend to overpredict light precipitation and underpredict or well-predict heavy precipitation. This is consistent with previous study results (Colle and Mass 2000; Colle et al. 1999, 2000).

Precipitation growth is affected by the environmental temperatures. Due to the fall velocity difference between rain droplets and ice particles, temperature impacts the precipitation fallout and distribution. Sinclair et al. (1997) noticed enhanced spillover of orographic precipitation onto lee slopes associated with low freezing level and strong cross-barrier flow. Zangl (2007) observed enhancement in the lee of narrow mountains in the Alps during storms with low freezing levels and attributed it to the combination of downwind advection and mountain wave descent of frozen hydrometeors. A reduced ridge-valley precipitation difference with decreasing temperature was found in both rain gauges and MM5 simulations over the Olympic Mountain (Minder et al. 2008). All these suggest the freezing level can change the precipitation fallout and thus the precipitation spatial distribution significantly. However, the change might be different for observations and model simulations. For example, previous studies (Garvert et al. 2005a; Colle et al. 2008) found model tends to overpredict the spillover into the immediate lee associated with overpredicted snow aloft.

Figure 4.9 shows the model daily mean precipitation and the B_e for the high and low freezing level composites (T_h and T_l). Precipitation is 2-3 times larger for T_h than T_l given the greater moisture flux at warmer temperatures. The large precipitation gradient along the coast indicates the large-scale synoptic (baroclinic wave) forcing is stronger for T_h, while T_l likely represents more post-frontal conditions. There is widespread overprediction from the Willamette Valley to the windward slopes and crest of the Cascades with B_e up to 170-250% for low freezing composite. In contrast, B_e is within 90%-150% over the Willamette Valley for T_h and there is no obvious overprediction except at some scattered locations. This confirms the model's tendency to overpredict when the temperature is cold and ice processes are dominant. B_p plots show similar contrast between the high and low freezing composites (not shown).

To better describe the spatial variation of B_e, Fig. 4.10 shows the B_e values across western WA/OR as a function of the longitude for the high and low freezing level composites, respectively. High freezing composite slightly underpredicts the precipitation over the coastal range with good prediction over the Willamette Valley and the Cascades. While there is overprediction over the further east of the Cascades. In contrast, a composite of the low freezing levels clearly overpredicts precipitation over the Willamette Valley and the immediate lee of the Cascades. This indicates model probably overestimate the spillover when the freezing level is low.

To relate the surface precipitation with the microphysics aloft, composites of Portland radar and model equivalent reflectivity are constructed for high and low freezing level composite, respectively (Fig. 4.11). Consistent with the surface gauge results, the 4-km MM5 predicts larger reflectivities and IWC above the freezing level for low freezing level composite than high freezing level composite. In contrast, radar observed comparable reflectivities above the freezing level (at the same temperature zone) though precipitation is much deeper for the high freezing level composite.

Other composite analyses have been also conducted based on the stability, wind direction, wind speed. No obvious patterns could be determined and thus the results are not presented.

4.5 Upstream moisture flux and model QPF

The physical connection between upslope flow and orographic rainfall has been highlighted in Smith (1979). Recently, Neiman et al. (2002) found very high (r^2=0.7) correlation between the magnitude of the upslope flow and the magnitude of the rain rate over the coastal mountains of the northern California during the California Landfalling Jets Experiment (CALJET) of the winter of 1997/98. They also found the layer of upslope flow that best correlates with orographic rainfall is near mountaintop. Similarly, Falvey and Garreaud (2007) found strong correlation between downstream precipitation and the upstream wind and moisture flux over a ten-year period in central Chile. They further emphasized that the positive correlation between rainfall and moisture flux is largely determined by the variability in the wind velocity.

The daily mean sounding from the 4-km MM5 and the SLE observations were averaged using a 0.5 inch threshold for those days with southwesterly (180-270 degree) flow in the lowest 1.5 km MSL. The MM5 overpredicts the winds by ~1 m s^{-1} near 0.7 km MSL, while it underpredicts the flow by 3-4 m s^{-1} above 1.5 km MSL. This overestimated wind in the boundary layer has been noted by Garvert et al. (2007) in the simulation of the IMPROVE-2 13-14 December 2001 case. The MM5 wind direction is generally 10 degrees more subgeostrophic than observed above 1.5 km MSL (Fig. 4.12). Due to the overestimated moisture below 1 km MSL and the overpredicted winds at low levels, MM5 has a mean moisture flux error of ~20 g s^{-1} m^{-2} around 0.8 km MSL (Fig. 4.12). The relative error of the column integrated moisture flux and moisture are 8.5% and 7.8%, respectively. In contrast, the relative error of the column integrated moisture flux and moisture at UIL are 5.6% and 4.7%, respectively (not shown). This persistent MM5 moisture error is not as large as at the model initialization time (~2%), which suggests that the moisture error is either advected from the Pacific or develops during the model integration. Using a smaller precipitation threshold, such as 0.1 inch, does not change the results significantly. In addition, comparison of PWV between the 21 large 4-km domain simulations and the control simulations show negligible reduction of moisture bias (< 0.4%).

The moisture flux is determined by the wind and moisture distribution, both of these are fundamental elements in evaluating model performance. Figure 4.13 shows the connection between the moisture flux at SLE and precipitation in the 1.33-km domain for model and observed. Not surprisingly, the correlation between RH weighted moisture flux and precipitation over the Cascades is high for both model and observations (squared correlation coefficient r^2 is 0.85 and 0.90 for model and observations, respectively). Model precipitation is generally larger than observed precipitations when the moisture fluxes are small.

To better quantify the connection between moisture flux and downstream precipitation, the simulated moisture and moisture flux errors were computed for overprediction (domain mean B_p > 120%) and underprediction (domain mean B_p <90%)

days, respectively. Moisture and moisture flux error between 1 and 4 km MSL for the overprediction days are generally ~ 0.5 g m^{-3} and ~10 g $s^{-1}m^{-2}$ larger than the underprediction days, respectively (Fig. 4.14). There is a moisture deficit between 1.5 and 4 km MSL for underprediction days, while model overpredicts moisture over the whole column for the overprediction days. It also indicates the model moisture flux error is mainly in the lower layer (below 1.5 km MSL).

To show an example of the moisture flux error relationship with model bias score, Figure 4.15 shows the B_e of days with large positive and negative moisture flux error (greater than one standard deviation of model moisture flux error), respectively. B_e of 200%-300% spreads over most of the domain for the positive moisture flux days (Fig. 4.15a). In contrast, B_e varies from 50% to 120% for most stations for negative moisture flux days (Fig. 4.15b).

Model QPF performance versus other environmental parameters, such as wind speed, wind direction, and precipitation rate were also analyzed. While there are variations in the precipitation pattern, there is no obvious systematical relation to these other parameters (not shown). Overall, the MM5 moisture flux errors seem to explain a large fraction of forecast precipitation errors. However, the model does overpredict precipitation at times when the moisture flux is well forecasted, especially when the freezing level is low (< 1.5 km MSL) as shown in previous section. For example, there are several overprediction days when the freezing level is lower than 1.5 km above MSL and negative moisture flux error (Fig. 4.16). The synoptic maps were compared with the MM5 for these 10 days and there were no obvious feature errors, and the model wind and temperature errors were relatively small. This indicates there are still likely systematic errors in ice microphysics within model BMPs as highlighted in Chapter 3 to increase precipitation errors at times.

A similar analysis is conducted using only the lower layer (925 to 850 mb) mean values for the moisture and moisture flux. Since the model winds are slight larger than observed at low levels, this method gives even larger model moisture flux error. But the results are similar to that using the previous method. Again, most of the overpredictions are related with the overpredicted moisture flux.

4.6 Case examples

Despite the good agreement between the modeled and observed seasonal precipitation, there is large variability of QPF performance for individual storms. For example, the 13-14 December IMPROVE event had precipitation overprediction (Garvert et al. 2005a), but no moisture flux was analyzed. Our analysis suggests that moisture flux error has an obvious impact on the model QPF. Moisture flux for IOP6 case is well simulated, which might explain the better precipitation verification for IOP6 as compared with the overprediction of the 13-14 case. Some representative cases were investigated to relate the precipitation errors with the moisture flux error, the freezing level height effect, and warm rain dominant storms.

a. 19-22 December 2005 case

During the four days of the storm, a series of low pressure systems developed and moved northward ~300 miles west of the WA/OR coast, bringing warm and moist air from the south towards the west coast region (Fig. 4.17). SSM/I images near 1800 UTC 21 December 2005 shows an "atmospheric river" transport large moisture (~32 mm PWV) toward south OR. Model depicts a moisture tongue with >50 kt winds further north to the WA/OR border at the same time. Satellite images show consecutive precipitation bands over the study region accompanying the active cyclone development (not shown).

Rain gauge data show 3-4 cm daily precipitation over the coastal range, with less than 2 cm precipitation over the Willamette Valley, and 2-3 cm precipitation over the WA/OR Cascades (Fig. 4.18a). In contrast, model precipitation is 4-5 cm over the windward slopes of WA/OR Cascades with a clear rain shadow in the lee (Fig. 4.18b). As a result, model overpredicts the precipitation by up to 2-3 times for most of the stations over the Cascades (Fig. 4.18c).

Time height plot at SLE indicates model overestimates the low level moisture and winds with a strong low level jet with winds up to 20 m s^{-1} compared with 10-15 m s^{-1} observed winds (Fig. 4.19). The overpredicted winds (~ 4 m s^{-1}) and moisture (~ 1 g m^{-3}) below 2 km MSL induce large moisture flux error (~ 50 g m^{-2} s^{-1}) below 2 km MSL (Fig. 4.20). This large overestimated moisture flux contributes to the overpredicted precipitation over the Cascades (Fig. 4.18c).

b. 02-08 November 2006 case

This is the heaviest flooding case of the 2006/07 season with daily mean precipitation over 8 cm for all the stations in the 1.33-km domain. This case basically shows that the model well predicts heavy precipitation with high freezing level when moisture and moisture flux are well simulated.

Model captures the moisture quite well with slightly stronger winds near ~ 1 km MSL. Model also depicts the dry air intrusion accompanying middle level trough passage at 1200 UTC 04 and 05 Nov 2006,respectively (Fig. 4.21). Though the model still overpredicts the low level winds by ~ 2 m s^{-1}, it predicts the moisture well from surface to the upper troposphere (Fig. 4.22). Corresponding to the well predicted synoptic features and moisture, the model predicts the precipitation well with bias score within 80-120% over most of the rain gauge sites (Fig. 4.23a). There are some underprediction with bias score < 70% in the valleys downwind of high mountain ranges.

c. 22-24 November 2006 case

This is a relatively cold case, which generates over 2 cm daily mean precipitation with freezing level near 1 km MSL. In contrast to 02-08 Nov case, there is clear precipitation spillover into the adjacent valleys (boxed region in Fig. 4.23b). Widespread overpredcition with B_e > 200% are over the higher ridges and mountains of the Cascades and the lee of Cascades. In contrast, B_e close to 100% is found in the upstream valley and windward slopes of the Cascades.

4.7 Summary

Two cool seasons high-resolution MM5 simulations (down to 1.33-km grid spacing) over the Pacific Northwest were evaluated. MM5 seasonal precipitation percentage of observed is generally within 90-130% over most of the rain gauge sites in the 1.33-km domain. While the model shows good skill in simulating the seasonal precipitation distribution and amounts, large errors exist for individual storm events.

Composite analyses suggest the model tend to overpredict the precipitation when the freezing level is low. The model precipitation bias scores generally decrease with the increasing temperatures and precipitation amounts. Comparison of model microphysics aloft with radar reflectivities indicates the model tends to overpredict the ice mass aloft when the freezing level is low. This results in overestimated spillover in the model than observed. In contrast, model underpredicts the ice mass aloft for the high freezing level composite. Other composite analyses do not reveal obvious dependence of model QPF performance on wind speed, wind direction, and stability.

Model winds, moisture, and temperatures are evaluated using the radiosonde data at Salem. The comparison indicates model systematically overpredict the moisture, especially in the lower layer. Model winds are 3-4 m s^{-1} less than observed above 2 km MSL, while there is a ~ 1 m s^{-1} overprediction at ~0.7 km MSL. As a result, model moisture flux is ~ 8% larger than observed. High correlations (r^2 up to 0.85 and 0.90 for MM5 and observations, respectively) between the RH-weighted moisture flux at Salem and the precipitation in the 1.33-km domain have been found for both the model and observations. Overall, model moisture errors seem to explain a large fraction of forecast precipitation errors.

The study suggests that a combination of model moisture flux error and a systematic ice microphysical error contribute to the model QPF errors. Thus improvement of QPF over complex terrain need better model physics and better moisture forecast, which might be sensitive to the model initialization.

Table 4.1 Mean B_p for all stations and the stations in four sub regions under different ambient conditions for the 1.33-km MM5 with daily precipitation > 0.1 inch for the 2006/07 season.

Ambient conditions	All stations	Upstream valley	Windward slope	crest	lee
Mean (98days)	1.22	1.50	1.25	1.15	1.63
T < -1 ^{o}C (37 days)	1.37	1.89	1.30	1.29	1.82
T > 4 ^{o}C (16 days)	1.04	1.09	1.20	0.98	1.26
stable (55 days)	1.22	1.42	1.34	1.14	1.57
unstable (35 days)	1.27	1.67	1.18	1.20	1.68
Wdir [180,270] (77 days)	1.22	1.48	1.24	1.14	1.62
Wdir[240,320](40 days)	1.30	1.67	1.16	1.24	1.72

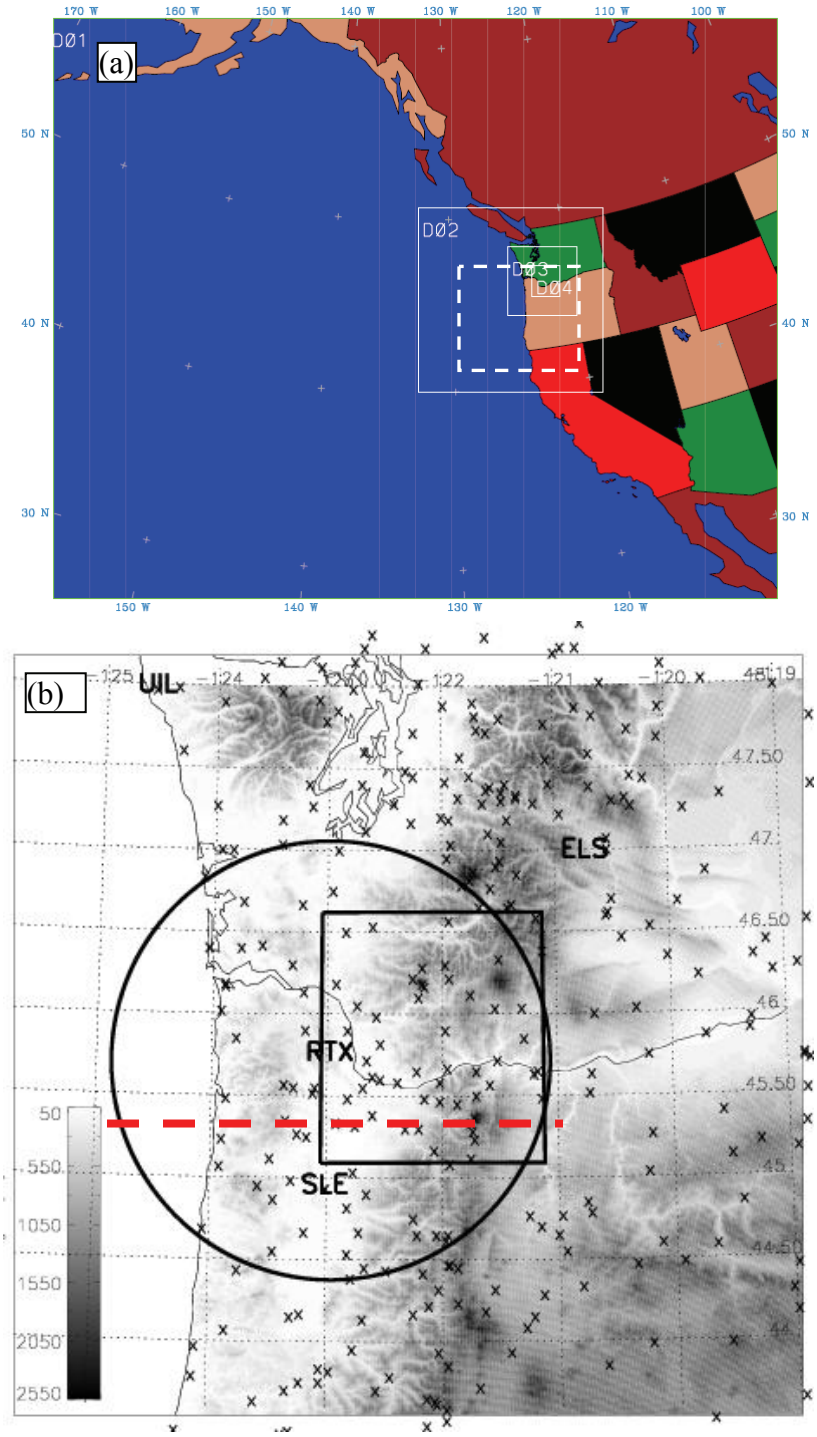

Figure 4.1 (a) MM5 domains. (b) Terrain over the study region with rain gauge sites (X) and other observational facilities (sounding at SLE and UIL, radar at Portland (RTX)). Circle represents the 150 km radar range and the rectangle represents the 1.33 km model domain. The dashed red line is the cross section used for model and radar composite shown in Fig. 4.12.

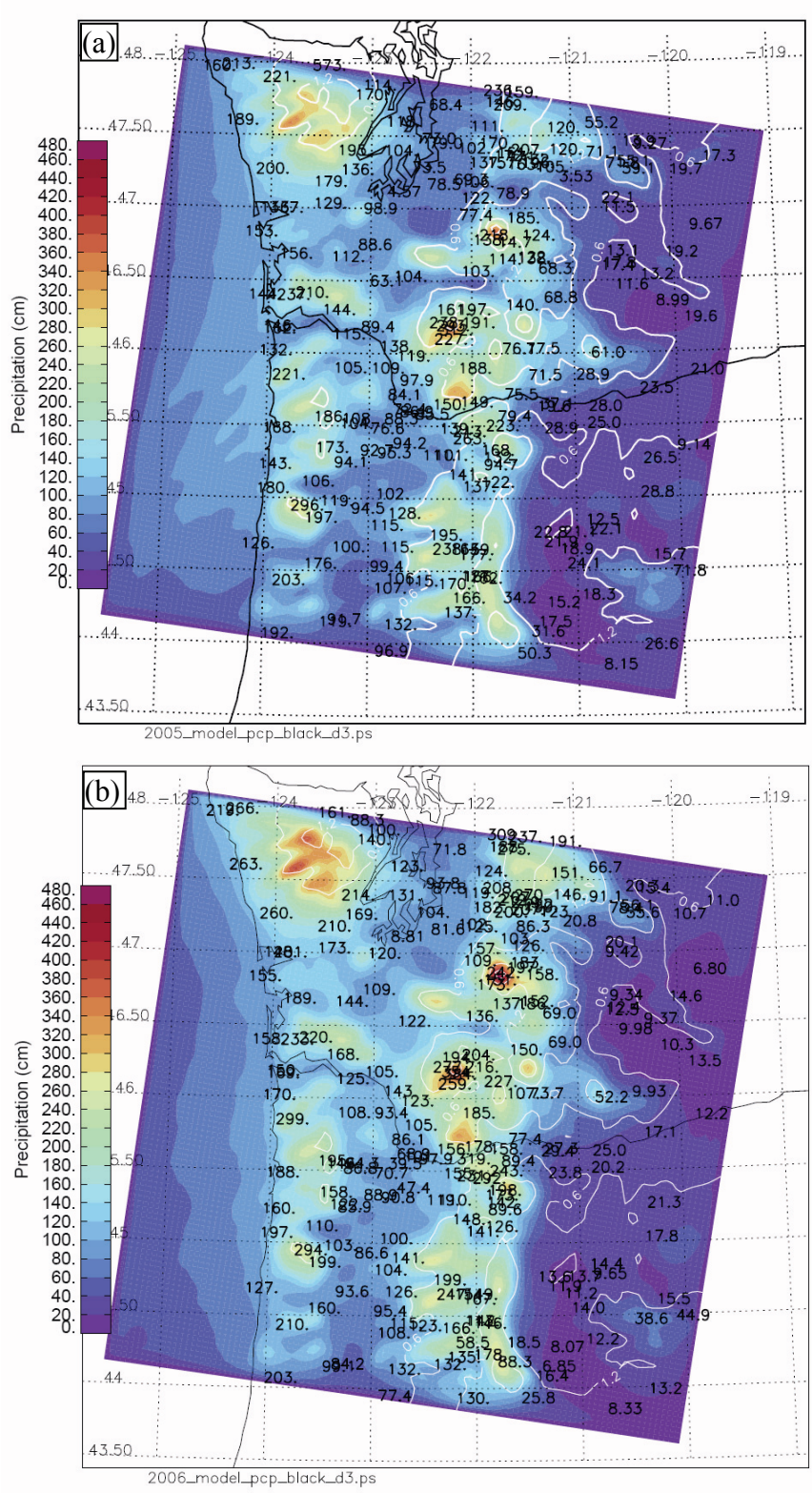

Figure 4.2 4-km MM5 seasonal precipitation (in cm, color shaded) with the observed seasonal precipitation (black numbers) overlaid for (a) the 2005/06 season, and (b) 2006/07 season. The terrain is contoured every 0.6 km in white.

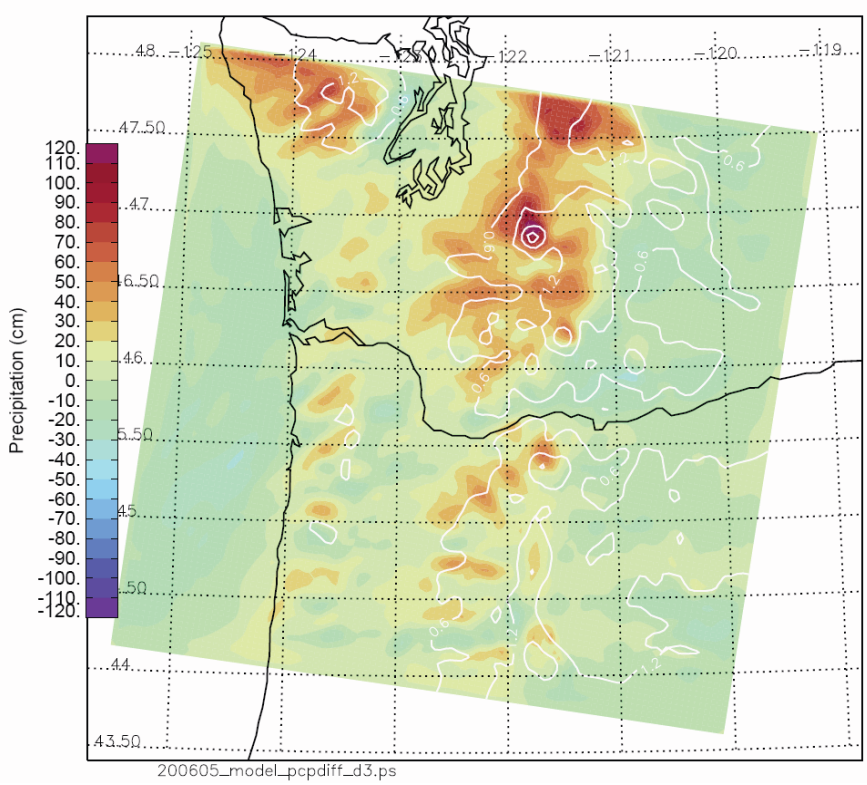

Figure 4.3 Seasonal precipitation difference (color shaded in cm) between the 2006/07 (using 2008 Thompson scheme) and 2005/06 season (using 2004 Thompson scheme) for the 4-km domain.

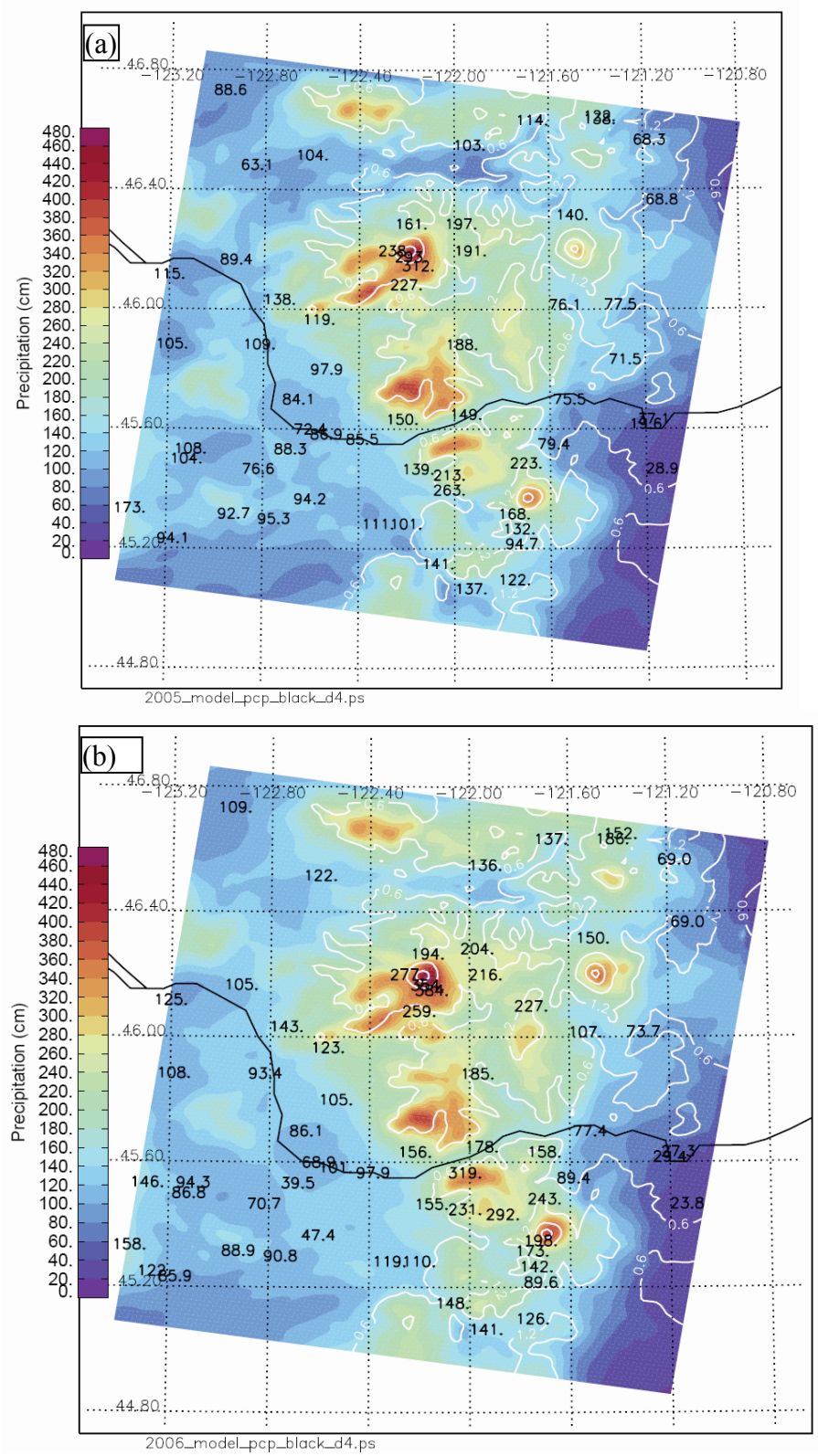

Figure 4.4 1.33-km MM5 seasonal precipitation (color shaded in cm) with the observed seasonal precipitation (black numbers) overlaid for (a) the 2005/06 season, and (b) 2006/07 season. The terrain is contoured every 0.6 km in white.

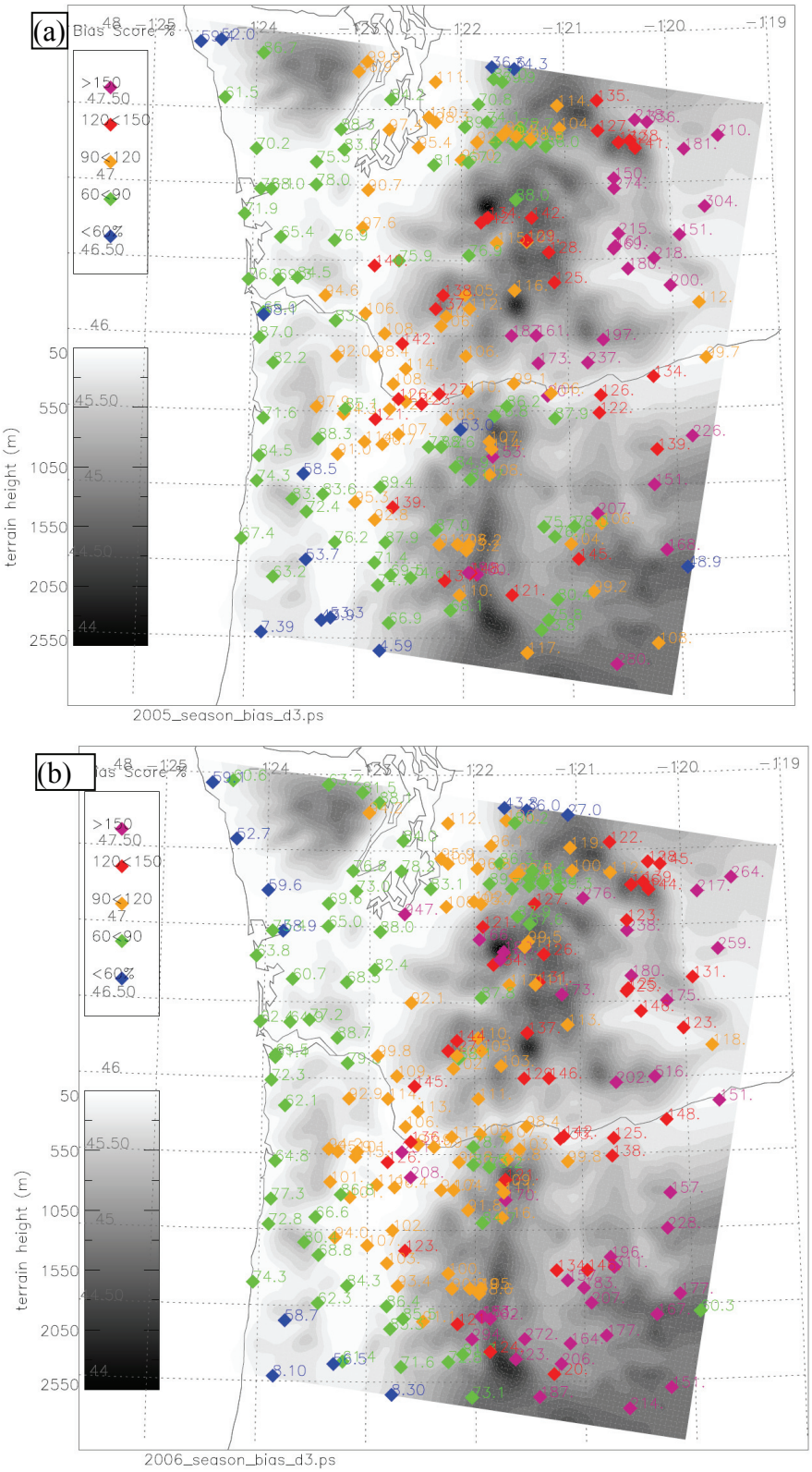

Figure 4.5 Bias score of seasonal precipitation for the 4-km MM5 for (a) 2005/06 season, and (b) 2006/07 season.

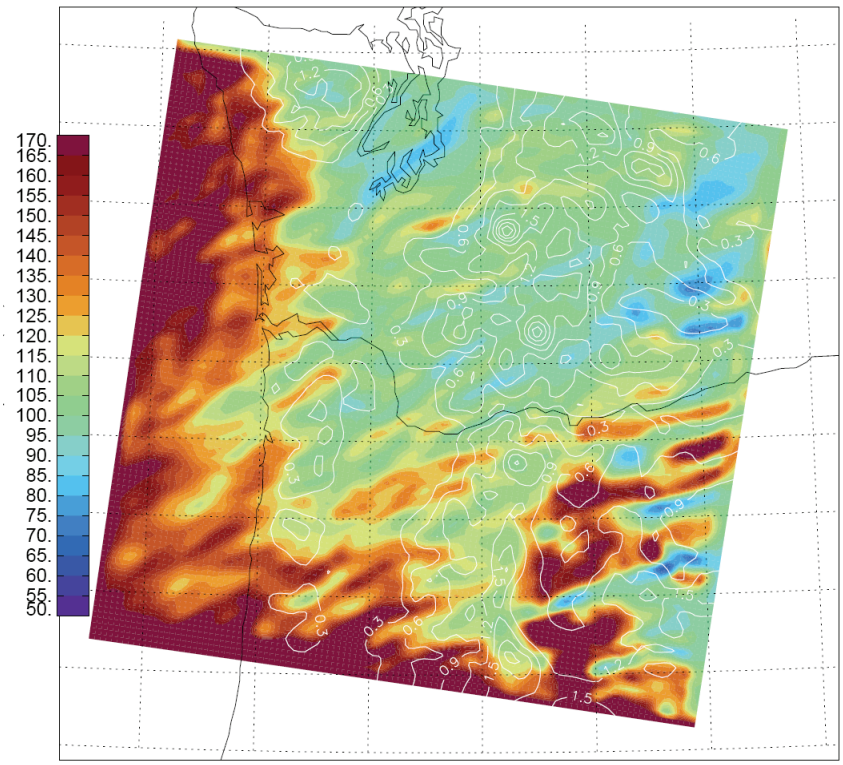

Figure 4.6 Ratio (color shaded in %) of total precipitation between the large 4-km domain simulations and control simulations (21 simulations in total).

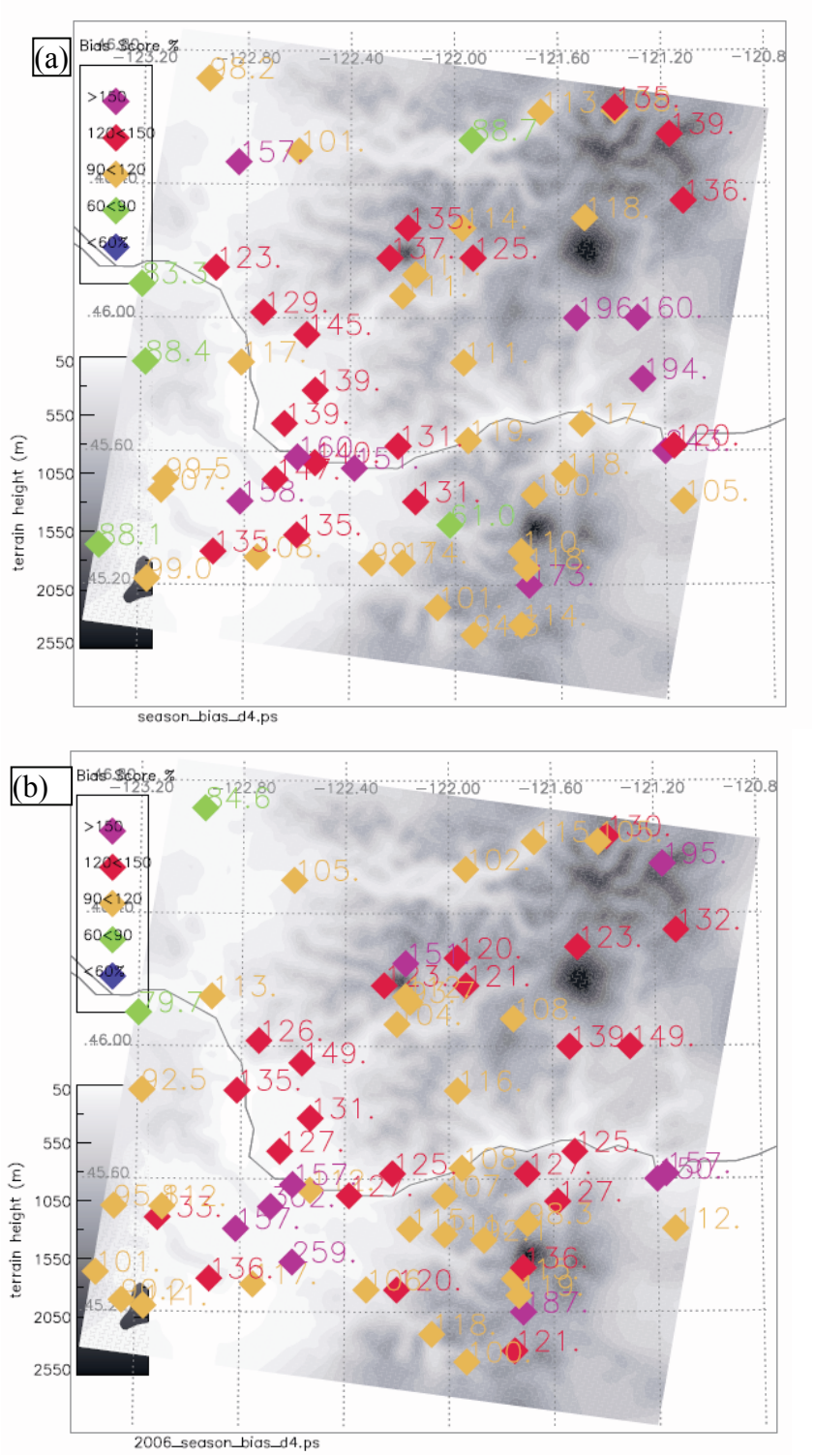

Figure 4.7 Seasonal bias score for the 1.33-km MM5 for (a) 2005/06 season, and (b) 2006/07 season.

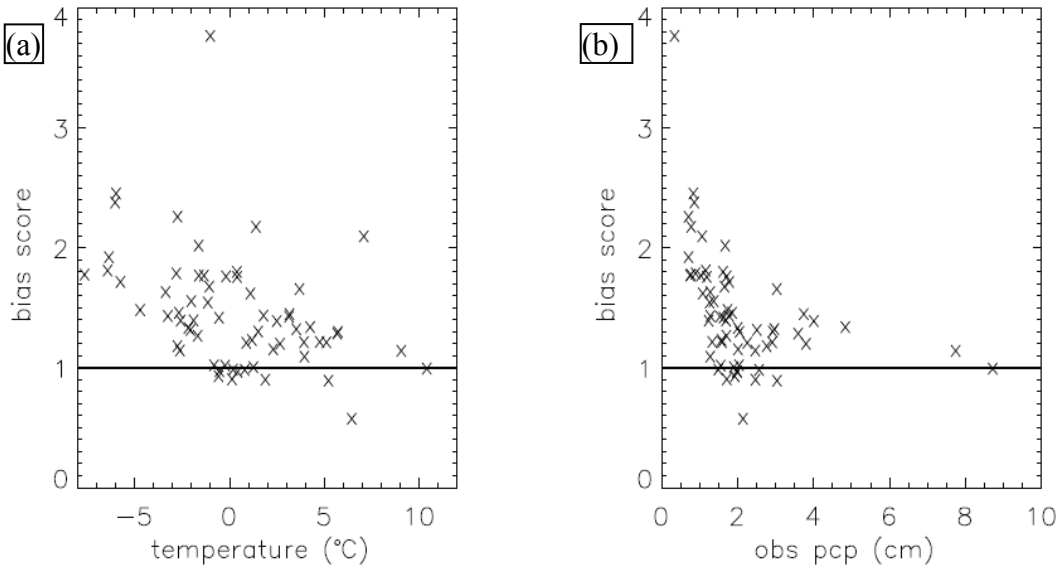

Figure 4.8 The dependence of MM5 bias score (B_p) on (a) temperature, and (b) precipitation magnitude.

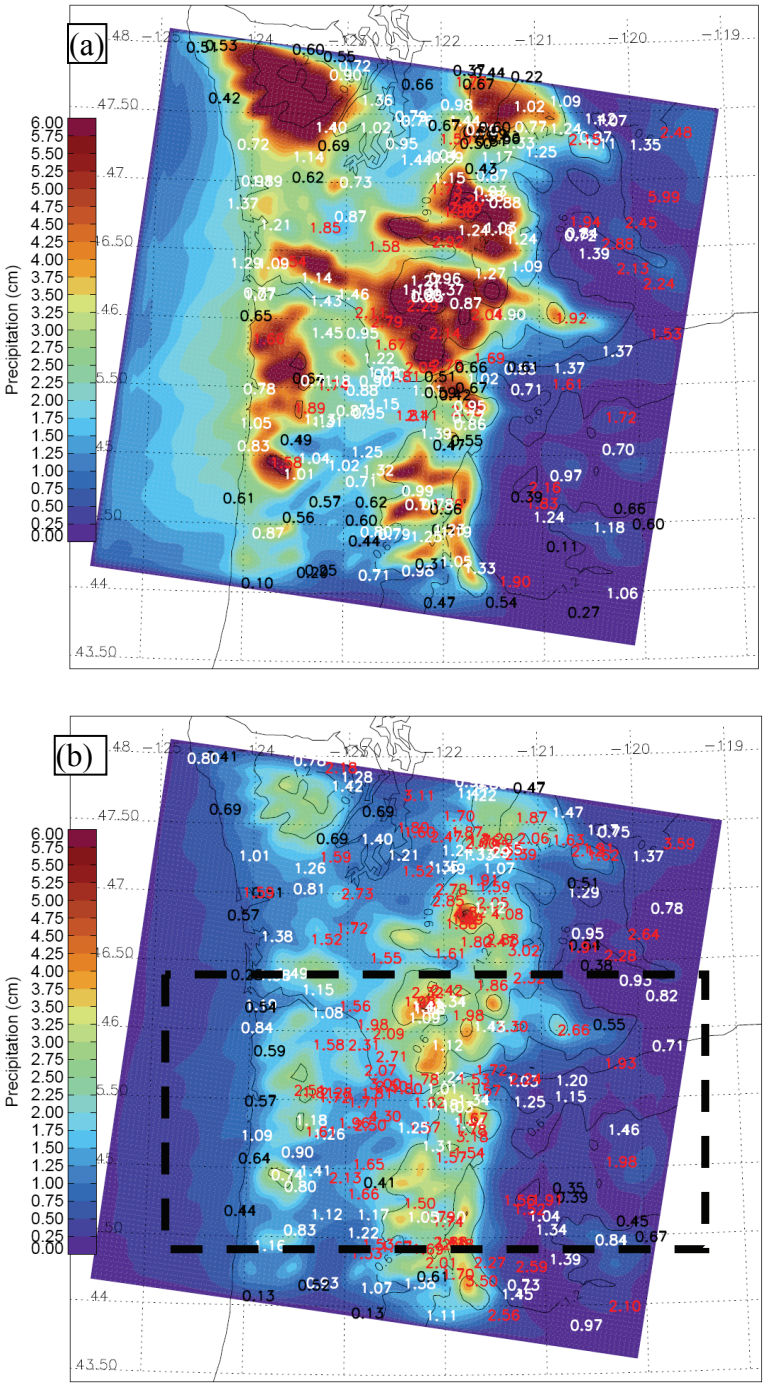

Figure 4.9 (a) 4-km MM5 mean daily precipitation (color shaded in cm) for the composite with Salem sounding temperature at 1500 m MSL larger than 4 ^{o}C. Numbers overlaid are the bias score (red > 1.5, black < 0.7, gray in between). Terrain is contoured every 0.6 km in black. (b) Same as (a) but for the composite with temperature at 1500 m MSL less than -1 ^{o}C.

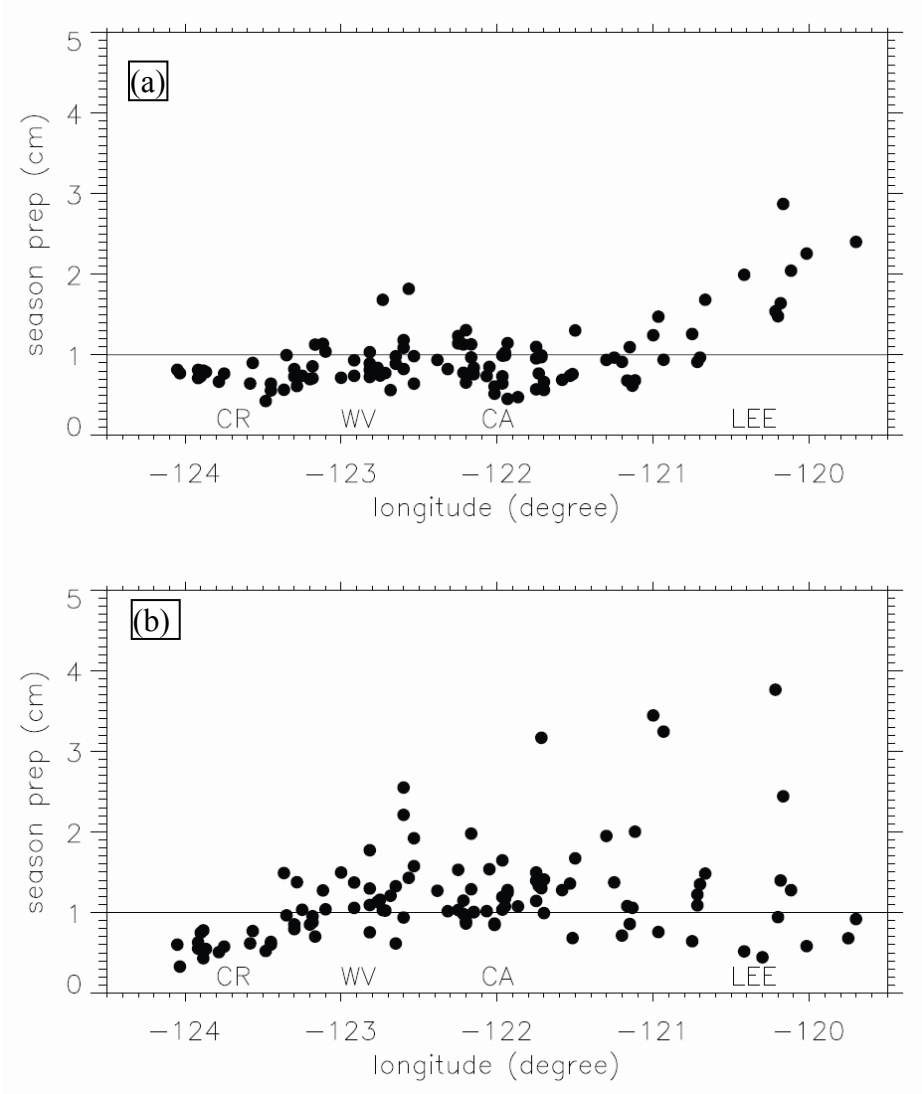

Figure 4.10 The west-east cross section showing the 4-km model bias score for (a) high freezing level composite (9 days) and (b) low freezing level composite (18 days). The stations in the black box in Fig. 4.9b (between 44.5 and 46.5 N) are plotted.

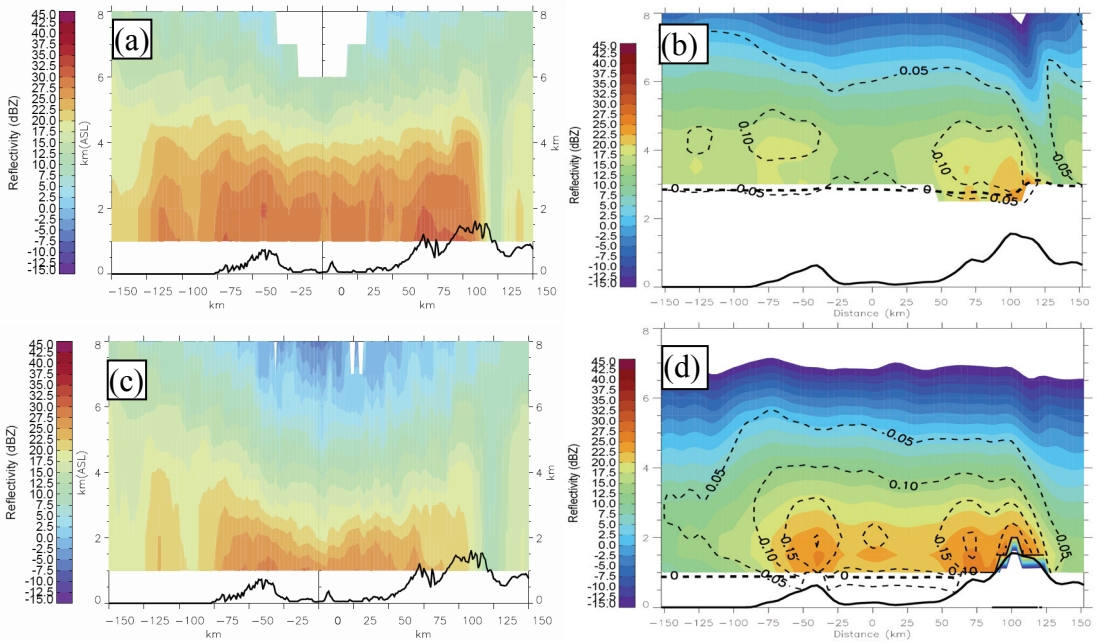

Figure 4.11 (a) Portland radar reflectivity (color shaded) along west-east cross section (along the red dashed line in Fig. 4.1b in the middle of Salem and Portland) for the high freezing level composite (b) Same as (a), but for the 4-km MM5 radar equivalent reflectivity with the snow mixing ratio (black line contours). (c) Same as (a), but for the low freezing level composite. (d) Same as (b), but for the low freezing level composite.

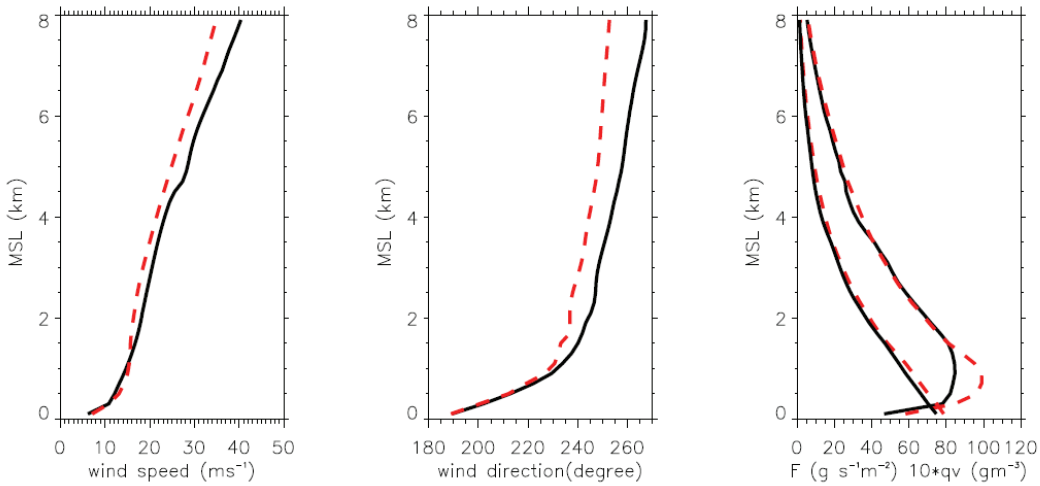

Figure 4.12 4-km MM5 (red dashed lines) and observed (black solid lines) wind speed, wind direction, moisture, and moisture flux at SLE for days with daily mean precipitation larger than 0.5 inch.

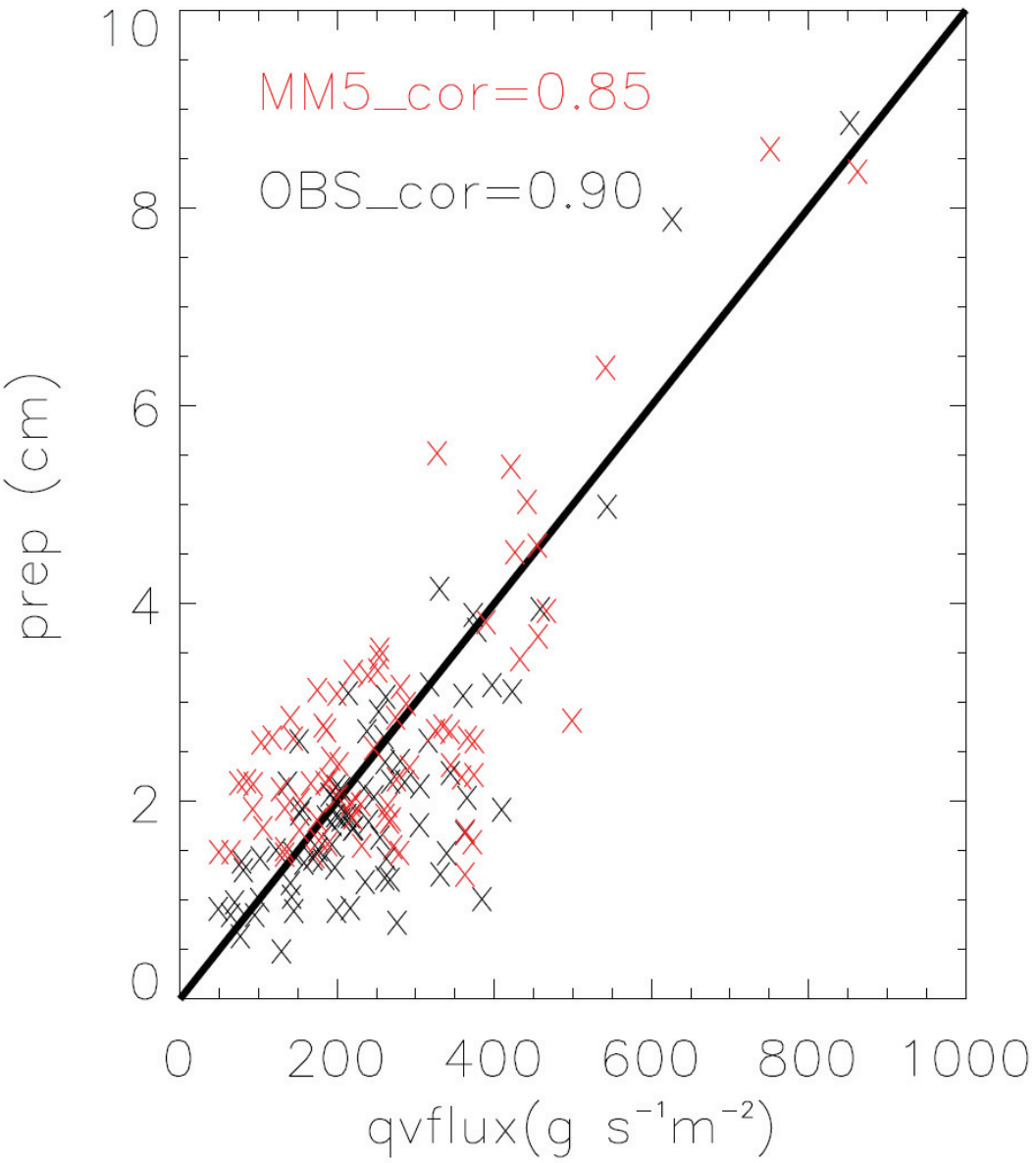

Figure 4.13 Scatter plot shows the correlation between the column-integrated moisture flux at SLE and daily mean precipitation for MM5 (red crosses) and observations (black crosses).

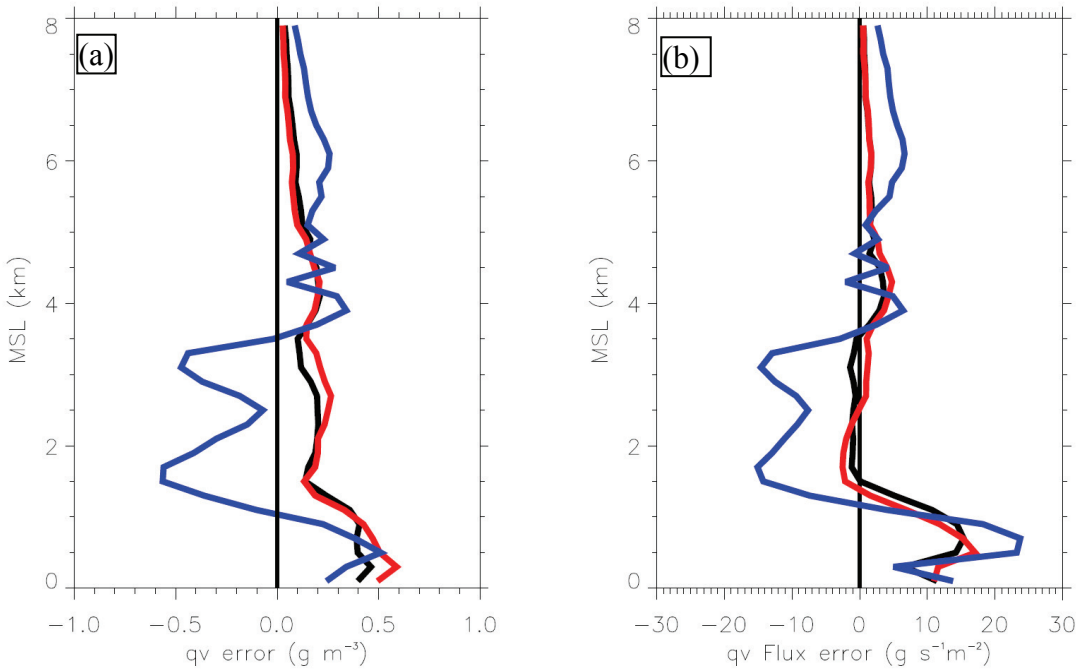

Figure 4.14 (a) Water vapor density error for the overprediction (red, 18 days), underprediction (blue, 6 days), and total (black, 53 days) days with daily mean precipitation larger than 0.5 inch for the 2006/07 season. (b) Same as (a) but for the water vapor flux error.

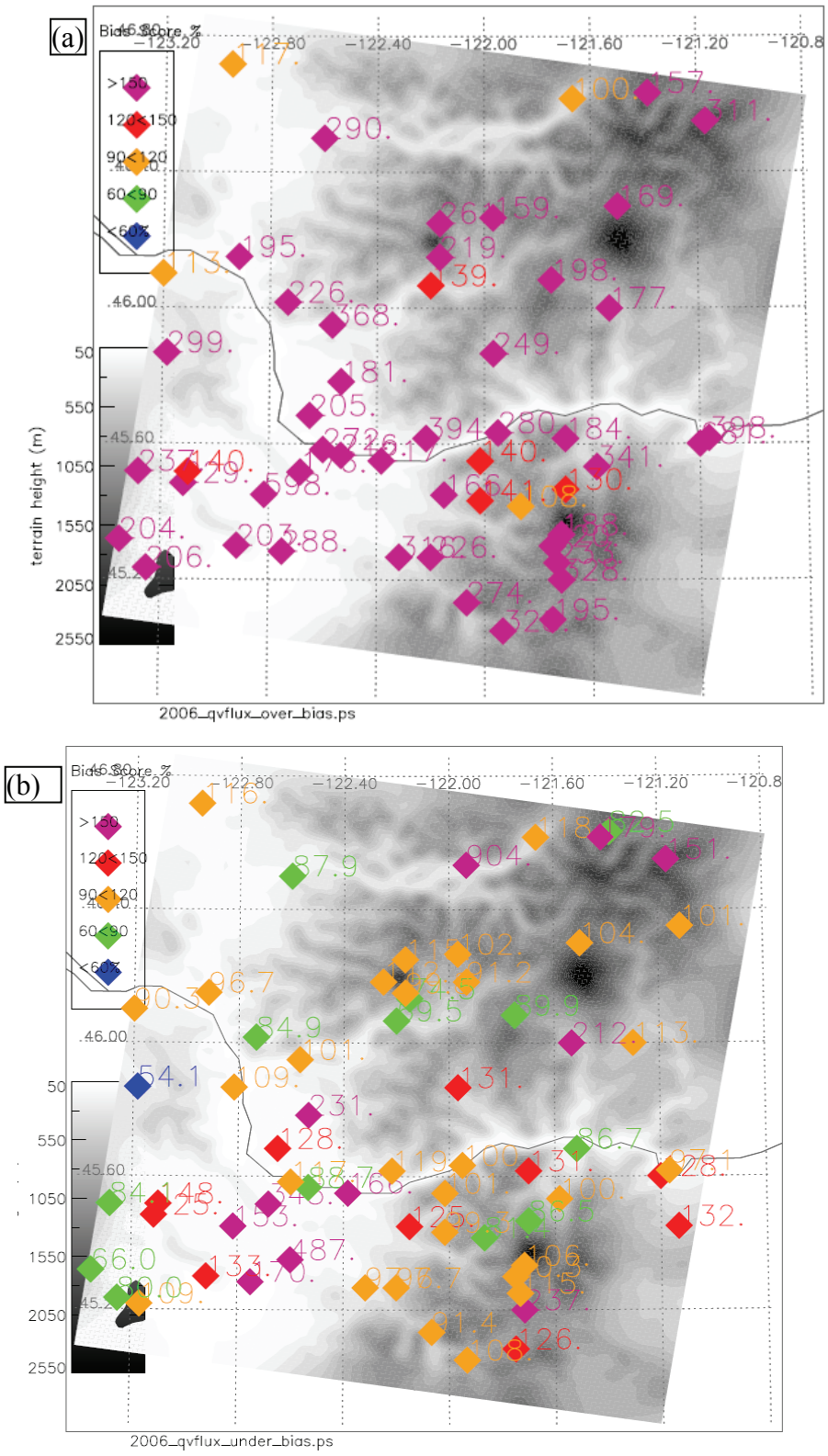

Figure 4.15 (a) Bias score (Be) plot for moisture flux overestimated days (9 days) for the 2006/07 season. (b) Same as (a), but for the moisture flux underestimated days (6 days).

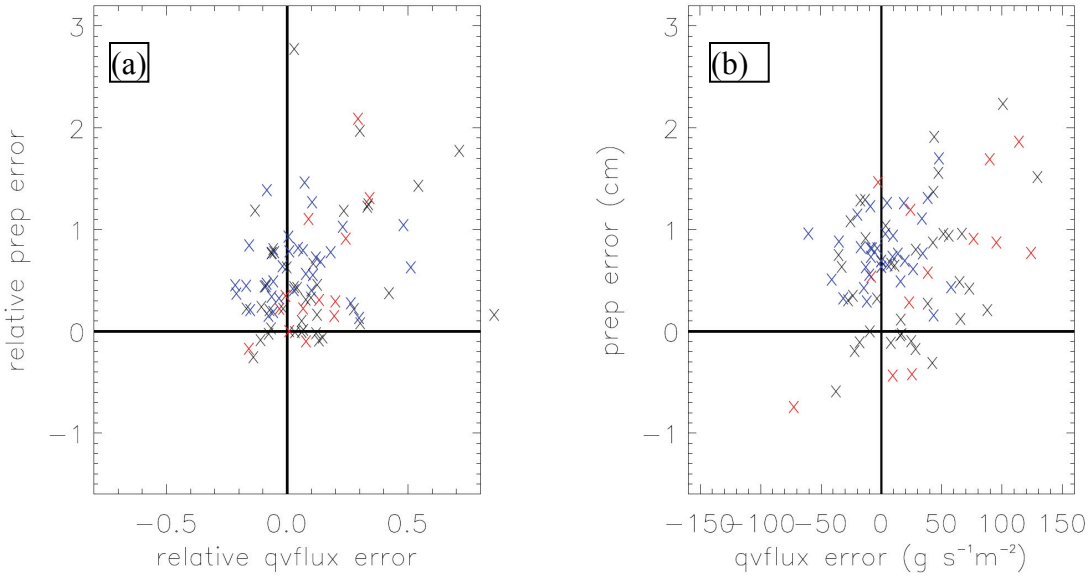

Figure 4.16 (a) MM5 relative error of moisture flux at SLE precipitation for all the days with daily mean precipitation > 0.5 inch (left panel). Blue crosses present the days with 1.5 km MSL temperatures at SLE colder than -1 ^{o}C, while red crosses presents the days with 1.5 km MSL temperatures at SLE warmer than 4 ^{o}C. (b) Same as (a), but show the absolute errors.

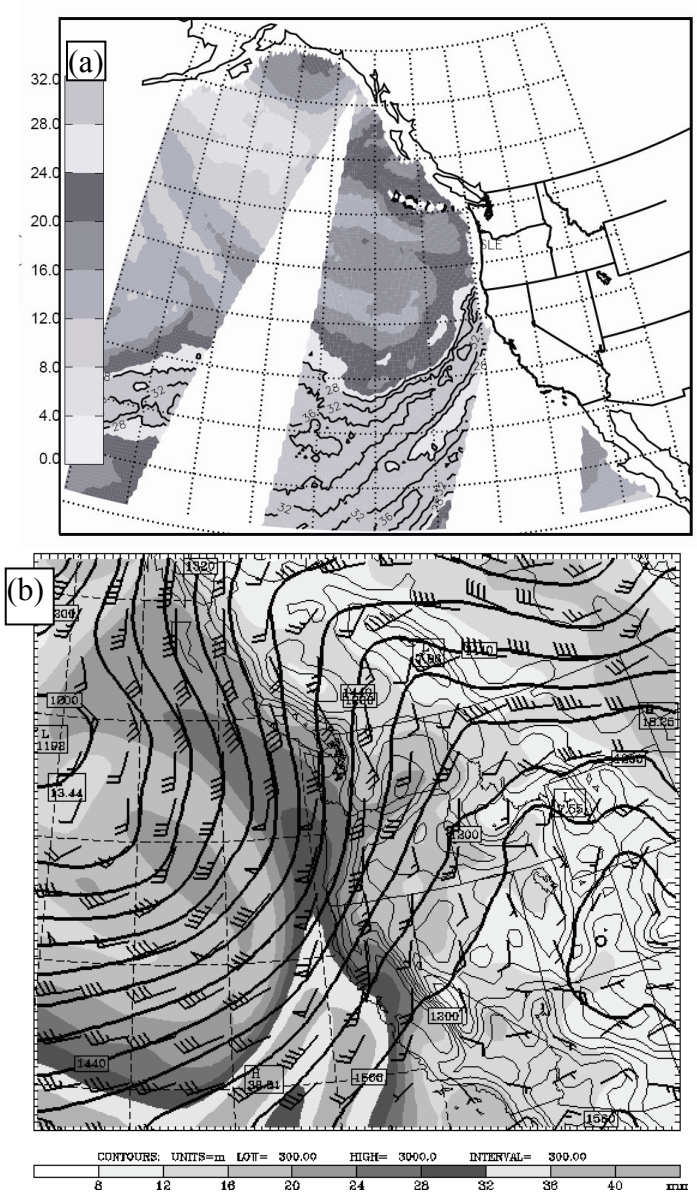

Figure 4.17 (a) Precipitable water vapor (PWV, shaded in mm) from SSM/I near 1800 UTC 21 December 2005. (b) 12-km MM5 PWV (shaded in mm) with winds and geopotential heights at 850 hPa at 1800 UTC 21 December 2005.

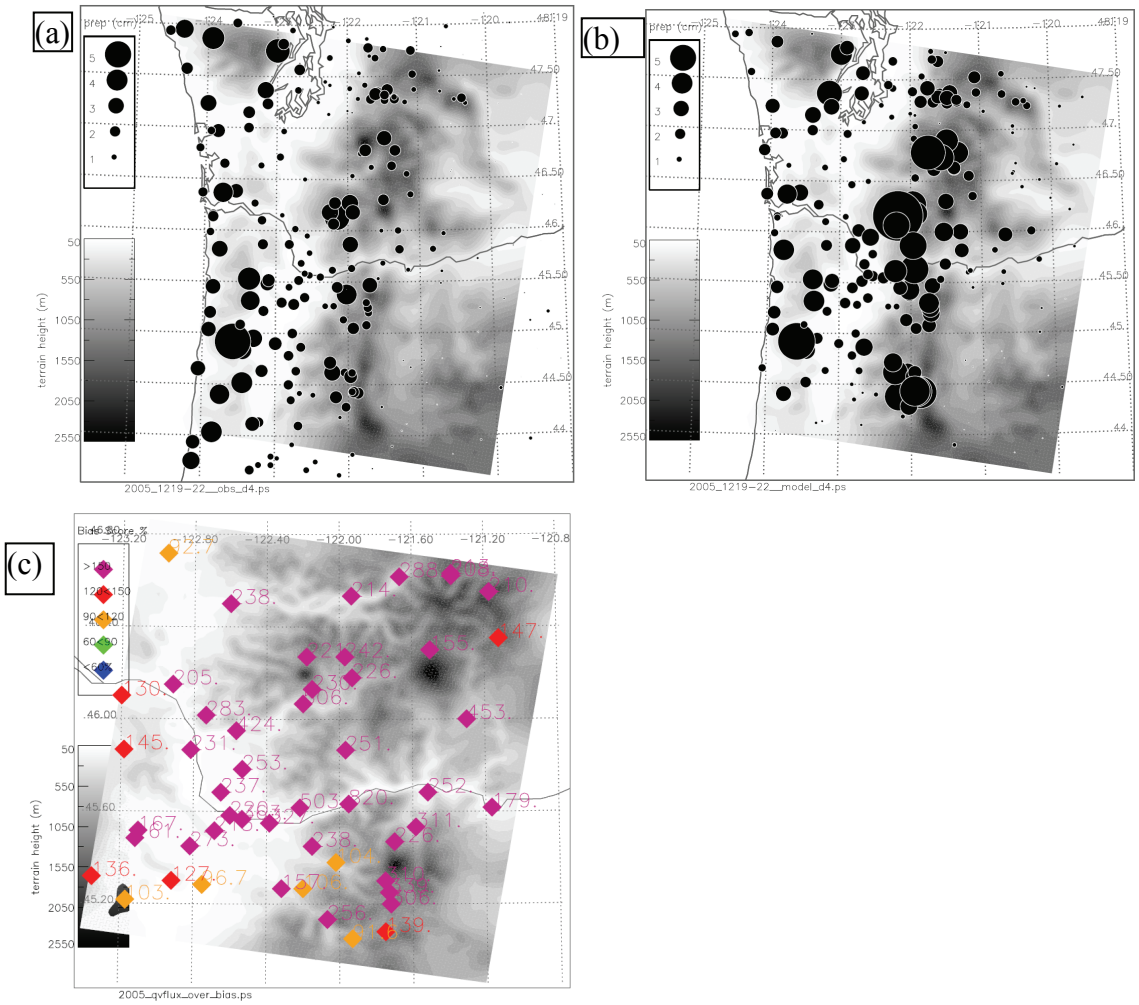

Figure 4.18 Daily average precipitation during a 4-day period (19-22 December 2005) from (a) rain gauges, (b) 4-km MM5, and (c) bias core.

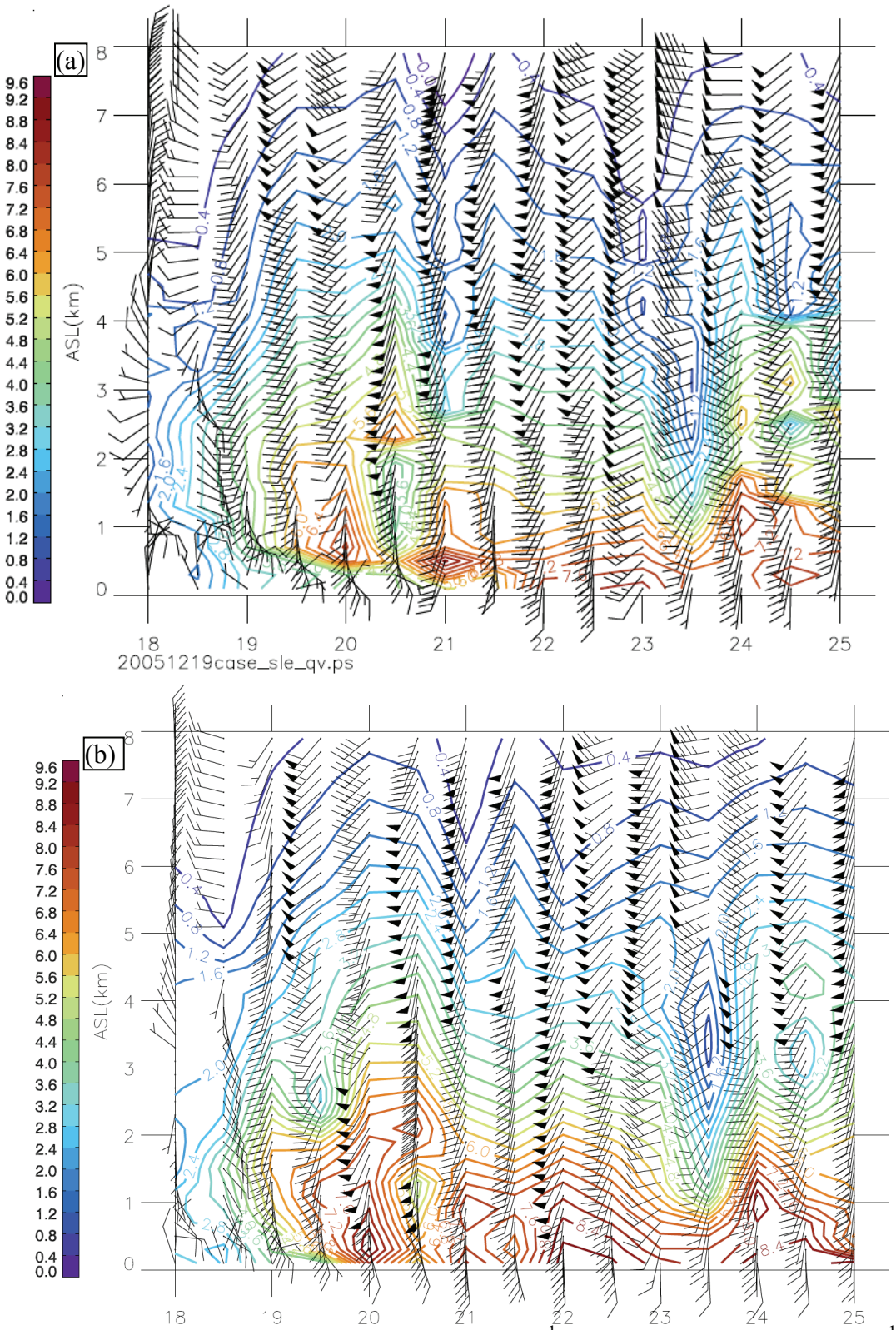

Figure 4.19 Time height plot showing the winds (m s^{-1}, one long bar represents 5 m s^{-1}) and moisture (color contoured in g m^{-3}) at SLE from (a) observed, and (b) 4-km MM5 from 0000 UTC 18 Dec to 0000 UTC 25 Dec 2005.

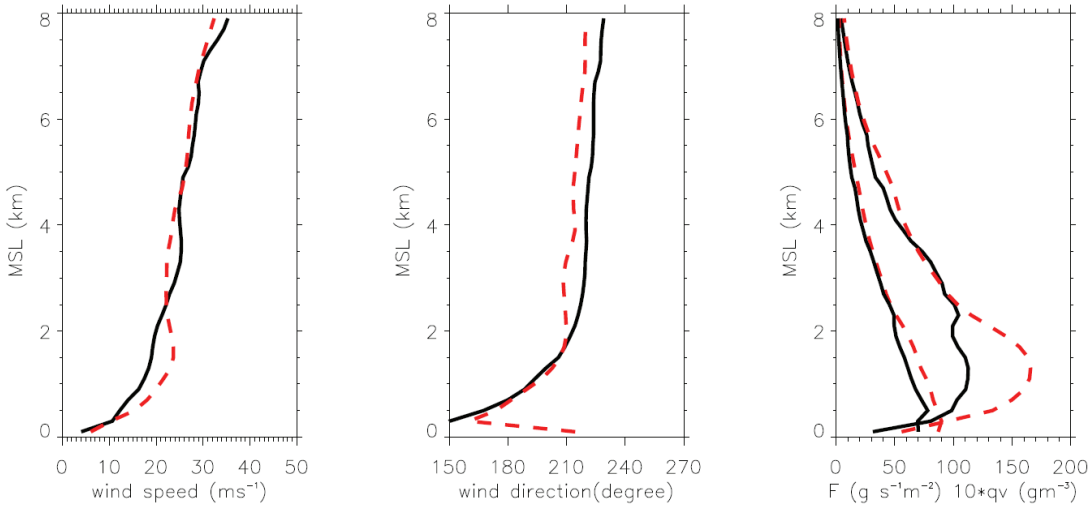

Figure 4.20 4-km MM5 (red dashed lines) and observed (black solid lines) wind speed, wind direction, moisture, and moisture flux at SLE during the 19-22 Dec 2005.

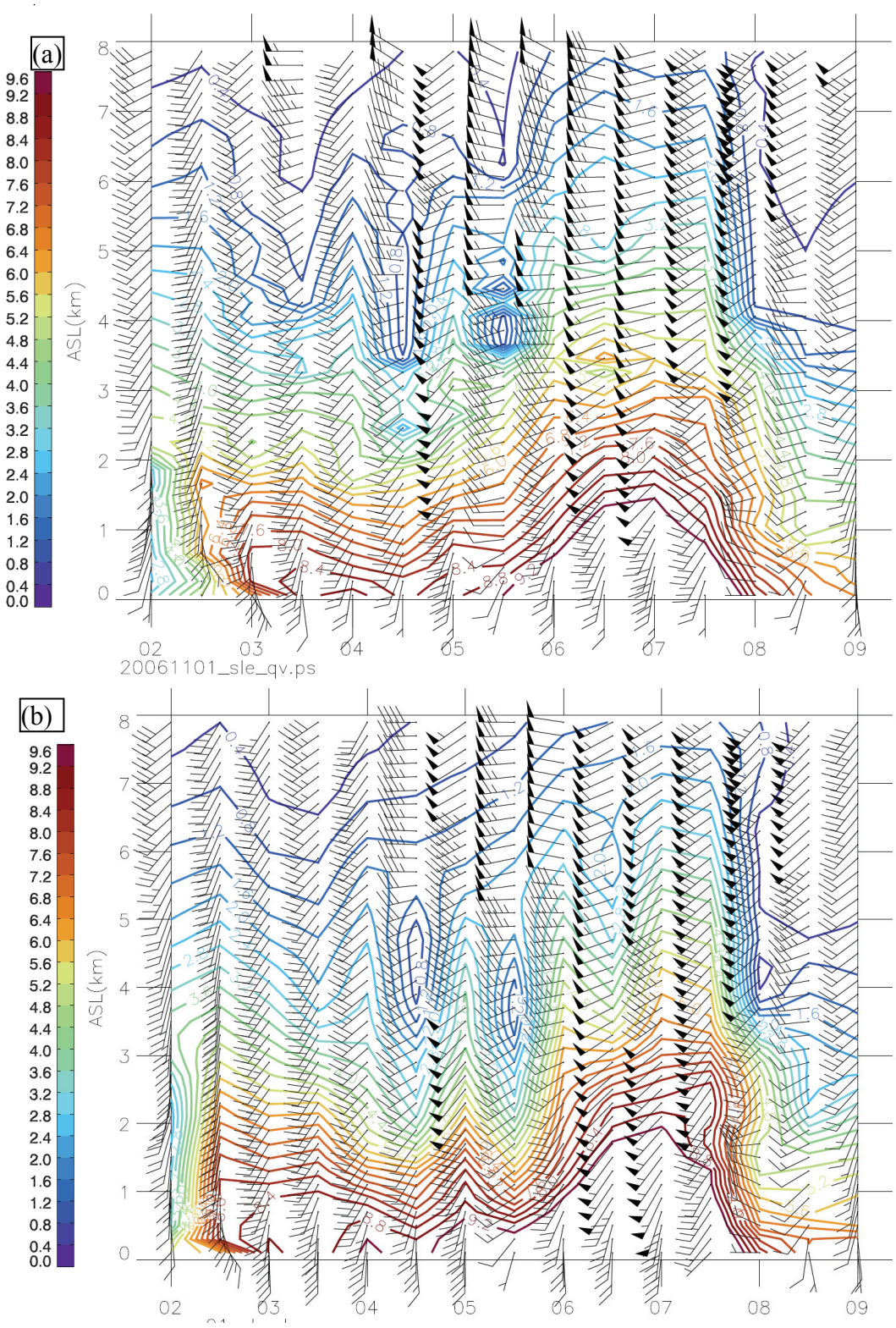

Figure 4.21 Time height plot showing the winds (m s^{-1}, one long bar represents 5 m s^{-1}) and moisture (color contoured in g m^{-3}) at SLE from (a) observed, and (b) 4-km MM5 from 0000 UTC 02 Nov to 0000 UTC 09 Nov 2006.

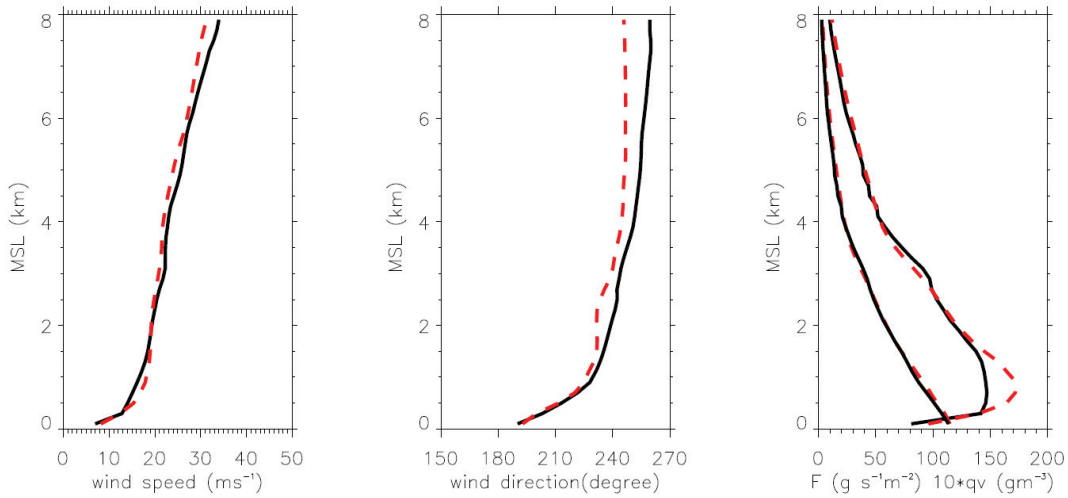

Figure 4.22 4-km MM5 (red dashed lines) and observed (black solid lines) wind speed, wind direction, moisture, and moisture flux at SLE during the 02-08 Nov 2006.

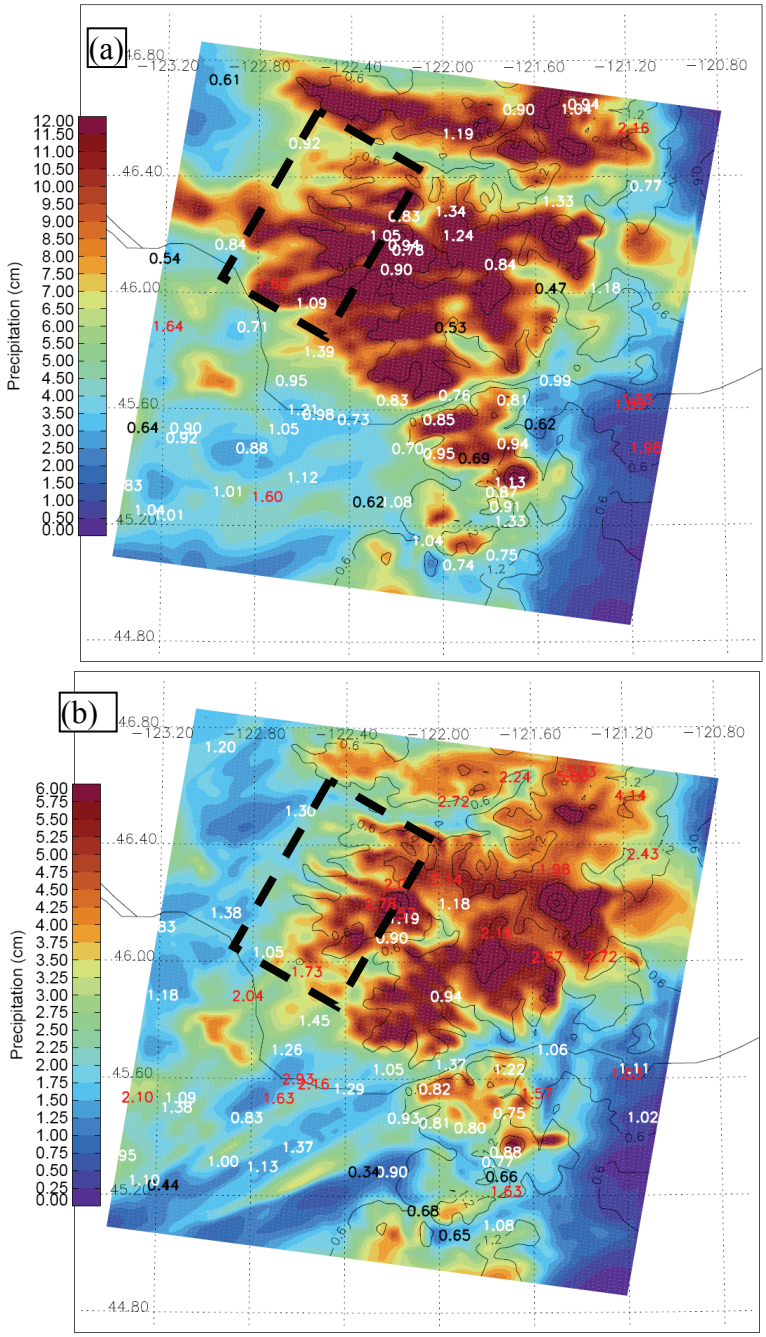

Figure 4.23 (a) 1.33-km MM5 mean daily precipitation (color shaded in cm) for the 02-08 Nov 2006 case. Numbers overlaid are the bias score (red > 1.5, black < 0.7, gray in between). Terrain is contoured every 0.6 km in black. (b) Same as (a) but for the 22-24 Dec 2006 case. Terrain is contoured in black. Note the precipitation scale for (a) is two times large as the scale in (b).

Chapter 5

Development of a New Bulk Microphysical Scheme

5.1 Introduction

There are a wide variety of bulk microphysical parameterizations (BMPs) available in the Weather Research and Forecasting (WRF) model, ranging from the simple Kessler BMP to the latest Thompson scheme (Thompson et al. 2008). One of the critical parameters in a BMP is the treatment of snow and graupel. Most BMPs treat snow and graupel by assuming spherical particles with constant density. However, in reality, ice particles have a variety of habits and complex structures, while riming changes and modifies the properties of ice particles. Most BMPs have an abrupt transition from snow to graupel, which neglects the partially rimed particles. Both ice habit and riming should be considered in BMPs to better represent ice processes and precipitation fallout.

In general, there have been two approaches to include habits in BMPs. One is to increase the numbers of prognosed variables to simulate the different habits explicitly (Straka and Mansell 2005), while the other is to estimate the preferred habit at each grid point based on the local conditions (Meyers et al. 1997), which can be tracked by partitioning the snow category into different habit types (Woods et al. 2007).

Rimed ice crystals and graupel are formed in mixed phase clouds containing both ice crystals and supercooled water drops. Riming occurs frequently and is a dominant precipitation pathway in the winter storms. The riming onset depends on the shape and size of ice crystals and the size of water drops (Pruppacher and Klett 1997). Riming changes the ice crystal properties, such as shape, size, mass, and fall velocity (Moismann et al. 1994; Moismann 1995; Barthazy and Schefold 2006). Partially rimed particles are often observed; while they are largely neglected in most microphysical parameterization schemes except some recently developed BMPs (Ferrier et al. 2001; Stoelinga et al. 2007; Morrison and Grabowski 2008).

Snow and graupel (or hail) are kept often as separate categories in traditional BMPs (Lin et al. 1983; Rutledge and Hobbs 1983; Ferrier 1994; Reisner et al. 1998; Hong et al. 2004; Thompson et al. 2004, 2008). Due to the large fall velocity difference between snow and graupel (or hail), the residence time and fallout of precipitation depends highly on the partition of snow and graupel, which has a large sensitivity on the surface precipitation distribution and precipitation efficiency (Chapter 3). By separately predicting the ice mixing ratios acquired through ice deposition versus riming, the riming effect on the mass and fall speed of snow can be considered (Stoelinga et al. 2007). Using a similar approach, Morrison and Grabowski (2008) considered the variation of particle

properties with particle size and rimed mass fraction. Due to the size dependent properties, the method can be easily applied in a bin scheme. However, the approach has its shortcomings: (1) only one habit type is used for nonspherical particles; (2) it is difficult to derive a continuous mass-diameter (m-D) and area-diameter (A-D) relationships over the whole size spectrum; (3) graupel size is smaller than partially-rimed particles; and (4) analytical integration of mass and fall velocity is impossible due to the size dependent m-D and velocity-diameter (V-D) relationships.

This chapter presents a new bulk microphysical scheme that has been developed and implemented in the WRF (SUNY scheme) model, which relates the crystal habits and degree of riming directly to the ice properties (m-D, A-D, and V-D). By introduction of a diagnosed varying degree of riming, the continuous spectrum from pristine ice to slightly rimed ice to heavily rimed snow and graupel can be represented. The framework and presentation of ice particles described here can be implemented in other BMPs.

5.2 Description of the new microphysical parameterization

a. Prognostic variables

The new scheme includes five prognostic variables: the mixing ratios of water vapor, nonprecipitating ice, precipitating ice (PI), cloud liquid water (CLW), and rain. Graupel is included in the PI category through the introduction of a degree of riming parameter. The microphysical processes are demonstrated in Fig. 5.1b and each source/sink term is described in Appendix A.

b. Cloud liquid water

A generalized Gamma distribution is used to describe the size distribution of cloud water particles.

$$N_c = N_{0c} D^{\mu} e^{-\lambda D} \tag{5.1}$$

Total number concentration of cloud droplets generally depends on the ambient aerosol distribution. In the scheme, the most representative numbers will be used for maritime (25 cm^{-3}) and continental air mass (1000 cm^{-3}) when aerosol information is not available. Future work will add the aerosol and its interaction with cloud microphysics.

The collision and coalescence of cloud droplets to form raindrops has been described as a simple autoconversion process only by accounting for the cloud liquid water content (Kessler 1969). More physically based autoconversion parameterizations (Berry 1968; Berry and Reinhardt 1975; Walko et al. 1995) have been implemented into some new BMPs (Thompson et al. 2004; Thompson et al. 2008; Hong et al. 2004). Using the generalized mean value theorem, Liu and Daum (2004) derived a new Kessler-type parameterization suggesting strong dependence of the autoconversion rate on liquid water content, droplet concentration, and relative dispersion (defined as the ratio of the standard deviation to the mean radius of the cloud droplet size distribution). More specifically, we use Eq. 27 in Liu and Daum (2004) with an assumed total cloud droplet number concentration of 25 cm^{-3} as a preliminary test.

c. Cloud ice

The division between the cloud ice and PI is based on the following observational findings. Based on aircraft observations, Heymsfield et al. (2007) found that the spherical assumption is good for ice particle with diameters smaller than 90 microns. For these small ice particles, a constant ice density (910 kg m^{-3}) is considered a reasonable approximation. It is known that small ice crystals under a threshold size are unable to collect small cloud droplets. The threshold size is about 100 microns for plates and about 50 microns for columnar crystals (Pruppacher and Klett 1997). Thus, a maximum size of 100 microns is applied for cloud ice in the scheme.

To simplify the description of ice in BMPs, a monodisperse distribution of ice has been widely used. However, observations indicated that an exponential distribution with a larger intercept parameter than snow describes the cloud ice size distribution better (Field et al. 2005). An exponential distribution with the intercept dependent on temperature following Fletcher (1962) is used for the cloud ice. The same approach for the cloud liquid water autoconversion was applied to cloud ice conversion to snow with a temperature-dependent collision efficiency.

d. Precipitating ice

1) Ice crystal habits

Due to their irregular shapes, the geometry of ice particles is often described with a maximum diameter or dimension (called as D later). Power laws have been widely used to describe the m-D, A-D, and V-D relationships for ice particles:

$$m = a_m D^{b_m}, \quad A = a_a D^{b_a}, \quad V = a_v D^{b_v} \tag{5.2}$$

Heymsfield et al. (2007) collected observations sampled from a wide range of temperatures to derive temperature-dependent coefficients (a_m and b_m) for the m-D relationship in Eq. 5.2 (see their Table 1). Using data collected in wave clouds, Baker and Lawson (2006) reported the A-D relationships for three crystal types (see their Table 4). These two studies provide the basis for the estimate of habit effect on m-D and A-D relationships in our BMP.

2) Riming intensity or degree of riming

Relatively few observations (Moismann et al 1994; Moismann 1995) have been reported to describe the degree of riming (later referred to the riming intensity, *Ri*, which represents either partially-rimed particles or the rimed mass fraction of all ice particles). *Ri* depends on the particle growth history, which basically depends on the relative contribution of riming growth and depositional growth. Riming growth is proportional to the cloud liquid water (CLW) content and depositional growth is proportional to ice content (Pruppacher and Klett 1997). For simplification, a diagnostic *Ri* dependent on environmental conditions and cloud properties is proposed.

One approach is to define *Ri* as a function of the amount of CLW and PI in the scheme. For the preliminary tests, *Ri* is diagnosed as:

$$Ri = \sqrt{\frac{CLW}{PI}} \tag{5.3}$$

and ranges from 0 (pristine ice particles) to 1 (graupel). *Ri* is only computed when both the CLW and PI are larger than a threshold of 0.01 g kg^{-1}. One limitation of the approach is that *Ri* would be underestimated (*Ri*=0) when PI with larger *Ri* sediments into a cloud water free region. *Ri* is also dependent on the vertical motion and temperature as they affect the condensation and cloud phase. More field observations, such as those collected in IMPROVE, will be utilized to further refine the *Ri* parameter in the future.

3) Mass-dimension and area-dimension relationships

In the m-D relationship, a_m can be considered as an effective density and b_m as a fractal dimension. Based on the "filling-in" concept proposed by Heymsfield (1982), the particle fractal dimension gradually increases with *Ri* and becomes 3 as the particle grows to a spherical graupel. Moismann et al. (1994, their Eq. 3) found that the rimed mass increased exponentially with riming intensity, which suggests a linear dependence of b_m on *Ri*. Moismann (1995, his Eq. 3) found that fall velocity of rimed particles increased as *Ri* increased. This suggests a linear increase of a_m with Ri^2 as illustrated in the derivation of V-D relationship later. More specifically, the first two terms in equations 5.4 and 5.5 are from Heymsfield et al. (2007) to reflect the habit effect as a function of ambient temperature:

$$a_m = c_0 + c_1 T + c_2 Ri^2 \tag{5.4}$$

$$b_m = C_0 + C_1 T + C_2 Ri \tag{5.5}$$

We utilize the temperature dependent A-D relationship derived by Baker and Lawson (2006) and include the effect of Ri to get:

$$a_a = d_0 + d_1 T + d_2 Ri \tag{5.6}$$

$$b_a = D_0 + D_1 T + D_2 Ri \tag{5.7}$$

in which c_2, C_2, d_2, and D_2 are determined to bound the b_a and b_m by 2 and 3, respectively, and to ensure the new m-D and V-D relationship cover the wide range of variability observed. These coefficients are put in Appendix.

4) V-D relationship

Particle fall velocity depends on the particle size, shape, degree of riming, and the orientation of falling particles (Hanesch 1999). Empirical expressions of fall velocity for various ice particle types have been developed (Locatelli and Hobbs 1974; Heymsfield and Kajikawa 1987 among others). These empirical fall velocity expressions have been used in BMPs for snow or graupel (Table 3.1 in Chapter 3). However, the fall velocity in these schemes generally picked one expression and the expression is not always consistent with the m-D and A-D relationships assumed in the schemes. For example, different V-D relationships of graupel have been used in WSM6, PLIN, THOM1 and THOM2 schemes (Table 3.1) though the same m-D relationship (spherical particle with

constant density of 400 kg m^{-3}) is used in these schemes. To derive a consistent fall velocity with particle mass and projected area in the new scheme, a theoretical approach based on boundary layer "assembly" (Abraham 1970) is used.

With the m-D and A-D relationships known, we follow the Best number (X) and Reynolds number (Re) approach to derive the V-D relationship (Bohm 1989; Mitchell 1996). This approach does not need an explicit drag coefficient and is relatively independent of the particle habit.

$$\mathrm{Re} = aX^b = \frac{DV}{\nu} \tag{5.8}$$

$$X = \frac{2gmD^2}{\rho_a \nu^2 A} \tag{5.9}$$

where g is the gravitational acceleration constant, ρ_a is the air density, and ν is the kinematic viscosity of the air. a =1.08 and b = 0.499 are taken from Mitchell (1996). Incorporating (5.7) and (5.8) and using the m-D and A-D relationships defined in Eq. 5.4-5.7, we get

$$a_v = a\nu\left(\frac{2ga_m}{\rho_a \nu^2 a_a}\right)^b \tag{5.10}$$

$$b_v = b(b_m - b_a + 2) - 1 \tag{5.11}$$

From eq. (5.9), we see a_m should be proportional to Ri^2 to ensure the dependence of V on Ri as found in Moismann (1995).

5) Ice capacitance

Ice particle capacitance is a function of the size and shape of the ice particle and it directly impacts the snow deposition and sublimation growth (Rogers and Yau 1989). Westbrook et al. (2008) showed that the capacitance of snow aggregates (b_m ~2) was only half that of a sphere. Since b_m linearly increases to 3 as Ri increases from 0 to 1, for simplicity, we assume (where C_s = 0.25 for dry snow):

$$C_s = 0.25(1 + Ri) \tag{5.12}$$

6) Snow size distribution

We still keep using the conventional exponential size distribution for snow though a generalized Gamma distribution has also been implemented into the scheme as in Thompson et al. (2008).

$$N_s = N_{0s} D^{\mu} e^{-\lambda D} \tag{5.13}$$

where N_{0s}, μ, and λ are the intercept, shape and slope parameter, respectively. Integrated over the whole size spectrum using the m-D to get the total mass, we get:

$$\lambda = \left(\frac{a_m N_{0s} \Gamma(b_m + \mu + 1)}{\rho q_s}\right)^{\frac{1}{b_m + \mu + 1}} \tag{5.14}$$

and the mass-weighted mean fall velocity:

$$V_m = a_v \frac{\Gamma(b_m + b_v + \mu + 1)}{\Gamma(b_m + \mu + 1)\lambda^{b_v}} \left(\frac{\rho_0}{\rho}\right)^{0.54} \tag{5.15}$$

Further development will consider a slope parameter that depends on temperature, *Ri*, and snow mass. Recent observations show that the snow slope parameter varies over a small range than intercept parameters for snow (Ryan 1996; Woods et al. 2007). The shape parameter has been shown to affect the sedimentation and microphysical processes significantly (Milbrandt and Yau 2005). With same intercept and slope parameters, larger shape parameter will skew more particles to moderate sizes, and thus reduce the mean mass diameter.

e. Microphysical processes parameterizations

All the microphysics in the new scheme apply the new size distributions, m-D, A-D, and V-D relationships to modify the microphysics parameterization accordingly as in Lin et al. (1983) and Rutledge and Hobbs (1983, 1984). These microphysical parameterizations are put in the Appendix.

In reality, ice depositional and riming growth occurs concurrently. As cloud liquid droplets accreted to the ice surface and freeze, latent heat is released and the surface temperature of ice particles increases. As a result, the supersaturation over the ice particle surface is reduced and so is the depositional growth (Kong and Yau 1997). Since the environmental temperature and moisture is only updated at each model time step in the scheme, for simulations with coarse resolution and a large time step, the error neglecting the riming effect on the depositional growth might be nontrivial. However, the ice depositional growth parameterization in most of traditional BMPs has not included this effect. The new scheme adds the riming growth effect on the depositional growth parameterization.

5.3 Justification of the approach

The new parameterization has been implemented into WRF version 2.2, with all the PI related processes in the scheme modified to include the newly derived m-D, A-D, and V-D relationships. Since the spectrum from snow to graupel share the same category in the new scheme, they also share the same processes. As compared with the traditional BMP with graupel, such as Thompson et al. (2004), the new scheme reduces the microphysical processes from over 40 to less than 20 (Fig. 5.1). As a result, the new scheme also saves simulation time by ~10% and ~30% in a full model and simple 2-D kinematic model, respectively.

Various m-D and V-D relationships have been derived from observations for different snow habits (Zikmunda and Vali 1972; Locateli and Hobbs 1974; Mitchell 1996 among others). To illustrate the impact of *Ri* on m-D and V-D, Fig. 5.2 shows the empirical m-D and V-D relationships for different habit types from Woods et al. (2007) and the m-D and V-D predicted in the SUNY scheme. As *Ri* increases from 0 to 1, the mass and fall velocity of PI increases and they cover a wide range encompassed by the

observed m-D and V-D relationships. The widely used spherical assumption with constant density for snow and graupel gives much larger mass compared with other habit types (cold type, needle, dendrite, sector), especially when the particle diameter is large. Dendrite ice particles fall relatively slow (~ 0.5 m s^{-1}), while cold type snow falls much faster (~1.5 m s^{-1}). It is clear as *Ri* increases from 0 to 1, the fall velocity of PI increase substantially from less than 0.3 m s^{-1} to more than 2.5 m s^{-1} for particles with ~ 2 mm maximum diameter.

In a recent paper, the fall velocity of graupel and of snowflakes of differing riming degree and consisting of different crystal types was investigated using observations of particle size, shape and fall velocity during 2 winter seasons (Barthazy and Schefold 2006). It is found that the fall velocity of snowflakes depends on both the riming degree and their crystal type composition. Both a_v and b_v in the V-D relationship in their study (their table 3) increase with the riming degree with b_v ranging from 0.20 to 0.40. The a_v and b_v derived in the new scheme also increase with riming degree and are generally within a comparable range (0.2 to 0.5) to this study. This implies the formulations for the PI properties are in reasonable range. However, more observations and theoretical studies are needed to better quantify the shape and *Ri* effect on ice particle mass and fall velocity as illustrated in the summary and future work chapter.

5.4 Preliminary tests

Since m-D and V-D relationships come into play in most of the microphysical parameterizations. It is expected the varying relationships proposed in the new scheme will impact the model simulation results presented in Chapter 3. The IMPROVE project collected comprehensive measurements from a variety of remote and in situ instruments. The wealth of observations gives an unprecedented opportunity for the rigorous testing of various BMP schemes. The new scheme is tested with the two well-studied IMPROVE-2 cases (13-14 and 4-5, Dec 2001, called IOP11 and IOP6 later).

a. Experiment setup

The 4-5 December 2001 case model setup is identical to that used in the Chapter 2 except the new SUNY scheme is used within WRF. For the 13-14 December 2001 case, the model setup follows the guidelines described in Grabowski (2006) and used by previous studies (Garvert et al. 2005a; Milbrandt et al. 2008). WRF version 2.2 is used with 1.33, 4, and 12 km domain nested within a 36-km domain. GFS analyses every 12-h were used for the initialization at 0000 UTC 13 December 2001 and the lateral boundary conditions for the full 36-h simulation. Four dimensional data assimilation (FDDA, analysis nudging, Stauffer and Seaman 1990) was used during the first 24 hours for the 36 and 12-km domain and then turned off gradually during a 6-h period. Physics used are modified Kain-Fritsch scheme (Kain and Fritsch 1993) for the 36 and 12-km domain and the medium range forecast (MRF) planetary layer scheme (Hong and Pan 1996). Total of four simulations were conducted using the new scheme, Thompson et al. (2004), Thompson et al. (2008), and Purdue Lin scheme (Chen and Sun 2002).

b. Precipitation and microphysics comparison for IOP6

Chapters 2 and 3 describe the detailed observed mesoscale evolution and model comparisons for IOP6. The four BMPs in WRF were evaluated and compared using the observations collected during the IOP6; thus, this section only briefly presents the comparison of precipitation and microphysics between the new scheme and THOM2 scheme.

The general pattern of the 12-h precipitation distribution is similar between the new SUNY scheme and the THOM2 scheme, with the SUNY scheme producing slightly more (1 cm) precipitation over the coastal range (Fig. 5.3), especially over the south part coastal range. There is also ~1 cm more precipitation over the windward ridges and crest of the Cascades in the new scheme. The new scheme reduces the spillover slightly with less (~0.2 cm) precipitation in the immediate lee and ~0.5 cm more precipitation in the further lee. Overall, the new scheme produces a comparable precipitation forecast as more complicated THOM2 scheme for the case.

The east-west cross section of hydrometeors meridionally-averaged over the black box in Fig. 5.3 was constructed for the two schemes (Fig. 5.4). The SUNY has 40% less IWC than the THOM2 over the Cascades, with maximum IWC of ~ 0.3 g m^{-3} compared with ~ 0.5 g m^{-3} of the THOM2 scheme. The CLW in the SUNY scheme is deeper (to ~3 km) over the Cascades than THOM2 with maximum near 0.25 g m^{-3} as compared with only 0.08 g m^{-3} for THOM2. Both the IWC and CLW in the SUNY scheme compares better with observations (see Table 3.1) than the THOM2 scheme. Interestingly, the new scheme predicts more IWC over the coastal range than THOM2. The reason is probably due to the boosting factor used for the snow fall speed in THOM2, which increases the snow fall speed where there is more CLW for riming growth, such as over the coastal range.

c. Large-scale comparison for IOP11

The synoptic and mesoscale evolution of the 13-14 December 2001 IMPROVE-2 event is described in detail in Garvert et al. (2005a). A large-scale baroclinic system moved inland from the Northern Pacific Ocean and resulted in strong cross-barrier flow in the lower troposphere at 0000 UTC 14 December 2001 (Fig. 5.5). Model 500-hPa trough was positioned just off the west coast with a 300-hPa jet up to 80 m s^{-1} behind the trough, which is close to the NCEP analysis (Fig. 5.5a). At 850-hPa, the lowest geopotential height over Vancouver Island in the model is 1185 m, which is slightly less than 1170 m in the analysis. The 850-mb winds along the Oregon coast are 55 knots at this time in both the analysis and forecast. The WRF predicted a surface low of 982 hPa over Vancouver Island, which is close to the analysis. Model large-scale features are also similar to the observations at other times (not shown).

Fig. 5.6 shows the simulated and observed wind speed and moisture at the UW mobile sounding site for 2100, 0000, and 0400 UTC, 13-14 December. Before the period of heavy frontal stratiform precipitation at 2100 UTC 13 December, the winds and

moisture profile were well simulated, but the WRF is slightly too dry above 3.5 km MSL. During the frontal passage period (around 0000 UTC), the model low level (2.5-4.5 km) winds are ~7 m s^{-1} too weak. There is also a positive (~10%) moisture error in the lower layer (below 4 km MSL) at this time. The agreement between model and observation is quite good in the post-frontal period (0400 UTC). These errors are similar to Garvert et al. (2005) using the MM5, so these WRF results can be compared.

d. Comparison of mesoscale features in IOP11

At 1800 UTC 13 December, a broad region of stratiform precipitation along the coast accompanied the mid-level trough (Fig. 5.7). Prefrontal showers are over the mountainous region at this time. The simulation reproduces the broad precipitation band along the coast to 35 dBZ as well as the prefrontal showers over the foothills of the Cascades (Fig. 5.7). At 0000 UTC 14 December, the frontal precipitation band was positioned over the S-Pol radar, with reflectivity values larger than 30 dBZ (Fig. 5.7). The simulation realistically captured the position and orientation of the frontal band, with a clear back edge off the coast. By 0400 UTC 14 December, the frontal band has passed the S-Pol site and there are post-frontal shower over the mountains. The simulation is 2-3 hours too fast with the frontal band already passed the Cascades.

e. Precipitation and microphysics comparison

THOM2 scheme produces two precipitation maxima over the coastal range and windward slopes of the Oregon Cascades (Fig. 5.8a). The SUNY scheme has ~20% more precipitation over the coastal range than the THOM2 (Fig. 5.8b). Over Cascades windward slopes, the SUNY scheme increases the precipitation over ridges and reduces the precipitation over the valleys by ~20%. SUNY scheme also reduces the precipitation spillover in the immediate lee of the Cascades by ~30%. Meanwhile, the LIN scheme in WRF increases the precipitation over the coastal range by ~50% and increases precipitation substantially over the Cascade windward slopes with much reduced precipitation in the lee. The difference between THOM1 and THOM2 is small with ~10% reduction for THOM1 mostly over the windward slopes of Cascades.

Verified with surface precipitation observations, SUNY scheme has a larger mean error (ME) over the coastal range and Cascades windward slope, with a 1.33-km domain mean ME of 0.46 cm and root mean square error (RMSE) of 1.14 cm, as compared to a ME of 0.36 cm and RMSE of 1.17 cm using THOM2 (Fig. 5.9). In contrast, the LIN scheme overpredicts across the coastal range and underpredicts in the lee, with the largest ME (0.62 cm) and RMSE (1.45 cm). THOM1 has similar bias score distribution as THOM2 with slightly lower ME (0.31 vs. 0.36 cm) and higher RMSE (1.24 vs. 1.17 cm). Overall, the SUNY scheme predicts surface precipitation comparable with the Thompson schemes.

For the microphysics verification aloft (Fig. 5.10), the SUNY scheme has more CLW (~0.2 to 0.4 g m^{-3}) over the windward slopes of Cascades, which verifies better with observations (0.2 to 0.26 g m^{-3}). However, all schemes underpredict the CLW over

the Cascade lee by ~0.1 g m^{-3}. The SUNY scheme predicts maximum ice water content (IWC) of ~0.7 g m^{-3} near 3.5 km MSL, compared with ~1.2 g m^{-3} by the Thompson schemes. As compared with the aircraft observations (Fig. 5.10), the SUNY scheme reduces the IWC overprediction aloft by ~50%.

Comparison of column integrated cloud liquid water depth (LWD) at Santium Junction (8 km west of the Cascades crest) indicates all the schemes could not represent the shallow liquid cloud well during the pre-frontal period (1400-2000 UTC 13 December) (Fig. 5.11). The SUNY scheme predicts the LWD well within 0.2 mm during the frontal passage period (2000 to 0200 UTC). While other schemes generally underpredict the LWD by ~50%. The fast reduction of LWD close to zero implies the model front passage is ~2 hours too fast.

Compared with observed *Ri* measured by P-3 (the ratio of graupel and total IWC), the new scheme predicts the observed *Ri* within 0.2 with very light riming in the lee and large riming over the windward slopes (Fig. 5.12).

5.5 Summary

A new approach for representing the ice microphysics considering both the ice habit and riming effect has been developed and tested. In contrast to traditional BMPs, the graupel category is included in the precipitation ice category by the introduction of a varying riming intensity. The new approach allows for physically-based representation of the ice particles with habit and riming intensity dependent properties, such as the mass, cross sectional area, and fall velocity relationships. Riming intensity is diagnosed from CLW and PI mass in the preliminary tests. The advantage of the new approach is the simplification of the scheme and thus the reduction in the computation time. It is also more physically-based considering the partially rimed particles and varying ice habits.

Preliminary tests of the new scheme suggest the proposed approach using a riming intensity (*Ri*) and continuous snow to graupel category is promising. For both IMPROVE-2 cases, precipitation and microphysics aloft using the new scheme are compared with observations and THOM2 scheme. The new scheme predicts slightly better surface precipitation amount and distribution, with less spillover into the immediate lee compared with observations. The new scheme reduces the IWC overprediction aloft significantly and verifies better with aircraft in situ measurements. It also increases the CLW prediction and compare better with observations than THOM2 scheme.

Appendix

The parameterization is modified based on Lin et al. (1983) and Rutledge and Hobbs (1984), with the snow being replaced by PI using the new A-D, m-D, and V-D relationships derived in Section 5.2, which will not be repeated here. We only present the parameterizations pertinent in this appendix. The P (kg kg^{-1} s^{-1}) represents the mass transformation rate.

a. Derivation of PI depositional growth

PI deposition and sublimation with the consideration of latent heat release due to concurrent riming growth can be derived as:

$$\frac{\partial m}{\partial t} = \frac{4\pi CFS_i}{g(t,p)} - \frac{L_s L_f}{KR_w T^2 g(t,p)}\left(\frac{\partial m}{\partial t}\right)_{rim} \tag{A5.1}$$

where C is capacitance, F is the ventilation factor, S_i is the supersaturation in respect to ice, L_s is the latent heat of sublimation and L_f is latent heat of fusion, R_w is gas constant for water vapor, and $g(t,p)$ is a thermodynamic quantity as defined in Rogers and Yau (1989).

F is generally given, for example, by Thorpe and Mason (1966):

$$F = 0.65 + 0.44 S_c^{1/3} (\mathrm{Re})^{0.5} \tag{A5.2}$$

where Sc is the Schmidt number, equal to 0.6, Re is the Reynolds number defined before, and ν is kinematic viscosity of the air. The rate equation is integrated over the PI size spectrum and we get:

$$P_{sdep} = \frac{4\pi CN_{0s}S_i}{g(t,p)}\left(\frac{0.65\Gamma(2+\mu)}{\lambda^{2+\mu}} + 0.44 S_c \left(\frac{a_v}{\nu}\right)^{1/2}\left(\frac{\rho_0}{\rho}\right)^{1/4}\frac{\Gamma(2.5+0.5b_v+\mu)}{\lambda^{2.5+0.5b_v+\mu}}\right) - \frac{L_s L_f a_a E N_{0s} q_s}{KR_w T^2 g(t,p)}\left(\frac{\rho_0}{\rho}\right)^{1/2}\frac{\Gamma(1+b_a+b_v+\mu)}{\lambda^{1+b_a+b_v+\mu}} \tag{A5.3}$$

b. Autoconversion

Different Kessler-type parameterizations were compared and a new parameterization of autoconversion was derived in Liu and Daum (2004). The new parameterization is:

$$P_{wau} = \left(\frac{3\rho}{4\pi\rho_w}\right)^2 \kappa_2 \beta_6^6 N^{-1} q_c^{\ 3} H(R_6 - R_{6c}) \tag{A5.4}$$

$$\beta_6^{\ 6} = \frac{(1+3\varepsilon^2)(1+4\varepsilon^2)\left(1+5\varepsilon^2\right)}{(1+\varepsilon^2)\left(1+2\varepsilon^2\right)} \tag{A5.5}$$

$$R_{6c} = \beta_6 R_{3c}, R_6 = \beta_6 R_3 \tag{A5.6}$$

where the coefficient $\kappa_2 \approx 1.9 \times 10^{11}$ is in $\mathrm{cm}^{-3}\ \mathrm{s}^{-1}$, N is the cloud droplet number concentration, ε is the relative dispersion, and H is the Heaviside function to consider the threshold process such that the autoconversion rate is negligible small when $R_6 < R_{6c}$. R_3 is the mean volume radius and R_{3c} is the threshold mean volume radius (generally set to 10 microns).

c. Coefficients in the A-D and m-D relationships

$c_0 = 0.004$, $c_1 = 6e5$, $c_2 = 0.16$
$C_0 = 1.85$, $C_1 = 0.003$, $C_2 = 1.15$
$d_0 = 1.28$, $d_1 = -0.012$, $d_2 = -0.6$
$D_0 = 1.70$, $D_1 = -0.0075$, $D_2 = 0.3$

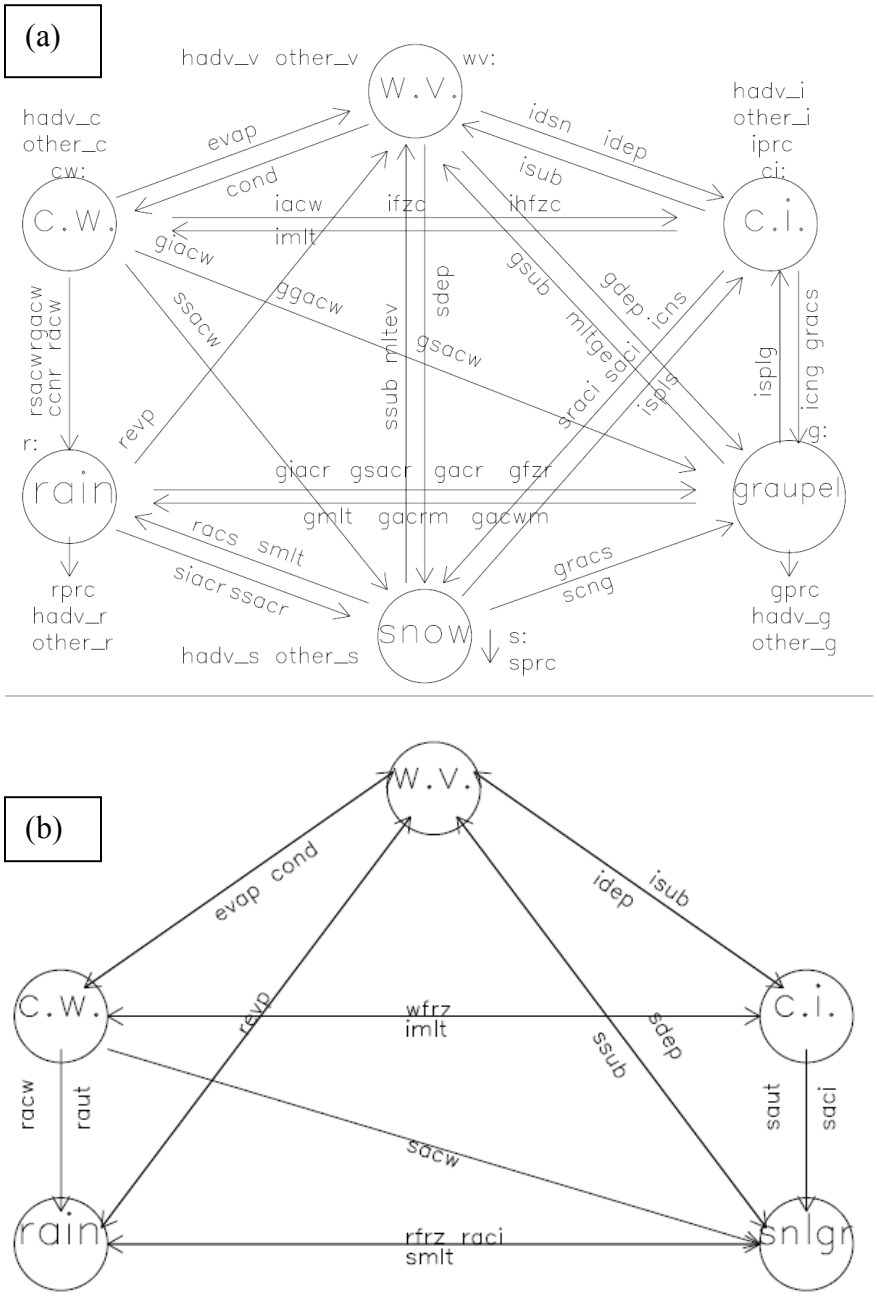

Figure 5.1 (a) Microphysical flowchart for the Thompson scheme. The circles represent the various water species (water vapor, cloud water, cloud ice, rain, snow, and graupel), and the arrows are the processes that link the species (see the appendix for the list of processes). (b) Same as (a), but for the new scheme.

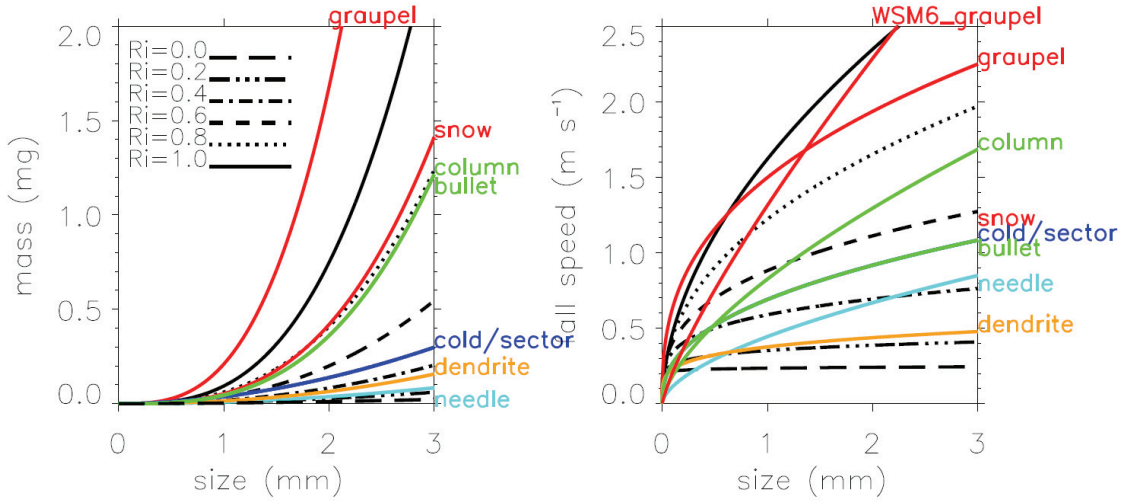

Fig. 5.2 m-D and V-D relationships (color lines) used in the Thompson et al. (2004) and for different types of ice particle from Locatelli and Hobbs (1974) as summarized in Woods et al. (2007). Temperature and riming intensity dependent m-D and V-D relationships used in the new scheme are in black line.

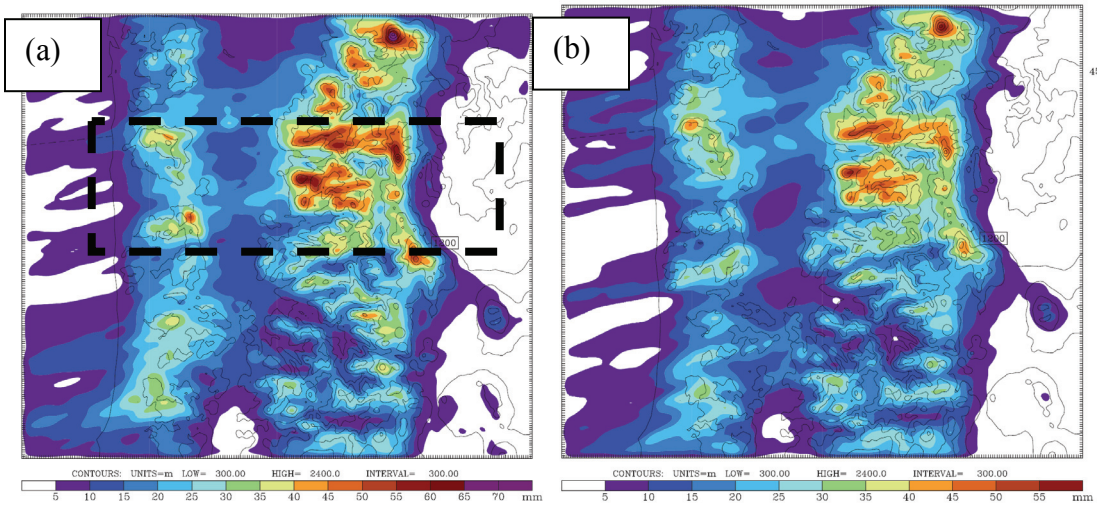

Figure 5.3 Storm 12-hour precipitation (color shaded every 5 mm) for the 1.33-km domain between 2000 UTC 4 Dec and 0800 UTC 5 Dec 2001 and 1.33-km terrain is contoured for reference for (a) SUNY and (b) THOM2 scheme.

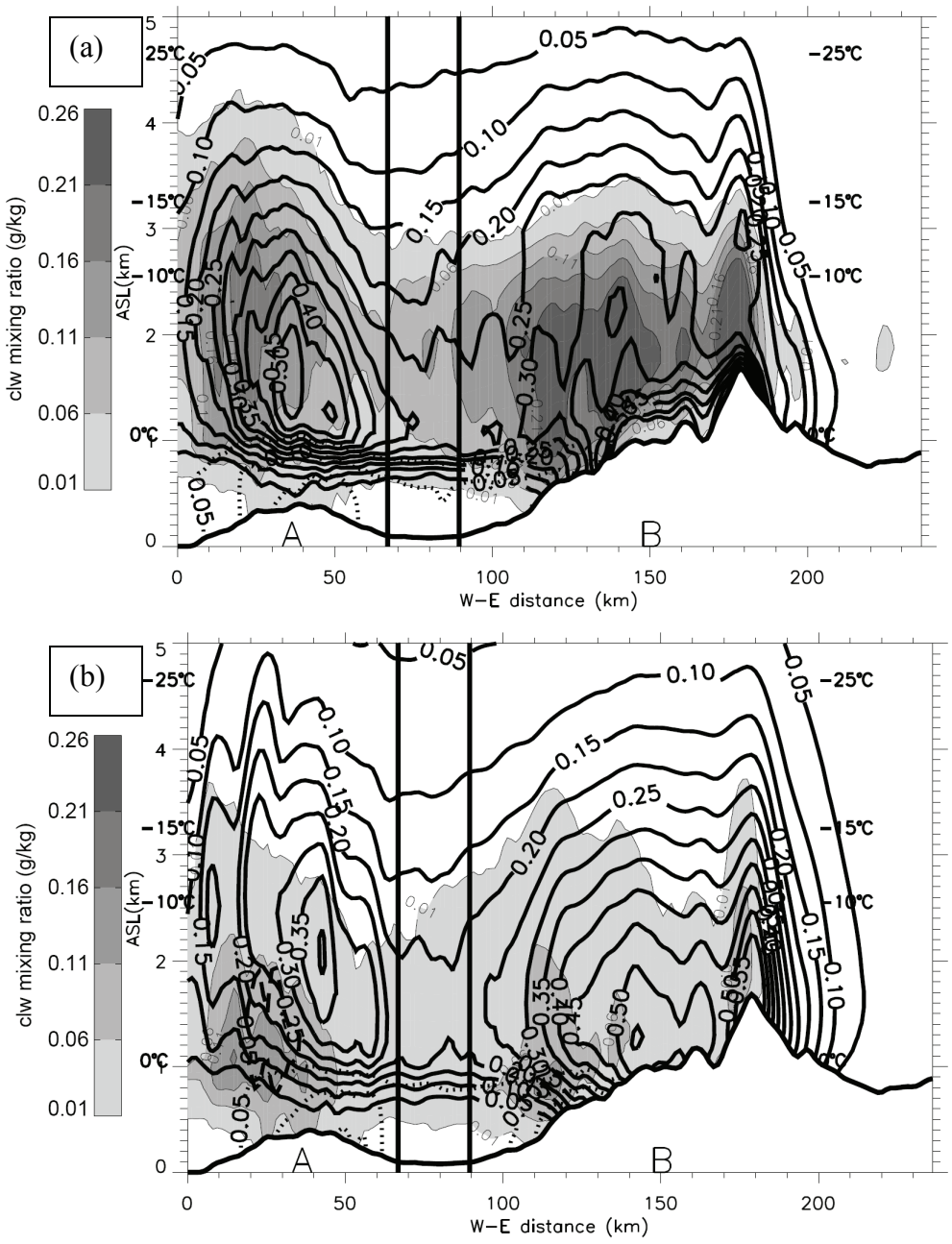

Figure 5.4 Meridionally-averaged west-east cross section over the box in Fig. 5.3 shows the mass concentration of mode CLW (shaded every 0.05 g m^{-3}), IWC (black solid, every 0.05 g m^{-3}), and rain (black dotted, every 0.05 g m^{-3}) for the (a) SUNY, and (b) THOM2 scheme. Model fields were averaged from 2300 to 0200 UTC 4-5 Dec 2001 (forecast hours 11-14) using model outputs at 15-min intervals.

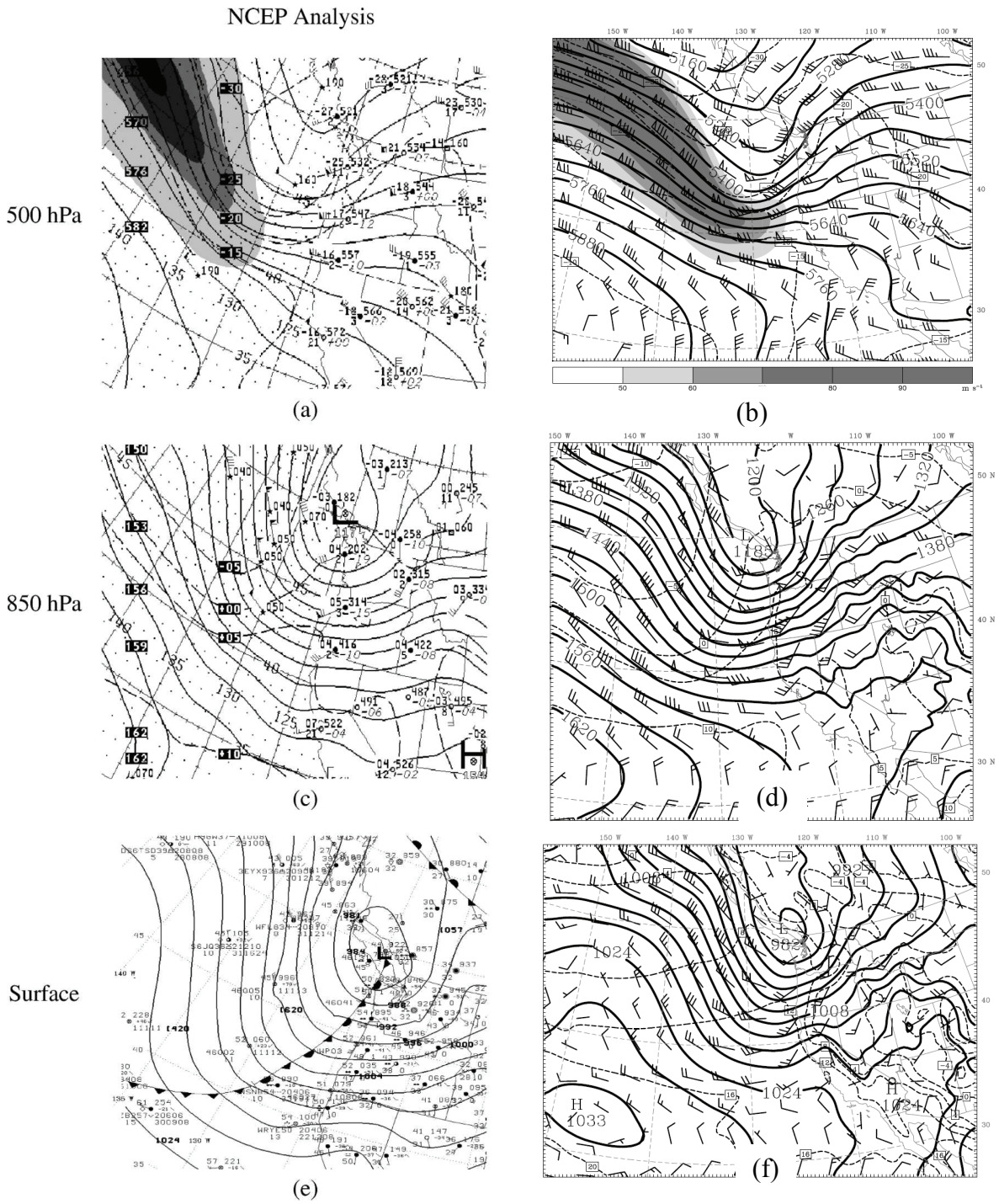

Figure 5.5 (a) NCEP 500-hPa analysis with 300-hPa winds greater than 110 kt shaded at intervals of 20 kt, (b) WRF 24-h 500-hPa forecast with 300-hPa winds shaded every 10 m s^{-1}, (c) NCEP 850-hPa analysis, (d) WRF 24-h 850-hPa forecast, (e) NCEP sea level pressure analysis, and (f) WRF 24-h forecast of sea level pressure. All for 0000 UTC 14 Dec 2001.

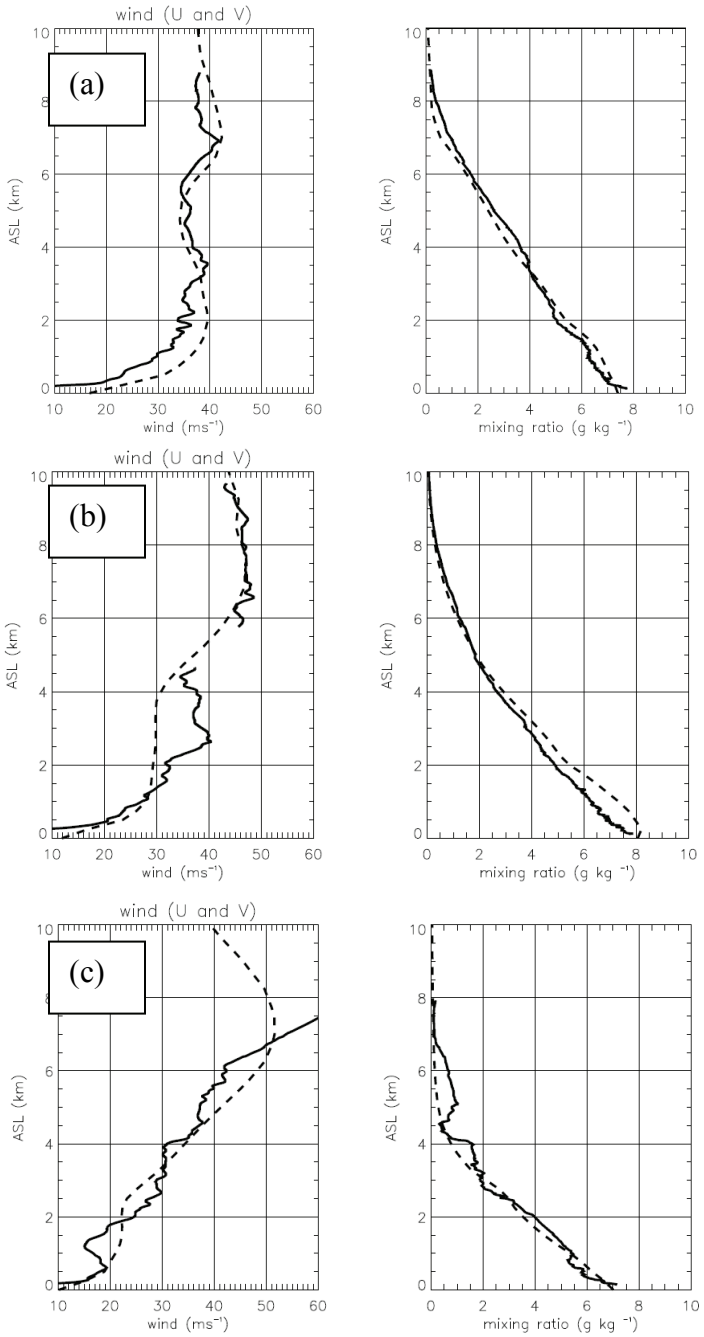

Figure 5.6 Model (dashed) and observed (solid) profiles of wind speeds (left panels) and water vapor mixing ratios (right panels) at UW at (a) 2100 UTC, (b) 0000 UTC, and (c) 0400 UTC, 13-14 December 2001.

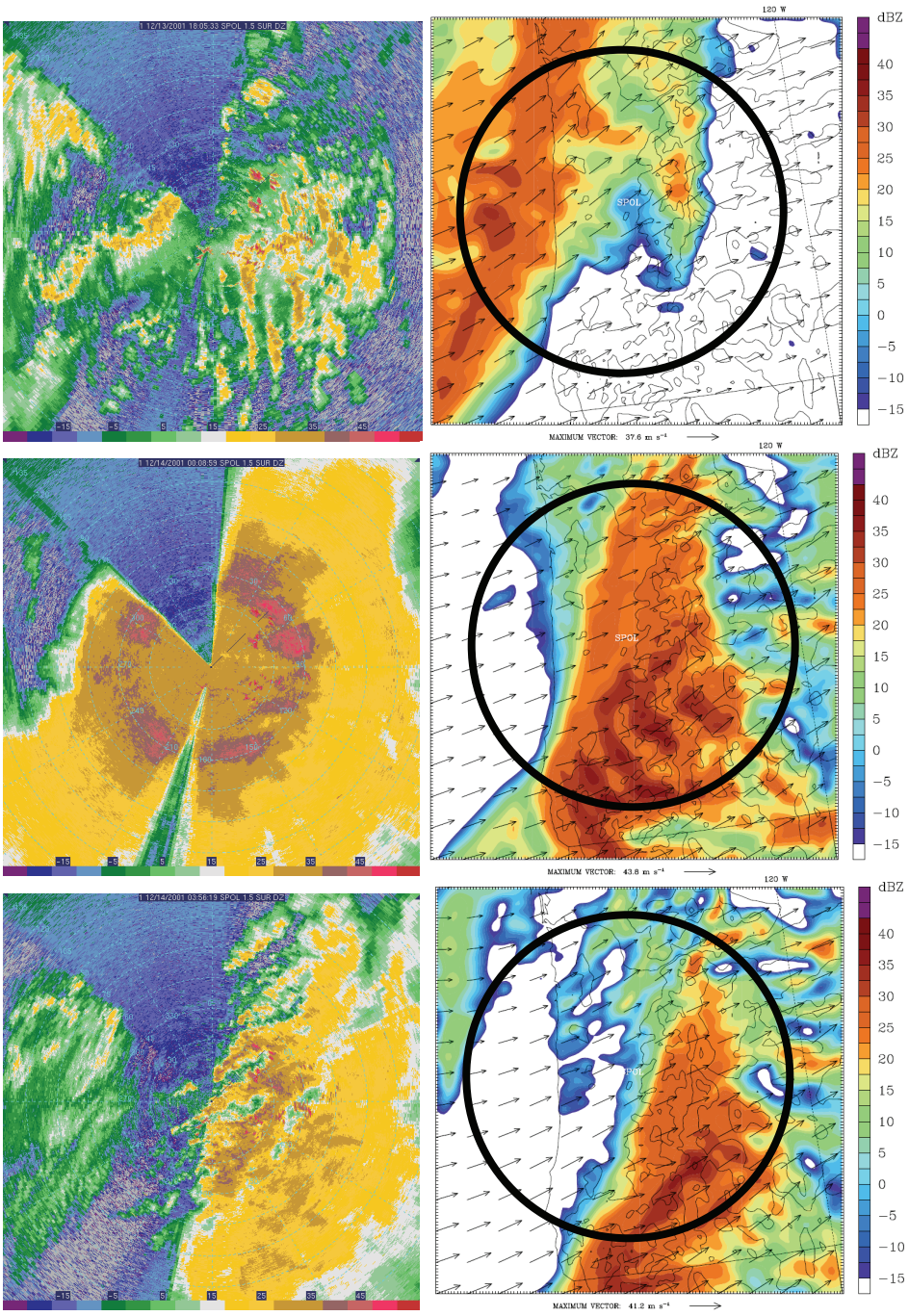

Figure 5.7 Reflectivity from the NCAR S-Pol radar (1.5º PPI, left panels), and the equivalent reflectivity from 4-km simulation (700 hPa, right panels) at 13 December 1800 UTC (top), 14 December 0000 UTC (middle), and 14 December 0400 UTC (bottom, 0200 UTC from model). Black circles in the right panel indicate the 150 km range from the S-Pol.

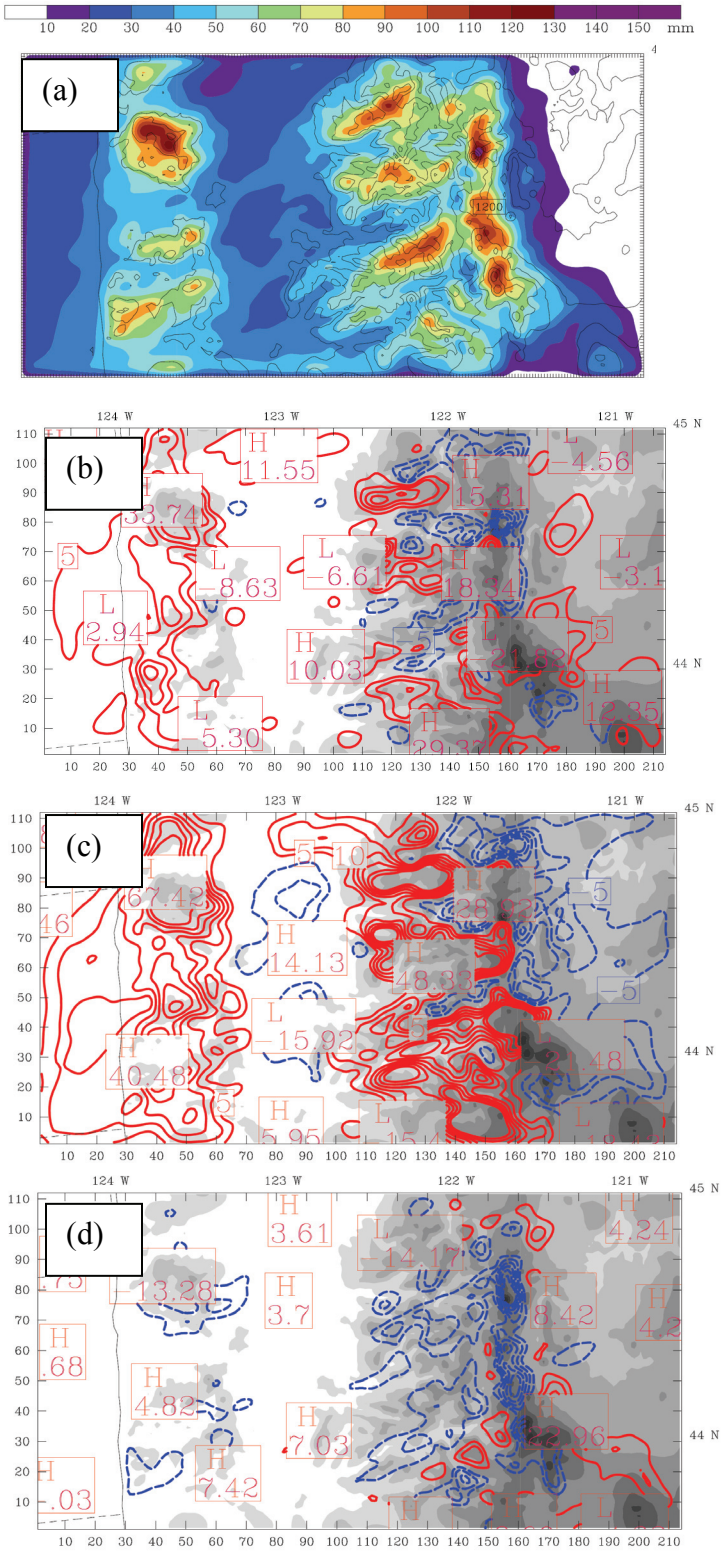
10 20 30 40 50 60 70 80 90 100 110 120 130 140 150 mm
(a)
1200
(b)
124 W
123 W
122 W
121 W
45 N
44 N
H 11.55
L −4.56
H 15.31
L −6.61
H 18.34
L −3.1
L −8.63
L 2.94
H 10.03
L −5.30
H 12.35
(c)
H 14.13
L −15.92
H 40.48
(d)
H 3.61
H 4.24
H 13.28
H 3.7
H 8.42
H 4.82
H 7.03
H 7.42

Figure 5.8 (a) Storm 18-hour precipitation (color shaded every 10 mm) for the 1.33-km WRF simulation using THOM2 scheme between 1400 UTC 13 Dec and 0800 UTC 14 Dec 2001 and 1.33-km terrain is contoured for reference. Surface precipitation difference (in mm) between the THOM2 (solid red lines indicate larger and dashed blue lines indicate smaller precipitation than THOM2) and (b) SUNY, (c) LIN, and (d) THOM1 scheme for the 1.33-km domain between 1400 UTC 13 Dec and 0800 UTC 14 Dec. The 1.33-km terrain is shaded every 300m for reference.

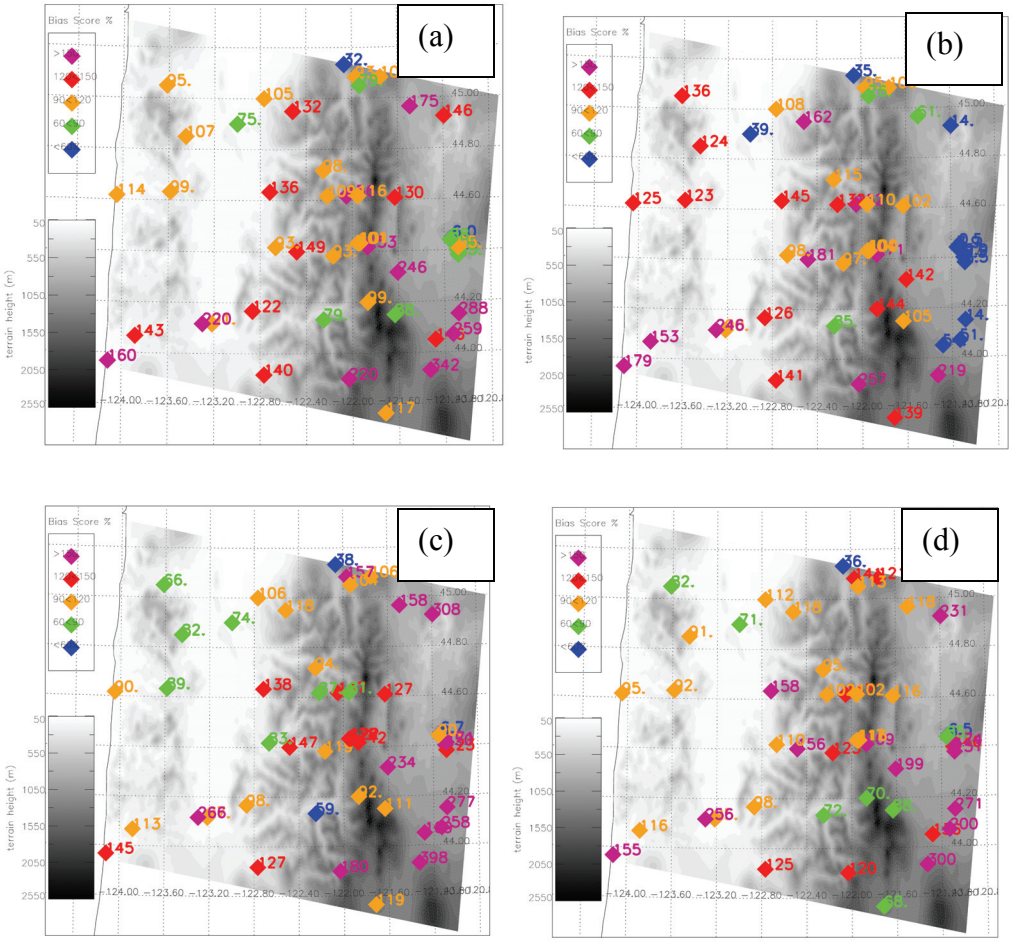

Figure 5.9 Percent of observed precipitation from the 1.33-km WRF at the preciitation gauge sites between 1400 UTC 13 Dec and 0800 UTC 14 Dec for the (a) SUNY, (b) LIN, (c) THOM1, and (d) THOM2 schemes.

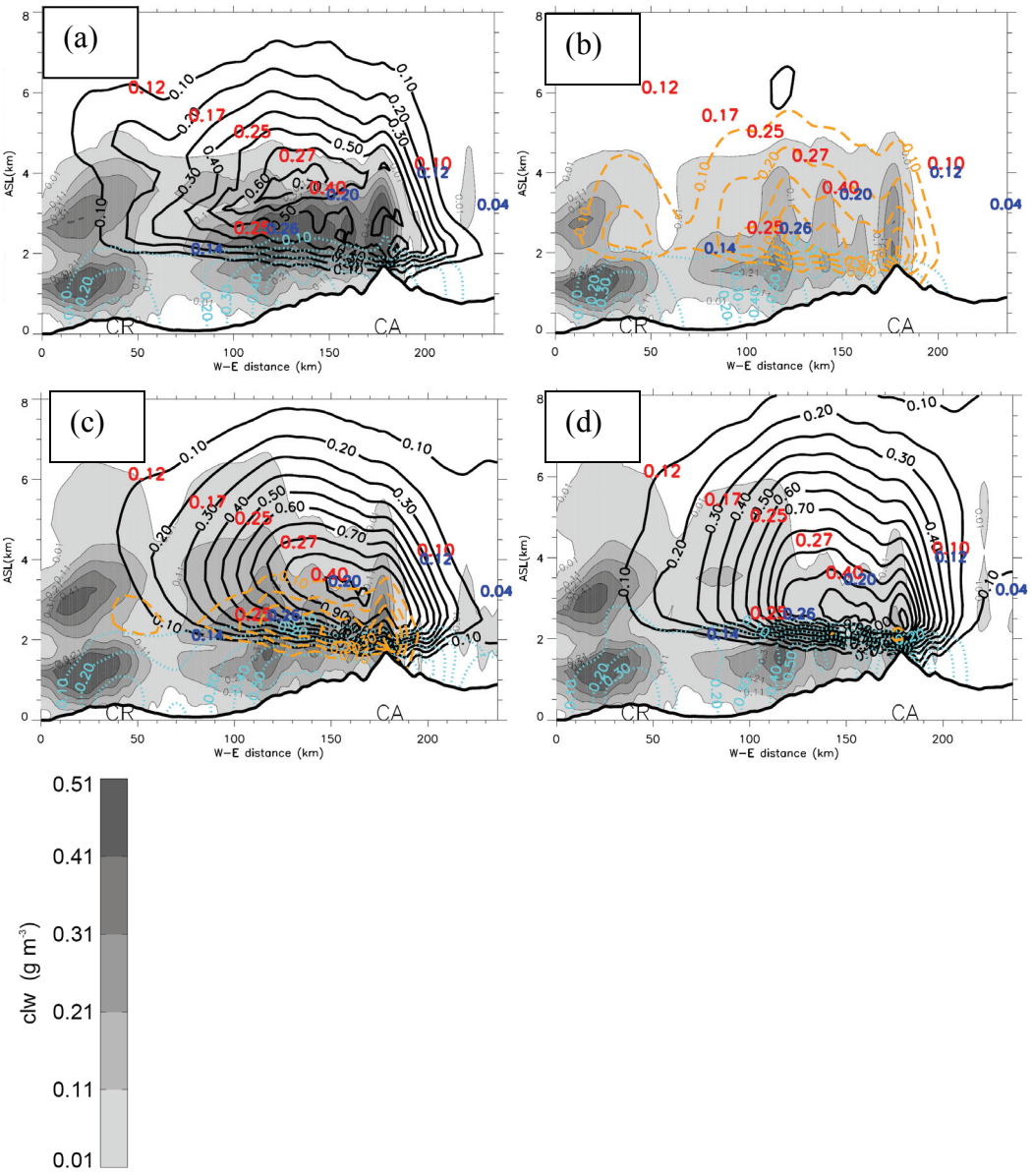

Figure 5.10 Meridionally-averaged west-east cross section over the box in Fig. 5.3 shows the mass concentration of mode CLW (shaded every 0.1 g m^{-3}), snow (black solid, every 0.1 g m^{-3}), graupel (orange dashed, every 0.1 g m^{-3}) and rain (green dotted, every 0.1 g m^{-3}) for the (a) SUNY, and (b) LIN scheme, (c) THOM1, and (d) THOM2 scheme. Model fields were averaged from 2300 to 0100 UTC 13-14 Dec 2001 (forecast hours 23-25) using model outputs at 15-min intervals. Overlaid numbers are leg averaged IWC (red) and CLW (blue) from P-3 and Convair aircraft.

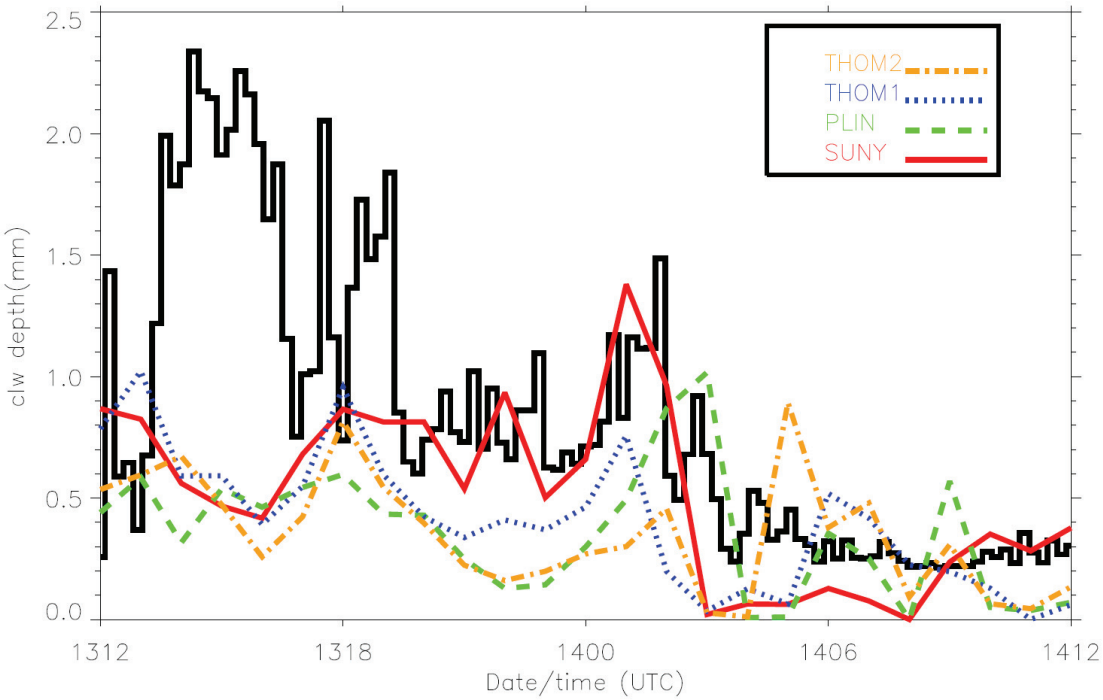

Figure 5.11 Vertically-integrated liquid water path (LWD) measured by the microwave radiometer at Santium Junction (SJ in Fig. 3.1b) and from the four 1.33-km microphysical simulations from 1200 UTC 13 Dec to 1200 UTC 14 Dec 2001.

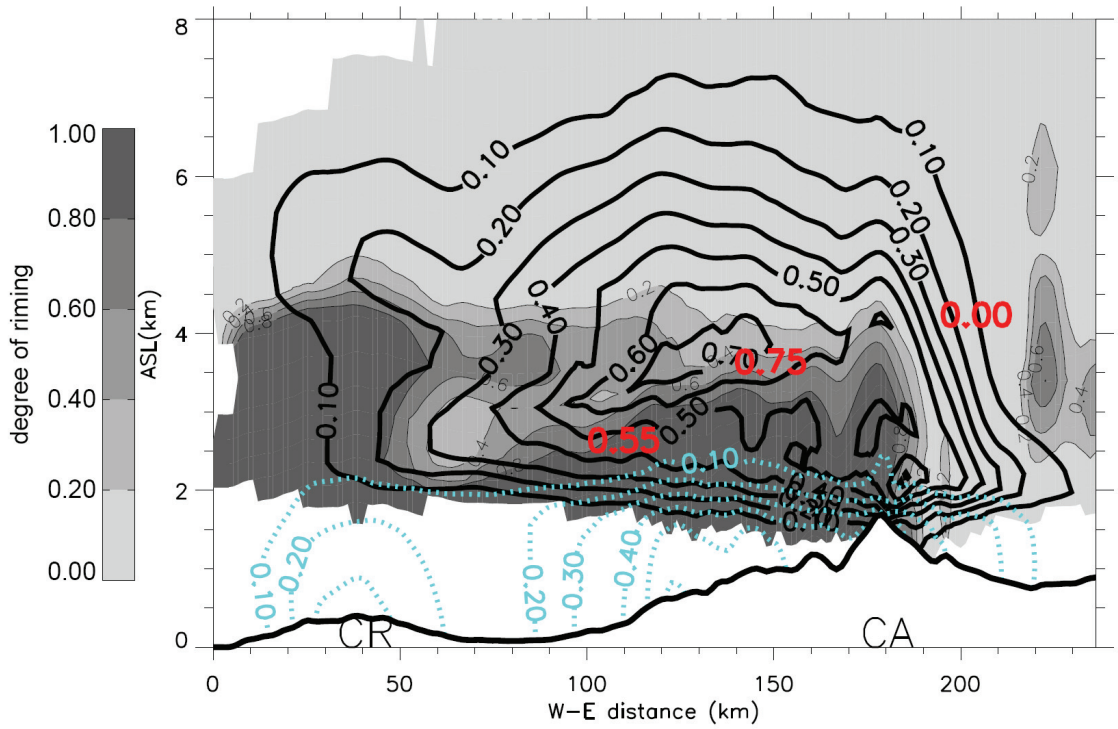

Figure 5.12 Same as Fig. 5.10, except shows the riming intensity (*Ri,* shaded every 0.2). Red numbers are the ratios between leg-averaged graupel mass concentration and IWC measured by the P-3.

Chapter 6
Summary and Future Work

6.1 Summary

This study presents a comprehensive investigation of numerical simulations of orographic precipitation and microphysics over the Pacific Northwest. Using observations from the IMPROVE-2 field experiment, the Weather Research and Forecasting (WRF) simulations of a moderate orographic precipitation case are verified. Several BMPs in WRF were compared and evaluated. To put these IMPROVE results in perspective with a full range of observed storm types, two cool seasons of MM5 simulations over the Pacific Northwest were conducted and evaluated using available observations, including a WSR-88D radar upstream of the Cascade Mountains. A new BMP considering both the ice habits and riming intensity is proposed to improve some of the deficiencies in traditional BMPs. The new BMP is tested using two IMPROVE-2 cases. Results from this study are briefly summarized in the following.

a. IMPROVE-2 IOP6

Chapter 2 describes the kinematic and precipitation evolution of a notably cold, unstable trough on 4-5 December 2001 during the second Improvement of Microphysical Parameterization through Observational Verification Experiment (IMPROVE-2) field project using the comprehensive observations and model simulations. The event features embedded convective cells propagating from the waters over the coastal range and intensifying due to the potential instability release and terrain lifting. These cells weaken slightly over the lee of coastal range and intensify and spread out over the wider and higher Cascades. Several sensitivity tests suggest both the frictional convergence and terrain lifting contribute to the comparable precipitation over the coastal range and Cascades. Due to the convective nature and moderate cross barrier flow, the small ridges over the windward slopes of the Cascades only contribute slightly (~2%) to the precipitation enhancement. No widespread overprediction of surface precipitation is found for the simulation as compared with the 13-14 case.

Using a variety of cloud and precipitation observations, four BMPs with graupel in WRF were compared and evaluated in Chapter 3. Radar and aircraft measurements emphasize the large variation of microphysics between the convective cells and the surrounding stratiform clouds. Large difference of surface precipitation and microphysics aloft are found among these schemes. More localized precipitation (precipitation bull

eyes) in the WSM6 and PLIN scheme is due to the dominance of graupel and overestimated fall velocity. In contrast, the two Thompson schemes are dominated by snow, which fall much slower than graupel. Sensitivity tests indicate the aggressive snow accretion of graupel in the WSM6 and PLIN scheme is the main reason for the graupel dominance. Large sensitivity of snow mass diameter relationship on surface precipitation and microphysics is found for these BMPs and indicates the importance of snow properties. A run with reduced snow depositional and sublimation growth reduces the snow aloft by 30%, however, CLW and graupel increase and compensate the snow reduction. A bulk box water budget proves that the positive definite advection method conserves water mass better and reduces the surface precipitation by 20-30%.

b. Evaluation of two cool seasons QPF

To investigate the systematic errors of BMPs and model QPF performance, two cool seasons (2005/06 and 2006/07 season) high-resolution MM5 simulations over the Pacific Northwest were evaluated. Though 1.33-km MM5 simulates the seasonal precipitation well with 90-130% bias score over most of the rain gauge sites, there are large variations of MM5 QPF performance from event to event. 4-km MM5 underpredicts the precipitation over the coastal range by ~20-30% with slightly overprediction over the Cascades windward slopes and crest.

High correlation between the upstream moisture flux and precipitation is found for both the MM5 simulations and observations. Model has a tendency to overpredict the low layer moisture flux (~8%) at Salem (in the lee of coastal range and upstream of the OR Cascades) due to the overestimated winds and moisture in the low layer (< 2 km MSL). While at Quillayute (UIL, at the coast of WA), the model moisture flux error is only ~ 3%. Larger moisture flux error in the lee of the coastal range than over the coast probably results from the model's precipitation underprediction over the coastal range. Less moisture depletion over the coastal range leaves more moisture left in the downstream. Overestimation of moisture flux at SLE and UIL at the model initial time (forecast hour 0) is negligible, which suggests the moisture flux error is generated during the model integration and is not a model initialization problem. This overestimated moisture flux contributes partly to the precipitation overprediction. However, the cause of the model moisture flux error is still under investigation.

Composite analyses indicate the model tends to overpredict the surface precipitation for the low freezing level storms MM5 also tends to overpredict storms with light precipitation. IWC above the freezing level of the low freezing level storms is ~ 2 times as that of high freezing level storms. In contrast, there is no obvious difference of the radar reflectivity between the two types of storms. This suggests the connection between the surface precipitation overprediction and ice microphysics errors aloft.

c. A new BMP

The case study and seasonal evaluation both suggest potential ice microphysics errors in model BMPs. Due to the complexity of ice microphysics in reality, BMPs have large uncertainty in parameterizing the ice microphysical processes. Conventional BMPs generally use two separating categories (snow and graupel) and could not represent the large variability of ice particles associated with different habits and degree of riming. A new approach considering both the ice habit and riming effect has been developed. In contrast to traditional BMPs, the graupel category is included in a precipitation ice category by the introduction of a varying riming intensity. Instead of using a fixed m-D or V-D relationship for the snow or graupel, the new approach use a temperature and riming intensity dependent m-D and V-D relationship. By doing so, both the habit and riming effect are considered and allow for more physically-based representation of the ice particles.

Preliminary tests of the new scheme using a diagnosed riming intensity suggest some promising results. The comparison with observations and other BMPs shows that the new scheme reduces the snow overprediction aloft and increases the CLW prediction. Both of these compared better with observations than other schemes. The surface precipitation prediction of the new scheme is comparable with more complex Thompson scheme. These preliminary tests suggest the proposed approach is on the right direction to improve ice microphysical parameterizations.

6.2 Future work

Based on the results of the thesis, the following future work is suggested:

(1) Further quantification of the upstream moisture effect on model precipitation forecast

Moisture flux provides the water source for the orographic precipitation. However, the sensitivity of model QPF on upstream moisture and moisture flux has not been investigated. An idealized WRF 2D mountain wave simulation with varying upstream moisture flux (varying mixing ratio and winds) can be used to determine the precipitation sensitivity on the upstream moisture flux. The work can be extended to a real case. WRF sensitivity simulations with varying upstream moisture perturbations are needed to investigate the corresponding change of microphysics aloft and surface precipitation. The study will quantify the moisture flux error effect and sensitivity on the microphysics and precipitation forecast.

(2) Freezing level height and the precipitation over coastal range and the Cascades

It is interesting that the moderate coastal range receives comparable precipitation as the much higher and wider Cascades climatologically. Additional work is needed to understand and determine the optimal environmental conditions for the coastal range to get larger or comparable precipitation as the Cascades. Idealized simulations with two mountain ranges to approximate the coastal range and Cascades can be conducted with varying freezing level height. The setup could evaluate the spillover problem and relate to the deficiencies in BMPs.

(3) IWC retrieval from WSR-88D radar and comparison with model IWC

Some good retrievals of ice water content (IWC) from the WSR-88D radar reflectivity are needed to evaluate the model ice mass prediction aloft and relate with the surface precipitation prediction. IWC retrieval from radar reflectivity has received attention recently (Liu and Illingworth 2000; Hogan et al. 2006; Protat et al. 2007; Heymsfield et al. 2008). Using a large mid-latitude aircraft datasets, Hogan et al. (2005) derived the IWC retrieval from the radar reflectivity factor and temperature. However, the retrieval gives poor estimate of IWC in mixed-phase conditions due to the riming effect on the particle density. The retrieval has been applied to the Portland WSR-88D radar and the retrieved IWC has been compared with MM5 predicted IWC. Preliminary comparison indicates MM5 generally underpredicts the IWC, especially at colder temperatures. Future work will incorporate the riming effect to improve the accuracy of retrieval in mixed-phase conditions. In addition, the uncertainty of the retrieval can be better quantified using direct measurements of IWC from a counterflow virtual impactor (CVI) probe (Twohy et al. 1997).

P3 measured the reflectivities and ice microphysics simultaneously during the IMPROVE. These datasets provide the opportunity to develop an IWC retrieval considering the riming effect since CLW is also measured along the flight track. The new derived IWC retrieval will be applied to WSR-88D radar and the retrieved IWC can be compared with MM5 IWC. By doing so, the connection between the ice mass aloft and the surface precipitation can be better quantified. The model tendency of overprediction under low freezing level conditions should be investigated and related to the ice mass prediction aloft. Future study can also focus on the precipitation rate, which is a combination of ice mass aloft and ice fall velocity.

(4) Further development of the new scheme and long-term evaluation

Future work will use more observations to better quantify *Ri* and its effect on the ice particle properties (mass, fall velocity, area). For example, a vertical pointing Doppler radar can be used to get the Doppler spectrum and the detection of graupel (Zawadzki et al. 2001). *In situ* measurements of CLW and ice particles will be collected by an aircraft flying a downward spiral over the vertical pointing radar site. The degree of riming determined by analysis of the ice images will be checked with the Doppler radar analysis. With CLW, IWC, and *Ri* known, an empirical relation for Ri can be derived and applied in the scheme

Other approaches to determine *Ri* will be tested in the new scheme. One approach is to follow the Eta Grid-scale cloud and precipitation (2001) scheme (EGCP01, Ferrier et al. 2002), which diagnoses the rimed mass fraction based on the PI mass from the riming growth and the total PI mass and saves it as a temporary array. *Ri* can also be prognosed directly from the rimed mass and total ice mass in the scheme. Another approach similar to Morrison and Grabowski (2008) without prognosing the ice mixing ratios acquired through riming and deposition separately will be also tested.

Due to the conventional Eulerian framework of the numerical models, the life history of the particles is lost during the model integration. A “property tracking” method can be developed to track the life history or the memory of the ice particles. The method

could eliminate the transition of ice particle properties as it falling through different environmental conditions.

To be used for convective storms and winter icing events, a switch will be added in the scheme to represent hail and sleet instead of graupel. New prognostic variables can also be added in the scheme to represent freezing rain or sleet to better simulate winter storms in terms of the precipitation types on the surface. A consistent cloud radiation package could be developed using the ice properties (cross section area) directly from the scheme.

The further developed and refined new scheme needs to be evaluated using more simulations. A new seasonal evaluation over the Pacific Northwest will be set up using WRF with the new scheme to evaluate its long-term performance.

References

Abraham, F. F., 1970: Functional dependence of drag coefficient of a sphere on Reynolds number. *Phys. Fluids*, **13**, 2194-2195.

Asencio, N., J. Stein, M. Chong, and F. Gheusi, 2003: Analysis and simulation of local and regional conditions for the rainfall over the Lago Maggiore Target Area during MAP IOP2b. *Quart. Roy. Meteor. Soc.*, **129**, 565–586.

Baker B., and R. P. Lawson, 2006: Improvement in determination of ice water content from two-dimensional particle imagery. Part I: Image-to-mass relationships. *J. Appl. Meteor. Climatol.*, **45**, 1282–1290.

Barstad, I., and R. B., Smith, 2005: Evaluation of an orographic precipitation model. *J. Hydrometeor.*, **6**, 85-99.

Baschek, B, R. Schefold, and E. Barthazy, 2004: How do updrafts and embedded convection influence riming. Proceeding of ERAD (2004): 261-267.

Baschek, B, and R. Schefold, 2006: Fall velocity of snowflakes of different riming degree and crystal types. *Atmos. Research*, **82**, 391-398.

Baumgardner D., 1983: An analysis and comparison of five water droplet measuring instruments. *J. Climate Appl. Meteor.*, **22**, 891–910.

Benoit, R., M. Desgagne, P. Pellerin, S. Pellerin, Y. Chartier, and S. Desjardins, 1997: The Canadian MC2: A semi-Lagrangian, semi-implicit wideband atmospheric model suited for finescale process studies and simulation. *Mon. Wea. Rev.,* **125**, 2382–2415.

Berry, E. X., 1968: Modification of the warm rain process. Proc. First Conf. on Weather Modification, Albany, NY, Amer. Meteor. Soc., 81–88.

Berry, E. X., and R. L. Reinhardt, 1974: An analysis of cloud drop growth by collection. Part IV: A new parameterization. *J. Atmos. Sci*., **31**, 2127–2135.

Bohm H., 1989: A general equation for the terminal fall speed of solid hydrometeors. *J. Atmos. Sci.*, **46**, 2419–2427.

Bougeault P., Coauthors, 2001: The MAP Special Observing Period. *Bull. Amer. Meteor. Soc*., **82**, 433–462.

Bousquet O., and B. F. Smull, 2003a: Airflow and precipitation fields within deep Alpine valleys observed by airborne Doppler radar. *J. Appl. Meteor.*, **42**, 1497–1513.

Bousquet O., and B. F. Smull, 2003b: Observations and impacts of upstream blocking during a widespread orographic precipitation event. *Quart. J. Roy. Meteor. Soc.*, **129**, 391–409.

Braun, S. A., R. Rotunno, J. B. Klemp, 1999: Effects of coastal orography on landfalling cold fronts. Part II: Effects of surface friction. *J. Atmos. Sci.*, **56**, 3366-3384.

Braun, S.A., 2006: High-Resolution Simulation of Hurricane Bonnie (1998). Part II: Water Budget. *J. Atmos. Sci.*, **63**, 43–64.

Brown, P. R. A., and H. A. Swann, 1997: Evaluation of key microphysical parameters in three-dimensional cloud-model simulation using aircraft and multiparameter radar data. *Quart. J. Roy. Meteor. Soc.*, **123**, 2245–2275.

Browning, K. A., F. F. Hill, and C. W. Pardoe, 1974: Structure and mechanism of precipitation and the effect of orography in a wintertime warm sector. *Quart. J. Roy. Meteor. Soc.,* **100**, 309-330.

Bruintjes, R. T., T. L. Clark, and W. D. Hall, 1994: Interactions between topographic airflow and cloud/precipitation development during the passage of a winter storm in Arizona. *J. Atmos. Sci.,* **51**, 48–67.

Chen S.-H., and W.-Y. Sun, 2002: A one-dimensional time dependent cloud model. *J. Meteor. Soc. Japan*, **80**, 99–118.

Colle, B. A., K. J. Westrick, and C. F. Mass, 1999: Evaluation of the MM5 and Eta-10 precipitation forecasts over the Pacific Northwest during the cool season. *Wea. Forecasting.,* **14**, 137–154.

Colle, B. A., C. F. Mass, and K. J. Westrick, 2000: MM5 precipitation verification over the Pacific Northwest during the 1997–1999 cool seasons. *Wea. Forecasting.*, **15**, 730–744.

Colle B. A., and C. F. Mass, 2000: The 5–9 February 1996 flooding event over the Pacific Northwest: Sensitivity studies and evaluation of the MM5 precipitation forecasts. *Mon. Wea. Rev*., **128**, 593–617.

Colle, B. A., 2004: Sensitivity of orographic precipitation to changing ambient conditions and terrain geometries: An idealized modeling perspective. *J. Atmos. Sci.,* **61**, 588–606.

Colle, B. A., and Y. Zeng, 2004: Bulk microphysical sensitivities and pathways within the MM5 for orographic precipitation. Part II: Impact of different bulk schemes, barrier width, and freezing level. *Mon. Wea. Rev.,* **132**, 2802–2815.

Colle B., M. Garvert, J. B. Wolfe, C. F. Mass, and C. P. Woods, 2005a: The 13–14 December 2001 IMPROVE-2 event. Part III: Simulated microphysical budgets and sensitivity studies. *J. Atmos. Sci.*, **62**, 3535–3558.

Colle B. A., J. B. Wolfe, W. J. Steenburgh, D. E. Kingsmill, J. A. W. Cox, and J. C. Shafer, 2005b: High-resolution simulations and microphysical validation of an orographic precipitation event over the Wasatch Mountains during IPEX IOP3. *Mon. Wea. Rev.*, **133**, 2947–2971.

Colle B.A., and S. E., Yuter, 2007: The impact of coastal boundaries and small hills on the precipitation distribution across southern Connecticut and Long Island, New York. *Mon. Wea. Rev.,* **135**, 933-954.

Colle, B. A., 2008: Two-dimensional idealized simulations of the impact of multiple windward ridges on orographic precipitation. *J. Atmos. Sci.,* in press.

Colle, B. A., Y. Lin, S. Medina, and B. Smull, 2008: Orographic modification of convection and flow kinematics by the Oregon coastal range and Cascades during IMPROVE-2. *Mon. Wea. Rev.,* in press.

Cooper W. A., 1986: Ice initiation in natural clouds. *Precipitation Enhancement—A Scientific Challenge, Meteor. Monogr.,* No. 43, Amer. Meteor. Soc., 29–32.

Cotton, W. R., and R. A. Anthes, 1989: *Storm and Cloud Dynamics.* 1st ed. Academic Press, 883 pp.

Cox, J.A.W., W.J. Steenburgh, D.E. Kingsmill, J.C. Shafer, B.A. Colle, O. Bousquet, B.F. Smull, and H. Cai, 2005: The Kinematic Structure of a Wasatch Mountain Winter Storm during IPEX IOP3. *Mon. Wea. Rev.*, **133**, 521–542.

Cressman G. P., 1959: An operational objective analysis system. *Mon. Wea. Rev.*, **87**, 367–374.

Cullen, M. J. P., 1993: The unified forecast/climate model. *Meteor. Mag.,* **122,** 81–94.

Doyle J. D., and N. A. Bond, 2001: Research aircraft observations and numerical simulations of a warm front approaching Vancouver Island. *Mon. Wea. Rev.*, **129**, 978–998.

Dudhia J., 1989: Numerical study of convection observed during the winter monsoon experiment using a mesoscale two-dimensional model. *J. Atmos. Sci.*, **46**, 3077–3107.

Durran, D. and J. Klemp, 1982: On the effects of moisture on the Brunt-Väisälä frequency. *J. Atmos. Sci.*, **39**, 2152–2158.

Ebert E. E., U. Damrath, W. Wergen, and M. E. Baldwin, 2003: The WGNE assessment of short-term quantitative precipitation forecasts (QPFs) from operational numerical weather prediction models. *Bull. Amer. Meteor. Soc.*, **84**, 481–492.

Falvey M., and J. Beavan, 2002: The impact of GPS precipitable water assimilation on mesoscale model retrievals of orographic rainfall during SALPEX'96. *Mon. Wea. Rev.*, **130**, 2874–2888.

Falvey, M., and R. Garreaud, 2007: Wintertime Precipitation Episodes in Central Chile: Associated Meteorological Conditions and Orographic Influences. *J. Hydrometeorol.*, **8**, 171–193.

Ferretti R., T. Paolucci, G. Giuliani, T. Cherubini, L. Bernardini, and G. Visconti, 2003: Verification of high-resolution real-time forecasts over the Alpine region during the MAP SOP. *Quart. J. Roy. Meteor. Soc.*, **129B**, 587–607.

Ferrier, B. S., 1994: A double-moment, multiple-phase, four-class bulk ice scheme. Part I: Description. *J. Atmos. Sci.,* **51**, 249–280.

Ferrier, B. S., Y. Jin, Y. Lin, T. Black, E. Rogers, and G. DiMego, 2002: Implementation of a new grid-scale cloud and precipitation scheme in the NCEP Eta model. Preprints, 15th Conference on Numerical Weather Prediction, San Antonio, TX, Amer. Meteor. Soc., 280-283.

Field P. R., R. J. Hogan, P. R. A. Brown, A. J. Illingworth, T. W. Choularton, and R. J. Cotton, 2005: Parametrization of ice-particle size distributions for mid-latitude stratiform cloud. *Quart. J. Roy. Meteor. Soc.*, **131**, 1997–2017.

Fletcher, N. H., 1962: Physics of Rain Clouds. Cambridge University Press, 386 pp.

Fowler, L. D., D. A. Randall, and S. A. Rutledge, 1996: Liquid and ice microphysics in the CSU General Circulation Model. Part 1: Model description and simulated microphysical processes. *J. Climate.,* **9**, 489–529.

Fritsch, J.M., and coauthors, 1998: Quantitative Precipitation Forecasting: Report of the Eighth Prospectus Development Team, U.S. Weather Research Program. *Bull. Amer. Meteor. Soc.*, **79**, 285–299.

Fukuta N., and T. Takahashi, 1999: The growth of atmospheric ice crystals: A summary of findings in vertical supercooled cloud tunnel studies. *J. Atmos. Sci.*, **56**, 1963–1979.

Garvert M. F., B. A. Colle, and C. F. Mass, 2005a: The 13–14 December 2001 IMPROVE-2 event. Part I: Synoptic and mesoscale evolution and comparison with a mesoscale model simulation. *J. Atmos. Sci.*, **62**, 3474–3492.

Garvert M. F., C. P. Woods, B. A. Colle, C. F. Mass, P. V. Hobbs, M. P. Stoelinga, and J. B. Wolfe, 2005b: The 13–14 December 2001 IMPROVE-2 event. Part II: Comparison of MM5 model simulations of clouds and precipitation with observations. *J. Atmos. Sci.*, **62**, 3520–3534.

Garvert, M. F., B. F. Smull, and C. F. Mass, 2007: Multiscale mountain waves influencing a major orographic precipitation event. *J. Atmos. Sci*. **64**, 711–737.

Georgis, J-F, F. Roux, M. Chong, and S. Pradier, 2003: Triple-Doppler radar analysis of the heavy rain event observed in the Lago Maggiore region during MAP IOP2b. *Quart. Roy. Meteor. Soc.*, **129**, 495–522.

Gilmore, M. S., J. M. Straka, and E. N. Rasmussen, 2004: Precipitation uncertainty due to variations in precipitation particle parameters within a simple microphysics scheme. *Mon. Wea. Rev.*, **132**, 2610–2627.

Girard, E. and J.A. Curry, 2001: Simulation of arctic low-level clouds observed during the FIRE Arctic Clouds Experiment using a new bulk microphysics scheme. *J. Geophys. Res.,* **106**, 15139-15154.

Grell, G. A., J. Dudhia, and D. R. Stauffer, 1994: A description of the fifth-generation Penn State/NCAR Mesoscale Model (MM5). NCAR Tech. Note NCAR/TN-398+STR, 138 pp. [Available from National Center for Atmospheric Research, PO Box 3000, Boulder, CO 80307.].

Grubisić V., R. K. Vellore, and A. W. Huggins, 2005: Quantitative precipitation forecasting of wintertime storms in the Sierra Nevada: Sensitivity to the microphysical parameterization and horizontal resolution. *Mon. Wea. Rev.* ***133,*** 2834-2859.

Hall, W. D, 1980: A detailed microphysical model within a two-dimensional dynamic framework: Model description and preliminary results. *J. Atmos. Sci.,* **37**, 2486–2507.

Hanesch M., 1999: Fall velocity and shape of snowflakes. Ph.D. thesis, Swiss Federal Institute of Technology, Zurich, Switzerland, 117 pp. [Available online at http://e-collection.ethbib.ethz.ch/cgi-bin/show.pl?type=diss&nr=1332.].

Hashino, T., and G. Tripoli, 2007: the spectral ice habit prediction system (SHIPS), part I: model description and simulation of vapor deposition process. *J. Atmos. Sci.,* **64**, 2210-2236.

Heymsfield A. J., 1982: A comparative study of the rates of development of potential graupel and hail embryos in high plains storms. *J. Atmos. Sci.*, **39**, 2867–2897.

Heymsfield A., and M. Kajikawa, 1987: An improved approach to calculating terminal

velocities of plate-like crystals and graupel. *J. Atmos. Sci.*, **44**, 1088–1099.

Heymsfield A. J., A. Bansemer, and C. H. Twohy, 2007: Refinements to ice particle mass dimensional and terminal velocity relationships for ice clouds. Part I: Temperature dependence. *J. Atmos. Sci.*, **64**, 1047–1067.

Heymsfield, A.J., and coauthors, 2008: Testing IWC Retrieval Methods Using Radar and Ancillary Measurements with In Situ Data. *J. Appl. Meteor. Climate*, **47**, 135–163.

Hill, F. F., K. A. Browning, and M. J. Bader, 1981: Radar and rain gauge observations of orographic rain over South Wales. *Quart. J. Roy. Meteor. Soc.*, **107**, 643-670.

Hogan R. J., M. P. Mittermaier, and A. J. Illingworth, 2006: The retrieval of ice water content from radar reflectivity factor and temperature and its use in the evaluation of a mesoscale model. *J. Appl. Meteor. Climatol.*, **45**, 301–317.

Hong, S.-Y., and H.-L. Pan, 1996: Nonlocal boundary layer vertical diffusion in a medium-range forecast model. *Mon. Wea. Rev.,* **124**, 2322–2339.

Hong, S.-Y., Juang H. H., and Q. Y. Zhao. 1998: Implementation of Prognostic Cloud Scheme for a Regional Spectral Model. *Mon. Wea. Rev*., **126,** 2621–2639.

Hong, S.-Y., Dudhia J., and S. H. Chen. 2004: A Revised Approach to Ice Microphysical Processes for the Bulk Parameterization of Clouds and Precipitation. *Mon. Wea. Rev.,* **132**, 103–120.

Hong S.-Y., and J.J. Lim, 2006: the WRF single-moment 6-class microphysics scheme (WSM6), 2006: *Journal of the Korean meteorological society*, **42**, 129-151.

Houze R. A., P. V. Hobbs, P. H. Herzegh, and D. B. Parsons, 1979: Size distributions of precipitation particles in frontal clouds. *J. Atmos. Sci*., **36**, 156–162.

Houze, R. and S. Medina, 2005: Turbulence as a mechanism for orographic precipitation enhancement. *J. Atmos. Sci.*, **62**, 3599–3623.

Janjic, Z. I., 1994: The step-mountain eta coordinate model: Further development of the convection, viscous sublayer, and turbulence closure schemes. *Mon. Wea. Rev.,* **122**, 928–945.

Jiang Q., and R. B. Smith, 2003: Cloud timescales and orographic precipitation. *J. Atmos., Sci*, **60**, 1159–1172.

Jiang, H., W. R. Cotton, J. O. Pinto, J. A. Curry, and M. J. Weissbluth, 2000: Cloud resolving simulations of mixed-phase arctic stratus observed during BASE: Sensitivity to concentration of ice crystals and large-scale heat and moisture advection. *J. Atmos. Sci.,* **57**, 2105–2117.

Kain J., and M. Fritsch, 1993: Convective parameterization for mesoscale models: The Kain–Fritsch scheme. The Representation of Cumulus Convection in Numerical Models, Meteor. Monogr., No. 24, Amer. Meteor. Soc., 165–170.

Kain, J. S., 2004: The Kain–Fritsch convective parameterization: An update. *J. Appl. Meteor.,* **43**, 170–181.

Kessler E., 1969: On the Distribution and Continuity of Water Substance in Atmospheric Circulations. Meteor. Monogr., No. 32, Amer. Meteor. Soc., 84 pp.

King W. D., D. A. Parkin, and R. J. Handsoworth, 1978: A hot wire liquid water device having fully calculated response characteristics. *J. Appl. Meteor.*, **17**, 1809–1813.

Kirshbaum, D.J., and D.R. Durran, 2005: Atmospheric Factors Governing Banded Orographic Convection. *J. Atmos. Sci.*, **62**, 3758–3774.

Koch, S. E., B. Ferrier, M. T. Stoelinga, E. Szoke, S. J. Weiss, and J. S. Kain, 2005: The use of simulated radar reflectivity fields in the diagnosis of mesoscale phenomena from high-resolution WRF model forecasts. *32nd Radar Meteorology Conference*, Albuquerque, New Mexico, CD-ROM, J4J.7.

Koenig, L.R., 1971: Numerical modeling of ice deposition. *J. Atmos. Sci*., **28**, 226-237.

Kruger, S. K., Q. Fu, K. N. Liou, and H.-N. S. Chin, 1995: Improvements of an ice-phase microphysics parameterization in numerical simulations of tropical convection. *J. Appl. Meteor.,* **34**, 281–287.

Lin Y. L., R. Farley, and H. D. Orville, 1983: Bulk parameterization of the snow field in a cloud model. *J. Climate Appl. Meteor*., **22**, 1065–1092.

Lin Y.-L., S. Chiao, T.-A. Wang, M. L. Kaplan, and R. P. Weglarz, 2001: Some common ingredients for heavy orographic rainfall and their potential application for prediction. *Wea. Forecasting*, **16**, 633–660.

Lin, Y., and B. A. Colle, 2008: The 4-5 December 2001 IMPROVE-2 event: Observed microphysics and comparison with the WRF model. *Mon. Wea. Rev*., accepted.

Liu C.-L., and A. J. Illingworth, 2000: Toward more accurate retrievals of ice water content from radar measurements of clouds. *J. Appl. Meteor.*, **39**, 1130–1146.

Liu, Y., and P. H. Daum, 2004: Parameterization of the autoconversion process. Part I: Analytical formulation of the Kessler-type parameterizations. *J. Atmos. Sci.*, **61**, 1539–1548.

Locatelli J., and P. Hobbs, 1974: Fall speeds and masses of solid precipitation particles. *J. Geophys. Res.*, **79**, 2185–2197.

Lohmann, U., N. McFarlane, L. Levkov, K. Abdella, and F. Albers, 1999: Comparing different cloud schemes of a single column model by using mesoscale forcing and nudging technique. *J. Climate.,* **12**, 438–461.

Lynn, B. H, A. P Khain, J Dudhia, D Rosenfeld, A Pokrovsky, and A Seifert, 2005: Spectral (bin) microphysics coupled with a mesoscale model (MM5). Part II: Simulation of a CaPE rain event with a squall line. *Mon. Wea. Rev.,* **133**, 59–71.

Manning K. W., and C. A. Davis, 1997: Verification and sensitivity experiments for the WISP94 MM5 forecasts. *Wea. Forecasting*, **12**, 719–735.

Marcus, S., J. Kim, T. Chin, D. Danielson, and J. Laber, 2007: Influence of GPS Precipitable Water Vapor Retrievals on Quantitative Precipitation Forecasting in Southern California. *J. Appl. Meteor.*, **46**, 1828–1839.

Marshall, J. S, and W. M Palmer, 1948: The distribution of raindrops with size. *J. Meteor.,* **5**, 165–166.

Marwitz, J. D., 1987a: Deep orographic storms over the Sierra Nevada. Part I: Thermodynamic and kinematic structure. *J. Atmos. Sci.*, **44**, 159-173.

Marwitz, J. D., 1987b: Deep orographic storms over the Sierra Nevada. Part II: The precipitation processes. *J. Atmos. Sci.*, **44**, 174-185

Medina, S. and R. Houze, 2003: Air motions and precipitation growth in alpine storms. *Quart. J. Roy. Meteor. Soc.,* **129**, 345–371.

Medina, S., B. Smull, R. Houze and M. Steiner, 2005: Cross-barrier flow during orographic precipitation events: Results from MAP and IMPROVE. *J. Atmos. Sci*., **62**, 3850–3598.

Medina, S., E. Sukovich, and R. A. Houze, Jr., 2007: Vertical structures of precipitation in cyclones crossing the Oregon Cascades. *Mon. Wea. Rev*., **135**, 3565-3586.

Meyers, M.P., R.L. Walker, J.Y. Harrington, and W.R. Cotton, 1997: New RAMS cloud microphysics parameterization. Part II: The two-moment scheme. Atmos. Res., **45**, 3-39.

Milbrandt J. A., and M. K. Yau, 2005: A multimoment bulk microphysics parameterization. Part I: Analysis of the role of the spectral shape parameter. *J. Atmos. Sci.*, **62**, 3051–3064.

Milbrandt, J.A, M.K. Yau, J. Mailhot, and S. Bélair, 2008: Simulation of an Orographic Precipitation Event during IMPROVE-2. Part I: Evaluation of the Control Run using a Triple-Moment Bulk Microphysics Scheme. *Mon. Wea. Rev.,* in press.

Minder J.R., D.R. Durran, G.H. Roe, and A.M. Anders, 2008: The climatology of small-scale orographic precipitation over the Olympic Mountains: Patterns and processes. *Quart. J. Roy. Meteor. Soc.,* **134**, 817-839.

Mitchell D. L., 1996: Use of mass- and area-dimensional power laws for determining precipitation particle terminal velocities. *J. Atmos. Sci*., 53, 1710–1723.

Morrison, H., and J. O. Pinto., 2005: Mesoscale Modeling of Springtime Arctic Mixed-Phase Stratiform Clouds Using a New Two-Moment Bulk Microphysics Scheme**.** *J. Atmos. Sci*., **62**, 3683–3704.

Morrison, H., J. A. Curry, and V. I. Khvorostyanov, 2005: A new double-moment microphysics scheme for application in cloud and climate models. Part I: Description. *J. Atmos. Sci.,* **62**, 1665–1677.

Morrison H., and W.W. Grabowski, 2008: A novel approach for representing ice microphysics in models: description and tests using a kinematic framework. *J. Atmos. Sci., in press.*

Mosimann L., E. Weingartner, and A. Waldvogel, 1994: An analysis of accreted drop sizes and mass on rimed snow crystals. *J. Atmos. Sci.*, **51**, 1548–1558.

Mosimann L., 1995: An improved method for determining the degree of snow crystal riming by vertical Doppler radar. *Atmos. Res.*, **37**, 305–323.

Neiman P. J., F. M. Ralph, A. B. White, D. E. Kingsmill, and P. O. G. Persson, 2002: The statistical relationship between upslope flow and rainfall in California's coastal mountains: Observations during CALJET. *Mon. Wea. Rev.*, **130**, 1468–1492.

Neiman P. J., P. O. G. Persson, F. M. Ralph, D. P. Jorgensen, A. B. White, and D. E. Kingsmill, 2004: Modification of fronts and precipitation by coastal blocking during an intense landfalling winter storm in southern California: Observations during CALJET. *Mon. Wea. Rev.*, **132**, 242–273.

Petersen W. A., and Coauthors, 1999: Mesoscale and radar observations of the Fort Collins flash flood of 28 July 1997. *Bull. Amer. Meteor. Soc*, **80**, 191–216.

Pielke, R. A., W. R. Cotton, R. Walko, C. J. Tremback,W. A. Lyons, L. D. Grasso, M. E. Nichols, M. D. Moran,D. A. Weseley, T. J. Lee, and J. H. Copeland. 1992. Acomprehensive meteorological modeling system—RAMS, *Meteorol. Atmos. Phys*., **49**, 69-91.

Pontrelli M. D., G. Bryan, and J. M. Fritsch, 1999: The Madison County, Virginia, flash flood of 27 June 1995. *Wea. Forecasting*, **14**, 384–404.

Protat A., J. Delanoë, D. Bouniol, A. J. Heymsfield, A. Bansemer, and P. Brown, 2007: Evaluation of ice water content retrievals from cloud radar reflectivity and

temperature using a large airborne in situ microphysical database. *J. Appl. Meteor. Climatol.*, **46**, 557–572.

Pruppacher H. R., and J. D. Klett, 1997: *Microphysics of Clouds and Precipitation*. 2nd ed. Kluwer Academic, 954 pp.

Ralph F. M., P. J. Neiman, G. A. Wick, and C. S. Velden, 2004: Satellite and CALJET aircraft observations of atmospheric rivers over the eastern North Pacific Ocean during the winter of 1997/98. *Mon. Wea. Rev.*, **132**, 1721–1745.

Ralph F. M., Coauthors, 2005: Improving short-term (0–48 h) cool-season quantitative precipitation forecasting: Recommendations from a USWRP workshop. *Bull. Amer. Meteor. Soc.*, **86**, 1619–1632.

Rauber R. M., 1992: Microphysical structure and evolution of a Central Sierra Nevada orographic cloud system. *J. Appl. Meteor.*, **31**, 3–24.

Reisner J., R. M. Rasmussen, and R. T. Bruintjes, 1998: Explicit forecasting of supercooled liquid water in winter storms using the MM5 mesoscale model. *Quart. J. Roy. Meteor. Soc.*, **124**, 1071–1107.

Richard E., A. Buzzi, and G. Zängl, 2007: Quantitative precipitation forecasting in the Alps: The advances achieved by the Mesoscale Alpine Programme. *Quart. J. Roy. Meteor. Soc.*, **133**, 831-846.

Roe G. H., 2005: Orographic precipitation. *Annu. Rev. Earth Planet. Sci.*, **33**, 645–671.

Roebber P. J., Swanson K. L., and J. K., Ghorai, 2008: Synoptic control of mesoscale precipitating systems in the Pacific Northwest. *Mon. Wea. Rev.,* in Press.

Rogers, R. R, and M. K Yau, 1989: *A Short Course in Cloud Physics*. Pergamon, 293 pp.

Rotstayn, L. D., 1997: A physically based scheme for the treatment of stratiform clouds and precipitation in large-scale models. Part 1: Description. *Quart. J. Roy. Meteor. Soc.,* **123**, 1227–1282.

Rotunno, R., R. Ferretti, 2001: Mechanisms of intense alpine rainfall. *J. Atmos. Sci.*, **58**, 1732-1749.

Rotunno, R., and R. A. Houze, Jr., 2007: Lessons on orographic precipitation from the Mesoscale Alpine Programme. *Quart. J. Roy. Meteor. Soc.,* **133**, 811-830.

Rutledge, S. A., and P. V. Hobbs, 1983: The mesoscale and microscale structure and organization of clouds and precipitation in mid-latitude cyclones: A model for the "seeder-feeder" process in warm-frontal rainbands. *J. Atmos. Sci.,* **40**, 1185–1206.

Rutledge, S. A., and P. V. Hobbs, 1984: The mesoscale and microscale structure and

organization of clouds and precipitation in midlatitude cyclones. XII: A diagnostic modeling study of precipitation development in narrow cold-frontal rainbands. *J. Atmos. Sci.,* **41**, 2949–2972.

Ryan B. F., 1996: On the global variation of precipitating layer clouds. *Bull. Amer. Meteor. Soc.*, **77**, 53–70.

Schultz, D.M., and Coauthors, 2002: Understanding Utah Winter Storms: The Intermountain Precipitation Experiment. *Bull. Amer. Meteor. Soc*., **83**, 189–210.

Sinclair M. R., D. S. Wratt, R. D. Henderson, and W. R. Gray, 1997: Factors affecting the distribution and spillover of precipitation in the Southern Alps of New Zealand—A case study. *J. Appl. Meteor.*, **36**, 428–442.

Skamarock W.C., J.B. Klemp, J. Dudhia, D.O. Gill, D.M. Barker, W. Wang, and J.G. Powers, 2005: A description of the Advanced Research WRF, Version 2. NCAR Tech. Note., NCAR/TN-468+STR, 88 pp. [Available from UCAR Communications, P.O. Box 3000, Boulder, CO 80307].

Skamarock W.C., 2006: Positive-definite and monotonic limiters for unrestricted-time-step transport schemes. *Mon. Wea. Rev.*, **134**, 2241–2250.

Skamarock W.C., and M.L. Weisman, 2008: The impact of positive-definite moisture transport on NWP precipitation forecast. Submitted to *Mon. Wea. Rev.*

Smith R. B., 1979: The influence of mountain on the atmosphere. *Adv. Geophys*., **21**, 87-230.

Smith, R. B., Q. Jiang, M. Fearon, P. Tabary, M. Dorninger, and J. Doyle, 2003: Orographic precipitation and air mass transformation: An alpine example. *Quart. J. Roy. Meteor. Soc.,* **129**, 433-454.

Smith R. B., I. Barstad 2004: A Linear Theory of Orographic Precipitation. *J. Atmos. Sci*., **61**, 1377–1391.

Smith R. B., I. Barstad and L. Bonneau, 2005: Orographic precipitation and Oregon's climate transition. *J. Atmos. Sci*., **62**, 177–191.

Smith, R.B., 2006: Progress on the theory of orographic precipitation. Chapter 1 in *Special Paper 398: Tectonics, Climate, And Landscape Evolution*, Geological Society of America, Boulder, Colorado.

Stauffer, D. R., and N. L. Seaman, 1990: Use of four-dimensional data assimilation in a limited area mesoscale model. Part I: Experiments with synoptic-scale data. *Mon. Wea. Rev.*, **118**, 1250–1277.

Stoelinga, M., and Coauthors, 2003: Improvement of microphysical parameterization through observational verification experiment. *Bull. Amer. Meteor. Soc*., **84**, 1807-1826.

Stoelinga M, H. McCormick, and J. D. Locatelli, 2007: Prediction of degree of riming within a bulk microphysical scheme. Presented on 22nd Conference on Weather Analysis and Forecasting/18th Conference on Numerical Weather Prediction.

Stoelinga M. T., J. D. Locatelli, and C. P. Woods, 2007: The occurrence of "irregular" ice particles in stratiform clouds. *J. Atmos. Sci.*, **64**, 2740–2750.

Straka J. M., and E. R. Mansell, 2005: A bulk microphysics parameterization with multiple ice precipitation categories. *J. Appl. Meteor.*, **44**, 445–466.

Tao W.-K., J. S. Simpson, and M. McCumber, 1989: An ice-water saturation adjustment. *Mon. Wea. Rev.*, **117**, 231–235.

Tao W.-K., and J. S. Simpson, 1993: Goddard cumulus ensemble model. Part I: Model description. *Terr. Atmos. Oceanic Sci.*, **4**, 35-72.

Tao, W.-K, and Coauthors, 2003: Microphysics, radiation and surface processes in a non-hydrostatic model. *Meteor. Atmos. Phys.,* **82**, 97–137.

Thompson, G., R. M. Rasmussen, and K. Manning, 2004: Explicit forecasts of winter precipitation using an improved bulk microphysics scheme. Part I: Description and sensitivity analysis. *Mon. Wea. Rev.,* **132**, 519–542.

Thompson, G., P.R. Field, R. M. Rasmussen, and W.D. Hall, 2008: Explicit forecasts of winter precipitation using an improved bulk microphysics scheme. Part II: Implementation of a new snow parameterization. *Mon. Wea. Rev.* In press

Tripoli, G. J., and W. R. Cotton, 1982: The ColoradoStateUniversity three-dimensional cloud/mesoscalemodel— 1982. Part I: General theoretical framework and sensitivity experiments, *J. Rech. Atmos.,* **16**, 185-220.

Twohy C. H., A. J. Schanot, and W. A. Cooper, 1997: Measurement of condensed water content in liquid and ice clouds using an airborne counterflow virtual impactor. *J. Atmos. Oceanic Technol.*, **14**, 197–202.

Vaillancourt P. A., A. Tremblay, S. G. Cober, and G. A. Isaac, 2003: Comparison of aircraft observations with mixed-phase clouds simulations. *Mon. Wea. Rev.*, **131**, 656–671.

Walko R. L., W. R. Cotton, M. P. Meyers, and J. Y. Harrington, 1995: New RAMS cloud microphysics parameterization. Part I: The single-moment scheme. *Atmos. Res.,* **38**, 29–62.

Westbrook C. D., R. J. Hogan, and A. J. Illingworth, 2008: The capacitance of pristine ice crystals and aggregate snowflakes. *J. Atmos. Sci*., **65**, 206–219.

White, A. B., P. J. Neiman, F. M. Ralph, D. E. Kingsmill, and P. O. G. Persson, 2003: Coastal orographic rainfall processes observed by radar during the California land-falling jets experiment. *J. Hydromet.*, **4**, 264–282.

Wilson, D.R. and Ballard, S.P., 1999. A microphysically based precipitation scheme for the UK Meteorological Office Unified Model. *Q.J.R. Meteorol. Soc.,* **125**, 1607-1636.

Woods, C.P., M.T. Stoelinga, J.D. Locatelli, and P.V. Hobbs, 2005: Microphysical Processes and Synergistic Interaction between Frontal and Orographic Forcing of Precipitation during the 13 December 2001 IMPROVE-2 Event over the Oregon Cascades. *J. Atmos. Sci.*, **62**, 3493–3519.

Woods, C.P., M.T. Stoelinga, J.D. Locatelli, 2007: The IMPROVE-1 Storm of 1–2 February 2001. Part III: Sensitivity of a Mesoscale Model Simulation to the Representation of Snow Particle Types and Testing of a Bulk Microphysical Scheme with Snow Habit Prediction. *J. Atmos. Sci.*, **64**, 3927–3948.

Wu, X., W. W. Grabowski, and M. W. Moncrieff, 1998: Long-term behavior of cloud systems in TOGA COARE and their interactions with radiative and surface properties. Part I: Two-dimensional modeling study. *J. Atmos. Sci.,* **55**, 2693–2714.

Zängl G, 2007. Small-scale variability of orographic precipitation in the Alps: Case-studies and semi-idealized numerical simulations. *Q. J. R. Meteorol. Soc.* **133**: 1701-1716.

Zawadzki I., F. Fabry, and W. Szyrmer, 2001: Observations of supercooled water and of secondary ice generation by a vertically pointing X-band Doppler radar. *Atmos. Res.*, **59–60**, 343–359.

Zikmunda, J., and G. Vali, 1972: Fall patterns ad fall velocities of rimed ice crystals. *J. Atmos. Sci.,* **29**, 1334-1347.

Zhao Q, F., and Carr, 1997: A Prognostic Cloud Scheme for Operational NWP Models. *Mon. Wea. Rev.,* **125**, 1931–1953.